Iron Catalysts for Fischer-Tropsch Synthesis derived from Metal-Organic Frameworks Fundamentals and Performance

Wezendonk, Tim

DOI
10.4233/uuid:0b35cd81-4299-48bf-8751-e9ba2488659b

Publication date
2018

Document Version
Final published version

Citation (APA)
Wezendonk, T. (2018). *Iron Catalysts for Fischer-Tropsch Synthesis derived from Metal-Organic Frameworks: Fundamentals and Performance*. [Dissertation (TU Delft), Delft University of Technology]. https://doi.org/10.4233/uuid:0b35cd81-4299-48bf-8751-e9ba2488659b

Iron Catalysts for Fischer-Tropsch Synthesis derived from Metal-Organic Frameworks: Fundamentals and Performance

Proefschrift

ter verkrijging van de graad van doctor
aan de Technische Universiteit Delft,
op gezag van de Rector Magnificus prof. dr. ir. T.H.J.J. van der Hagen;
voorzitter van het College voor Promoties,
in het openbaar te verdedigen op
vrijdag 2 maart 2018 om 10:00 uur

door
Tim Arnold WEZENDONK
Master of Science in Chemical Engineering, Technische Universiteit Delft
geboren te Duiven

Dit proefschrift is goedgekeurd door de promotoren
Prof. dr. J. Gascon Sabate en Prof. dr. F. Kapteijn

Samenstelling van de promotiecommissie

Rector Magnificus	Voorzitter
Prof. dr. F. Kapteijn	Technische Universiteit Delft, promotor
Prof. dr. J. Gascon Sabate	Technische Universiteit Delft, promotor

Onafhankelijke leden

Prof. dr. J.J.C. Geerlings	Technische Universiteit Delft
Prof. dr. M. Rønning	Technisch-natuurwetenschappelijke Universiteit van Noorwegen
Prof. Dr. A. Martínez Feliu	Polytechnische Universiteit van Valencia
Prof. Dr. Dipl.-Ing. M. Claeys	Universiteit van Kaapstad
Dr. ir. A.P. van Bavel	Shell Global Solutions International
Prof. dr. E.J.R. Sudhölter	Technische Universiteit Delft, reservelid

Het onderzoek beschreven in dit proefschrift is uitgevoerd binnen de sectie Catalysis Engineering van de afdeling Chemical Engineering aan de faculteit Technische Natuurwetenschappen van de Technische Universiteit Delft.

Proefschrift, Technische Universiteit Delft
Met samenvatting in het Nederlands
ISBN: 978-94-028-0962-6

Ontwerp omslag: Tim A. Wezendonk
Gedrukt door Ipskamp Printing, Enschede

Table of Contents

Chapter

1

Introduction to the Metal-Organic Framework Mediated Synthesis Method and the Fischer-Tropsch Synthesis

In this general introduction, an explanation to the novel catalyst synthesis using metal-organic frameworks (MOFs) is given. This MOF mediated synthesis (MOFMS) is a highly flexible synthesis method, in which an array of different Fe-MOFs can be used to produce unique catalysts combining a high loading of active metal and a high dispersion of the nanoparticles. The utilization of iron-based MOFs in the MOFMS results in the formation of Fe@C catalysts for the Fischer-Tropsch synthesis (FTS) process, where non-petroleum feedstock is converted toward conventional bulk chemicals and liquid transportation fuels through a polymerization reaction of the gaseous feedstock derived from coal, biomass or natural gas. Current challenges in iron-based FTS include achieving increased stability and activity of the catalysts. This thesis focusses on the development of MOFMS for the use of Fe@C as highly active and stable FTS catalyst and elucidates the structural and chemical changes the MOF undergoes during transformation into FTS catalyst. Furthermore, the Fe@C catalysts are an excellent model system to control the formation of active phase iron carbides during Fischer-Tropsch synthesis, and as such allow for a fundamental study into the intrinsic activity and stability of the various iron carbide phases.

This chapter contains parts of the following publications:

L. Oar-Arteta, T.A. Wezendonk, X. Sun, F. Kapteijn, J. Gascon, Metal–Organic Framework-Mediated Synthesis in Catalysis, in: *Nanotechnology in Catalysis*, Wiley-VCH Verlag GmbH & Co. KGaA, **(2017)**, pp. 225-250

L. Oar-Arteta, T.A. Wezendonk, X. Sun, F. Kapteijn and J. Gascon, *Mater. Chem. Front.*, **(2017)**, 1, 1709-1745.

1.1 General Introduction

Supported metals and metal oxides are amongst the most widely used heterogeneous catalysts. Most oxidation, redox, CO insertion or hydrogen transfer reactions require such catalytic materials. Metal oxides comprise bulk structures of which the specific surface is related to the performance of the catalyst, while the bulk of the material contributes to its stability. In order to achieve highly active catalysts, much effort now revolves around converting bulk systems to dispersed nanoparticles on porous supports, thus increasing the number of surface atoms where catalysis takes place. The choice of support is crucial as it provides the high surface area for stabilizing and anchoring the active component. The active phase – support interactions, dictated by the surface chemistry of the support and the nanoparticles, are responsible for the dispersion and the chemical state of the active phase [1]. The tendency of nanoparticles to grow into larger crystallites is an impediment for high and stable catalytic performance. Exemplarily, loss of active surface area by metal particle growth is a major cause of irreversible deactivation for supported catalysts. In specific cases, particle growth may be mitigated by tuning the properties of individual nanoparticles, such as size, composition and interaction with the support [2]. Novel nanotechnology tools and synthetic advances have provided new roads for the manufacture of support structures for improved catalysts with high concentrations of dispersed nanoparticles. In addition, fundamental studies have helped to identify the exact nature and the role of active sites, providing invaluable feedback to catalysis engineers. These combined advances have led to the design of new catalysts comprising improved size- and shape distributions of the active phase located on more specific supports with an increasingly desired nature of the structure [3, 4]. Nevertheless, engineering heterogeneous catalysts with molecular precision is an ongoing challenge that may eventually allow the rational design of materials with predictable properties [5].

Alongside the advances in nanotechnology, worldwide research into the production of conventional fuels and commodity chemicals from alternative feedstocks has increased tremendously, mainly due the depletion of crude oil resources and environmental concerns. The Fischer-Tropsch synthesis (FTS) is a process for the flexible production of key chemicals and fuels from non-petroleum-based feedstocks. The synthesis reaction comprises a heterogeneously catalyzed polymerization, where synthesis gas is converted into a wide spectrum of hydrocarbon chains (**Equation 1.1**) [6-8]. The synthesis gas, or syngas, a mixture of CO and H_2, is typically derived from natural gas, coal, or biomass, without the need for petroleum-based feedstock. Cobalt, ruthenium, iron and nickel are all active metals in FTS, but only iron and cobalt are used industrially. Although the use of a cheaper iron catalyst is economically preferred over the widely used cobalt catalyst, manufacturing methods that prevent the fast deactivation of iron catalysts due to sintering, carbon deposition, and phase changes have proven challenging. Owing to their high intrinsic activity, stability and selectivity towards long chain hydrocarbons, cobalt-based catalysts remain the preferred choice for the

production of liquid fuels. However, iron-based catalysts have some superior properties over cobalt-based catalysts, especially for coal- or biomass-derived syngas, namely: 1) Iron is much cheaper and more widely available than cobalt; 2) Iron is active in the water-gas-shift reaction under typical FTS conditions (**Equation 1.2**), enabling the *in situ* readjustment of the H_2/CO molar ratio for the conversion of hydrogen-lean syngas originating from coal or biomass (**Equation 1.3**) [6]; and 3) under high temperature FT conditions (HTFT), the product slate of iron catalysts is more directed toward short-chain unsaturated hydrocarbons and short-chain oxygenates, both among the most important bulk chemicals. The HTFT operational regime is therefore often referred to as Fischer-Tropsch to Olefins (FTO). The main challenge of iron-based FTS catalysts is to overcome high deactivation rates due to sintering, carbon deposition, and iron phase changes, i.e., interconversion of the active iron carbide phase into iron oxides [6, 7, 9, 10]. Under FTS conditions, bulk iron catalysts display poor mechanical stability and fragment due to carbon deposits or to density differences between the iron phases [11, 12]. The catalyst fragmentation may result in the formation of fines which leads to detrimental reactor performance and operational problems such as pressure drop and eventual fouling. Hence, the design of new and highly active catalysts is severely limited by stability issues under FTS.

$$x\,\mathrm{CO} + 2x\,\mathrm{H_2} \rightarrow x\,(-\mathrm{CH_2}-) + x\,\mathrm{H_2O} \quad (\mathbf{1.1})$$

$$y\,\mathrm{H_2O} + y\,\mathrm{CO} \rightarrow y\,\mathrm{H_2} + y\,\mathrm{CO_2} \quad (\mathbf{1.2})$$

$$(x+y)\,\mathrm{CO} + (2x-y)\,\mathrm{H_2} \rightarrow x\,(-\mathrm{CH_2}-) + (x-y)\,\mathrm{H_2O} + y\,\mathrm{CO_2} \quad (\mathbf{1.3})$$

In the last few years, metal-organic frameworks (MOFs) have drawn the attention of the research community in field of heterogeneous catalysis as possible candidates for advanced catalyst design. MOFs are crystalline compounds consisting of infinite lattices built up of an inorganic secondary building unit (SBU) comprising metal ions or clusters, and organic linkers, connecting the SBUs by coordination bonds of moderate strength (**Figure 1.1**). MOFs contain three well-differentiated parts where the catalytic function can be allocated: the metal cluster, the organic linker, and the pore space [13]. Abundant examples in literature have demonstrated the potential of MOFs in catalysis [14-18]. However, MOFs are not only envisioned as catalytic solids themselves, but also as precursors for developing new materials with improved catalytic properties. The conversion of a MOF into a heterogeneous catalyst was coined MOF mediated synthesis (MOFMS), which in essence consists of a heat treatment under a certain atmosphere. Depending upon the heat treatment and its atmosphere, MOF precursors are converted into different types of bulk and supported catalytic materials ranging from metal oxides to nanostructured carbons and composites of nanoparticles embedded in a carbon matrix.

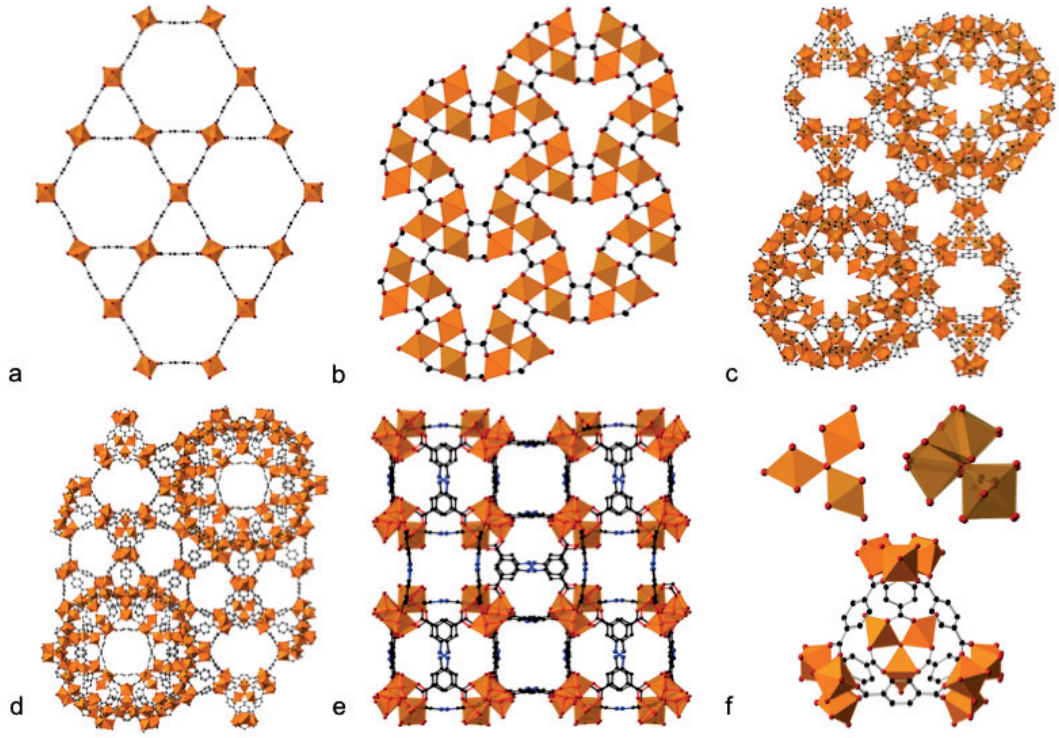

Figure 1.1 Some of the Fe-MOF topologies that are used in this Thesis: **a** MIL-68 **b** MIL-88A **c** MIL-100 **d** MIL-101 **e** MIL-127 and **f** the coordination of iron trimers and super tetrahedra present in the different structures.

In this thesis, the MOFMS is presented as a new method to produce highly dispersed iron nanoparticles in a carbon matrix for use as Fischer-Tropsch catalysts. Key characteristics of these Fe@C catalysts are the very high iron loading combined with an optimal dispersion of the active ironcarbide phase. The unique iron spatial confinement and the absence of large iron nanoparticles in the MOF-derived materials minimize catalyst deactivation, resulting in unrivalled activity and stable operation. In **Section 1.2** of this thesis, the history and context of the novel synthesis method MOFMS are reported. A short review of the MOFMS with Fe-based MOFs toward Fe@C catalysts is presented and the relevancy of this novel technique for the preparation of heterogeneous catalysts is highlighted. Before reviewing the different Fe@C catalytic applications found in literature, important parameters for the design of new catalysts *via* MOFMS are considered. The abovementioned section serves as an introductory reading to **Chapter 2 and Chapter 4** of this thesis, wherein the use of various Fe-MOFs as precursor for Fischer-Tropsch catalysts is investigated, and the fundamentals of the framework carbonization and the relation between pyrolysis temperature and the iron phase, loading, and dispersion are elucidated. In **Section 1.3** of this thesis, the current state-of-the-art regarding iron carbide phase correlation to FTS performance is assessed, reviewing the behavior of

unsupported and supported catalysts during the various activation methods and under subsequent FTS conditions. Thereafter, the correlation between the type of catalyst and activation method applied is established, in order to derive synthesis conditions for hexagonal carbide ε'-$Fe_{2.2}C$ and Hägg carbide χ-Fe_5C_2. The abovementioned section therefore serves as introductory reading to **Chapter 5** of this thesis, where MOFMS was applied as excellent tool for the controlled synthesis of a model system for fundamental understanding of the performance of iron carbides in the Fischer-Tropsch synthesis reaction. In **Section 1.4** of this thesis, the objectives of this thesis are formulated and a detailed outline of all the chapters is presented.

1.2 Metal-Organic Framework Mediated Synthesis (MOFMS)

1.2.1 Relevancy of MOMFS for Heterogeneous Catalysis

First, the synthesis of nanostructured metal oxides has been intensively investigated in recent years, with special emphasis on controlling the shape, composition and porosity of the resulting metal oxide [19]. The MOFMS is a promising technique for tailoring metal oxides in a simple manner. Calcination of MOFs in air is the usual approach for the preparation of metal oxides through MOFMS, although acid leaching and other heat treatments have also been applied. Second, carbon materials have found an increasing importance in catalytic processes, often acting as catalyst support or as active phase itself, due to the high surface area, chemical inertness and weak metal support interaction [20-22]. The main challenge in the case of carbon catalysts lies in the development of novel methods to tailor the porosity and morphology of the carbonaceous nanostructures [23]. Carbonization of MOFs yields well-structured hierarchical carbons by removing the metal phase during or after MOF carbonization by volatilization at high temperature or acid leaching, respectively. Third, supported catalysts comprise the high surface area for dispersing and anchoring the active metal or metal oxide nanoparticles, however, the tendency of nanoparticles to grow into larger crystallites is an impediment for stable catalytic performance [24]. Pyrolysis of the MOF in inert atmosphere leads to highly dispersed metal phases encapsulated in a porous carbon matrix, where the spatial restriction created by the carbon confinement minimizes sintering of the nanoparticles. The pyrolysis in inert atmosphere at temperatures above the MOF decomposition temperature may result in various degrees of framework carbonization, and is therefore the preferred strategy to obtain carbon embedded metal nanoparticles as supported catalyst analogue. However, contrary to the approach for carbons, the metal phase is retained in the resulting material, and typically, the framework is not fully carbonized. Thus, during the heat treatment, a part of the organic ligand decomposes and evaporates to the gas phase, whereas the remainder is partially carbonized into the carbon matrix in which the nanoparticles are embedded. A graphical summary of the approaches in MOFMS is depicted in **Figure 1.2**. Sun *et al.* [25] and Xia *et al.* [26] recently reviewed the extensive use of MOFMS during the last years in the field of electrochemical energy storage and conversion.

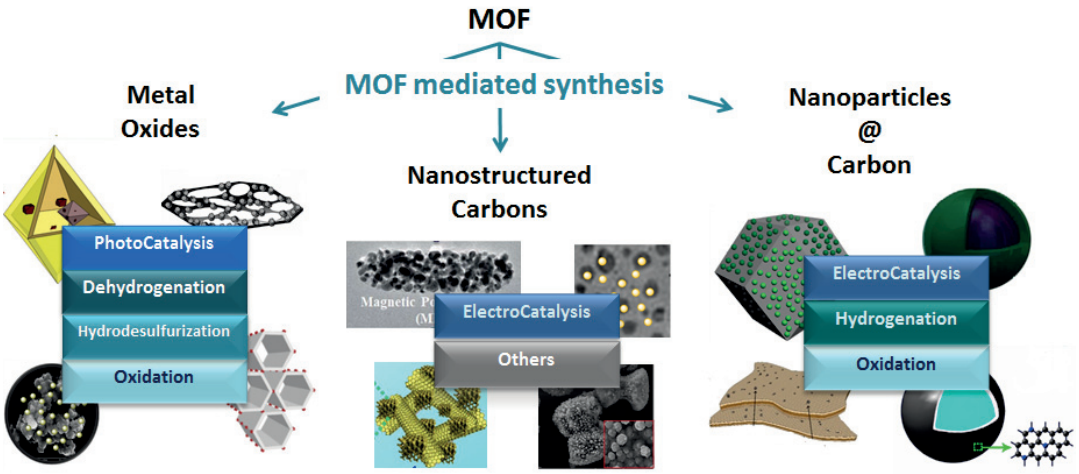

Figure 1.2 Examples of nanostructures obtained through the three main approaches in MOF Mediated synthesis and their applications in catalysis.

Oar-Arteta *et al.* [27, 28] provided very extensive reviews of MOFMS for the production of heterogeneous catalysts, gaining insight onto the matter by covering all the metals used in MOMFS. Nonetheless, the following sections are limited to Fe-MOFs in particular, given this thesis is devoted to the development of Fe@C materials for use in the Fischer-Tropsch synthesis reaction. It aims to give a comprehensive overview of the current situation of Fe-based MOFMS in heterogeneous catalysis synthesis, alongside providing the guidelines for the design of new generations of catalytic materials using MOFs as sacrificial agents.

1.2.2 General Considerations for MOFMS

When the decomposition temperature of the metal-organic framework is exceeded, the metal ions in the clusters lose coordination and form clusters that eventually become nanoparticles. The Gibbs free energy, reduction potential of metal ions and the proximity of the whether or not functionalized and partially carbonized linkers predict the formation of nanoparticles in a metallic, oxidic, or carbidic phase. During the formation of the nanoparticles, the mobility of the metal atoms is mainly determined by the Hüttig temperature and controls the particle size of the clusters. After confinement in the carbonized matrix, the Tammann temperature of the metal species governs the size of the resulting nanoparticles during the prolonged heating. Finally, according to the vapour pressure of the metal species, the metal phase will be retained in the material or evaporates. The organic linker plays a decisive role in defining the final porosity of the carbon matrix and its composition, but also the oxidation state of the metal species in the catalyst. For instance, oxygen-functionalized linkers will favour oxidation of species whereas nitrogen in the linker may result in the formation of highly

dispersed M-N species in the final catalyst. The proximity of additional carbon sources may induce increased degrees of reduction or carburization of metals during the pyrolysis. In contrast, calcination in air of the pristine MOF is a more straightforward procedure in the sense that it always leads to the formation of the corresponding metal oxide. In this case, the organic linker is readily volatilized when the decomposition temperature of the framework is exceeded. Further increasing of the temperature allows for tuning of the porosity of the metal oxide. However, adding a pyrolysis step prior to the calcination enhances the porosity of the resulting material to a large degree. The boiling point and associated vapour pressure of oxides is usually too high to consider possible evaporation during the MOFMS under oxidizing atmosphere. Although the organic linker plays an essential role in the composition of the final catalyst, it is the nature of the metal element that governs the MOF mediated synthesis and defines the characteristics of the resulting heterogeneous catalyst. In short, the parent MOF is selected according to the metal in its framework, whereas the organic linker and the synthesis conditions are intended as the tools for optimizing the final properties of the MOF mediated catalyst. Hence, MOF decomposition will follow according to its physical and chemical properties, of which the Gibbs free energy and Tammann and Hüttig temperature are key for understanding the obtained properties of the MOFMS-derived catalyst. Below, additional insight into these synthesis parameters is provided.

The Gibbs free energy (ΔG) of a reaction quantifies the thermodynamic potential necessary to allow a reaction to occur under given conditions. For the oxidation of metals, a negative value for ΔG indicates that the oxidation can proceed spontaneously without external inputs, while a positive value indicates that it will not commence. Widely used in extractive metallurgy, the Ellingham diagram (**Figure 1.3**) displays the formation free energy of oxides *versus* temperature [29]. The lower the position of a metal in the Ellingham diagram, the greater is the stability of its oxide and besides, the intersection of two lines in this diagram implies an oxidation-reduction equilibrium. Therefore, reduction using a given reductant is possible at temperatures above the intersection point where the ΔG line of that reductant is lower on the diagram than that of the metallic oxide to be reduced. In the MOFMS, the carbon formed during the heat treatment acts as the reducing agent and reduction of metal oxides is carried out by a carbothermic reaction. Likewise, when the number of electrons involved is the same, the Gibbs free energy of the oxidation follows exactly the opposite trend to the reduction potential of the corresponding metal ion for different metals. Accordingly, Das *et al.* quantified that MOFs comprising metal ions with a standard reduction potential of -0.27 V or higher, such as Co, Ni and Cu, always form pure metal nanoparticles during pyrolysis in N_2 up to 900 °C, whereas MOFs comprising metal ions with a reduction potential lower than -0.27 V, such as Mg, Al, Mn, Zn or Cr, tend to combine with the oxygen present in the organic part of the MOF and form metal oxide nanoparticles during the same pyrolysis treatment [30].

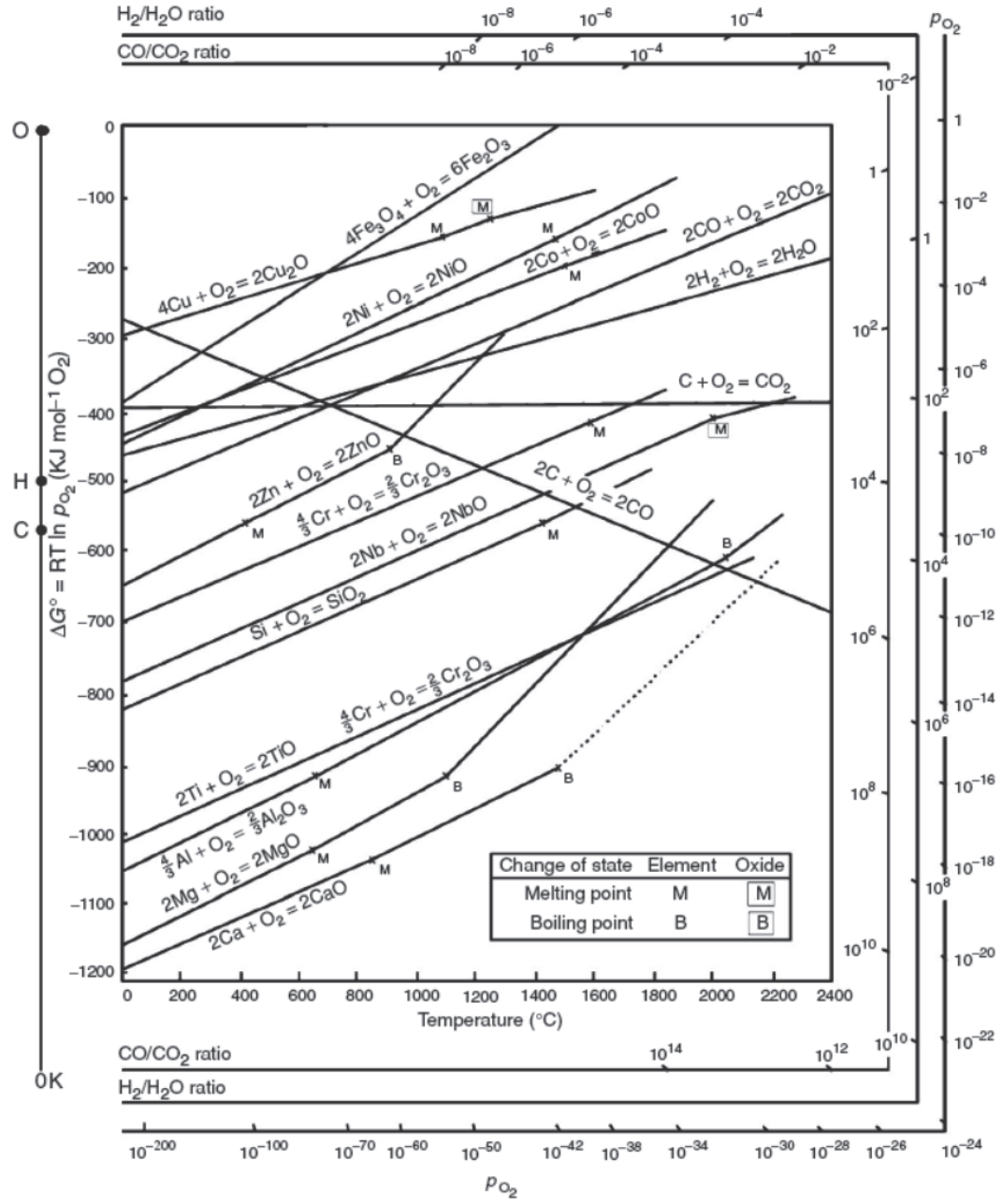

Figure 1.3 Ellingham-diagram for formation of oxides based on their standard free energy of formation over the temperature range, associated with reductant ratios and oxidizing potential [31].

Table 1.1 Melting points (T_m) and boiling (T_b) points of different metals [32].

Metal	T_m / °C	T_b / °C
Al	660	2519
Cr	1907	2671
Co	1495	2927
Cu	1085	2560
Fe	1538	2861
Mg	650	1090
Mn	1246	2061
Ni	1455	2913
Ru	2334	4150
Ti	1668	3287
V	1910	3407
Zn	420	907
Zr	1855	4409

As already mentioned at the start of this section, the Tammann and Hüttig temperature of the metal species are of high importance to the MOFMS. The Tammann temperature is approximately half the melting point of the metal under consideration, and the Hüttig temperature is approximately one third of the melting point of the metal (**Table 1.1**). In the lower temperature range of the Hüttig temperature, the surface species and atoms in defects acquire sufficient mobility to sinter and agglomerate. Increasing temperatures in the range of the Tammann temperature allow atoms and molecular segments in the solid to acquire sufficient energy for their bulk diffusion and reorganization of the structure. In the MOFMS, the Tammann temperature of the metal species is typically above the temperature required to make the organic framework collapse, whereas the Hüttig temperature is achieved during the thermal treatment. Therefore, during the framework decomposition, the metal ions in the MOF clusters start colliding and forming the corresponding nanoparticles. Increasing the temperature boosts the build-up of larger particles at the expense of smaller ones in what is better known as sintering. In line with the thermodynamics of the Gibbs free energy, metals, metal oxides, metal carbides, or a mixture of nanoparticles are formed. In short, the Tammann and Hüttig temperature of different metal species delimit the temperature range in which the MOFMS must proceed if control over nanoparticle size is to be achieved. Likewise, the vapour pressure of the

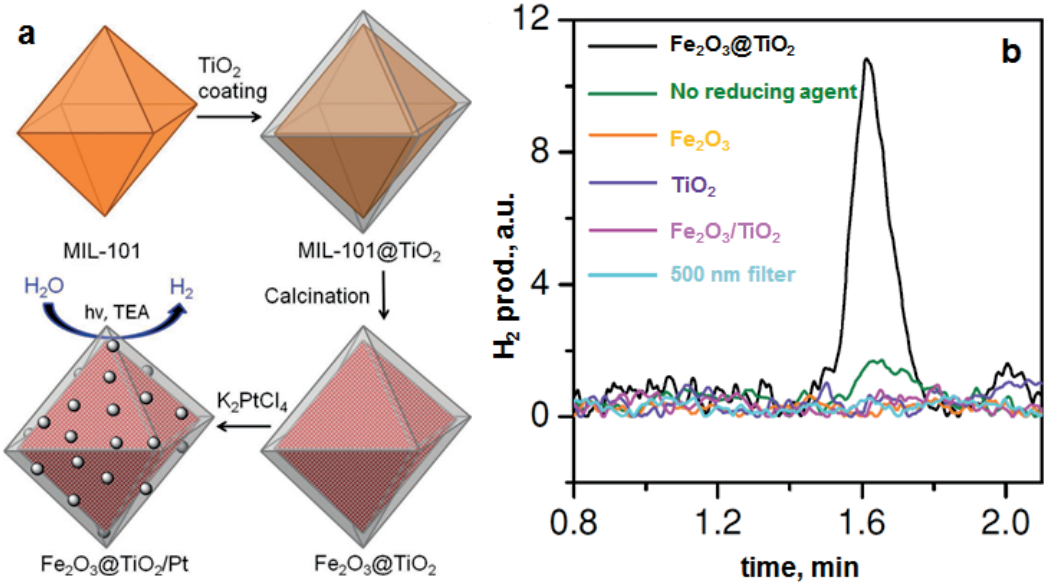

Figure 1.4 a MOF-templated synthesis of Fe_2O_3@TiO_2 by coating MIL-101(Fe) with TiO_2 followed by calcination, and its use for photocatalytic hydrogen production after depositing Pt particles **b** The H_2 peaks in GC analysis of the headspace using 0.5 mg of different catalyst samples [33].

formed metallic species or mixture of them needs also to be taken into consideration in order to remove or retain the metal species in the final catalytic material.

1.2.3 MOFMS for Heterogeneous Catalyst Synthesis

Iron minerals are ubiquitous in nature and there is abundant availability of them at minimal cost [34]. Hematite is the most common iron containing ore, but iron is widely distributed in other minerals such as magnetite and taconite. The melting point of metallic iron is 1538 ˚C, its boiling point is 2861 ˚C and the reduction potential of Fe^{3+} and Fe^{2+} are 0.04 and 0.41 V, respectively. The magnetic nature of iron enables its easy separation from aqueous media; its high boiling point ensures high iron loading after pyrolysis and the formation of carbides due to carbon incorporation in the iron lattice and prompts the metallic, carbidic, oxidic dynamic system in the pyrolysis. As in the case of Co and Cu, Fe also catalyses the formation of graphitic layers around its surface. Iron catalysis with MOFMS embraces Fe/N/C systems for ORR catalysis for fuel cell applications, Fe-mixed-C systems for nitro/chloro conversion and separation from waste water, among others.

De Krafft *et al.* reported a simple MOF-templated strategy for the synthesis of crystalline octahedral nanoshells combining the desired photocatalytic properties from both types of oxides **(Figure 1.4)** [33]. In their work, they coated MIL-101(Fe) particles with an amorphous shell of titania by acid-catalyzed hydrolysis and condensation of titanium(IV) bis (ammonium lactato) dihydroxide (TALH) in

water [35], followed by calcination in air at 550 °C for 16 h. They found the resulting crystalline Fe_2O_3@TiO_2 nanoparticles to have interesting photophysical properties as they exhibited photocatalytic hydrogen production from water using visible light, while neither component alone was able to do so. Kim and Yoon [36] reported the pyrolysis of MIL-100(Fe) and the effects of furfuryl alcohol (FA) added to the MOF-pores acting as carbon precursor. They displayed the ferromagnetic properties of the polycrystalline Fe_2O_3@C system, allowing for facile particle separation from a slurry phase. Elemental analysis revealed very minor hydrogen content, clearly indicating the conversion of the organic linkers toward carbonaceous materials upon pyrolysis. Indeed, the highest carbon loading of the composite material was obtained when fully soaking the MOF in FA, filling the interstitial sites of the MOF crystals in addition to the pores. Banerjee *et al.* [37] pyrolyzed MIL-53(Fe) at 500 and 600 ˚C to produce Fe_3O_4-carbon nanocomposites as recyclable adsorbent material for removal and recovery of environmental pollutants. The sample pyrolyzed at 500 ˚C was highly hydrophobic due to the presence of small micropores around 0.8 nm in diameter and absence of hydrophilic surface groups, much contrary to the sample pyrolyzed at 600 ˚C comprising larger mesopores with an average size of 2 nm. This allowed for effective separation of oil/water mixtures using the super hydrophobic sample, achieving separation factors values over 40. The recyclability of the material is excellent, due to its magnetic character, retaining over 75% of the separation capacity after 9 cycles. Quin *et al*. reported the synthesis of $CoFe_2O_4$ nanocomposites from Fe-containing MOF (MIL-100-Fe) for phenol oxidation in aqueous solution using peroxymonosulfate as oxidant [38]. They immobilized cobalt nitrate hexahydrate into the pores of MIL-100 by incipient wetness impregnation and calcined it at different temperatures (400-600°C). The resulting magnetic nanoparticles reduced phenol concentration more than 95% after 120 min and the regenerated catalysts exhibited good performance and stability in phenol degradation. Likewise, Dong *et al.* reported the preparation of magnetic porous carbons (MPCs) as supports for Au and Pd noble metal NPs [39]. They obtained the MPC through calcination of Fe-MIL-88A up to 700 °C under N_2 for 1 h. The reaction rate constant k was calculated to be 1 x 10^{-2} s^{-1} and 1.2 x 10^{-2} s^{-1} for the reaction catalyzed using Au/MPC [40] and Pd/MPC [41] nanocatalysts, respectively. For a quantitative comparison, the activity parameter $k´ = k/C_m$ was introduced, defined as the ratio of the rate constant k to the concentration of the active sites (g L^{-1} Au or Pd) added. Thus, $k´$ was calculated to be $k´_{Au}$ = 2.54 L $s^{-1}g^{-1}$ and $k´_{Pd}$ = 23.48 L $s^{-1}g^{-1}$ for Au/MPC and Pd/MPC, respectively. The value of activity parameter $k´$ reported for Au NP based catalysts, namely, Au/graphene catalyst, is 0.396 L $s^{-1}g^{-1}$ and the Pd NP based catalyst Pd polypyrrole has an activity parameter $k´$ of about 2.94 L $s^{-1}g^{-1}$. Accordingly, both Au/MPC and Pd/MPC nanocatalysts exhibited an excellent catalytic activity for the reduction of 4-nitrophenol (4-NP) in comparison with most other reported catalysts [40]. Moreover, the Pd/MPC catalyst showed high efficiency toward hydrodechlorination of chlorophenols. In both the synthesized catalysts, the MPC provided a large surface area and mesopores on which the Au and Pd NPs were finely dispersed. The catalysts could be easily recovered from the reaction mixture by

using a magnet because of the magnetic NPs encapsulated in the porous carbon, and could be conveniently reused. These methods are presented by the authors as an eco-friendly strategy to convert nitro- and chloro-compounds. A short while ago, Li *et al*. implemented the MOFMS in the hydrogenation of nitro compounds by developing a highly efficient, low-cost, and magnetically recyclable γ-Fe_2O_3@porous carbon catalyst [42]. In their study, Fe-MIL-88A samples were thermally treated at different temperatures and times in N_2 to afford Fe-based NPs encapsulated inside porous carbon. The reduction of nitrobenzene to aniline in the presence of hydrazine hydrate ($N_2H_4 \cdot H_2O$) was first used to explore the catalytic activity of different catalysts. As a result, the catalyst pyrolyzed at 500 °C for 1 h gave the best activity and could be readily recycled with an external magnet being reused at least 10 times without any loss of activity. They concluded that at this temperature the small γ-Fe_2O_3 NPs were well dispersed inside the porous carbon, which effectively limited the aggregation and growth of the high-density NPs and still facilitated the transportation of substrates, intermediates and products. Encouraged by the excellent performance of Fe-500-1h in the reduction of nitrobenzene, a wide variety of functionalized nitro compounds were also investigated. As a result, most of the corresponding substituted anilines were obtained with high conversion and selectivity. Notably, halogen-substituted nitroarenes were effectively reduced to the corresponding haloaromatic amines without obvious dehalogenation. This catalyst also showed absolute selectivity in the reduction of nitroarenes in the presence of other functional groups, including amino, phenolic hydroxyl and alcoholic hydroxyl. Last but not least, it was also able to offer a high chemoselectivity in the reduction of substituted nitroarenes with quite challenging reducible functional groups, including nitrile, aldehyde and ketone, giving the only product of corresponding anilines while the reducible functional groups were unchanged. Cao *et al.* [43] grew the MIL-88(Fe) on a porous 3D graphene structure and pyrolyzed the material first in Ar at 450 ˚C and subsequently in air at 380 ˚C to synthesize porous metal oxides on a graphene support. It showed extremely good charge/discharge cyclability as the anode of Li-ion battery, fully retaining its specific capacity of 864 mA h g^{-1} after 50 cycles. The graphene support effectively stabilized the Fe_2O_3 nanoparticles during the Li incorporation and release, as the control experiment of pyrolyzed/calcined unsupported MIL-88(Fe) showed a fast decay of the specific capacity toward 261 mA h g^{-1} after 50 cycles. The rate capacity of the MOFMS Fe_2O_3/graphene catalyst at high current densities (2-5 A g^{-1}) was higher than composites of iron oxides and graphene. Lee *et al.* [44] pyrolyzed Fe-MIL-88-A and Fe-MIL-88-B in a range of temperatures between 600-1000 ˚C under nitrogen flow, creating magnetic nanoparticle-embedded porous carbon materials. XRD results showed that the iron phase shifted from a mix of Fe_2O_3 and Fe_3C at 600 ˚C to fully metallic Fe at 1000 ˚C. The porosity of the carbon materials went through an optimum at 800 ˚C, indicating pore collapse and decreasing surface areas at elevated temperatures. The two Fe-MOFs pyrolyzed at 800 ˚C were used for waste water treatment using methylene blue as

model compound, obtaining adsorption capacities values of 60.2 and 83.9 mg g^{-1} for pyrolyzed MIL-88-A and MIL-88-B, respectively.

Additionally, the MOFMS has been applied in various attempts to improve catalysis of the oxygen reduction reaction (ORR) for fuels cell applications. In order to obtain the desired Fe/N/C composites, different synthesis procedures have been followed. For example, pyrolysis of low-boiling temperature Zn-based MOFs produce highly porous carbons that provide excellent support surface for iron nanoparticles. Similarly, Fe-based MOFs, often with amino-functionalized linkers, are pyrolyzed to produce Fe/N/C in a one-step synthesis. The main difference between the two synthetic pathways is the location of the Fe species. Lower surface loadings can be achieved through impregnation of the pyrolyzed MOF, however; only Fe-MOF pyrolysis results in the formation of encapsulated iron nanoparticles in the carbon matrix. Morozan *et al.* [45] used the most complex MOFMS strategy comprising a first pyrolysis of FA impregnated ZIF-8 at 1100 ˚C, subsequent Fe and N functionalization by impregnation and ball milling, followed by secondary Ar pyrolysis at 1050 ˚C and even a third NH_3 pyrolysis at 950 ˚C. The various approaches generated metallic and carbidic iron next to large fractions of FeN_4 species in a micro- and mesoporous carbonaceous matrix, of which larger mesopores did not further enhance the catalytic ORR activity. The boost in PEMFC performance after ammonia pyrolysis was ascribed to the increase the surface area, interconnecting existing active sites for catalysis instead of increasing the active site density. Zhang *et al.* [46] concluded that iron species indeed are crucial to the catalytic performance, ruling out that the initial activity loss of the Fe/N/C catalysts is due to the Fenton reaction of Fe with H_2O_2. Furthermore, the kinetics of Fe/N/C and Fe-free N/C catalysts during ORR were similar, revealing that micropore flooding through electro-oxidation of the carbon surface was indeed the main reason for the activity drop, in agreement with their previous study [47].

Mao *et al.* [48] mixed MIL-100(Fe) with aminotetrazole and pyrolyzed the materials at temperatures between 600-900 ˚C to produce Fe-N-C composites. The products were washed with HCl to produce N-doped carbon shells encapsulating the metallic iron nanoparticles, removing Fe_3C and Fe_2O_3 particles on the carbon surface. The treatment resulted in doubling of the micropore area, liberating cavities to trap oxygen while exposing active sites. The electrocatalytic properties of the materials showed that increasing pyrolysis temperatures resulted in increased current density and a positive shift of the onset potential during linear sweep voltammetry. The trend can be related to the facilitated electron transfer by the enhanced graphitic crystallinity witnessed in XRD. The highest catalytic activity can be achieved with the sample pyrolyzed at 800 ˚C (NC-800); the authors argue that higher pyrolysis temperatures decrease the N-doping and thus number of active sites, in agreement with lowered N-content from EDS results. Cyclic voltammetry showed that NC-800 outperformed metal-free N-doped carbons, confirming the involvement of iron in catalysis. Furthermore, the MOF-based catalyst showed improved stability during continuous ORR compared to the commercial Pt-C catalyst

and comprised a higher methanol tolerance. In another study, Afsahi *et al.* [49] used a sodalite-like Fe-MOF consisting of benzene tris tetrazole linkers to obtain hybrid Fe-N-C after pyrolysis in the range of 700-1000 ˚C. The products were subsequently acid leached in 1 M H_2SO_4 and heat treated under the pyrolysis temperature under NH_3 atmosphere. XRD of the pyrolyzed samples show multi-crystalline iron phases including iron carbides, oxides, sulphides and nitrides, with all patterns showing much resemblance. Acid leaching removed the unstable iron oxides and sulphides, and after NH_3 heat treatment Fe-N-C catalysts were produced. The particle size of the iron spheres varies between 10-60 nm, which are dispersed in highly porous cube-shaped carbon material. After acid wash, the iron content drastically reduced from 40 wt% to around 5-10 wt%, an increase in pyrolysis temperature was found to further carbonize the structure, removing N species. The methodological approach allowed the authors to conclude that the ORR catalytic activity originates from the pyridinic and quaternary nitrogen species. Additionally, the performance of the catalysts in a fuel cell did not exceed the one from Dodelet's group [50], and it is believed that the higher iron content plays a prominent role in the reduced activity. Li *et al.* [51] pyrolyzed ball-milled MIL-101(Fe) mixed with melamine in a range of temperatures between 500-1000 ˚C to obtain Fe/Fe_3C embedded in graphite layers and carbon nanotubes. High temperatures above 700 ˚C and melamine carbon precursor were necessary to produce the graphitic nature and to form the carbon nanotubes. Raman spectra confirmed the more graphitic nature of high temperature samples, nearly doubling the G-band over I-band intensity values. The ORR activity in terms of onset potential was very close to commercial Pt-C, and the electron transfer number from the Koutecky–Levich plots was estimated 3.6 compared to 3.7 for Pt-C. Zhao *et al.* [52] pyrolyzed nanocrystalline spindles of MIL-88B-NH_2 in Ar at 900 ˚C to produce very active ORR catalysts. XPS results indicated that the amino-type nitrogen was completely converted into pyridine- and quaternary-type nitrogen species, forming a well-integrated Fe/N/C catalyst. The micro- and mesoporous matrix of the catalyst was found to exist dominantly of amorphous carbon, with layered graphite species surrounding the iron nanoparticles. The power density of an alkaline direct methanol fuel cell increased 1.7 times when using the pyrolyzed MOF as compared to the commercial Pt/C catalyst. Furthermore, the MOF-derived catalyst showed superior stability toward methanol poisoning, whereas the current of the commercial Pt/C decreased by 80% upon introduction of 2 M methanol during chronoamperometric response measurements at 0.84 V in oxygen saturated 0.1 M KOH.

Recently, MOFs have been used as a precursor to produce iron catalysts for the Fischer-Tropsch synthesis reaction. Bing An *et al.* [53] used a Fe-MIL88B MOF with dicarboxylic linkers to obtain large external surface iron particles to properly assess the active phase with microscopy (**Figure 1.5**). They found that the pyrolysis additionally leaves behind carbonates on the iron surface, which is liberated during FTS. They confirm that the Hägg carbide phase is an active phase in HTFT, as the microscope results of spent catalysts evidence iron carbide surface growth on the surface of the

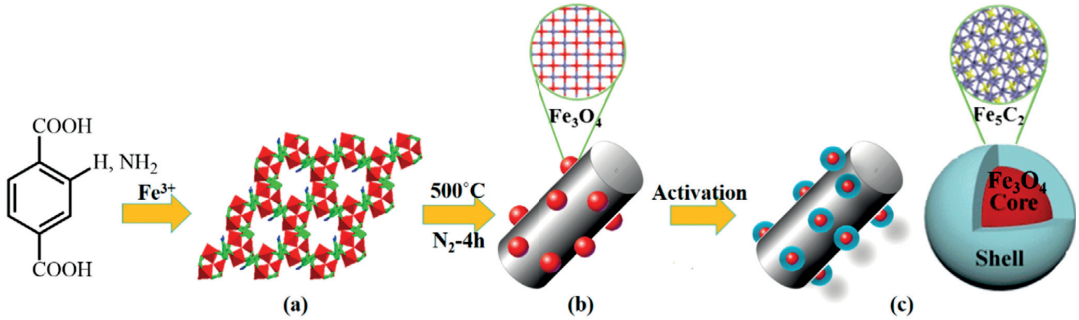

Figure 1.5 Synthesis scheme for the preparation of Fe-MIL-88B/C- and Fe-MIL-88B-NH2/C nanocomposites from isostructural iron-MOF precursors **a** MOF precursors **b** pyrolysis and **c** iron nanocomposites with carburized surface.

large iron oxide particles. Because of the slower active phase evolution, steady state conversion is achieved after only 60 h instead of 3 h for the system with much smaller particles [54]. High activities were achieved at 300 ˚C with the activity correlating to the development of the carbide shell on the large particles. Interestingly, a control experiment employing pyrolyzed molecular Fe-oxo clusters showed little activity, underlining the importance of a long-range order framework-type of precursor for pyrolysis and generating dispersed iron nanoparticles.

1.2.4 Perspective

Metal-organic frameworks (MOFs) have emerged as exemplary precursors for the manufacture of highly active catalysts through the MOF mediated synthesis (MOFMS). MOFMS embraces a wide range of synthetic techniques, though the basic definition of MOFMS refers to a single-step heat treatment of the parent MOF. In this process, the properties of the MOF together with the heat treatment conditions such as activating atmosphere, temperature, time and heating ramp, dictate the final properties of the MOF-derived catalyst, allowing for an unprecedented freedom in design. As highlighted by the examples above, an array of nanoparticles in the metallic, oxidic or carbidic phase can be confined in the carbon matrix obtained through decomposition of the pristine MOF, where every approach generates unique structural properties that result in many cases in improved catalytic performance.

The biggest advantage of this new methodology lies in the huge degree of freedom that it offers. The large metal dispersion in the original MOF renders a very high final metal dispersion and exquisite size control of the confined nanoparticles. The inverse proportionality between iron loading and dispersion, found in many traditional synthesis methods, is only applicable in MOFMS for metal loadings exceeding 40 wt% where particle sizes increases to about 5-10 nm. Moreover, further development and modification of the technique via utilization of different activation atmospheres,

introduction of additional functionalized components to the MOF by ion exchange or impregnation, intermediate pyrolysis steps and others, has already led to sophisticated catalytic systems that are not likely manufactured by any other means. This approach does not only lead to improved heterogeneous catalysts but is an excellent tool for the design of model systems that help generate knowledge through fundamental understanding of the catalytic reactions.

Probably the aspect that raises most concern regarding the MOFMS approach, is the fact that highly engineered, porous and crystalline, and very often expensive, materials are simply destroyed and this may look like something unaffordable from an industrial point of view. However, this is not always the case. Some of the aforementioned MOF mediated materials are highly competitive from an economic point of view compared to other more sophisticated synthetic procedures and their counterparts obtained by conventional methods [55]. Moreover, keeping in mind a certain level of pragmatism, the main target of catalyst synthesis is the design and preparation of outstanding catalysts and the MOFMS is an excellent tool to this end. On the other hand, one should also consider that a large part of the final price of a MOF comes from extensive washing steps needed to purify the as-synthesized materials. Obviously, the nature and depth of these steps required for MOFMS are far milder and this should lead to moderate prices of the hard template. Moreover, if the stability and activity of the resulting catalysts is increased by orders of magnitude, lower catalyst makeup costs and less process operation interruptions can severely impact the economical attractiveness in a good manner. Nevertheless, specific viability studies apply depending on the MOF precursor and synthesis conditions utilized in different cases.

1.3 Iron Carbides as Active Phase in FTS

1.3.1 Iron Carbides Associated with FTS

Iron carbides are unmistakably associated with the active phase for Fischer-Tropsch synthesis (FTS). The formation of these carbides is highly dependent on the catalyst formulation, the activation method and the operational conditions. Because of this highly dynamic system, studies on active phase performance often lack the direct correlation between catalyst performance and iron carbide phase. In the following sections, the iron carbides identified as active phase in FTS are reviewed and the activation methods that allow control in the formation of iron carbides are summarized.

In the early years surrounding the discovery of the atmospheric-pressure synthesis, Fischer postulated that the primary step before hydrogen addition is the carbon monoxide dissociation, and thus, the formation of carbides as intermediate compounds in the reaction [56, 57]. Cobalt, nickel and iron, three metals that display FTS activity, react at 200 ˚C with carbon monoxide to form carbides, and carbon balances of synthesis reactions and product analysis of the decomposition of spent catalysts indicated that carbides were formed during the synthesis [58]. At this time, catalyst

characterization techniques were still emerging, as only fifteen years had passed since the Nobel Prize in Physics was awarded to the Braggs for their work on X-ray diffraction (XRD), and it would be another five before Brunauer and Emmett started publishing on Van der Waals adsorption isotherms. The first iron-phase characterization studies were performed on the high-temperature Fischer-Tropsch (HTFT) catalyst, fused bulk iron catalysts with low surface area, where the iron phase was resolved by magnetization experiments [59]. The temperature-dependent magnetic moments allowed for quantification of the iron phase during FTS, and showed that, after complete reduction, iron was converted in magnetite and Hägg carbide (around 45 % and 50 %, resp.) with small amounts of metallic iron remaining. The composition of the catalyst changed, as the magnetite phase gradually increased during operation, whereas the Hägg carbide phase decreased and was oxidized and interconverted to another iron carbide phase [60]. This fundamental view on the dynamics of iron catalysts has not changed much up to date.

The discovery of Mössbauer absorption spectroscopy and the further development of XRD allowed the characterization of small iron nanoparticles on supported catalysts, and several iron carbides were identified over the years [61-73]. In addition, the application of X-ray photoelectron spectroscopy (XPS) and X-ray absorption spectroscopy (XANES/EXAFS) further stimulated the FTS carbide-phase studies. The carbide phases found in literature associated with FTS are ε-Fe_2C, ε'-$Fe_{2.2}C$, Fe_7C_3 χ-Fe_5C_2, and θ-Fe_3C, however, generally the monoclinic Hägg carbide (χ-Fe_5C_2) and hexagonal closed packed carbide (ε'-$Fe_{2.2}C$) are the predominant carbide phases found (**Figure 1.6**). Debate emerged regarding activity and selectivity of the different iron carbides, now that it became more widely accepted that carbides are the active phase. Many studies have focused on the efficient conversion of the fresh catalyst into an active one in order to optimize their performance [12, 74-96]. Particularly, Mössbauer studies coupled with catalytic tests provide good insight into the effect of the activation protocol and operational regime on the carbide phase. However, the focus of these papers was often limited; either the differences in the evolution of the active phase were investigated or the performance of the catalysts acquired through different activation protocols was reported. Hence, the main conclusion usually derived is that one activation method is preferred over the other, for a wide variety of reasons, and that a coexistence of carbide phases could be obtained. Nonetheless, through the combined knowledge of these numerous studies we have come a long way in establishing a relation between the iron carbide phase and catalyst activity. The following section as summarized the work on iron carbide characterization and performance studies in Fischer-Tropsch synthesis. In particular, the activation methods employed to obtain certain iron carbides phases are distinguished in order to derive conditions for formation of hexagonal carbide ε'-$Fe_{2.2}C$ and Hägg carbide χ-Fe_5C_2.

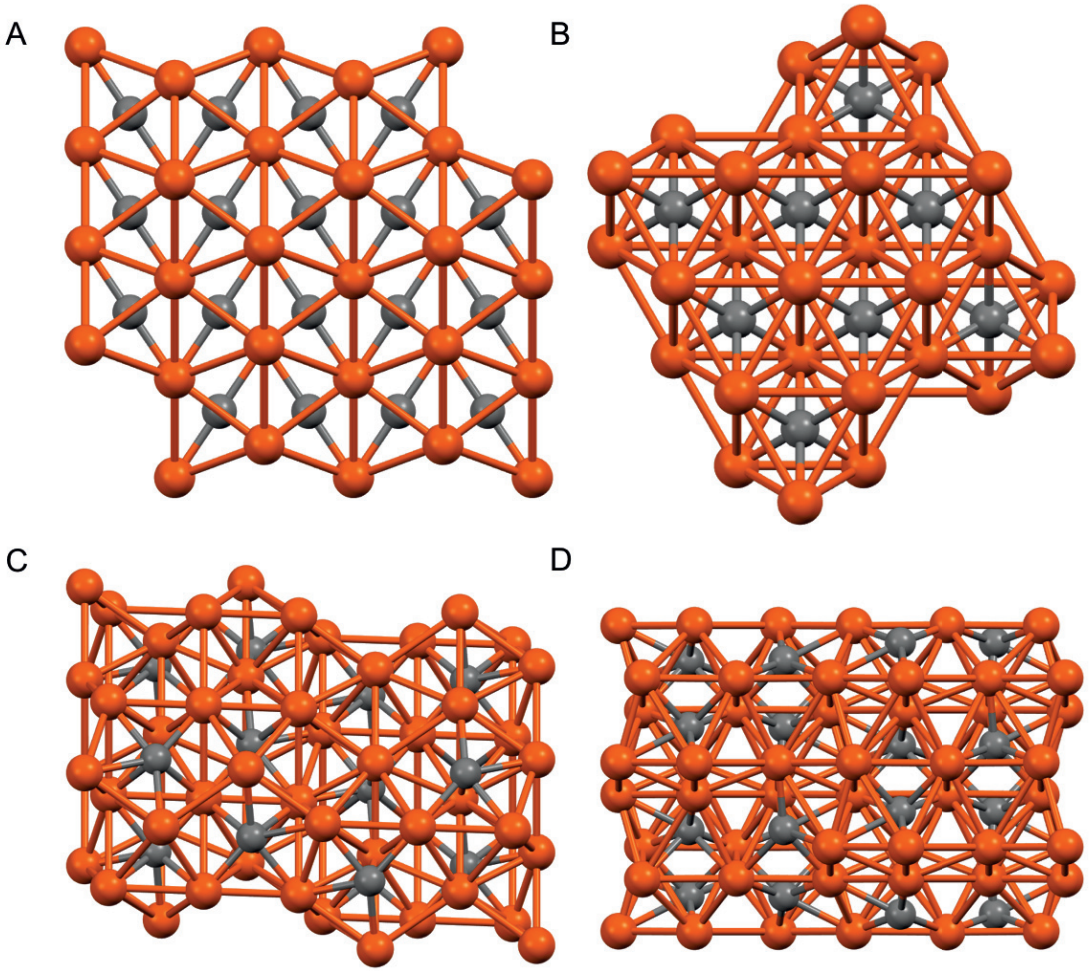

Figure 1.6 Crystallographic structures of **A,B** hexagonal carbide ε'-$Fe_{2.2}C$ and **C,D** Hägg carbide χ-Fe_5C_2 with a view along the b-axis in **A,C** and along the c-axis in **B,D**. The iron atoms are depicted as orange spheres and the carbon atoms as grey spheres [72, 97].

1.3.2 Review of Iron Carbides in FTS

Shultz *et al.* [74] converted reduced bulk iron catalysts to Hägg carbides and tested them under various pressures. The absence of other carbide phases was stated explicitly. At the highest operating pressure of 21.4 bar, rapid deactivation was measured as opposed to lower deactivation rates under pressures of 7.8, 11.1 and 14.5 bar. Increased rates of carbide oxidation were measured at elevated pressures, and thus, the authors proposed that the carbide could be oxidized by the FTS product water to form magnetite and carbon. The particle deterioration by oxidation and elemental carbon formation was likely the cause of deactivation, as no increase in methane selectivity was

found at 21.4 bar, but the reactor plugged by caking of segregated particles. Amelse, Butt and Schwartz [76] synthesized a pure ε'-$Fe_{2.2}C$ carbide from a 5 wt% Fe/SiO_2 under atmospheric syngas conditions and established the *in situ* Mössbauer characterization. The catalyst showed little activity in its reduced state, gaining activity during carburization, while the product distribution shifted to higher hydrocarbons. The carbide was very stable under reaction conditions, and the authors argued that support interaction may induce stabilization of the hexagonal carbide. They also established the relative stability of the carbides, ε'-$Fe_{2.2}C$, χ-Fe_5C_2, and θ-Fe_3C, with increasing temperature. Raupp and Delgass [77-79] showed with 10 wt% Fe on SiO_2 and 10 wt% Fe on MgO that depending on the particle size and support, different iron carbide phases could be obtained. The smaller iron particles favored hexagonal carbides, and the larger ones Hägg carbides. Usually, the latter phase was obtained with bulk unpromoted iron, and the study established a particle size limit of 10 nm where nanoparticle behavior moves to bulk iron. They furthermore demonstrated there is a clear time dependence on carbide formation depending on the precursor and on the particle size, where smaller particles carburize faster than the larger ones. The FTS reaction rate was found directly proportional to the bulk carburization of the iron phase, indicating that the bulk iron acts as a surface-carbon getter and therefore controls the active-site density of the catalyst. The carburization was found to be highly dynamic, as hexagonal phases were formed and again consumed while establishing the steady-state Hägg carbide phase. Additionally, hydrogenation experiments of the carbides after hours of operation showed that they are not specifically prone to methane formation, in agreement with other studies that show that the carbidic carbon is relatively inert compared to the carbide surface [98]. Schäfer-Stahl [80] demonstrated that small reduced iron nanoparticles under FTS temperatures as low as 140 ˚C readily carburize into a mixture of ε'-$Fe_{2.2}C$ and χ-Fe_5C_2 phases, and the degree of carburization increased when applying a higher temperature of 185 ˚C, while the FTS activity increased concomitantly. Increasing the temperature to 320 ˚C under higher partial pressures of hydrogen produced Hägg carbides of somewhat increased size, which were still very active at the initial temperature of 140 ˚C. When applying a temperature of 320 ˚C under a hydrogen-lean atmosphere, the carbide phase partly degraded to magnetite, and did not exhibit FTS activity at 140 ˚C. Recarburization of the oxidized catalyst took several days at elevated temperatures, regenerating the catalyst activity. Niemantsverdriet *et al.* [81] stated explicitly that both the nature of the catalyst and the reaction conditions determined the combination of carbides that was found. Metallic iron catalysts under FTS conditions at low temperatures on formed a doped metallic iron structure or a low-crystalline Fe_xC carbide, following with increasing temperature to ε', χ, and θ, all in increasing ratios of presence. After 48 h of FTS at 240 ˚C, the 30 nm iron particles had carburized into 38 % ε' and 62 % χ carbide. The maximum catalyst activity was achieved when all ferrite had disappeared and was converted to carbide. Afterwards, activation by carbon laydown took place. They showed that support effects played a role in obtaining higher carbon containing carbides at

similar activation, possibly due to the smaller particle size of Fe/TiO_2/CaO, where ε'-$Fe_{2.2}C$ was found a stable phase even at temperatures of 350 ˚C. Successively [82], the authors explored the possible mechanisms of the active phase formation, and summarized the three fundamental ways of correlating the rate of hydrocarbon formation: it is proportional to the amount of bulk carbide; it is in competition with the rate of bulk carbide formation, not necessarily as carbide surface active phase; or it is dependent on the rate of surface complexes of iron, carbon, and hydrogen formed on the bulk carbide. Jung [83, 84] *et al.* showed that the type of carbon support has a large influence on the resulting catalyst. Conducting graphitic-type carbon resulted in large iron nanoparticles with ferromagnetic behavior, whereas insulating amorphous-type carbon produced highly dispersed iron nanoparticles with superparamagnetic behavior when the supports were impregnated with an iron nitrate solution. The type of carbide formed during FTS was different for the two supports, as operation at 275 ˚C produced ε'-$Fe_{2.2}C$ for the latter catalyst and a mixture of χ-Fe_5C_2 and hexagonal carbides for the former. The highly dispersed iron displayed a lesser degree of reduction under similar activation conditions, however, the increased support interaction was likely the cause for the high stability during FTS. The small hexagonal carbides displayed superior activity and a constant product distribution comprising lower methane selectivity compared to the larger particles with coexistent carbide phases and compared to traditional iron supported on alumina. Reymond, Mériaudeau and Teichner [85] performed experiments on reduced and fresh iron oxide and showed that the kinetics of carburization are different for the two starting materials. Ferrite is instantaneously activated and then deactivates rater quickly, whereas hematite takes over 5 h in atmospheric syngas to reach its maximum activity, and has a better overall stability and steady state activity. The authors interpreted the results that the carbon dissociates on intermediate Fe_3O_4 which was found present at the surface, and thus must be an active phase. A redox-type mechanism on Fe_3O_4 was proposed, as it continuously oxidized to hematite and reduced back to magnetite. It must however, be said that catalyst samples were transferred in air to the XPS, a protocol highly discouraged in the years that had yet to come [99]. Furthermore, the run is at absolute methanation conditions of H_2/CO=9 at 1 atm, at which reduction of the surface oxide is swift, which allows subsequent carburization. Extrapolating the deactivation profile of the catalyst would indeed suggest far from optimized lifetime of the iron oxide catalyst as well. Nonetheless, the authors argue that the difference between oxide-core carbides and ferrite-derived carbides is the amount of surface carbon, and that laydown on the latter is far more pronounced. Blanchard *et al.* [86] used excessive temperatures of 500 ˚C for hydrogen reduction of Fe_2O_3 next to a moderate reduction of 10 wt% Fe supported on SiO_2 and activation under methanation conditions. Not surprisingly, the high-temperature reduction produced catalysts without any steady-state activity, as even without investigating the iron phase, the particles would have sintered tremendously. The authors furthermore showed that calcination prior to methanation increased the catalytic performance of the unsupported iron oxides, strengthening the concept of sintering induced by water partial pressures or anionic residues. Additionally, the

supported particles did not show such a profound decrease in activity when subjected to the high-temperature reduction, indicative of far lower mobility of iron through support stabilization. These catalysts also showed the formation of hexagonal carbides, an indication that far smaller particles are obtained that are effectively carburized. The catalysts with the smallest initial particle size displayed the highest activity and do not present carbide signals in XRD, most likely due to the very small average crystallite sizes of the carbide phase formed. Nonetheless, the views on the redox-type FTS mechanism on magnetite that was proposed by Reymond were further examined. Kuivila, Stair and Butt [87] arrived at similar conclusions when finding only a 22% Hägg carbide bulk contribution of and just 3% on the surface of their unreduced iron catalyst after 48 h of operation, by which they deduce the oxide must be the active phase. Dictor and Bell [88] investigated reduced and fresh iron oxides and showed that in the coexistence of both phases the Hägg carbide contribution dominates, while some hexagonal phase carbide is formed. However, the reduction of hematite results in much larger particles and they therefore show less activity, in addition to a higher rate of deactivation during time on stream. Furthermore, the absence of initial activity on oxides and the slow rise in activity during FTS, indicates that the oxide takes more time to be progressively converted to mixtures of surface carbides and is a clear indication of a carbide active phase. In addition, the product distributions and kinetics over the reduced and unreduced oxide after many hours of operation are very similar, while no evidence for a Fe_3O_4 phase was found by XRD. They therefore dismiss the theory of Reymond and Kuivila of FTS active oxides. Shroff *et al.* [12] showed that catalysts consisting of only magnetite did not display FTS performance, and the transformation of the oxide into a carbide was prerequisite for FTS activity. The oxide transformation into a carbide phase was without noticeable metallic iron intermediate in TEM nor in XRD. Furthermore, the micrographs of catalysts confirm that carbide formation is a shell-buildup process around the oxide core by diffusion of carbon into the lattice and oxygen to the outside, in accordance with Niemantsverdriet's competition model. By measuring the carbon content of spent samples, Hägg carbides were estimated as the nature of the carbide. After the maximum conversion is achieved following an induction period where the iron is completely converted to carbide, enhanced carbon deposition on the surface initiates catalyst deactivation. The transformation into carbides results in differences in crystallite sizes and iron-phase density, and in addition with inactive carbon deposition on the surface, the catalyst particles segregate and deactivate further. Indeed, the TEM study shows that carbides are always covered in 2-4 nm carbon shells, the reason why XPS detects very low amounts of surface iron. This means that the unattenuated signal of an oxide therefore rules the iron chemical state in XPS. For that reason, the authors argued that assigning magnetite as active phase by *ex situ* XPS measurements is highly unreliable. Bukur *et al.* [89] investigated effects of the activation procedure on a doubly promoted precipitated iron catalyst. They showed that the oxide to carbide transition through syngas jumps from hematite quickly to magnetite and then develops slowly into the carbide phase. Ferrite obtained after hydrogen reduction developed under FTS conditions into the ε' carbide phase, whereas oxides

converted through syngas or CO pretreatment would turn into χ carbide. The initial activity of the readily carburized catalysts exceeded that of reduced catalysts, which showed a prolonged induction period over 100 h, in contrast to a significant deactivation of the carburized catalysts. A remarkable difference in methane selectivity was obtained, as carburized catalysts displayed much lower methane selectivity than reduced catalysts, 7-9 % compared to 4-5 %, respectively. In addition to lower amounts of methane, increased amounts of high molecular weight products were obtained from pre-carburized catalysts. Finally, the formed carbides could eventually be interconverted into a different carbide phase or deactivated into magnetite due integral reactor operation and the associated large difference in gas composition over the reactor bed, resulting in an oxidizing gas atmosphere in the bottom part. Carbon buildup in the reactor was associated with the deactivation into the iron oxide phase. O'Brien *et al.* [90] investigated the effect of pretreatment on the activity and selectivity of precipitated Fe/Si/K catalysts in slurry phase FTS. Activation in pure carbon monoxide resulted in the highest activity as carbides were readily formed, and mixtures of ε'-$Fe_{2.2}C$ and χ-Fe_5C_2 were obtained. The methane selectivity of 8-9 % was lower for these carburized catalysts than for the syngas activated ones, where methane selectivities around 10-15 % were obtained in addition to lower long-chain hydrocarbon selectivities. A correlation was established between the initial FTS activity and the hydrogen partial pressure during syngas activation. Depending on the hydrogen partial pressure, oxidizing conditions are created due to product water that leads to the formation of the inactive magnetite phase. Herreyre *et al.* [91] investigated the carburization of a supported iron oxide catalyst**.** Hydrogen reduction of the hematite phase to ferrite is fast at 535 ˚C, as both the degree of reduction and rate at which it occurs increases with temperature. At these high temperatures, the carbon monoxide disproportionation reaction takes place and carburizes the iron into cementite. The rate of carbon deposition was a function of the reaction time and thus, likely due to the degree of carburization. The reaction rate had already dropped significantly after 4 h at a degree of carburization of 88 %, whereas a completely deactivated catalyst and fully carburized phase was obtained after 19 h. Bukur, Lang and Ding [92] carried out activation-procedure experiments with a precipitated iron catalyst in a stirred tank reactor similar as in their fixed-bed experiments. Reduction of the iron oxide produced ferrite and magnetite, which were quickly converted to carbides, whereas the bulk oxide was slowly converted into the carbide phase. Activation of CO and subsequent FTS resulted in the formation of Hägg carbides, whereas reduction of the catalysts led to the formation of hexagonal carbides. The degree of carburization of the two activation methods after 110 h was 46 % and 37 %, respectively. In addition to the carbide phases, large amounts of superparamagnetic species were found, indicative of very small nanoparticles. The activity of the hydrogen reduced sample and carburized sample were nearly identical, as the use of mild reduction conditions under high hydrogen flow rates would prevent subsequent deactivation. Furthermore, the authors argued that the origin of the bulk phase formation may be related to the differences in particle sizes. Li *et al.* [93, 94] investigated the carbide phase and conversion profile of

an unpromoted precipitated iron catalyst after activating the catalyst in carbon monoxide for 24 h. The obtained iron phase consisted of nearly pure Hägg carbide, and initial activity peaked just under 90 % conversion. For the subsequent 450 h, carbon monoxide conversion decreased to about 12 %, in a similar fashion to the iron phase that completely re-oxidized to magnetite. The oxidizing atmosphere at high initial conversion provided the onset of deactivation, however, full oxidation was achieved even when conversion levels were very low in the later stages of operation. The authors argue that the onset of re-oxidation causes changes in the carbide surface that alters the oxidation potential of adsorbed species as to form magnetite, which intermediate oxide is not re-activated by the reducing atmosphere under low conversion levels. Transient kinetic experiments on precipitated iron oxides showed that the FTS induction period under atmospheric pressure is extremely short, in the timescale of catalytic turnover, and that very little bulk carbide is necessary for activity. Moreover, the degree of carburization increased with time, whereas methane production remained constant. The surface is described as a dynamic phase consisting of oxygen and carbon vacancies, surface oxygen, and where carbon atoms are occupying lattice positions in the underlying bulk. The bulk is a viewed as a thermodynamically stable carbide or oxide phase, which eventually can be segregated from the surface as progressive carburization results in smaller surface carbide crystallites. Hao *et al.* [95] showed that an increasing syngas activation pressure retarded the rate of carburization on co-precipitated iron catalysts, and thus created a lower degree of carburization after comparable timeframes. However, the carbon dioxide content in the effluent gas increased with activation pressure, which was likely due to increased WGS activity. Additionally, the carbide composition shifted with increasing pressure from a mixture with high amounts of ε'-$Fe_{2.2}C$ to a mixture with equal amounts of ε'-$Fe_{2.2}C$ and χ-Fe_5C_2. The initial FTS activity decreased with increasing activation pressure, which is not related to the changes in the final degree of carburization (50-65 %). On the contrary, it seems that enhanced re-oxidation rates under increased residence times at higher pressures can induce deactivation, either by carbon deposition or sintering. De Smit [96] *et al.* established a thermodynamic model on the basis of the carbon chemical potential to predict formation of iron carbide phases. Low FTS reaction temperatures and high partial pressures of carbon monoxide generate a high carbon chemical potential, whereas high temperature FTS accompanying low partial pressures of carbon monoxide produce a low carbon chemical potential. The combination of thermodynamics with kinetic factors such as carbon diffusion limitations in crystal lattices, and energetic contributions from structure deformation, resulted in a qualitative interpretation of carbide formation from metallic iron that is in agreement with previous observations. Experiments with an iron catalyst activated at a low and high carbon chemical potential demonstrated that indeed, the highest contribution of ε'-$Fe_{2.2}C$ was obtained at a high chemical potential, whereas a low chemical potential resulted in 94 % of χ-Fe_5C_2. The catalyst comprising hexagonal carbide displayed the highest activity of the two, and was active for WGS, while it did not deactivate during operation.

Analysis of the spent catalyst showed that oxidation of the bulk had taken place to some extent, however, no incremental amount of carbon was formed. The catalyst with a majority of Hägg carbide presented lower activity, and additionally, deactivated during operation as notably more carbon was formed. The catalyst did not display similar WGS activity, and after reaction, significant amounts of cementite coexisted with the initial carbide phase.

1.3.3 Iron Carbides related to Activation Procedure and FTS Conditions

To summarize, reduction or carburization of bulk iron oxides and the subsequent employment of FTS conditions nearly always results in a mixture of Hägg χ-Fe_5C_2 and hexagonal ε'-$Fe_{2.2}C$ carbides, often with the former as the dominant phase. Reduction of the iron oxides leads to ferrite and magnetite, where the former carburizes quickly and shows instantaneous activity, but deactivation of this unsupported phase is swift and more profound than on oxide-derived carbides. Loss of activity is related to carbon deposition on the surface and segregation of the carbide phase from the bulk iron. Moreover, the activation step itself is very important, as it can drastically alter performance. Hydrogen reduction produces a high amount of water during a relative short period, whereas in contrast, much slower carbon monoxide or syngas carburization forms much slower additional carbon dioxide as a product at far lower partial pressures. Insufficient water removal during hydrogen reduction may therefore be a problem, causing sintering or particle segregation as the iron phase goes through several re-oxidation and reduction cycles. Though the oxide phase is carburized slower in carbon monoxide or syngas, it seemingly does not go through the ferrite phase. Carburized iron oxide catalysts are more stable possibly due to the structural conformity maintained by the slower diffusion and recombination of the surface and bulk phase, being better able to take on differences in density. When a supported catalyst is used that allows the formation of small iron nanoparticles, it is possible to produce a single phase of hexagonal ε'-$Fe_{2.2}C$ carbides. A lower degree of reduction, indicative of increased support interaction, does seem to help the stability of such catalysts and interconversion of the carbide phase is possible on supported iron catalysts. These supported catalysts also display less deterioration from hydrogen reduction when mild reductions are used together with higher hydrogen flow rates, possibly by the same stabilization as stated above.

1.4 Outline of this Thesis

This thesis describes the use of metal-organic frameworks (MOFs) as precursor to produce high-potential iron catalysts for the Fischer-Tropsch synthesis (FTS) reaction by the MOF mediated synthesis (MOFMS).

In **Chapter 2** of this thesis, the first report on the design of Fe-based FTS catalysts from novel MOF mediated synthesis (MOFMS) method is presented. Herein, the commercially available Fe-BTC is used in the MOFMS to produce a range of Fe@C catalysts while applying identical pyrolysis

conditions. The main goal here is to synthesize stable iron-based FTS catalysts by isolating and anchoring the highly dispersed iron clusters in the MOF structure, as it is hypothesized that the carbonization of the framework creates a carbon matrix that is able to maintain the spatial arrangement of the initial iron clusters. Additionally, the iron loading is altered by the addition of a carbon source into the pristine MOF. The major research question in this chapter therefore encompasses the influence of pre-pyrolysis cluster confinement by additional carbon sources, in search for a correlation between the iron loading and dispersion, as the combination of the two is key in obtaining highly active catalysts. Furthermore, the carbon-based product selectivity is optimized by FTS performance testing of a series of potassium-promoted Fe@C catalysts.

In **Chapter 3** of this thesis, the conversion of the Fe-BTC MOF into an Fe@C FTS catalyst is investigated in depth by *in situ* X-ray absorption and Mössbauer spectroscopy. The main goal of this chapter is to understand the pyrolysis process, i.e., under which conditions and to what extent does the linker carbonize and at which point are the Fe(III)-oxo clusters reduced into iron nanoparticles. The major research question in this chapter comprised the influence of the pyrolysis temperature on the iron loading and dispersion, as it is hypothesized that the degree of carbonization of the MOF structure, influenced by the pyrolysis temperature, controls the iron loading of the resulting catalyst. It is furthermore expected the high dispersion is lost at temperatures far above the decomposition temperature. The focus of this research is thus summarized as to find a pyrolysis temperature that produces an optimum in activity and stability during FTS performance testing.

In **Chapter 4** of this thesis, the effect of the MOF precursor on the resulting Fe@C catalyst is investigated. In this study, different MOFs are employed, while using fixed pyrolysis conditions to ensure similar degrees of framework carbonization. The main goal of this chapter is to isolate the most important parameter of the MOF structure to obtain the most active and stable catalyst. It is hypothesized that the iron nanoparticle confinement and dispersion are influenced by the iron-cluster distance and coordination to the linker, and thus the major research question herein comprises the correlation of the spatial distribution of the initial MOF to the final Fe@C physiochemical properties. The results can provide insight into promising MOF structures that would produce even better performing catalysts. Moreover, all the MOFs used in this study are from a commercial supplier, as possibilities are assessed to implement MOFs into industrial catalysis.

In **Chapter 5** of this thesis, a fundamental study is performed on the role of iron carbides in FTS. The main goal is to unravel whether differences exist in the catalytic performance of various iron carbides, and whether a certain iron carbide phase is preferred in terms of activity, stability and selectivity. The main challenge, as highlighted in the above section, and thus the main goal of this work, is to obtain single-phase iron carbides in a controlled manner. The controlled formation of these iron carbides is paramount, as the only way to demonstrate the intrinsic performance of these carbide phases, is to maintain all other physiochemical properties identical. Therefore, the accurate characterization of

fresh and spent catalysts will be carried out together to establish whether changes in dispersion arise from different activation methods. *In situ* Mössbauer spectroscopy studies are performed to determine the degree of reduction, and the type and amount of iron carbide phase formed under the exact conditions at which FTS performance testing is carried out.

Please note that all chapters have been written as individual publications and can be read independently. As a result, some overlap may be present.

References

[1] Deutschmann, O., Knözinger, H., Kochloefl, K., Turek, T., *Heterogeneous Catalysis and Solid Catalysts*, in: Ullmann's Encyclopedia of Industrial Chemistry, Wiley-VCH Verlag GmbH & Co. KGaA, **2000**.
[2] Prieto, G., Zečević, J., Friedrich, H., de Jong, K.P., de Jongh, P.E., *Nat Mater*, 12 (**2013**) 34-39.
[3] Zaera, F., *J. Phys. Chem. Lett.*, 1 (**2010**) 621-627.
[4] Zaera, F., *Catal. Lett.*, 142 (**2012**) 501-516.
[5] Conley, M.P., Copéret, C., Thieuleux, C., *ACS Catal.*, 4 (**2014**) 1458-1469.
[6] Abelló, S., Montané, D., *ChemSusChem*, 4 (**2011**) 1538-1556.
[7] Sun, B., Xu, K., Nguyen, L., Qiao, M., Tao, F., *ChemCatChem*, 4 (**2012**) 1498-1511.
[8] Dry, M.E., *Catal. Today*, 71 (**2002**) 227-241.
[9] de Smit, E., Weckhuysen, B.M., *Chem. Soc. Rev.*, 37 (**2008**) 2758-2781.
[10] Pendyala, V.R.R., Graham, U.M., Jacobs, G., Hamdeh, H.H., Davis, B.H., *ChemCatChem*, (**2014**).
[11] Kalakkad, D.S., Shroff, M.D., Köhler, S., Jackson, N., Datye, A.K., *Appl. Catal., A*, 133 (**1995**) 335-350.
[12] Shroff, M.D., Kalakkad, D.S., Coulter, K.E., Kohler, S.D., Harrington, M.S., Jackson, N.B., Sault, A.G., Datye, A.K., *J. Catal.*, 156 (**1995**) 185-207.
[13] Gascon, J., Corma, A., Kapteijn, F., Llabrés i Xamena, F.X., *ACS Catal.*, 4 (**2014**) 361-378.
[14] Farrusseng, D., Aguado, S., Pinel, C., *Angew. Chem. Int. Ed. Engl.*, 48 (**2009**) 7502-7513.
[15] Corma, A., García, H., Llabrés i Xamena, F.X., *Chem. Rev.*, 110 (**2010**) 4606-4655.
[16] Lee, J., Farha, O.K., Roberts, J., Scheidt, K.A., Nguyen, S.T., Hupp, J.T., *Chem. Soc. Rev.*, 38 (**2009**) 1450-1459.
[17] Li, B., Leng, K., Zhang, Y., Dynes, J.J., Wang, J., Hu, Y., Ma, D., Shi, Z., Zhu, L., Zhang, D., Sun, Y., Chrzanowski, M., Ma, S., *J. Am. Chem. Soc.*, 137 (**2015**) 4243-4248.
[18] Llabres i Xamena, F.X., Gascon, J., *Towards Future MOF Catalytic Applications*, in: Metal Organic Frameworks as Heterogeneous Catalysts, The Royal Society of Chemistry, **2013**, pp. 406-424.
[19] Deng, S., Kurttepeli, M., Cott, D.J., Bals, S., Detavernier, C., *J. Mater. Chem. A*, 3 (**2015**) 2642-2649.
[20] Lam, E., Luong, J.H.T., *ACS Catal.*, 4 (**2014**) 3393-3410.
[21] Planeix, J.M., Coustel, N., Coq, B., Brotons, V., Kumbhar, P.S., Dutartre, R., Geneste, P., Bernier, P., Ajayan, P.M., *J. Am. Chem. Soc.*, 116 (**1994**) 7935-7936.
[22] Rodríguez-reinoso, F., *Carbon*, 36 (**1998**) 159-175.
[23] Enterría, M., Figueiredo, J.L., *Carbon*, 108 (**2016**) 79-102.
[24] Campbell, C.T., Parker, S.C., Starr, D.E., *Science*, 298 (**2002**) 811-814.
[25] Sun, J.-K., Xu, Q., *Energ. Environ. Sci.*, 7 (**2014**) 2071-2100.
[26] Xia, W., Mahmood, A., Zou, R., Xu, Q., *Energ. Environ. Sci.*, 8 (**2015**) 1837-1866.
[27] Oar-Arteta, L., Wezendonk, T., Sun, X., Kapteijn, F., Gascon, J., *Metal–Organic Framework-Mediated Synthesis in Catalysis*, in: Nanotechnology in Catalysis, Wiley-VCH Verlag GmbH & Co. KGaA, **2017**, pp. 225-250.
[28] Oar-Arteta, L., Wezendonk, T., Sun, X., Kapteijn, F., Gascon, J., *Mater. Chem. Front.*, 1 (**2017**) 1709-1745.
[29] Ellingham, H.J.T., *Journal of the Society of Chemical Industry, London*, 63 (**1944**) 9.
[30] Das, R., Pachfule, P., Banerjee, R., Poddar, P., *Nanoscale*, 4 (**2012**) 591-599.
[31] Birks, N., Meier, G.H., Pettit, F.S., *Introduction to the High Temperature Oxidation of Metals*, 2 ed., Cambridge University Press, Cambridge, **2006**.
[32] Green, D.W., Perry, R.H., *Perry's Chemical Engineers' Handbook, Eighth Edition*, McGraw-Hill Professional, **2007**.
[33] deKrafft, K.E., Wang, C., Lin, W., *Adv. Mater.*, 24 (**2012**) 2014-2018.
[34] Munoz, M., Domínguez, P., de Pedro, Z.M., Casas, J.A., Rodriguez, J.J., *Appl. Catal., B*, 203 (**2017**) 166-173.
[35] Lee, S.-w., Drwiega, J., Wu, C.-Y., Mazyck, D., Sigmund, W.M., *Chem. Mater.*, 16 (**2004**) 1160-1164.
[36] Kim, E., Yoon, M., *J. Porous Mater.*, 22 (**2015**) 1495-1502.
[37] Banerjee, A., Gokhale, R., Bhatnagar, S., Jog, J., Bhardwaj, M., Lefez, B., Hannoyer, B., Ogale, S., *J. Mater. Chem.*, 22 (**2012**) 19694-19699.

[38] Qin, F.-X., Jia, S.-Y., Liu, Y., Han, X., Ren, H.-T., Zhang, W.-W., Hou, J.-W., Wu, S.-H., *Mater. Lett.*, 101 (**2013**) 93-95.
[39] Dong, Z., Le, X., Liu, Y., Dong, C., Ma, J., *J. Mater. Chem. A*, 2 (**2014**) 18775-18785.
[40] Li, J., Liu, C.-y., Liu, Y., *J. Mater. Chem.*, 22 (**2012**) 8426-8430.
[41] Xue, Y., Lu, X., Bian, X., Lei, J., Wang, C., *J. Colloid Interface Sci.*, 379 (**2012**) 89-93.
[42] Li, Y., Zhou, Y.-X., Ma, X., Jiang, H.-L., *Chemical Communications*, (**2016**).
[43] Cao, X., Zheng, B., Rui, X., Shi, W., Yan, Q., Zhang, H., *Angew. Chem. Int. Ed.*, 53 (**2014**) 1404-1409.
[44] Lee, H.J., Cho, W., Lim, E., Oh, M., *Chem. Commun.*, 50 (**2014**) 5476-5479.
[45] Morozan, A., Sougrati, M.T., Goellner, V., Jones, D., Stievano, L., Jaouen, F., *Electrochim. Acta*, 119 (**2014**) 192-205.
[46] Zhang, G., Chenitz, R., Lefèvre, M., Sun, S., Dodelet, J.-P., *Nano Energy*, 29 (**2016**) 111-125.
[47] Yang, L., Larouche, N., Chenitz, R., Zhang, G., Lefèvre, M., Dodelet, J.-P., *Electrochim. Acta*, 159 (**2015**) 184-197.
[48] Mao, C., Kong, A., Wang, Y., Bu, X., Feng, P., *Nanoscale*, 7 (**2015**) 10817-10822.
[49] Afsahi, F., Kaliaguine, S., *J. Mater. Chem. A*, 2 (**2014**) 12270-12279.
[50] Proietti, E., Jaouen, F., Lefèvre, M., Larouche, N., Tian, J., Herranz, J., Dodelet, J.-P., *Nat Commun*, 2 (**2011**) 416.
[51] Li, J.-S., Li, S.-L., Tang, Y.-J., Han, M., Dai, Z.-H., Bao, J.-C., Lan, Y.-Q., *Chem. Commun.*, 51 (**2015**) 2710-2713.
[52] Zhao, S., Yin, H., Du, L., He, L., Zhao, K., Chang, L., Yin, G., Zhao, H., Liu, S., Tang, Z., *ACS Nano*, 8 (**2014**) 12660-12668.
[53] An, B., Cheng, K., Wang, C., Wang, Y., Lin, W., *ACS Catal.*, 6 (**2016**) 3610-3618.
[54] Santos, V.P., Wezendonk, T.A., Jaén, J.J.D., Dugulan, A.I., Nasalevich, M.A., Islam, H.-U., Chojecki, A., Sartipi, S., Sun, X., Hakeem, A.A., Koeken, A.C.J., Ruitenbeek, M., Davidian, T., Meima, G.R., Sankar, G., Kapteijn, F., Makkee, M., Gascon, J., *Nat Commun*, 6 (**2015**) 1-8.
[55] Luo, Y., Estudillo-Wong, L.A., Cavillo, L., Granozzi, G., Alonso-Vante, N., *J. Catal.*, 338 (**2016**) 135-142.
[56] Fischer, F., Tropsch, H., *Brennst.-Chem.*, 7 (**1926**) 97.
[57] Fischer, F., Tropsch, H., *Brennst.-Chem.*, 11 (**1930**) 489.
[58] Fischer, F., Tropsch, H., *Ges. Abh. Kenntn. Kohle*, 10 (**1930**) 313.
[59] Pichler, H., Kruger, E., *Brennstoff-Chemie*, 47 (**1966**) 368.
[60] Malan, O.G., Louw, J.D., Ferreira, L.C., *Brennst.-Chem.*, 42 (**1961**) 209-212.
[61] Barton, G.H., Gale, B., *Acta Crystallogr.*, 17 (**1964**) 1460-1462.
[62] Eckstrom, H.C., Adcock, W.A., *J. Am. Chem. Soc.*, 72 (**1950**) 1042-1043.
[63] Fasiska, E.J., Jeffrey, G.A., *Acta Crystallogr.*, 19 (**1965**) 463-471.
[64] Hägg, G., *Z. Kristallogr.*, 89 (**1934**) 92.
[65] Hofer, L.J.E., Cohn, E.M., Peebles, W.C., *J. Am. Chem. Soc.*, 71 (**1949**) 189-195.
[66] Hofmann, U., Groll, E., *Z. Anorg. Allg. Chem.*, 191 (**1930**) 414-428.
[67] Senateur, J.P., Fruchart, R., Michel, A., *Compt. Rend.*, 255 (**1962**) 1615.
[68] Herbstein, F.H., Snyman, J.A., *Inorg. Chem.*, 3 (**1964**) 894-896.
[69] Ron, M., Mathalone, Z., *Physical Review B*, 4 (**1971**) 774-777.
[70] Mitchell, J.J., *J. Chem. Phys.*, 21 (**1953**) 1153-1159.
[71] Pichler, H., Merkel, H., *Brennst.-Chem.*, 31 (**1950**) 33-42.
[72] Nagakura, S., *J. Phys. Soc. Jpn.*, 14 (**1959**) 186-195.
[73] Mitchell, J.J., *The Journal of Chemical Physics*, 21 (**1953**) 1153-1159.
[74] Shultz, J.F., Hall, W.K., Seligman, B., Anderson, R.B., *J. Am. Chem. Soc.*, 77 (**1955**) 213-221.
[75] Bernas, H., Campbell, I.A., Fruchart, R., *J. Phys. Chem. Solids*, 28 (**1967**) 17-24.
[76] Amelse, J.A., Butt, J.B., Schwartz, L.H., *J. Phys. Chem.*, 82 (**1978**) 558-563.
[77] Raupp, G.B., Delgass, W.N., *J. Catal.*, 58 (**1979**) 348-360.
[78] Raupp, G.B., Delgass, W.N., *J. Catal.*, 58 (**1979**) 337-347.
[79] Raupp, G.B., Delgass, W.N., *J. Catal.*, 58 (**1979**) 361-369.
[80] Schäfer-Stahl, H., *Angew. Chem. Int. Ed.*, 19 (**1980**) 729-731.
[81] Niemantsverdriet, J.W., Van der Kraan, A.M., Van Dijk, W.L., Van der Baan, H.S., *J. Phys. Chem.*, 84 (**1980**) 3363-3370.

[82] Niemantsverdriet, J.W., van der Kraan, A.M., *J. Catal.*, 72 (**1981**) 385-388.
[83] Jung, H.J., Vannice, M.A., Mulay, L.N., Stanfield, R.M., Delgass, W.N., *J. Catal.*, 76 (**1982**) 208-224.
[84] Jung, H.J., Walker, P.L., Vannice, A., *J. Catal.*, 75 (**1982**) 416-422.
[85] Reymond, J.P., Mériaudeau, P., Teichner, S.J., *J. Catal.*, 75 (**1982**) 39-48.
[86] Blanchard, F., Reymond, J.P., Pommier, B., Teichner, S.J., *J. Mol. Catal.*, 17 (**1982**) 171-181.
[87] Kuivila, C.S., Stair, P.C., Butt, J.B., *J. Catal.*, 118 (**1989**) 299-311.
[88] Dictor, R.A., Bell, A.T., *J. Catal.*, 97 (**1986**) 121-136.
[89] Bukur, D.B., Koranne, M., Lang, X., Rao, K.R.P.M., Huffman, G.P., *Appl. Catal., A*, 126 (**1995**) 85-113.
[90] O'Brien, R.J., Xu, L., Spicer, R.L., Davis, B.H., *Energy & Fuels*, 10 (**1996**) 921-926.
[91] Herreyre, S., Gadelle, P., Moral, P., Millet, J.M.M., *J. Phys. Chem. Solids*, 58 (**1997**) 1539-1545.
[92] Bukur, D.B., Lang, X., Ding, Y., *Appl. Catal., A*, 186 (**1999**) 255-275.
[93] Li, S., O'Brien, R.J., Meitzner, G.D., Hamdeh, H., Davis, B.H., Iglesia, E., *Appl. Catal., A*, 219 (**2001**) 215-222.
[94] Li, S., Ding, W., Meitzner, G.D., Iglesia, E., *J. Phys. Chem. B*, 106 (**2002**) 85-91.
[95] Hao, Q., Bai, L., Xiang, H., Li, Y., *J. Nat. Gas Chem.*, 18 (**2009**) 429-435.
[96] de Smit, E., Cinquini, F., Beale, A.M., Safonova, O.V., van Beek, W., Sautet, P., Weckhuysen, B.M., *J. Am. Chem. Soc.*, 132 (**2010**) 14928-14941.
[97] Retief, J.J., *Powder Diffr.*, 14 (**2013**) 130-132.
[98] Matsumoto, H., Bennett, C.O., *J. Catal.*, 53 (**1978**) 331-344.
[99] Shroff, M.D., Datye, A.K., *Catal. Lett.*, 37 (**1996**) 101-106.

Chapter

2

Metal-Organic Framework (MOF) Mediated Synthesis of Highly Active and Stable Fischer-Tropsch Synthesis Catalysts

Depletion of crude oil resources and environmental concerns have driven a worldwide research on alternative processes for the production of fuels and commodity chemicals. Iron-based Fischer-Tropsch synthesis is a process for flexible production of key chemicals and fuels from synthesis gas originating from non-petroleum-based sources. Although the use of an iron catalyst would be preferred over the widely used cobalt catalyst, manufacturing methods that prevent their fast deactivation due to sintering, carbon deposition, and phase changes have proven challenging. In this Chapter, a new strategy to produce highly dispersed iron carbides embedded in a matrix of porous carbon (Fe@C) is presented. Very high iron loadings above 40 wt% are achieved, while maintaining an optimal dispersion of the active iron carbide phase when a metal-organic framework (MOF) is used as catalyst precursor. The unique iron spatial confinement and the absence of large iron nanoparticles in the obtained materials minimize catalyst deactivation, resulting in unrivalled active and stable operation.

This chapter is based on the following publication:

V.P. Santos, T.A. Wezendonk, J.J. Delgado Jaén, A.I. Dugulan, M.A. Nasalevich, H. Islam, A. Chojecki, S. Sartipi, X. Sun, A.A. Hakeem, A. Koeken, M. Ruitenbeek, T. Davidian, G.R. Meima, G. Sankar, F. Kapteijn, M. Makkee, and J. Gascon ***Nat. Commun.,*** 2015, 6:6451, 1-8.

2.1 Introduction

The growing concerns about oil depletion have spurred worldwide interest in finding alternative feedstocks for important petrochemical commodities and fuels. Fischer-Tropsch synthesis (FTS) is a heterogeneous catalyzed polymerization reaction where syngas, a mixture of CO and H_2, derived from natural gas, coal, or biomass, is converted into a wide spectrum of hydrocarbon chains [1-3]. Cobalt, ruthenium, iron and nickel are all active metals in FTS, but only iron and cobalt are used industrially. Owing to their high intrinsic activity towards long chain hydrocarbons, cobalt-based FTS catalysts remain the preferred catalyst choice for the gas-to-liquids processes (GTL). However, Fe-based catalysts have some superior properties over Co-based catalysts, especially for syngas derived from coal or biomass, namely: 1) cheap and widely available compared to Co; 2) active in the water-gas-shift reaction under typical FTS conditions, enabling the *in situ* readjustment of the H_2/CO molar ratio for the conversion of hydrogen-lean syngas originating from coal or biomass [1]; and 3) under high temperature FTS conditions (HTFT), the product slate of Fe-based catalysts is more directed to short chain unsaturated hydrocarbons and short chain oxygenates, both among the most important chemical building blocks.

The main challenge in the design of Fe-based FTS catalysts lies in overcoming the high deactivation rates due to sintering, carbon deposition, and iron phase changes (interconversion of Hägg carbide phase into iron oxides) [1, 2, 4, 5]. Under FTS conditions, bulk Fe catalysts display a poor mechanical stability and tend to fragment due to carbon deposits or to density differences between iron oxide and iron carbide phases [6, 7]. Catalyst fragmentation results in the formation of fines which leads to reactor operation problems such as pressure drop and possible fouling. A strategy to minimize the nucleation of carbon deposits is to reduce the size of the α-Fe_2O_3 crystallite precursors. SiO_2, ZnO, TiO_2, and Al_2O_3 are often added as structural promoters in order to increase the dispersion of iron. The main drawback of these supports is the formation of mixed oxides that are hardly reducible and therefore non-active for FTS, such as iron silicates and titanates [8-10].

Carbon supports in the form of activated carbon, carbon nanofibers (CNF), carbon nanotubes(CNT), carbon spheres, and glassy carbon have been proposed as supports for Fe-based FTS catalysts [2, 11]. The main advantage of these materials is their chemical inertness, high specific surface area, tunable pore structure, and surface chemistry. Generally, carbon supported catalysts are prepared in a multi-step process: (1) carbonization of an organic precursor, (2) physical or chemical activation of the carbon product, (3) deposition of the active component by incipient wetness impregnation (IWI) [11, 12], ion-exchange [13], or chemical vapor deposition [14], and (4) thermal treatment involving calcination or reduction to form metal oxide or metallic nanoparticles. This process is usually non-continuous and the distribution of the active phase is frequently compromised during the high-temperature steps, especially when high loadings are targeted. The alternative, direct carbonization

of dispersed iron in various polymers usually results in the formation of iron nanoparticles with a very broad particle size distribution [15-17].

Recently, Metal-organic frameworks (MOFs) have emerged as promising precursors for the synthesis of nanomaterials, because of their unique structure, atomic metal dispersion and textural properties [18-25]. For example, by using MOF-5 as a template and furfuryl alcohol (FA) as an additional carbon source, porous carbons have been synthesized as electrode materials for supercapacitors [20, 25], whereas Fe_2O_3/TiO_2 nanocomposites were synthesized from MIL-101(Fe) for photocatalytic water splitting [19]. Herein, a simple, tunable, and scalable MOF Mediated Synthesis (MOFMS) strategy for the preparation of exceptionally dispersed Fe nanoparticles in a porous carbon matrix (Fe@C) is reported. The resulting materials display outstanding catalytic FTS performance, with high activity and stability.

2.2 Experimental

2.2.1 Synthesis of Fe@C and K-Fe@C catalysts

The Fe based MOF *Basolite® F300* was used as a sacrificial template for the preparation of the different Fe@C catalysts. Basolite F300 (Fe-BTC), $C_9H_3FeO_6$; BTC = 1,3,5-benzenetricarboxylate) consists of oxo-centered trimers of Fe^{3+} cations connected by trimesate anions [26]. In order to vary the iron loading of the resultant catalyst, a carbon precursor is added to the MOF precursor. In a typical synthesis, furfuryl alcohol (FA) was dissolved in methanol and impregnated on Fe-BTC by incipient wetness impregnation. Subsequently, the FA accommodated inside the pores was polymerized at 80 ˚C and 150 ˚C for 14 h and 6 h, respectively, under nitrogen atmosphere, using a heating rate of 2 ˚C min^{-1}. The carbonization was carried out at 500 ˚C for 8 h, under nitrogen atmosphere. The iron loading was tuned by adjusting the amount of FA dissolved in methanol. The synthesized catalysts are denoted as 'Z-Fe@C', with Z representing the weight percentage of Fe in the catalyst. After every pyrolysis treatment, the materials were passivated at room temperature, using a 2.5 vol% O_2 in N_2 for 2 h. Owing to the outstanding effect of alkali promotion on iron-based catalysts for HTFT toward lower olefins [27-29], a series of potassium promoted samples was also synthesized. The potassium-promoted catalysts were prepared by incipient wetness impregnation. K_2CO_3 was dissolved in a mixture of water and methanol (50:50) and impregnated inside the pores of Fe@C to achieve the desired K promotion level. The resultant material was heated up to 80 ˚C for 2 h and carbonized at 500 ˚C for 4 h under nitrogen atmosphere, using a heating rate of 2 ˚C min^{-1}.

2.2.2 Catalyst characterization

2.2.2.1 Pyrolyzed Fe@C catalysts

TGA experiments were performed in a Mettler Toledo TGA/SDTA851e apparatus by heating the sample from RT to 1000 ˚C at a rate of 10 ˚C min^{-1} in a flow of 100 mL·min^{-1} synthetic air. Nitrogen adsorption and desorption isotherms were recorded on a QuantaChrome Autosorb-6B at 77 K. Samples were previously evacuated at 150 ˚C for 16 h. The BET method was used to calculate the surface area. High-angle annular dark field scanning transmission electron microscopy (HAADF-STEM) images were recorded on a *JEOL2010F instrument* by using an electron probe of 0.5 nm of diameter at a diffraction camera length of 10 cm. High-resolution transmission electron microscopy (HRTEM) images were recorded on the same microscope with 0.19 nm spatial resolution. XPS measurements were performed on a *K*-alpha Thermo Fisher Scientific spectrometer using a monochromatic Al *K*α X-ray source. Samples were prevented from exposure to ambient conditions using an integrated glove box. The measurements were carried out with a spot size of 300 µm at ambient temperature and chamber pressure of about 10^{-7} mbar using a flood gun for charge compensation. Spectra are averages of 10 scans and were calibrated by the binding energy of core level C*1s* at 285 ±0.025 eV. Analysis and processing was performed with Thermo Avantage v5.52 software using a Lorentzian-Gaussian (L/G) ratio of 0.3 for peak fitting with S-shaped background correction. The binding energy reported is within ±0.1 eV. The relative surface concentrations were calculated from the integral of each core level peak and further converted to surface atomic concentrations by the atomic sensitivity factors.

2.2.2.2 in situ *spectroscopy of Fe-BTC Pyrolysis and Fe@C FTS*

Transmission ^{57}Fe Mössbauer absorption spectra were collected at 300 K with a constant-acceleration spectrometer using a ^{57}Co(Rh) source. Velocity calibration was carried out using an α-Fe foil. The Mössbauer spectra were fitted using the Mosswinn 3.0i program [30]. The spectra were measured at room temperature after cooling the sample in the reaction mixture after each treatment. One Mössbauer spectrum is recorded each time until a satisfactory signal-to-noise ratio is achieved (10-15 h). The pristine Fe-BTC was loaded into the *in situ* cell and pyrolysis according to the abovementioned protocol commenced. For the reduction step, the cell containing the pyrolysed sample was cooled to 400 ˚C and exposed to a flow of 10 vol% H_2 in He The dominant Hägg carbide species were evaluated after performing 5 h of HTFT reaction at 340 ˚C and 15 bar. Experimental uncertainties in reported values for isomer shift ± 0.01 mm s^{-1}, quadrupole splitting ± 0.01 mm s^{-1}, Line width ± 0.01 mm s^{-1}, hyperfine field ± 0.1 T, and the spectral contribution ± 3%.

X-Ray absorption spectroscopy (XAS) was performed at BL22, ‘Core level absorption and emission spectroscopies’, beam line of ALBA in Barcelona, Spain. The beam line is equipped with Si(111) and

Si(311) monochromators and operates in the range of energies between 2.6 and 36 keV. In this particular experiment, the Si(111) monochromator and Rh-coated toroid mirror were employed. The materials were studied using Fe *K*-edge (ca. 7111 eV). In a typical *in situ* experiment, Fe-BTC was diluted with boron nitrate to achieve a desired edge jump value of around unity. The solid mixture was then pelletized by applying 2 tonne cm^{-2} pressure for 5 min. Subsequently, the sample was placed in an in *situ* cell described elsewhere [31]. The cell is equipped with Kapton windows and was used in transmittance mode. The sample environment is continuously purged with a flow of He of 20 cm^3 min^{-1} and heating was applied with increments of 50 ˚C and measurements were obtained after reaching the set point. Once the sample reached 450 ˚C, XAS spectra were collected until no further changes were observed. For the reduction step, the cell containing the pyrolysed sample was cooled to 400 ˚C and exposed to a flow of 10 vol% H_2/He. The flow rate was 20 cm^3 min^{-1} and the cell pressure was 1 bar. The reduction process was monitored by EXAFS/XANES for 3 hours. The sample was subsequently exposed to Fischer-Tropsch (FTS) conditions at 340 ˚C and 2 bar in a flow of CO/H_2 (1:1) mixture under a flow rate of 60 cm^3 min^{-1}.

The collected spectra were pre-analysed for glitches and merged by using the ATHENA software package [32]. The package files were exported to VIPER for background subtraction and normalization using the automated protocol implemented in the program [33]. The normalized μ(E) curves were subsequently transformed to the reciprocal space. Fitting of the experimental spectra was performed by using EXCURVE version 9.273 [34]. Iron foil was used as a standard to determine the amplitude reduction factor. The model used for simulating the room temperature EXAFS spectrum of Fe-BTC was based on the crystallographic data reported by Ferey and co-workers on MIL-100(Fe) [26]. In order to fit the spectrum of the pyrolyzed MOF at elevated temperatures, this model was employed as starting parameter, while introducing additional shells into the model until satisfactory fitting was achieved.

2.2.3 Catalytic tests of Fe@C and K-Fe@C

FTS experiments were performed in a 48-flow fixed-bed micro-reactor setup, which allowed running up to 48 reactions in parallel under similar feed composition and process conditions. In order to avoid condensation of products at high conversion levels, an inert gas flow (N_2) was injected downstream the reactor to each flow. For all experiments, ~10 mg (20 μL) of fresh catalyst with the particle size of 177–420 μm was diluted with 100 μL SiC particles of the same size. Samples were firstly activated *in situ* at 425 ˚C for 3 h under 3 bar of pure H_2 followed by cooling to 340 ˚C under H_2 flow at the same pressure. After increasing the pressure to the process value of 20 bar, a 10 cm^3 min^{-1} flow consisting of CO 45 vol%, H_2 45 vol%, and He 10 vol% was introduced. A rate of 2 ˚C min^{-1} was applied for all the heating and cooling steps. A *Siemens Maxum* Process GC, equipped with multiple columns and detectors in parallel, analyzed permanent gases as well as hydrocarbon products up to C7 in the gas

phase online. In the first column (*Carboxen* 1010, 10 m × 0.32 mm) N_2, CO, CH_4, and CO_2 were separated at 60 ˚C and analyzed by TCD. In the second column (Al_2O_3/KCl, 10 m × 0.32 mm) with FID detection, separation between all C_1–C_4 components was achieved at 160 ˚C.

CO conversion (%), carbon selectivity (%) and molar fraction (-) of each product were defined by equations (1), (2), and (3), respectively, where X_{CO} stands for CO conversion, F indicates the molar flow, S is the carbons selectivity towards a product with n carbon atoms and y is the molar fraction of a hydrocarbon C_n. Catalytic activity is expressed as iron time yield (*FTY*), defined as the number of CO moles converted to hydrocarbons per gram of Fe (w_{Fe}) per second. The apparent turn over frequency (*TOF*) was calculated for catalysts with known metal dispersion (D) using the molar mass of iron (M_{Fe}) and the degree of carburization (Δ).

$$X_{CO} = \frac{F_{in,CO} - F_{out,CO}}{F_{in,CO}} \qquad \text{Eq. (1)}$$

$$S_{Cn} = \frac{nF_{Cn}}{F_{CO_2} + \sum_{n=1}^{N} nF_{Cn}} \qquad \text{Eq. (2)}$$

$$y_{Cn} = \frac{F_{Cn}}{\sum_{n=1}^{N} F_{Cn}} \qquad \text{Eq. (3)}$$

$$FTY = \frac{X_{CO} F_{in,CO}(1 - S_{CO2})}{w_{Fe}} \qquad \text{Eq. (4)}$$

$$TOF = \frac{FTY\, M_{Fe}}{D\, \Delta} \qquad \text{Eq. (5)}$$

2.3 Results and Discussion

2.3.1 Pyrolyzed Fe@C catalysts

TGA demonstrated that the catalyst containing the highest amount of Fe was prepared by direct pyrolysis of Fe-BTC at 500 ˚C without impregnation with FA. The Fe loading of Fe@C varies between 25 to 38 wt% (**Table 2.1 and Figure A2.1**), decreasing with increasing amount of carbon precursor. Thus, the produced furan resin inside the pores of the MOF displays a lower degree of carbonization after pyrolysis of the precursor. The textural properties of the carbonized MOFs were evaluated by N_2 adsorption at 77 K, summarized in **Table 2.1 and Figure A2.2**. The pyrolysis of highly microporous

Fe-BTC without impregnated FA produces a micro- and mesoporous material with a moderate BET area of 130 $m^2\ g^{-1}_{cat}$; this is the surface area calculated per total gram of catalyst including 38 wt% of Fe. A hysteresis type H3 between adsorption and desorption branches at intermediate pressure of $P/P_0 \approx 0.4$, indicates the presence of mesoporous cavities with a very wide size distribution [35]. In contrast, samples synthesized with additional carbon source are highly microporous with BET surface areas ranging from 320 to 350 $m^{2\cdot}\ g^{-1}$. The absence of mesoporosity and associated increase in microporosity indicates a different carbon pore network is formed by situating of FA inside the MOF prior to pyrolysis, as the obtained carbons of FA-Fe@C are denser than 38-Fe@C.

Transmission electron microscopy on the synthesized catalysts demonstrates the high degree of dispersion of Fe nanoparticles confined within the porous carbon matrix, regardless the Fe loading (**Figure 2.1 and Figure A2.3**). HAADF-STEM allows unequivocal measurement of the particle size of Fe nanoparticles, as maximum contrast is achieved between Fe and the C matrix (**Figure A2.3**). Furthermore, STEM-EDX mapping results on 250 x 250 nm areas confirm the high amount of monodispersion and absence of large agglomerates. HR-TEM analysis reveals that several rings of graphitic carbon are formed around the occasionally encountered larger nanoparticles on the outskirts of the carbon matrix grains. Based on these analyses, the mean particle size varies between 2.5 and 3.6 nm for different catalysts. There is no apparent correlation between the amount of FA impregnated in the MOF pores and the Fe nanoparticle size, although it is clear that particle size can be significantly decreased by the higher degree of confinement of Fe through the addition of furan resins in the MOF. The calculated Fe phase dispersions values reach up to 39%, and have, to the best of our knowledge, never been reported in literature for such highly loaded Fe catalysts. X-ray diffraction results (XRD) substantiate the presence of iron nanocrystallites, as very weak diffraction patterns are obtained for the Fe@C catalysts (**Figure A2.4**). The main diffraction bands of 38-Fe@C originate from pseudo-crystalline Fe oxides, with minor hints of metallic Fe and Fe carbides in the

Table 2.1 Textural characterization of the synthesized catalysts (Fe@C) and MOF precursor. $\boldsymbol{V_{FA}}$ volume FA impregnated prior to pyrolysis $\boldsymbol{S_{BET}}$ specific surface area calculated by BET method $\boldsymbol{S_{meso}}$ mesoporous surface area calculated by t-plot method $\boldsymbol{d_p}$ average Fe nanoparticle size obtained from 900+ particle counts in TEM.

Catalyst	V_{FA} / $cm^3\ g^{-1}$	S_{BET} / $m^2\ g^{-1}$	S_{meso} / $m^2\ g^{-1}$	d_p / nm
25-Fe@C	0.9	320	17	3.3
27-Fe@C	0.5	351	20	2.5
31-Fe@C	0.3	327	17	2.6
38-Fe@C	-	130	62	3.6
Basolite F-300 Fe-BTC	n.a.	840	-	n.a.

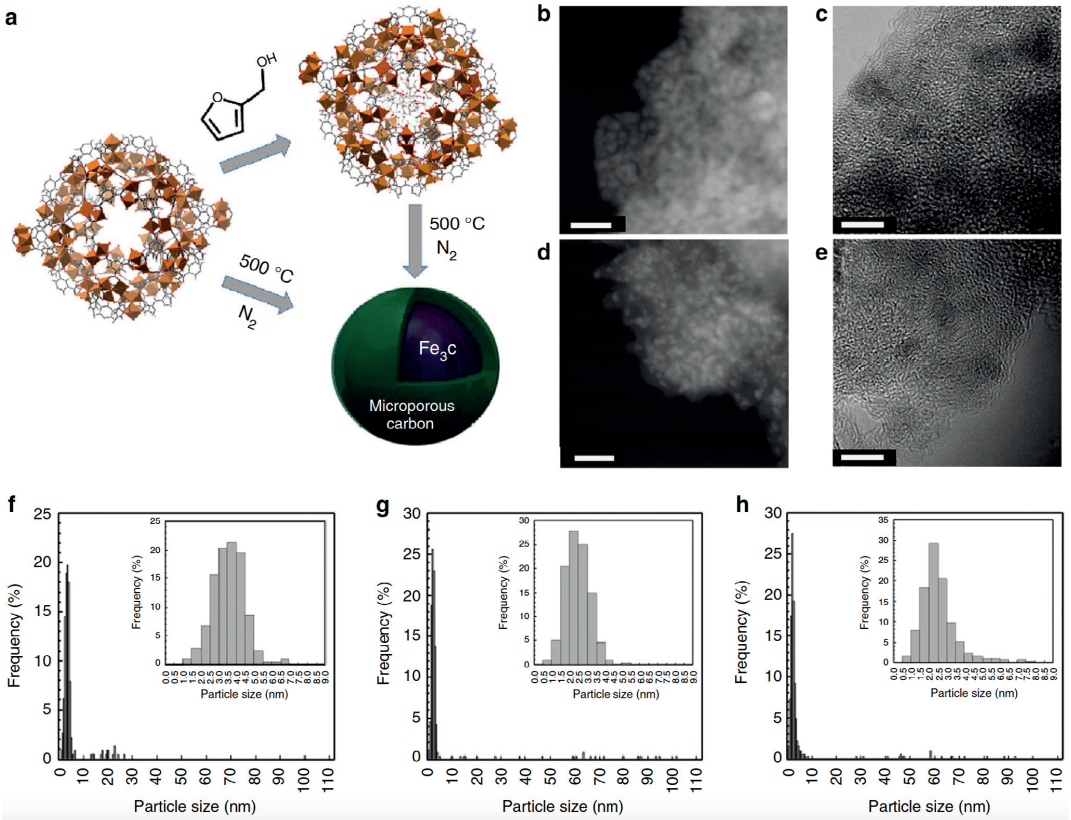

Figure 2.1 MOF-mediated synthesis (MOFMS) strategy and electron microscopy characterization. **A** MOFMS strategy for the Fe-based FTS catalysts: direct pyrolysis of Basolite F-300 Fe-BTC and impregnation of the MOF with carbon source FA followed by pyrolysis **B** HAADF-STEM micrograph of 38-Fe@C (scale bar: 20 nm) **C** HR-TEM micrograph of 38-Fe@C (scale bar: 5 nm) **D** HAADF-STEM of 25-Fe@C (scale bar: 20 nm) **E** HRTEM of 25-Fe@C (scale bar: 5 nm) **F** Particle size distribution histograms obtained from TEM analysis counting at least 900 nanoparticles for 38-Fe@C **G** 31-Fe@C **H** 27 Fe@C. The inserts in the histograms panels **F, G, H** depict the particle size distribution of nanoparticles smaller than 9 nm; representing in every case more than 95% of the nanoparticles counted in the samples.

region 52-53 ˚. Addition of the pre-pyrolysis furan resins increasingly defines the Fe oxide diffractions at 35 ˚ and 41 ˚, and results in substantial diffraction patterns assigned to Fe carbides in the 52-53 ˚ region. The long-range order of θ-Fe_3C, visible as a shoulder at 44 ˚and distinct diffractions at 56 ˚ and 59 ˚, suggests that increased confinement renders the onset of Fe carbide formation. The main bands and satellites obtained in the X-ray photoelectron spectroscopy (XPS) spectra of 25-Fe@C and 31-Fe@C at 724.9 eV and 711.3 eV confirm the dominant presence of surface Fe oxides much resembling Fe_3O_4 (**Figure A2.5**), while the sharp peaks around 707.4-707.8 eV ($Fe2p_{3/2}$) and 720.9-720.5 eV ($Fe2p_{1/2}$) demonstrate the coexistence of undetermined surface Fe_xC species [36-39]. The

Fe*2p*$_{3/2}$ carbide region comprises slightly lower binding energies for samples prepared with higher FA loadings, suggesting the formation of different surface carbide species with possible higher carbon concentration. For example, χ-Fe_5C_2 has a reported binding energy of 707.3 eV, while for carbides with a more covalent character or decreased carbon concentration, lower binding energies are found, for example at 706.9 eV. Three different types of surface oxygen species can be identified from the XPS O*1s* core level spectra (**Figure A2.6**): the band at 530.1-531.1 eV is characteristic of Fe_3O_4 [36, 40, 41], while the higher energy bands around 532.5 and 534.5 eV correspond to the presence of surface oxygen groups such as C=O and COO, respectively [42]. The FA loading significantly increases the oxygen functionalization on the surface of the carbon, as the relative amount of oxygenated groups on 25-Fe@C is about 78 %, whereas on 31-Fe@C it decreases to 68 %. These results are analogous to the declined degree of carbonization of the MOFs with incorporated furan resins, consequently resulting in an increased carbon and oxygen content proportional to the FA impregnation in the pristine MOF. Furthermore, XPS displays that only minor amounts of Fe are located at the outer surface of the catalysts. The values of relative Fe contributions range between 6-9 wt%, thus confirming the high degree of confinement and encapsulation of the Fe phase within the carbon matrix.

Table 2 The Mössbauer fitted parameters for the *in situ* pyrolysis of Fe-BTC and HTFT of 38-Fe@C**.** Displayed are the isomer shift *IS*, quadrupole splitting *QS*, Line width *Γ*, Hyperfine field and spectral contribution.

Catalyst	*IS* / mm s^{-1}	*QS* / mm·s^{-1}	*Hyperfine field* / T	*Γ* / mm·s^{-1}	Phase	Spectral contribution / %
Basolite F-300	0.42	0.54	-	0.55	Fe^{3+}	100
38-Fe@C	0.20	0.30	-	0.49	Fe^{3+} (SPM Fe_xC)	26
	1.06	0.58	-	0.72	Fe^{2+} (FeO)	74
38-Fe@C	0.01	-	33.3	0.52	Fe^0	76
H_2, 400 ˚C, 1 bar	0.13	0.52	-	0.51	Fe^{3+} (SPM Fe_xC)	16
	1.06	0.46	-	0.51	Fe^{2+} (FeO)	8
38-Fe@C	0.23	-	18.1	0.64	χ-Fe_5C_2 (I)	39
H_2/CO=1, 340 ˚C,	0.28	-	21.7	0.50	χ-Fe_5C_2 (II)	26
5 h, 15 bar	0.19	-	10.5	0.65	χ-Fe_5C_2 (III)	21
	0.26	0.69	-	0.64	Fe^{3+} (SPM Fe_xC)	9
	1.06	0.72	-	0.91	Fe^{2+}	5

2.3.2 *in situ* spectroscopy of Fe-BTC Pyrolysis and Fe@C FTS

In situ Mössbauer spectroscopy was applied during the pyrolysis process to gain insight into the chemical nature of the Fe species formed upon carbonization of the MOF precursor (**Figure 2.2A and Table 2.2**). The spectrum of the MOF precursor shows the presence of 100 % high-spin Fe^{3+} in an octahedral environment, in agreement with literature data [26]. During carbonization, these species undergo partial reduction and are converted into 26 % of superparamagnetic Fe_xC iron carbide, and 76 % FeO Wüstite phase (**Table 2.2**). Additional Mössbauer experiments were carried out with the *in situ* pyrolyzed MOF, exposing it to activation and FTS conditions (**Figure 2A and Table 2.2**). After exposure of the samples to H_2 at 400 ˚C, most of the Fe atoms (76%) reduce to metallic Fe, while some Fe_xC and Fe^{2+} structures are still present in the spectra. Exposure of the sample to 5 h of FTS reaction conditions, 340 ˚C, 15 bar, H_2/CO = 1, converts 86 % of the Fe atoms into active χ-Fe_5C_2 Hägg carbide species. We speculate that the remaining Fe_xC superparamagnetic phase either originates from the initial carbonization procedure as ill-defined carbide crystallites derived from the MOF structure, or it corresponds to very small Hägg carbide species obtained during HTFT. The 95 % degree of carburization demonstrates that the Fe nanoparticles are highly accessible and that almost all metal loaded in the matrix can be utilized for catalysis. The experimental observations from Mössbauer spectroscopy were supported by *in situ* X-ray absorption spectroscopy (XAS) studies. Simulating the spectrum of Basolite F-300 yielded parameters listed in **Table A2.1** that closely match the ones deduced from X-Ray data refinements for MIL-100(Fe) [26].

The spectrum of Fe@C is remarkably different from Fe-BTC. XANES analysis on the pyrolysed solid reveals the reduction of Fe^{3+} centers of Fe-BTC to Fe^{2+} (**Figure 2.2B**). Moreover, simulation of the EXAFS results in Fe – O distances close to the ones found in Wüstite (**Table A2.1**) [43]. In addition, new scatterers emerge relating to Fe-C at the distance of 2.12 Å, and Fe-Fe at longer distances. Based on the fitting parameters and in line with the Mössbauer data, it is concluded that freshly pyrolysed Fe@C consists of a mixture of Wüstite and iron carbides. The H_2 reduction of the Fe@C catalyst (**Table A2.1 and Figure A2.7**) increases the coordination number of Fe-Fe at 2.53 Å which is consistent with the formation of metallic iron [44]. The exposure of the reduced sample to FTS conditions slightly reduces the contribution of Fe-Fe at around 2.53 Å and at the same time leads to a substantial increase in the long-distance iron scatterers (**Figure A2.7**). These results confirm that Fe^0 formed upon reduction is further transformed to carbidic phase under syngas conditions. However, one should note the difference in H_2 concentrations used in *in situ* Mössbauer and XAS experiments, as the lower concentration in the latter diminishes the degree of reduction of Fe@C after H_2 reduction.

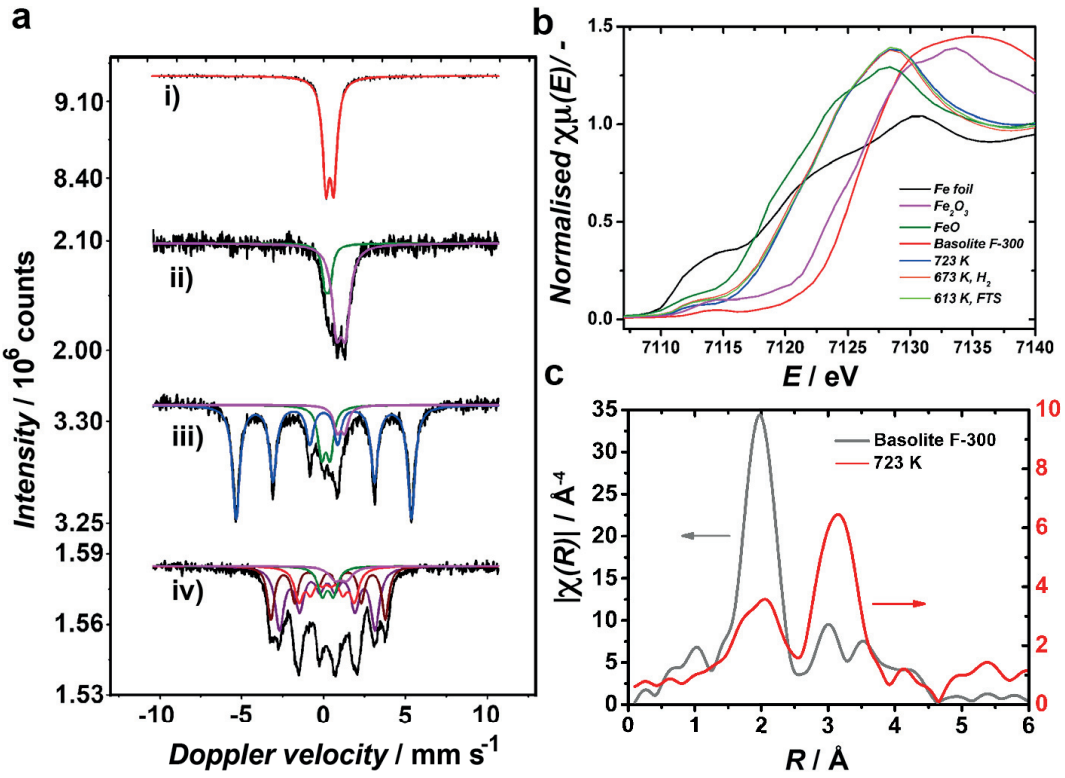

Figure 2.2 Spectroscopic characterization. **A** Mössbauer spectra obtained at room temperature after different successive treatments: **i)** Fresh Basolite F-300 Fe-BTC **ii)** 38-Fe@C obtained after pyrolysis at 450 ˚C **iii)** 38-Fe@C after reduction under atmospheric H_2 atmosphere at 400 ˚C and **iv)** 38-Fe@C after exposure to HTFT conditions of 340 ˚C, 1 bar and H_2/CO = 1 **B** XANES spectra of Fe-edge measurement standards: iron foil, Fe_2O_3, and FeO alongside Basolite F-300 Fe-BTC at room temperature, 38-Fe@C obtained after pyrolysis at 500 ˚C, 38-Fe@C reduced at 400 ˚C by 10 vol% H_2/He under atmospheric pressure, 38-Fe@C after 5 h under HTFT conditions of 340 ˚C, 1 bar and H_2/CO = 1 **C** EXAFS spectra of Basolite F-300 at 225 ˚C and 38-Fe@C at 450 ˚C.

2.3.3 Catalytic tests of Fe@C and K-Fe@C

The Fe@C catalysts were tested in the HTFT regime at 340 ˚C, 20 bar, H_2/CO = 1, and a gas hourly space velocity *GHSV* of 30,000 h^{-1}. The time-on-stream (*TOS*) evolution of CO conversion for the unpromoted Fe@C catalysts is presented in **Figure 2.3A**. Independently of the preparation method, all the materials showed very high and stable conversion levels, ranging between 72 and 77% after 90 h on stream. Under the applied process conditions, the main difference found as a consequence of the FA addition is the catalyst activation period. Samples containing the highest

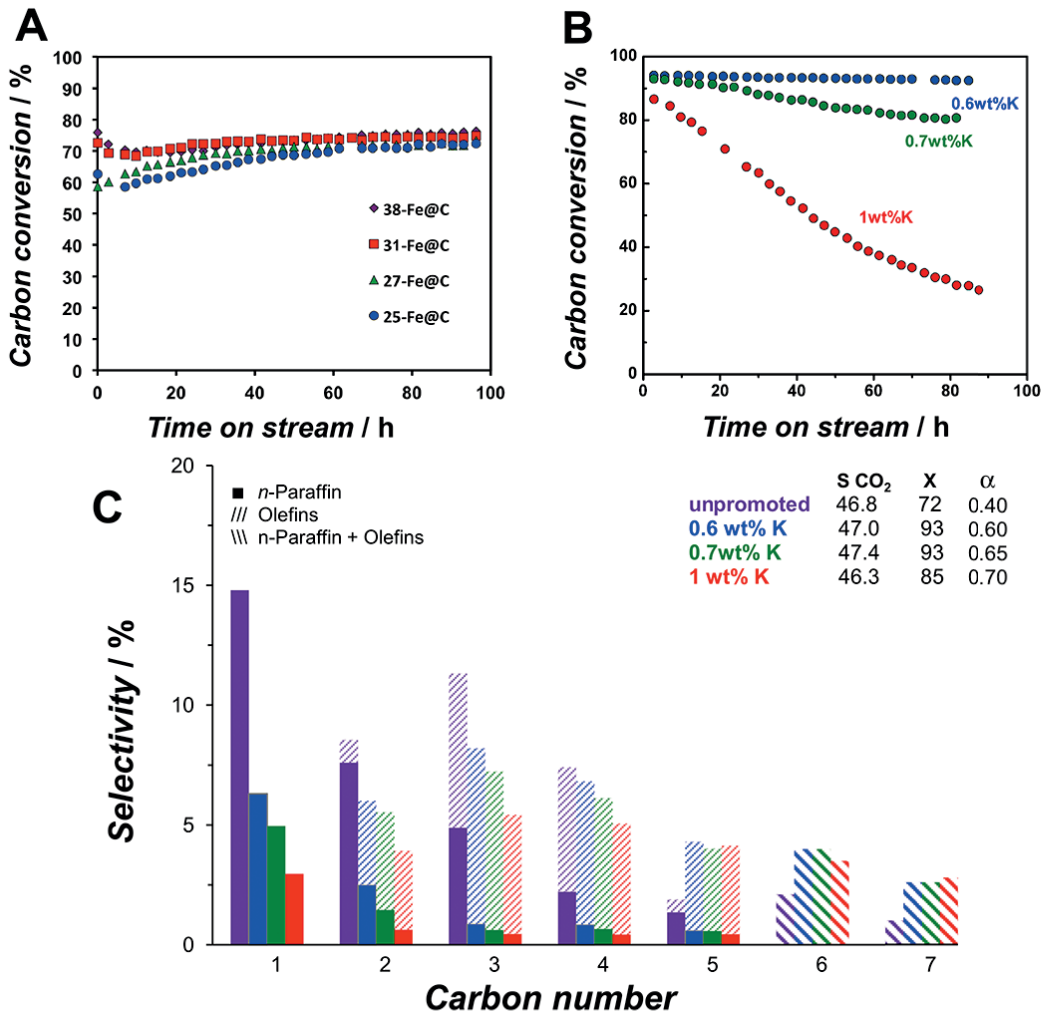

Figure 2.3 Catalytic performance of Fe@C and K-Fe@C. **A** Time evolution of CO conversion for the unpromoted Fe@C catalysts **B** Time evolution of CO conversion for K-promoted 38-Fe@C catalysts **C** Product distribution after 10 h *TOS* for the unpromoted and promoted 38-Fe@C under 340 ˚C, 20 bar, H_2/CO = 1, and *GHSV* of 30,000 h^{-1}.

amount of Fe, such as 38- and 31-Fe@C, display steady state operation after 30 hours on stream, while catalysts synthesized with a higher amount of FA show a longer induction period spanning over 60 h. These results are attributed to the interconversion of the incrementally present cementite phase in the FA loaded catalysts, corresponding to the higher carbon contents displayed by TGA and the cementite bulk phase confirmed by XRD. The reduction of these highly confined iron carbide nanocrystallites would prove difficult under the short period of H_2 reduction, and need over 60 h

under HTFT conditions to carburize into active phase Hägg carbides. Moreover, diffusion limitations as a consequence of their more microporous nature cannot be excluded, affecting the local H_2 or H_2/CO concentration during reduction and FTS, respectively.

Nevertheless, in spite of these longer activation times, the product selectivity after 90 h on stream is similar for all four catalysts (**Figure A2.8 and Table A2.2**). These results indicate that through the addition of the furan resin, a more intimate interaction is created with the Fe clusters during Fe-BTC pyrolysis, resulting in a different bulk Fe phase and smaller nanoparticles. On the contrary, while the nature of the freshly synthesized catalysts is different, the Fe phase under HTFT conditions seems to equalize. The product selectivity of Fe@C follows the Anderson-Schulz-Flory (ASF) distribution, with chain growth probability (α) ranging from 0.40 to 0.44, where the higher values are obtained for the FA impregnated catalysts (**Table 2.4**). Accordingly, the CH_4 selectivity varies between 15.8 and 14.0 %, alongside a near-maximum water-gas-shift (WGS) activity witnessed by CO_2 selectivity above 46.8 %. The selectivity towards lower olefins in the C_2-C_5 region ranges from 14.6 up to 15.5% (**Table A2.2**). Furthermore, the incorporation of an additional carbon source seems to serve as a structural promotor, since no deactivation was observed for any of the Fe@C catalysts. Even though the particle size can be substantially decreased by more effectively spacing out the iron clusters of the MOF prior to pyrolysis, the increased dispersion of the iron nanoparticles has not changed their stability.

The initial catalytic activities are expressed as iron time yield, mol of CO converted to hydrocarbons per gram of Fe per second (*FTY*), and as apparent turnover frequency (*TOF*); the values of these performance indicators for Fe@C samples are summarized in **Table 2.4**. Furthermore, relevant data from literature for other HTFT catalysts comprising various Fe loading, supported on carbon nanofibers (X-Fe/CNF) [11] and oxidised carbon nano-tubes (20-Fe/O-CNT) [45], are included in **Table 2.4** as well. The catalysts prepared by the MOFMS route display much higher *FTY* in comparison with X-Fe/CNT, and crucially, the inverse proportionality between Fe loading and dispersion is absent for the Fe@C catalysts. For example, 27-Fe@C is over 3 times more active than 1-Fe/CNF and almost two orders of magnitude more active than 20-Fe/CNF. While the 1 wt% Fe/CNF comprises FTY in the similar order of 10^{-4} mol_{CO} g_{Fe}^{-1} s^{-1}, increasing the Fe loading on this catalyst drastically lowers its activity. Thus, the combination of a high dispersion and high loading is the unique result of the MOF carbonization, leading to highly active and stable HTFT catalysts. Moreover, the carbon support does not induce strong metal support interaction (SMSI), rendering near-full carburization of the Fe phase. These results coincide with those on 20-Fe/O-CNT and 40-Fe/O-CNT, where the Fe phase was completely carburized into Hägg carbide after 50 h *TOS* [45]. In contrast, the Fe/CNF catalysts contain nearly 50 % of iron oxides after 15 h of exposure to syngas, in which period the activity had declined substantially [11]. In addition, the impressive FTS rates of Fe@C catalysts are coupled to near-maximum WGS rates (**Scheme A2.1**), allowing for high rates of

removal of water from the catalyst surface. Enhanced WGS activity is a likely cause for maintaining the degree of carburization under HTFT. Furthermore, we speculate that the hydrophobic carbon of the encapsulating matrix might aid in avoiding oxidation of the active carbide phase under reaction conditions [46].

Poor stability of Fe catalysts is generally observed for systems with high initial dispersion that quickly deactivate to form larger Fe particles, often accompanied with the continuous structural and chemical transformations of the iron phases, in addition to the formation of inactive carbon deposits on the catalyst surface [28]. The striking stability of the Fe@C catalysts is attributed to the fact that the Fe nanoparticles are spatially restricted in the porous carbon matrix, highly accessible to reagent gases and thus fully carburizing inside the carbon environment. Furthermore, the results at high conversion suggest that catalysts are sufficiently active in the hydrogenation and chain propagation of the surface carbon moieties. To display the outstanding stability of Fe@C under higher H_2/CO partial pressures, additional catalytic tests were performed on 38-Fe@C at higher space velocities of 190,000 h^{-1}. These results are summarized in **Figure A2.10** and confirm very stable performance over more than 220 h under differential conditions.

Table 2.4 Catalytic performance of unpromoted Fe catalysts after 4 h *TOS* under 340 °C, 20 bar, and H_2/CO = 1. Reported are CO conversion X_{CO}, activity per gram of Fe per second *FTY*, apparent turnover frequency *TOF*, and chain growth probability α. The catalytic performance of comparable catalytic systems in HTFT is also included: Fe supported on carbon nanofibers (X-Fe/CNF) and Fe supported on oxidized carbon nanotubes (20-Fe/O-CNT).

Catalyst	d_p / nm	*GHSV** / $cm^3\ g^{-1}\ min^{-1}$	X_{CO} / %	*FTY* / 10^{-4} $mol_{CO}\ g^{-1}_{Fe}\ s^{-1}$	$TOF_{apparent}$ / s^{-1}	α / -	References
25-Fe@C	3.3	1000	59	4.9	0.11	0.43	This work
27-Fe@C	2.6	1000	60	4.4	0.07	0.44	This work
31-Fe@C	2.8	1000	70	4.4	0.07	0.42	This work
38-Fe@C	3.6	1000	72	3.8	0.08	0.40	This work
1-Fe/CNF	2.1	100	10	1.4	0.08	0.30	[11]
5-Fe/CNF	3.2	100	11	0.2	0.02	0.34	[11]
20-Fe/CNF	6.9	100	10	0.06	0.01	0.44	[11]
20-Fe/O-CNT	8	833	27	1.4	-	0.45	[45]

**GHSV* is expressed as $cm^3\ g^{-1}\ min^{-1}$ for direct comparison with other catalysts.

To further enhance the selectivity of the catalysts to valuable products, a study on the optimal loading of potassium on Fe@C was carried out. Conversion profiles and product distributions of 38-Fe@C catalysts promoted with 0.6, 0.7 and 1.0 wt% of K are shown in **Figure 2.3B and Figure 2.3C**, respectively. All alkali promoted samples display an increase in initial activity, decrease in methane selectivity and increase in olefin content of the hydrocarbon products. Although a very impressive HTFT methane selectivity below 3 % can be obtained with 1.0K-38-Fe@C, it does not produce a stable catalyst. Optimized K-promotion of 0.6 wt% results in an equally stable catalyst as Fe@C, but with far lower selectivity to methane below 6 % compared to the original 15 %. In addition to a decrease in C_1 selectivity, results K-promotion of Fe@C in an overall decrease in the hydrogenation ability of the iron carbide surface. The chain growth probability α gradually increases when higher concentrations of potassium are present on the catalyst surface, ranging from 0.4 for the unpromoted 38-Fe@C up to 0.7 for 1.0K-38-Fe@C (**Figure A2.9**). Moreover, the significant increase in the olefin content in the product distribution indicates that chain termination by secondary hydrogenation of olefins to paraffins was decreased. The ethylene-to-ethane ratio concurrently grows with K promotion from 0.2 for the unpromoted Fe@C to 1.4, 2.8 and 5.3 for 1.0K-38-Fe@C. The yield toward desired products after 90 h therefore increases from 9 % C_2-C_4 olefins to 16.3 % C_2-C_4 olefins for 38-Fe@C and of 0.6K-38-Fe@C, respectively.

The modulation of the hydrogenation ability was suggested to originate from the facilitation of CO dissociation on the iron carbide surface. However, our unpublished results on isotopic labelling studies indicate that there is no reversible CO adsorption on Fe@C during HTFT, implying dissociative CO adsorption on the surface [47]. These results are in agreement with postulates by Dry *et al.* [48] that K increases the heat of adsorption of CO and weakens the adsorption of H_2, which in turn increases the relative surface concentration of C compared to H under HTFT reaction conditions. The overall decline in hydrogenation upon increasing K concentration and the associated maximized olefin content are in perfect agreement with the postulates. Hence, it seems likely that the deactivation witnessed on the highest amounts of K-Fe@C is due to excessive amounts of carbon deposition on the catalyst surface.

The above-mentioned characterization and catalytic performance results highlight the great potential of the MOFMS approach: (i) high Fe loadings in FTS catalysts up to 40 wt% with (ii) an optimal dispersion of the active phase comprising Fe nanoparticles below 4 nm which are (iii) efficiently transformed into FTS-active iron carbides embedded in a porous carbon matrix that (iv) prevents unwanted deactivation phenomena, thus providing highly stable and active HTFT catalysts. The performance of Fe@C catalysts is substantiated by comparing their productivity to that of available data on commercial catalysts, such as the traditional Ruhrchemie [49, 50] and Sasol [51] catalysts for HTFT (**Table A2.3**). The MOF-derived catalysts display productivities on a total catalyst weight basis

of one order of magnitude higher than these benchmarks, even when the Fe@C catalysts contain lower amounts of iron.

2.4 Conclusions

In summary, it was demonstrated that the MOF Mediated Synthesis (MOFMS) is a promising route for the precise design and synthesis of Fe-based FTS catalysts. The high Fe loadings that can be realized through this preparation method are accompanied by a high dispersion of the metal phase because of the encapsulation in a highly porous carbon matrix. Catalysts prepared following this approach display an intimate contact between Fe and C, facilitating the formation of highly dispersed Hägg carbides which results in unrivalled FTS activity and exceptional stability. The spatial restriction created by the carbon confinement minimizes sintering and oxidation of the active Hägg carbide phase. The performance of Fe@C catalysts herein presented is substantiated by comparing their productivity to that of available data on commercial benchmark catalysts, demonstrating that the MOF-derived catalysts display productivities one order of magnitude higher than these industrial standards. The simple and potentially universal design strategy of MOFMS opens the door to the controlled manufacture of highly dispersed and stable metal nanoparticles in porous matrices, one of the major challenges in materials science and industrial catalysis.

References

[1] Abelló, S., Montané, D., *ChemSusChem*, 4 (**2011**) 1538-1556.
[2] Sun, B., Xu, K., Nguyen, L., Qiao, M., Tao, F., *ChemCatChem*, 4 (**2012**) 1498-1511.
[3] Dry, M.E., *Catal. Today*, 71 (**2002**) 227-241.
[4] de Smit, E., Weckhuysen, B.M., *Chem. Soc. Rev.*, 37 (**2008**) 2758-2781.
[5] Pendyala, V.R.R., Graham, U.M., Jacobs, G., Hamdeh, H.H., Davis, B.H., *ChemCatChem*, (**2014**) n/a-n/a.
[6] Kalakkad, D.S., Shroff, M.D., Köhler, S., Jackson, N., Datye, A.K., *Appl. Catal., A*, 133 (**1995**) 335-350.
[7] Shroff, M.D., Kalakkad, D.S., Coulter, K.E., Kohler, S.D., Harrington, M.S., Jackson, N.B., Sault, A.G., Datye, A.K., *J. Catal.*, 156 (**1995**) 185-207.
[8] Kang, S.-H., Bae, J.W., Woo, K.-J., Sai Prasad, P.S., Jun, K.-W., *Fuel Processing Technology*, 91 (**2010**) 399-403.
[9] Barrault, J., Forquy, C., Menezo, J.C., Maurel, R., *React Kinet Catal Lett*, 15 (**1980**) 153-158.
[10] Park, J.-Y., Lee, Y.-J., Khanna, P.K., Jun, K.-W., Bae, J.W., Kim, Y.H., *Journal of Molecular Catalysis A: Chemical*, 323 (**2010**) 84-90.
[11] Torres Galvis, H.M., Bitter, J.H., Davidian, T., Ruitenbeek, M., Dugulan, A.I., de Jong, K.P., *J. Am. Chem. Soc.*, 134 (**2012**) 16207-16215.
[12] Kang, S.-H., Bae, J., Sai Prasad, P.S., Jun, K.-W., *Catal Lett*, 125 (**2008**) 264-270.
[13] G. Yun, H., I. Woo, S., S. Chung, J., *Appl. Catal.*, 68 (**1991**) 97-116.
[14] Guczi, L., Kiricsi, I., *Applied Catalysis A: General*, 186 (**1999**) 375-394.
[15] Sajitha, E.P., Prasad, V., Subramanyam, S.V., Eto, S., Takai, K., Enoki, T., *Carbon*, 42 (**2004**) 2815-2820.
[16] Bystrzejewski, M., Klingeler, R., Gemming, T., Büchner, B., Rümmeli, M.H., *Nanotechnology*, 22 (**2011**) 315606.
[17] Maleki, A., Kamalzare, M., *Catalysis Communications*.
[18] Gascon, J., Corma, A., Kapteijn, F., Llabrés i Xamena, F.X., *ACS Catal.*, 4 (**2013**) 361-378.
[19] deKrafft, K.E., Wang, C., Lin, W., *Adv. Mater.*, 24 (**2012**) 2014-2018.
[20] Liu, B., Shioyama, H., Jiang, H., Zhang, X., Xu, Q., *Carbon*, 48 (**2010**) 456-463.
[21] Amali, A.J., Sun, J.-K., Xu, Q., *Chem. Commun.*, 50 (**2014**) 1519-1522.
[22] Lee, H.J., Cho, W., Lim, E., Oh, M., *Chem. Commun.*, 50 (**2014**) 5476-5479.
[23] Masoomi, M.Y., Morsali, A., *Coord. Chem. Rev.*, 256 (**2012**) 2921-2943.
[24] Wu, A., Liu, D., Tong, L., Yu, L., Yang, H., *CrystEngComm*, 13 (**2011**) 876-882.
[25] Liu, B., Shioyama, H., Akita, T., Xu, Q., *J. Am. Chem. Soc.*, 130 (**2008**) 5390-5391.
[26] Horcajada, P., Surble, S., Serre, C., Hong, D.-Y., Seo, Y.-K., Chang, J.-S., Greneche, J.-M., Margiolaki, I., Ferey, G., *Chem. Commun.*, (**2007**) 2820-2822.
[27] Huo, C.-F., Wu, B.-S., Gao, P., Yang, Y., Li, Y.-W., Jiao, H., *Ang. Chem. Int. Ed.*, 50 (**2011**) 7403-7406.
[28] Torres Galvis, H.M., de Jong, K.P., *ACS Catal.*, 3 (**2013**) 2130-2149.
[29] Raje, A.P., O'Brien, R.J., Davis, B.H., *Journal of Catalysis*, 180 (**1998**) 36-43.
[30] Klencsár, Z., *Nucl. Instrum. Methods Phys. Res., Sect. B*, 129 (**1997**) 527-533.
[31] Guilera, G., Rey, F., Hernández-Fenollosa, J., Cortés-Vergaz, J.J., *Journal of Physics: Conference Series*, (**2103**) 012057.
[32] Ravel, B., Newville, M., *Journal of Synchrotron Radiation*, 12 (**2005**) 537-541.
[33] Klementev, K.V., *J. Phys. D: Appl. Phys.*, 34 (**2001**) 2241.
[34] Gurman, S.J., Binsted, N., Ross, I., *Journal of Physics C: Solid State Physics*, 17 (**1984**) 143.
[35] Groen, J.C., Peffer, L.A.A., Pérez-Ramírez, J., *Microporous Mesoporous Mater.*, 60 (**2003**) 1-17.
[36] Gurgul, J., Łątka, K., Hnat, I., Rynkowski, J., Dzwigaj, S., *Microporous Mesoporous Mater.*, 168 (**2013**) 1-6.
[37] Kuivila, C.S., Stair, P.C., Butt, J.B., *J. Catal.*, 118 (**1989**) 299-311.
[38] Sosinsky, B.A., Norem, N., Shelly, J., *Inorg. Chem.*, 21 (**1982**) 348-356.
[39] Yamashita, T., Hayes, P., *Appl. Surf. Sci.*, 254 (**2008**) 2441-2449.
[40] Kuivila, C.S., Butt, J.B., Stair, P.C., *Appl. Surf, Sc.*, 32 (**1988**) 99-121.

[41] Grzybek, T., Papp, H., Baerns, N., *Applied Catalysis*, 29 (**1987**) 335-350.
[42] Albers, P., Deller, K., Despeyroux, B.M., Schäfer, A., Seibold, K., *Journal of Catalysis*, 133 (**1992**) 467-478.
[43] Jette, E.R., Foote, F., *The Journal of Chemical Physics*, 1 (**1933**) 29-36.
[44] Swanson, H.E., Tatge, E., United, S., *Standard X-ray diffraction powder patterns. Vol. I, Data for 54 inorganic substances*, National Bureau of Standards, [Washington, D.C.], **1953**.
[45] Schulte, H.J., Graf, B., Xia, W., Muhler, M., *ChemCatChem*, 4 (**2012**) 350-355.
[46] de Smit, E., Cinquini, F., Beale, A.M., Safonova, O.V., van Beek, W., Sautet, P., Weckhuysen, B.M., *J. Am. Chem. Soc.*, 132 (**2010**) 14928-14941.
[47] Wang, T., Tian, X.-X., Li, Y.-W., Wang, J., Beller, M., Jiao, H., *ACS Catal.*, 4 (**2014**) 1991-2005.
[48] Dry, M.E., Shingles, T., Boshoff, L.J., Oosthuizen, G.J., *J. Catal.*, 15 (**1969**) 190-199.
[49] Torres Galvis, H.M., Bitter, J.H., Khare, C.B., Ruitenbeek, M., Dugulan, A.I., de Jong, K.P., *Science*, 335 (**2012**) 835-838.
[50] Büssemeier, B., Frohning, C.D., Horn, G., Kluy, W., US4564642, in, 1986.
[51] de Klerk, A., Maitlis, P.M., *What Can We Do with Fischer–Tropsch Products?*, in: Greener Fischer-Tropsch Processes for Fuels and Feedstocks, Wiley-VCH Verlag GmbH & Co. KGaA, **2013**, pp. 81-105.

517547-L-sub01-bw-Wezendonk
Processed on: 20-2-2018

Annex

2

Metal Organic Framework (MOF) mediated synthesis of Highly Active and Stable Fischer-Tropsch Synthesis Catalysts

A2.1 Results

A2.1.1 Pyrolyzed Fe@C catalysts

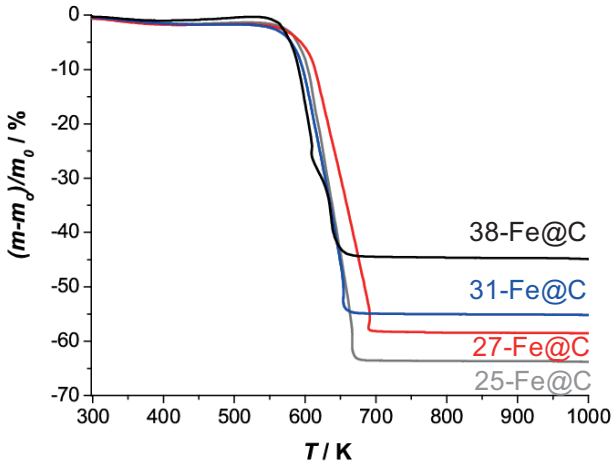

Figure A2.1 TGA profile of Fe@C catalysts under air while ramping up with 10 ˚C min^{-1}.

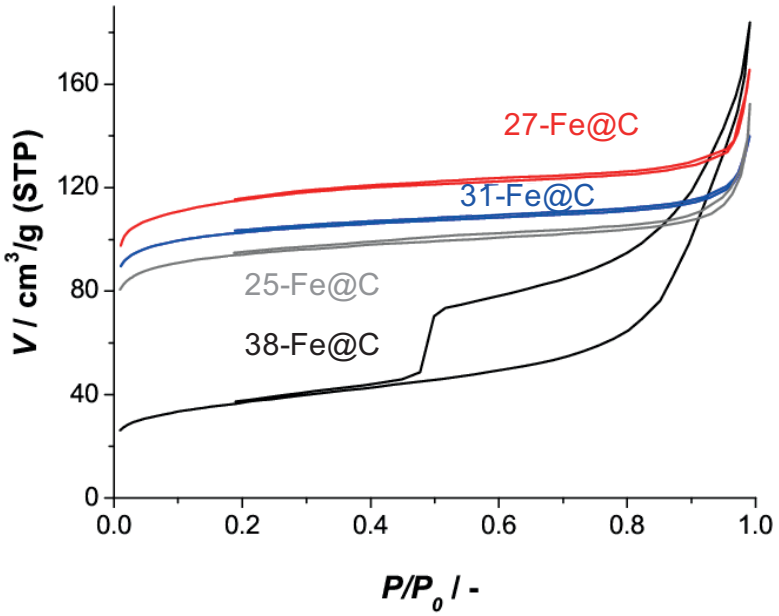

Figure A2.2 Nitrogen adsorption-desorption isotherms at 77 K displaying the effect of FA addition on the textural properties of Fe@C.

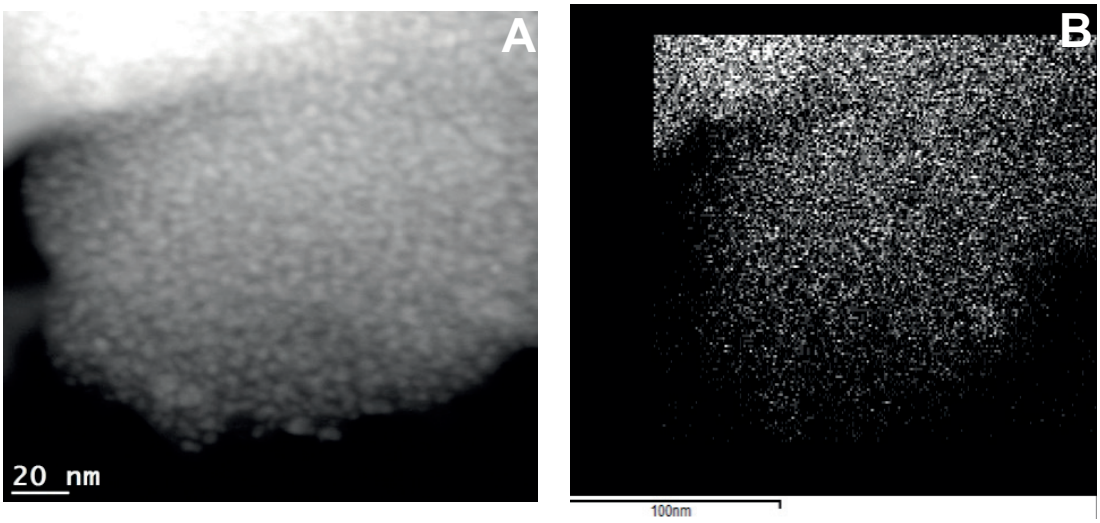

Figure A2.3 TEM analysis displaying **A** HAADF-STEM micrograph of 38-Fe@C and **B** Fe EDX mapping.

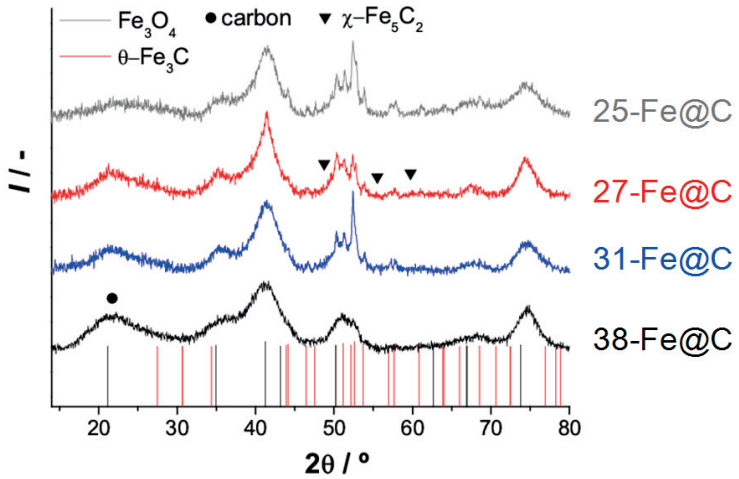

Figure A2.4 Powder X-ray diffraction patterns of Fe@C catalysts prepared with different amounts of carbon precursor FA impregnation prior to pyrolysis at 500 ˚C.

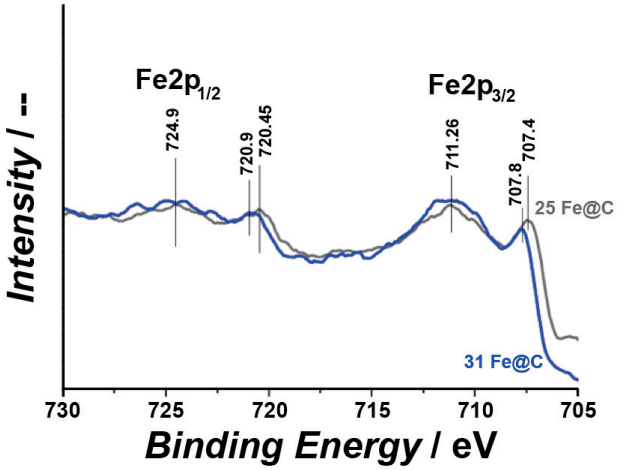

Figure A2.5 Fe2*p* core level spectra of 31-Fe@C and 25-Fe@C.

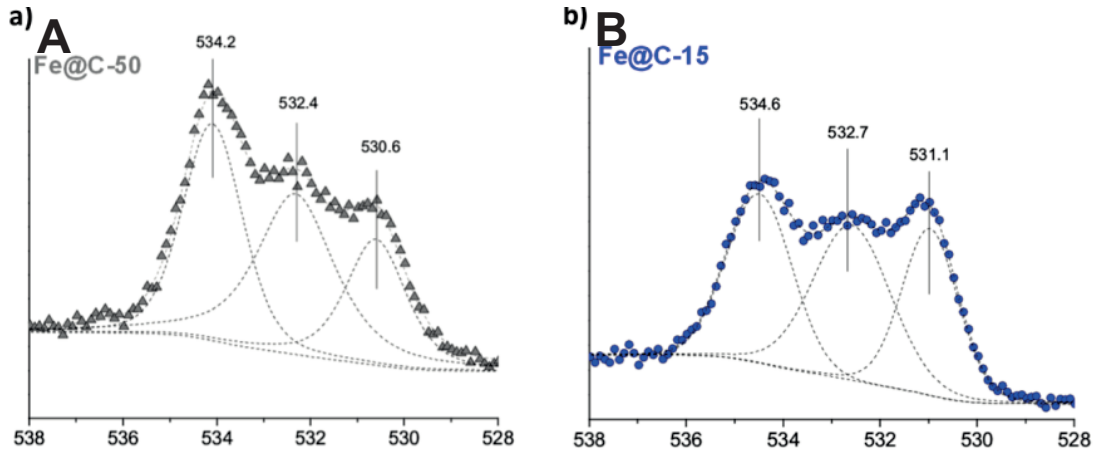

Figure A2.6 O*1s* core level XPS spectra of **A** 25-Fe@C and **B** 31-Fe@C.

A2.1.2 *in situ* spectroscopy of Fe-BTC Pyrolysis and Fe@C FTS

Table A2.1 Calculated EXAFS refinement parameters. The k and R space data are displayed in **Figure A2.7**. The amplitude reduction factor, S_0^2 = 0.75, was calculated from Fe foil standard was the same in all cases. (*): fixed parameters.

Sample	*Shell number*	*Coordination number*	*Scatterer*	*Bond distance* (Å)	*Disorder parameter* $2\sigma^2$ / Å^2	*Energy shift (eV)*	*R-factor*
Basolite	1	6 *	O	2.00±0.00	0.014±0.001	-0.3±0.3	20
F-300	2	4 *	C	2.96±0.02	0.019±0.004		
298 K	3	2 *	Fe	3.33±0.01	0.016±0.001		
Fe@C	1	2.2±0.2	C	2.12±0.01	0.026±0.002	-7.3±0.2	40
He,	2	2.3±0.2	O	2.25±0.01	0.026±0.002		
450 ˚C	3	0.5±0.1	Fe	2.50±0.01	0.033±0.001		
	4	4.0±0.3	Fe	3.06±0.01	0.033±0.001		
	5	5.6±0.3	Fe	3.22±0.01	0.033±0.001		
	6	2.4±0.2	Fe	3.41±0.01	0.034±0.002		
Fe@C	1	2.0±0.4	C	2.16±0.03	0.026±0.004	-8.0±0.4	62
10 vol%	2	2.1±0.3	O	2.29±0.02	0.026±0.004		
H_2 in He,	3	1.2±0.2	Fe	2.53±0.01	0.033±0.001		
400 ˚C, 3	4	3.0±0.3	Fe	3.05±0.01	0.033±0.001		
h, 1 bar	5	4.7±0.7	Fe	3.19±0.01	0.033±0.001		
	6	1.7±0.7	Fe	3.36±0.04	0.034±0.2		
Fe@C	1	2.7±0.6	C	2.10±0.03	0.022±0.002	-6.1±0.3	38
H_2/CO=1	2	2.5±0.4	O	2.19±0.02	0.023±0.002		
340 ˚C, 5	3	0.8±0.1	Fe	2.54±0.01	0.033±0.001		
h, 1 bar	4	8.8±0.3	Fe	3.09±0.00	0.033±0.001		
	5	6.7±0.6	Fe	3.28±0.01	0.033±0.001		
	6	2.9±0.6	Fe	3.51±0.02	0.034±0.002		

For the calculation of *R-factors* the EXCURVE software uses the following equation

$$R = \sum_{i}^{N} \left[\frac{1}{\sigma_i} \left(\left| \chi_i^{\exp}(k) - \chi_i^{th}(k) \right| \right] \times 100\%$$

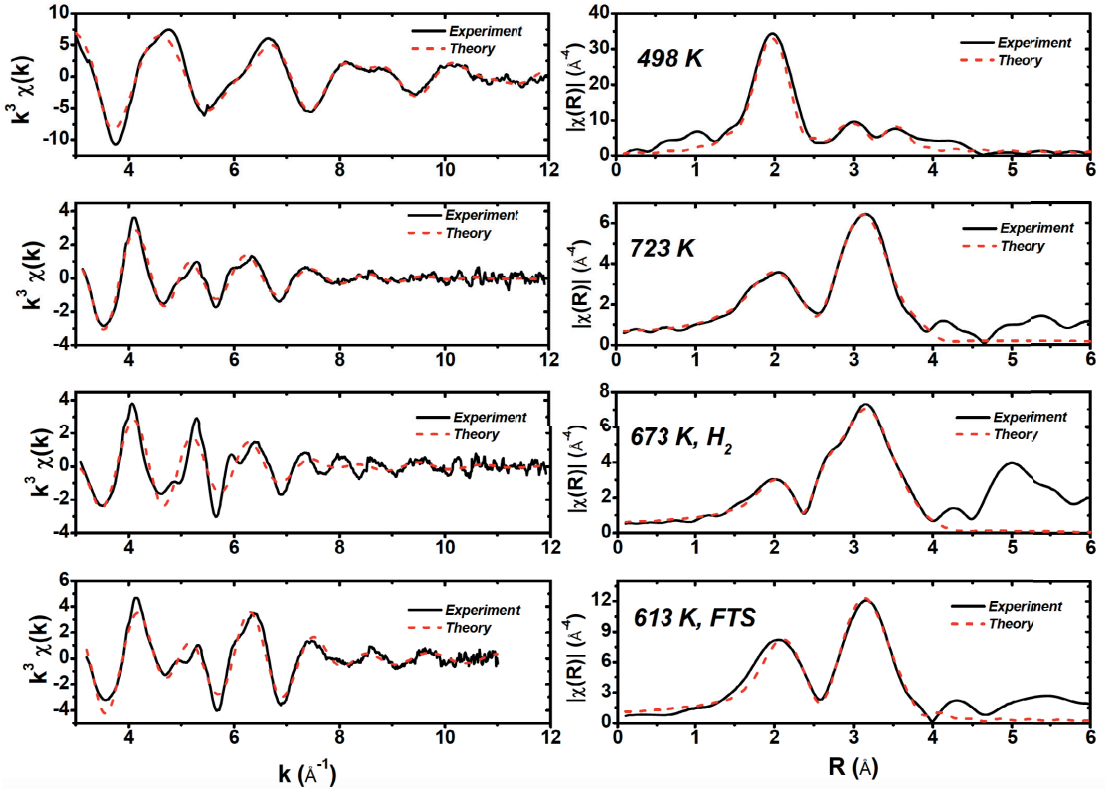

Figure A2.7 Experimental (*black, solid*) and simulated (*red, dashed*) EXAFS spectra in *k* (*left*) and *R* (*right*) space, from top to bottom: Basolite F-300 Fe-BTC at 225 ˚C; 38-Fe@C at 450 ˚C; 38-Fe@C atmospherically reduced at 400 ˚C by 10 vol% H_2/He; 38-Fe@C after 5 h HTFT conditions of 340 ˚C, CO/H_2=1, and 2 bar.

2.1.3 Catalytic tests of Fe@C and K-Fe@C

Table A2.2 CO conversion and carbon selectivity to products over Fe@C after 100 h *TOS* at 340 ˚C, 20 bar, H_2/CO =1 and *GHSV* of 30,000 h^{-1}.

Catalyst	X_{CO} / %	*S* / %					
		C_1	$C_{2=}$-$C_{5=}$	C_2-C_5	CO_2	$C_{2=}/C_2$	$C_{3=}/C_3$
25-Fe@C	72	14.6	15.9	12.7	44.8	0.24	2.3
27-Fe@C	73	14.4	15.3	12.6	45.6	0.24	2.3
31-Fe@C	75	15.0	15.8	12.0	46.4	0.24	2.6
38-Fe@C	76	15.5	14.6	14.4	46.0	0.18	1.8

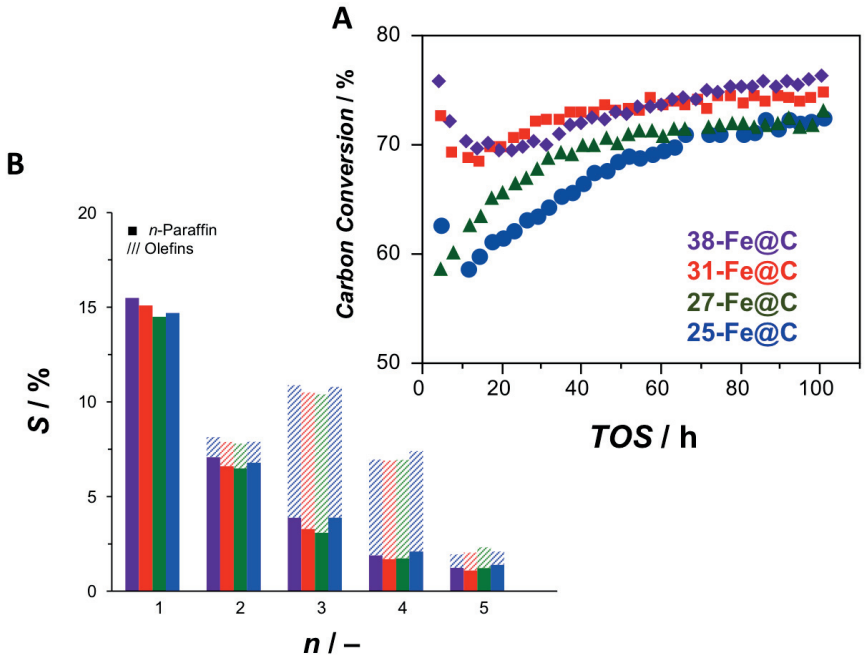

Figure A2.8 A Time evolution of conversion during HTFT with 340 ˚C, 20 bar, H_2/CO = 1, and *GHSV* of 30,000 h^{-1} and **B** carbon selectivity of FTS products after 100 h *TOS*.

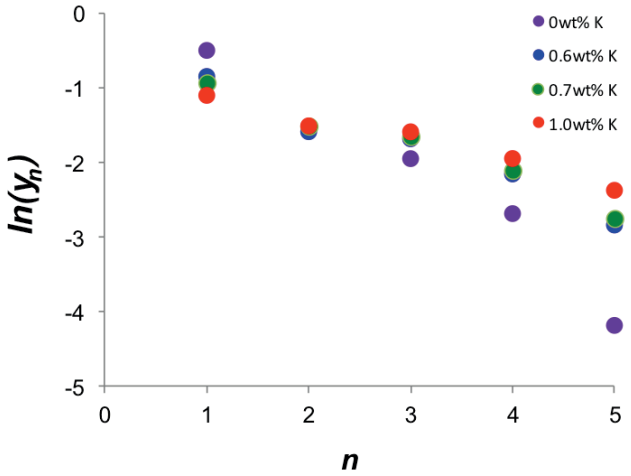

Catalyst	α / -
0.0K-38-Fe@C	0.40
0.6K-38-Fe@C	0.60
0.7K-38-Fe@C	0.65
1.0K-38-Fe@C	0.70

Figure A2.9 ASF distribution plot (logarithm of the molar fraction y_n of the C_n component in the product versus carbon number *n*) for unpromoted and promoted 38-Fe@C after 100 h *TOS* at 340 ˚C, 20 bar, H_2/CO= 1 and *GHSV* of 30,000 h^{-1} in order to derive chain growth probability alpha *α* (*vide infra*).

The chain growth probability *α* is defined as the ratio of the rate of chain growth propagation and the rate of chain termination according to the equation below, and ranges between 0 and 1.

$$a = \frac{r_{\text{propagation}}}{r_{\text{propagation}} + r_{\text{termination}}}$$

$$x\mathrm{CO} + 2x\mathrm{H_2} \rightarrow x(-\mathrm{CH_2}-) + x\mathrm{H_2O} \quad (1)$$

$$y\mathrm{H_2O} + y\mathrm{CO} \rightarrow y\mathrm{CO_2} + y\mathrm{H_2} \quad (2)$$

$$(x+y)\mathrm{CO} + (2x-y)\mathrm{H_2} \rightarrow x(-\mathrm{CH_2}-) + (x-y)\mathrm{H_2O} + y\mathrm{CO_2} \quad (3)$$

Scheme A2.1 FTS reaction (1) concurrent with full WGS activity (2) results in maximum 50% CO_2 selectivity (3)

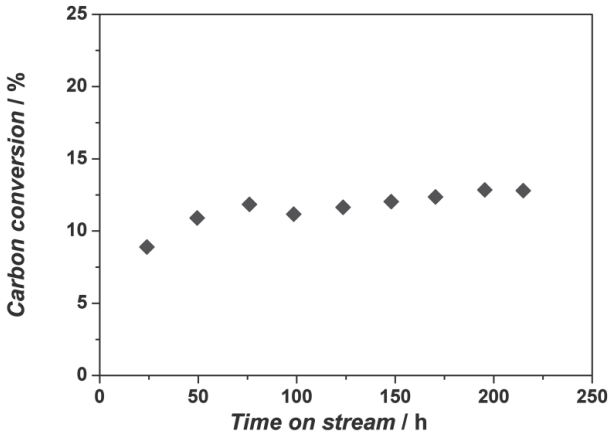

Figure A2.10 Time evolution of CO conversion during HTFT under 340 ˚C, 20 bar, H_2/CO = 1, and *GHSV* of 190,000 h¯1 for the unpromoted 38-Fe@C catalyst under differential conditions for over 220 h.

Table A2.3 Productivities of promoted 0.6K-38Fe@C and commercial Fe catalysts.

Catalyst	*FTY*[a] / mol_{CO} g_{Fe}^{-1} s^{-1}	Catalyst Productivity / L $kg^{-1}s^{-1}$	References
0.6K-38-Fe@C	$4.38x10^{-4}$	6.9[b]	This work
Ruhrchemie	$4.90x10^{-6}$	0.1[b]	[1]
Fused HTFT (Slurry reactor)[d]	-	0.7[c]	[2]
Fused HTFT (Fluidized reactor)[d]	-	0.2[c]	[2]

[a] Iron time yield *FTY*, mol of CO converted to hydrocarbons excluding CO_2 per second per gram of iron

[b] Volume of CO converted per time (L s^{-1}) per mass of catalyst (kg^{-1})

[c] Volume of syngas converted per time (L s^{-1}) per mass of catalyst (kg^{-1})

[d] Temperature range of 320-330 °C

References

[1] Büssemeier, B., Frohning, C.D., Horn, G., Kluy, W., US4564642, in, 1986.
[2] de Klerk, A., Maitlis, P.M., *What Can We Do with Fischer–Tropsch Products?*, in: Greener Fischer-Tropsch Processes for Fuels and Feedstocks, Wiley-VCH Verlag GmbH & Co. KGaA, **2013**, pp. 81-105.

Chapter

3

Elucidating the Nature of Fe species during Pyrolysis of the Fe-BTC MOF into Highly Active and Stable Fischer-Tropsch Catalysts

In this Chapter, a combined *in situ* XAS, DRIFTS and Mössbauer study was performed to elucidate the changes in structural, electronic and local environment of Fe and C during pyrolysis of the metal organic framework Fe-BTC towards highly active and stable Fischer-Tropsch synthesis (FTS) catalysts (Fe@C). Fe-BTC framework decomposition is characterized by decarboxylation of its trimesic acid linker, generating a pyrolytic carbon matrix around Fe nanoparticles. Pyrolysis of Fe-BTC at 400 ˚C (Fe@C-400) favors the formation of highly dispersed hexagonal carbides (ε'-$Fe_{2.2}C$, d_p = 2.5 nm) while at temperatures of 600 ˚C (Fe@C-600) mainly Hägg carbides are formed (χ-Fe_5C_2, d_p = 6.0 nm). Extensive carburization and sintering occur above these temperatures, as at 900 ˚C the predominant phase is cementite (θ-Fe_3C, d_p = 28.4 nm). Thus, the loading, average particle size and degree of carburization of Fe@C catalysts can be tuned by varying the pyrolysis temperature. Performance testing under high-temperature Fischer-Tropsch (HTFT) conditions showed no significant changes in the initial turnover frequency (*TOF*) for pyrolysis temperatures up to 600 ˚C. However, methane formation is minimized when higher pyrolysis temperatures are applied. The material pyrolyzed at 900 ˚C showed longer induction periods and did not reach steady state conversion under the conditions studied. None of the catalysts showed deactivation during 80 h time on stream, maintaining high Fe time yield (*FTY*) in the range of 0.19–0.38 $mmol_{CO}\ g_{Fe}^{-1}\ s^{-1}$, confirming the outstanding activity and stability of this family of Fe@C FTS catalysts.

This chapter is based on the following publication:

T.A. Wezendonk, V.P. Santos, M.A. Nasalevich, Q.S.E. Warringa, A.I. Dugulan, A. Chojecki, A. Koeken, M. Ruitenbeek, G. Meima, H. Islam, G. Sankar, M. Makkee, F. Kapteijn and J. Gascon ***ACS Catal.,*** 2016, 6, 3236−3247

3.1 Introduction

As the conventional oil reserves are currently a matter of concern, alternative feedstock is sought to provide solutions to a growing energy market [1-3]. Natural gas and coal are widely available and their efficient conversion to transport fuels and chemicals is a key challenge in current research [4]. The Fischer-Tropsch synthesis (FTS) is a prime example of a catalytic process that has been thoroughly investigated, is widely applied in industry, and after all is still subject of major innovative research [5-9]. Whereas Fe is predominantly used in high temperature Fischer-Tropsch (HTFT) processes, the more expensive Co catalyst is applied in the majority of low temperature Fischer-Tropsch (LTFT) processes to produce e.g. diesel fuels via hydrocracking of FTS waxes [10, 11]. Co catalysts are inherently more active at lower temperatures and their stability is retained for longer time on stream [12, 13]. Fe catalysts, on the other hand, are much more stable in operation with regard to changing operating conditions and poisoning, e.g. conversion and methane selectivity can vary largely over Co catalysts with changes in operating conditions [12, 14]. The ideal FTS catalyst would consist of the activity and stability of Co and the robustness of Fe towards changing operating conditions [15]. Hence, the search for the ultimate FTS catalyst continues. Recently, focus in metal-organic framework (MOF) research has shifted towards application of MOFs and the optimization of their active sites for heterogeneous catalysis [16]. Taking up this view a bit further, MOFs have also been identified as very efficient precursors for producing metal oxide nanoparticle systems for catalysis by means of heat treatment [17-27]. Pyrolysis of an Fe-doped ZIF-8 MOF resulted in highly dispersed α-Fe_2O_3 particles located both in the graphitized MOF structure and on its surface [18]. In addition, high temperature pyrolysis of Zn based MOFs had previously displayed to produce very porous carbons [28-33]. The MOF template approach can also result in metal oxide nanocomposites when calcination is carried out [34]. In contrast to pyrolysis, the carbon content of the MOF is completely eliminated by calcination. However, the pyrolysis of MOFs produces metal nanoparticles in a carbon matrix suitable for application as heterogeneous catalyst.

The use of the MOF mediated synthesis (MOFMS) for the production of metal nanoparticles embedded in a carbon matrix is versatile. First, there is a vast amount of possible MOF structures, and therefore the active site metal can be optimized in many different ways. Nanoparticle-carbon composites are often denoted as M@C, with M being the metal or metal oxide nanoparticle. The synthesis of Co@C, Sn@C and Fe@C or Fe_2O_3@C have been readily described in literature, and applications are found in battery and magnetic materials, as well in aqueous solution separation and oxygen reduction catalysts for fuel cells [20-25]. Second, the pyrolysis conditions can be very well controlled. For example, by varying the range of temperatures, a carbon matrix with various porosity and metal nanoparticles with different particle size distributions can be produced [23-25]. The metal content of these compounds can vary greatly, and values reported of around 50 wt% up to 84 wt% for the as synthesized samples are not uncommon. Interestingly, high metal loadings accompanied

by high dispersion can be obtained. Though, particle agglomeration is enhanced at higher temperatures, possibly by sintering and coalescence phenomena. Because of the carbon nature of the matrix, graphitization will take place at higher temperatures.

The optimal combination of the maximum loading with the highest dispersion, anchored firmly in a stable matrix, is key in heterogeneous catalysis. Recently, the potential of the MOFMS method to produce Fe@C catalysts with unprecedented activity in HTFT was reported by our group [35]. By understanding the formation of these materials using the MOFMS, possibly a wide range of materials can be engineered to produce more active and stable catalysts for use in many applications. In this paper, the physiochemical properties of the Fe-based MOF during pyrolysis are elucidated in both *in situ* and *ex situ* experiments. Framework decomposition and Fe phase evolution are followed in experiments where the pyrolysis temperature is varied, and the obtained catalysts are characterized with regard to Fe nanoparticle size, accessibility and nature of the active site. The catalytic performance is determined in the HTFT regime, and the obtained structure-activity relations give insight in why the created catalysts display such high activity and stability.

3.2 Experimental

3.2.1 Catalyst Synthesis

Fe nanoparticles embedded in a porous carbon matrix (Fe@C) were produced by the pyrolysis of Fe-BTC, an iron-1,3,5-benzenetricarboxylate with chemical formula $C_9H_3FeO_6$ [35]. Fe-BTC was purchased from Sigma-Aldrich under the trade name Basolite™ F-300 and was used without further purification. Pyrolysis of Fe-BTC was carried out in a quartz tubular reactor (approx. *L* = 1.0 m x *ID* = 5.0 cm) located horizontally in a ceramic fiber oven (Carbolite, Sheffield) where around 1.0 g of the MOF was placed in a ceramic crucible and subjected to heat treatment in a nitrogen atmosphere (150 cm^3_{STP} min^{-1}, space velocity 4.5 h^{-1}). The pyrolysis temperature was varied at 400, 500, 600 and 900 ˚C, the ramp rate and dwell time were fixed at 2 ˚C min^{-1} and 8 h, respectively. Before exposure to ambient conditions each material was passivated at room temperature using a stream of 5 vol% O_2 in N_2 for 2 h. The synthesized catalysts are denoted herein as “Fe@C-T”, with T representing the pyrolysis temperature in ˚C.

3.2.2 Characterization

3.2.2.1 Thermogravimetric analysis (TGA)

TGA was performed on a Mettler Toledo TGA/SDTA1 with sample robot (TSO 801RO) and gas control (TSO 800GC1). The temperature was linearly increased from 25 to 1000 ˚C at a heating rate of 5 ˚C min^{-1} under air or He flow. Dwell times of 15 min were set at intermittent temperature stages

to monitor pyrolysis of Fe-BTC. TGA in air was carried out to calculate Fe loading on the carbon-matrix catalysts assuming the Fe_2O_3 phase residual mass.

3.2.2.2 In situ *diffuse reflectance infrared Fourier transformed spectroscopy (DRIFTS) mass spectrometry (MS)*

DRIFTS was carried out in a Nicolet 8700 machine equipped with a high temperature and pressure cell using a liquid nitrogen cooled MCT/A detector. Around 100 mg of Fe-BTC powder was placed in the DRIFT cell confined in a three-window chamber. Pyrolysis was performed under He atmosphere from RT to 550 ˚C using a heating rate of 5 ˚C min^{-1}. The He flow rate of 20 cm^3_{STP} min^{-1} was directed through the catalyst bed. Spectra were recorded from 4000 to 1000 cm^{-1} wavenumbers with 128 scans and a resolution of 4 cm^{-1}. The DRIFT spectra reported are obtained at set point temperature when no further change in the spectra was observed. A mass spectrometer was connected to continuously monitor and record the composition of the outlet gas stream.

3.2.2.3 In situ *X-ray absorption spectroscopy (XAS)*

X-Ray absorption spectroscopy was performed at BL22, 'Core level absorption and emission spectroscopies', beam line of ALBA (Barcelona, Spain). The beam line is equipped with Si(111) and Si(311) monochromators and operates in the range of energies between 2.6 and 36 keV. In this particular experiment the Si(111) monochromator and Rh-coated toroid mirror were employed. The materials were studied using Fe *K*-edge (ca. 7111 eV). Fe-BTC was diluted with boron nitride to achieve a desired edge jump value of around unity. The solid mixture was pelletized by applying 2 tonnes/cm^2 pressure for 5 min. Subsequently, the sample was placed in an *in situ* cell. The cell was used in transmittance mode. The sample environment is continuously purged with a flow of He of 20 cm^3_{STP} min^{-1} and heating was applied. XAS spectra were collected continuously up to 450 ˚C, until no further changes were observed. For the reduction step, the cell containing the pyrolyzed sample was cooled down to 400 ˚C and exposed to a flow of 10 vol% H_2/He for 3 h at 20 cm^3_{STP} min^{-1} at a cell pressure of 1 bar. Fischer-Tropsch experiments were subsequently carried out at 340 ˚C with an equimolar flow of CO and H_2 of 20 cm^3_{STP} min^{-1} at 2 bar. XAS data analysis is described in detail in **A3.1**.

3.2.2.4 In situ *Mössbauer absorption spectroscopy (MAS)*

Transmission ^{57}Fe Mössbauer spectra were collected at 300 and 4 K with a sinusoidal velocity spectrometer using a ^{57}Co(Rh) source. Velocity calibration was carried out using an α-Fe foil. The source and the absorbing samples were kept at the same temperature during the measurements. The experiments were performed in a high-pressure Mössbauer *in situ* cell developed at Reactor Institute Delft. The reduction was carried out at 400 ˚C in H_2 for 3 h prior to starting FTS. The carbide

species were evaluated after performing 5 h of FTS reaction at 340 ˚C and 15 bar with an equimolar CO/H_2 mixture. The spectra were measured at liquid He temperature, after cooling the sample after each treatment in the reaction mixture. Detailed information on the Mössbauer experiments can be found in **A3.1**.

3.2.2.5 N_2-physisorption

Textural properties were determined by performing N_2-physisorption on a Micromeritics Tristar II at 77 K. All samples were evacuated at 175 ˚C for 16 h prior to measurement. Data analysis was performed with Microactive software V3.00. The BET area was determined by direct fitting of points in the P/P_0 = 0.05-0.15 domain, constraining the upper boundary of the relative pressure window using the two-point BET method [36]. Total pore volume was measured at P/P_0 = 0.95 where no inter-particle condensation occurred, the external surface area and microporous volume were determined by the *t*-method, obtaining a linear fit in the De Boer thickness of at least 10 data points.

3.2.2.6 X-ray diffraction (XRD)

Powder XRD was carried out on a Bruker D8 Advance diffractometer operating in Bragg-Brentano geometry using Cu $K\alpha$ radiation with wavelength of 0.15406 nm and a Lynxeye position sensitive detector. Measurements were carried out with coupled θ-2θ scan between 5° - 115°, step size 0.041˚ 2θ, counting time per step of 1 s and sample rotating of 30 rpm. Data evaluation and background subtraction was done in Bruker software Diffrac.EVA V3.2 using the ICDD pdf4 database.

3.2.2.6 High-resolution transmission electron microscopy (HR-TEM)

High-resolution transmission electron micrographs were collected on a JEOL model JEM-2010 working at 200 kV with a LaB_6 filament. It reaches a line resolution of 0.14 nm and a point resolution of 0.25 nm. It is equipped with an Orius 831 camera from Gatan. A suspension in ethanol is made with the sample and ground with a mortar and pestle. The suspension is further dispersed in an ultrasonic bath for 5 min. A drop of that suspension is deposited onto a Au grid covered with lacey carbon and left to dry in air. Values for dispersion (*D*) were obtained using the average particle size from the particle size distribution (PSD) obtained through manual counting. The procedure is described in **A3.1**.

3.2.3 Catalytic performance testing

The catalyst performance tests were conducted in the high-pressure reactor assembly module-I (HPRAM-I[37, 38]) system at the Dow Chemical Company. It consists of 48 reactors that can be operated simultaneously at various process conditions, gas feed systems, exit modules with flow splitters, and gas chromatograph analyzers (Siemens Maxum-II). For activity testing, ~10 mg (20

mm^3) of fresh catalyst with the particle size of 177–420 µm was diluted with 100 mm^3 SiC particles of similar size range. First, samples were activated *in situ* in a 90/10 vol% H_2/He mixture at 425 ˚C for 3 h at 3 bar followed by cooling to 340 ˚C under N_2 flow at the same pressure. After increasing the pressure to the process set point of 20 bar, a 10 cm^3_{STP} min^{-1} flow consisting of CO 45 vol%, H_2 45 vol% and He 10 vol% was introduced. These operating conditions are hereby referred to as high-temperature Fischer-Tropsch (HTFT) conditions. Catalytic activity is expressed as Fe time yield (*FTY*), defined as the number of moles of CO converted to hydrocarbons per gram of Fe per second. The calculation of CO conversion (X_{CO}), product selectivity (S_i), and turnover frequency (*TOF*) are described in **A3.1**.

3.3 Results

3.3.1 *In situ* characterization during pyrolysis and FTS

3.3.1.1 TGA

A TG analysis under He flow of Fe-BTC was carried out to determine the pyrolysis temperature for catalyst synthesis. In **Figure A3.1** the TG and corresponding differential TG curves are plotted for Fe-BTC pyrolysis up to 1000 ˚C. Clearly distinguishable are the three regions where severe weight losses occur. The first steep loss in mass of Fe-BTC is observed just beyond 250 ˚C up to 400 ˚C, the second loss is around 450 ˚C and the third at 550 ˚C. The sum of first two losses accounts for a weight loss of ~50 %, assigned to the decomposition of the linker. In the third region, an additional loss of ~15 wt% is observed. Finally, at temperatures above 700 ˚C, the material shows a gradually increasing additional weight loss of 10 %.

3.3.1.2 DRIFTS-MS

In situ DRIFTS experiments coupled with mass spectrometer (MS) effluent analysis were performed to get insight into the structural changes of Fe-BTC during pyrolysis. At first glance, the IR spectra of the MOF at room temperature (RT) comprise the absorbances of highly hydrated carboxylic acids (**Figure A3.2**). The very broad absorbance of 2500-3600 cm^{-1} in **Figure 3.1A** is ascribed to O-H stretching of adsorbed water molecules in the pores of the MOF and to contributions of O-H stretching of carboxylic acids [39, 40]. A small C-H overtone of aromatic compounds is visible at 1890 cm^{-1} prior to the congested fingerprint region. In **Figure 3.1B**, the asymmetric ν_{as}(C=O) and symmetric carboxylate stretching ν_s(C=O) are found around 1500-1750 cm^{-1} and 1300-1500 cm^{-1}, respectively [41]. In the region 1100-1300 cm^{-1}, minor ν(C-O) vibrations are found that are attributed to free trimesic acid (TMA) [42]. While carboxylate vibrations ν(C=O) overlap with the phenyl ring stretching in the range 1400-1600 cm^{-1}, the characteristic substituted aromatic ν(C=C) of TMA can be

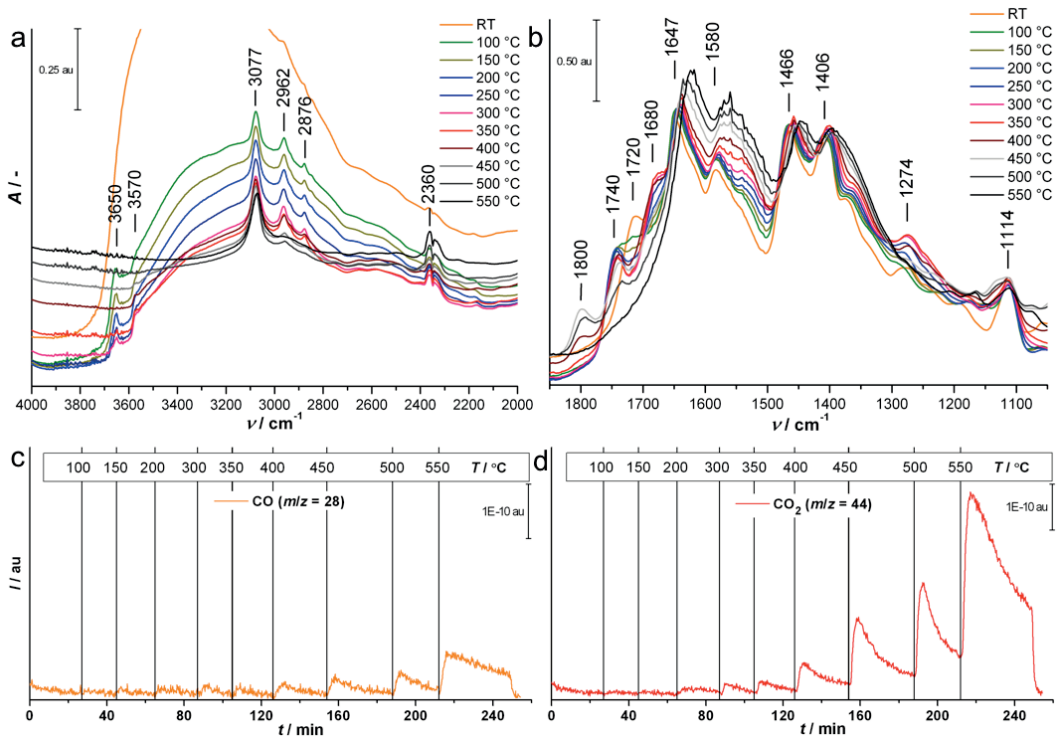

Figure 3.1 *In situ* DRIFTS and MS results of Fe-BTC pyrolysis in He with DRIFT spectra obtained at set point temperatures showing **A** the region 2000-4000 cm^{-1}, **B** the region 1050-1850 cm^{-1} and continuously recorded MS of effluent gases **C** CO and **D** CO_2 of the same experiment, indicated when set-point temperature was changed.

found at 1114 cm^{-1}. Increasing the temperature to 150 ˚C leads to extensive removal of water from the structure, both seen in IR and in the MS spectra of **Figure A3.3**. This dehydration of the pores reveals the sharp O-H stretching of the hydration and hydroxylation of the coordinatively unsaturated Fe sites (CUS) at 3650 and 3570 cm^{-1}, as well as sp^2 and sp^3 C-H stretching at 3077 cm^{-1} and just below 3000 cm^{-1}, respectively. The aromatic C-H stretch belongs to the framework, whereas the absorbance from aliphatic contributions is, per definition, not part of Fe-BTC [41]. Taking a closer look at synthesis methods, these peaks are very characteristic of ν(C-H) vibrations of DMF. In the carboxylate-stretching region there is a notable blue shift in ν(C=O) at 1720 to 1740 cm^{-1}. Increased heating to 200 ˚C reveals the evolution of a new peak at 1680 cm^{-1} and growing ν(C-O) vibrations between 1100-1300 cm^{-1}, both a result of increased appearance of free acid. The magnitude of absorbance grows steadily until reaching a temperature of 350 ˚C, implying significant mobility of uncoordinated linker in the framework. At 350 ˚C, the ν(O-H) vibration at 3650 cm^{-1} of water bound to the CUS virtually disappears, followed by the one at 3570 cm^{-1} upon reaching 400 ˚C. Together with

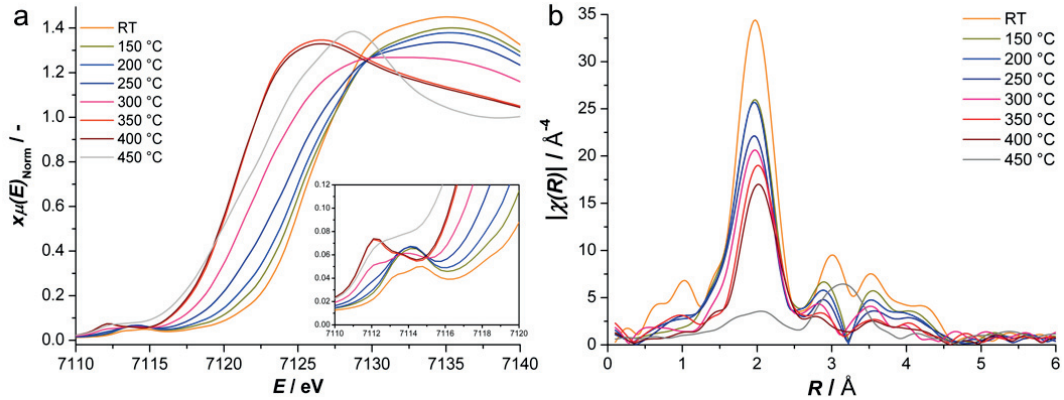

Figure 3.2 *In situ* XAS spectra of Fe-BTC pyrolysis in He showing in **A** the XANES with pre-edge insert and in **B** the magnitude of the Fourier transformed EXAFS signal of the same experiment.

the disappearance of ν(O-H) vibrations, the free acid ν(C=O) and ν(C-O) vibrations start to decay, a first evidence of structural breakdown. Furthermore, a new band arises at 1800 cm^{-1}, attributed to ν(C=O) vibration of acid anhydride, possibly resulting from interconversion of two carboxylic acids by a dehydration mechanism [43]. At this temperature, the release of carbonaceous products such as carbon monoxide and carbon dioxide is measured in the MS (**Figure 3.1C and Figure 3.1D**). Thus, framework decomposition through major decarboxylation starts at 400 ˚C. Up to 500 ˚C there are signals present of free acid and the anhydride, indicating a gradual carbonization of the framework with temperature. At 550 ˚C, the O-H stretching and C-H sp^3 vibrations are absent, as are the free acid and anhydride bands; the resulting aromatic carbon comprises a severely lessened oxygen-functionalized surface. Moreover, the decarboxylation has led to pronounced bands of carbon dioxide in the gas phase and adsorbed on the surface of the carbon.

3.3.1.3 in situ XAS

The MOF decomposition and Fe phase evolution were further characterized by *in situ* XAS. At RT, the Fe-BTC XANES spectrum (**Figure 3.2A**) is characterized by a pre-edge peak around 7113.5 eV that corresponds to a dipole-forbidden *1s-3d* transition and a main edge peak (*1s-4p* transition) at 7124.8 eV, both characteristics of Fe(III) electronic state [44]. The position of the edge peak is slightly shifted to higher energies relative to α-Fe_2O_3, as a result of the different local coordination environment of Fe(III) in the trimeric clusters [44]. The pre-edge feature of Fe-BTC is characterized by a doublet with centroids at 7113.3 and 7114.5 eV (energy splitting equal to 1.2 eV), with the first transition being slightly less intense than the second transition. The energy splitting separation is characterized by the type of coordination and is around 1.5 eV for octahedral sites and around 0.67 eV for tetrahedral sites. Based on this information, the local symmetry of Fe in the MOF is close to

distorted octahedral, in agreement with previous studies [44]. Upon heating to 200 ˚C, although there is no significant change in the edge peak position, the pre-edge peak features changed significantly. In particular, the pre-edge absorption area increases ~1.4 times and the doublet peak disappears. Both features can be assigned to dehydration causing a reduction in *d*-orbital occupancy, coordination number and symmetry degree. Overall, these data suggest the prevalence of Fe(III) in the temperature range up to 200 ˚C and modifications in the local coordination of Fe caused by the removal of solvent. Further increase in temperature from 250 to 400 ˚C causes a shift of the pre-edge and edge peak to lower energies thus demonstrating the partial reduction of Fe(III) to Fe(II) (**Figure A3.4**). In addition, the area, energy splitting separation and ratio of the pre-edge peaks changed significantly. The pre-edge spectrum recorded within 250-400 ˚C is characterized by a doublet in which the energy splitting and centroid position decreases upon an increase in temperature, in agreement with a decrease in symmetry. Furthermore, the ratio between the first and second peaks increases upon heating. Increasing the temperature to 450 ˚C does not further decrease the edge energy, but increases the intensity of the white line and decreases the sharpness of the pre-edge feature. This is consistent with a change in the nature of the Fe(II) species. The lack of sharpness in the pre-edge feature is in agreement with a lower tetrahedral symmetry of Wüstite. Comparison of the XANES spectrum of Fe@C with reference FeO (**Figure A3.5**) shows that the white line intensity is higher for the catalyst, which may indicate the presence of carbidic structures [45]. After the exposure of the pyrolyzed compound to diluted H_2 for 3 h (**Figure A3.6A**), the degree of reduction seems very low. The rising edge maintains its steep shape and the magnitude of the pre-edge features does not increase significantly with respect to α-Fe foil. In subsequent Fischer-Tropsch experiments, the white line intensity remains high, whereas the decrease in pre-edge features is minor. This XANES spectrum looks much similar to that of χ-Fe_5C_2, and given the resemblance with the pyrolyzed material at 450 ˚C, confirms the contribution of carbidic species in the produced catalyst as well [46].

The experimental observations from XANES are supported by *in situ* EXAFS. Simulating the spectrum of Fe-BTC yielded the parameters listed in **Table A3.2** that closely matches the ones deduced from X-ray data refinements for MIL-100(Fe) [47, 48]. According to this model, the scattering atoms are composed of i) six oxygen atoms in the first shell directly bonded to Fe with Fe-O distance of 2.0 Å; ii) four carbon atoms of the carboxyl groups in the second shell with Fe-C distance of 2.96 Å; iii) two iron atoms of the nearest octahedral (Fe-Fe) in the third shell at a distance of 3.328 Å [47, 48]. During pyrolysis up to 250 ˚C, there is a gradual decrease in the coordination number of carbon in the second coordination shell from 4 to 2.6, without changes in Fe-O and Fe-Fe distances (**Figure 3.2B**). The Fe-C distance of the second shell increases slightly, together with the local disorder around Fe, effects that can be linked to temperature effects and water and free acid removal. Further increase in temperature from 250 to 400 ˚C causes a large drop in the coordination

number of iron from 2.0 to 0.9, further decreasing carbon from 2.6 to 1.7 and oxygen from 6.0 to 4.5. These values indicate that the framework is degrading by removal of carbon monoxide or dioxide, effectively losing its third shell Fe neighbors from the trimers. At temperatures above 400 ˚C there is a significant change in the EXAFS spectrum, suggesting a complete collapse of the MOF network. Simulation of the EXAFS signals of the pyrolyzed material results in i) new features emerging related to first shell carbidic Fe-C at the distance of 2.12 Å; ii) second shell Fe-O distances close to the ones found in Wüstite and iii) third shell Fe-Fe at longer distances of 2.5 Å. Additionally, there is a very large increase in fourth, fifth and sixth shell Fe-Fe at distances larger than 3.0 Å with higher coordination numbers between 2.4 and 5.6. Based on these fitting parameters, it is concluded that the pyrolyzed material consists of a mixture of Wüstite and iron carbide nanoparticles. When this *in situ* prepared catalyst is subjected to reduction for 3 h at 400 ˚C in diluted H_2, a small shoulder appears in the fine structure around 2.5 Å corresponding to metallic Fe (**Figure A4.6A**). The coordination number of Fe in the third shell increases as well, however the degree of reduction looks low. The EXAFS spectrum of the sample after 5 h FTS shows many differences from the reduced sample. First, a significant increase in the carbon coordination number in the first shell is visible. Second, the coordination number for Fe in the higher shells greatly increases. Thus, the EXAFS spectrum of the sample after the FTS experiment clearly displays the formation of Fe carbide phase upon exposure to syngas conditions at elevated temperature and pressure.

3.3.1.3 in situ MAS

In situ Mössbauer absorption spectroscopy is applied during the pyrolysis process to determine the nature and extent of carburization of Fe species. It was shown before that the spectrum of the pristine MOF recorded at RT comprised 100% high-spin Fe(III) in an octahedral environment, in agreement with literature data and XAS analysis [35]. During pyrolysis, these species are converted into reduced (Fe(II), α-Fe) and an intermediate carbidic iron (Fe_xC) (**Figure 3.3A-C and Figure A3.7A-C**), in agreement with *in situ* XAS. The presence of Wüstite is confirmed at liquid He temperature, as the spectrum is unambiguously fitted with Fe^{2+} and Fe^{3+} magnetic contributions assigned to cubic and non-cubic sites [49, 50]. The temperature of pyrolysis controls the distribution of these species; at temperatures near framework collapse of 450 ˚C, Wüstite is the main iron component (73%) with lower amounts of Fe_xC (27%). The increase in the pyrolysis temperature to 600 ˚C fully reduces FeO to metallic iron, while the amount of Fe_xC remains constant (**Figure 3.3D-F**). Thus, the Fe@C-400 sample only displayed a slight degree of reduction prior to FTS conditions, in contrast to full reduction of Fe@C-600. Upon the exposure to syngas at high temperature Fischer-Tropsch conditions, much higher concentrations of iron carbides are found on Fe@C regardless of the pyrolysis temperature. However, the type and amount of the iron carbide formed strongly depends on the pyrolysis temperature. Exposure to HTFT conditions for the sample pyrolyzed at

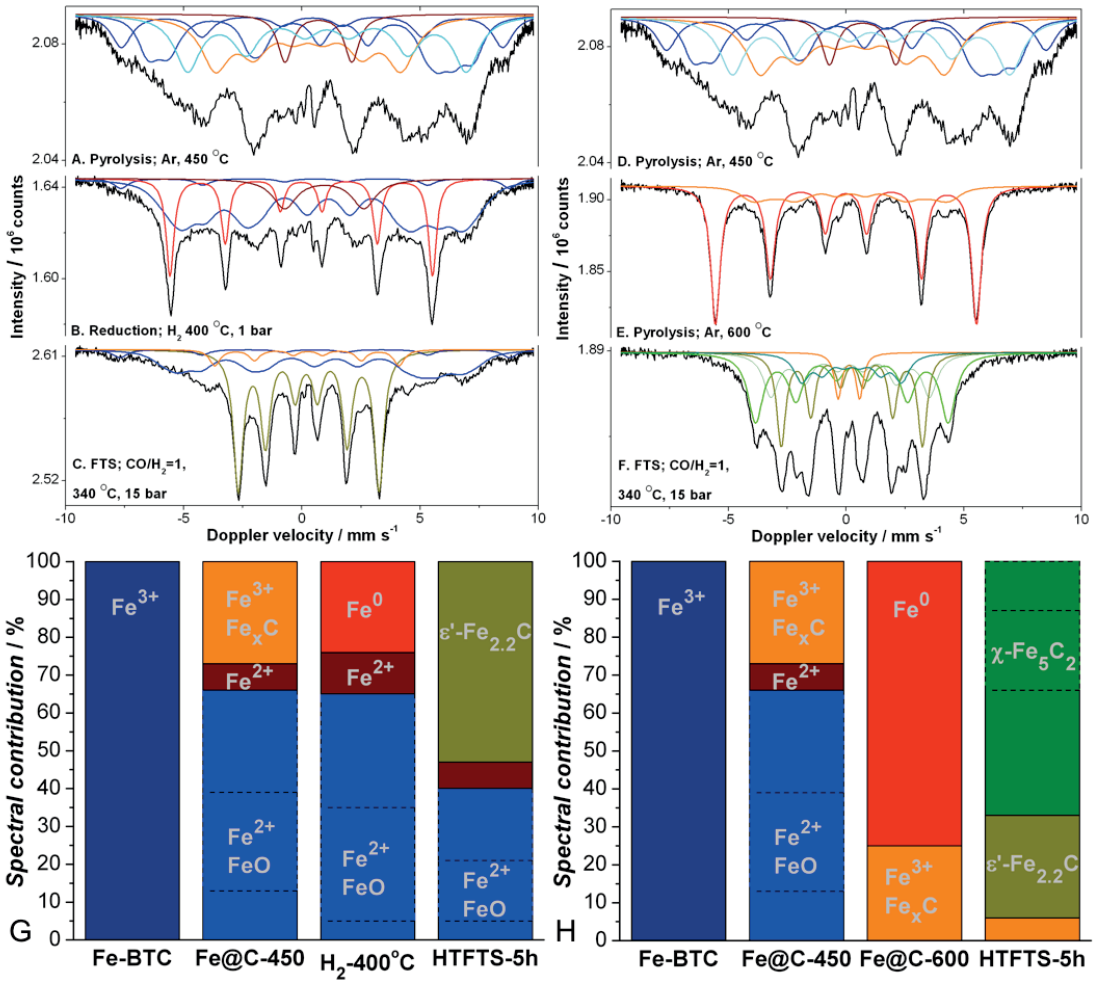

Figure 3.3 *In situ* Mössbauer spectra **A-F** measured at 4.2 K and accompanying fitting results **G-H** of Fe-BTC pyrolyzed in Ar at temperatures up to 450 ˚C **A-C** and 600 ˚C **D-F**. The samples were subsequently exposed to 5 h HTFT conditions of 340 ˚C, 15 bar of CO/H_2=1. See **Table A3.3 and Table A3.4** for values of the spectral fitting.

450 ˚C mainly results in the formation of ε'-$Fe_{2.2}C$ (hexagonal carbide, 53%) with the balance remaining in the Wüstite phase, while HTFT conditions exposure for the sample pyrolyzed at 600 ˚C results in a fully carburized phase that consists mainly of χ-Fe_5C_2 (Hägg carbides, 67%) with the balance hexagonal carbides (**Figure 3.3G-H, Figure A3.7D-F and Table A3.3, Table A3.4**). No metallic iron was found in the samples after exposure to syngas.

3.3.2 Characterization of Fe@C catalysts

3.3.2.1 Iron loading and textural properties

TGA in air of the Fe@C samples displayed a high loading of Fe in the resulting catalysts (**Table 3.1**). In Fe@C-400 the Fe-loading was 34.4 wt%, the value increasing to 53.4 wt% for Fe@C-900. The extent of carbonization is in line with the *in situ* pyrolysis TGA. The textural properties of the catalysts were found to have a different dependency on the pyrolysis temperature. Fe-BTC is a microporous MOF with a zeolitic MTN-type framework and is characterized by high surface areas [51, 52]. Through Fe-BTC- pyrolysis, part of the surface area is lost, producing mesoporous materials with surface areas from 71 to 339 $m^2\ g^{-1}$ (**Table 3.1 and Figure A3.8**). A pyrolysis temperature of 400 ˚C is below the boundary temperature of generating noteworthy carbon porosity, as the surface area of the Fe@C-500 has quadrupled. As the pyrolysis temperature increases further, the BET area and microporosity also increase reaching a maximum around 600 ˚C. An increase in the temperature to 900 ˚C significantly decreases the surface area and microporosity. Regardless of the pyrolysis temperature, all the samples show a type H3 hysteresis loop between adsorption and desorption branches at medium pressure of around P/P_0 = 0.4, indicating the presence of cylindrical pores with a very wide pore size distribution.

3.3.2.2 Long range order of iron and nanoparticle size

Fe@C samples evaluated by X-ray diffraction showed contributions of several Fe phases (**Figure A3.9A**). Evidently, the meta-stable iron carbide and Wüstite are not the most abundant crystalline phases in the passivated material. Up to pyrolysis to 600 ˚C the samples are identified as nanocrystalline, consisting of broad Bragg diffractions and low-intensity signals. These samples show dominant features of maghemite (γ-Fe_2O_3) and different carbide phases. The region between 35-50˚ 2θ is congested with signals owing to mixed-carbide and metallic iron species, but a clear trend in

Table 3.1 Fe loading (w_{Fe}), average nanoparticle size (d_p), and textural properties (BET area, S_{BET}; external surface area, S_{ext}; total pore volume, V_P; and micropore volume, V_μ) of the Fe@C catalysts and MOF precursor Fe-BTC.

Catalyst	w_{Fe} / %	d_p / nm	S_{BET} / $m^2\ g^{-1}$	S_{ext} / $m^2\ g^{-1}$	V_P / $cm^3\ g^{-1}$	V_μ / $cm^3\ g^{-1}$
Fe-BTC	21.0	-	1021	62	0.45	0.40
Fe@C-400	34.4	2.3	71	66	0.15	0.00
Fe@C-500	38.0	3.6	281	139	0.30	0.06
Fe@C-600	42.0	6.0	339	205	0.32	0.06
Fe@C-900	53.4	28.4	217	201	0.30	0.01

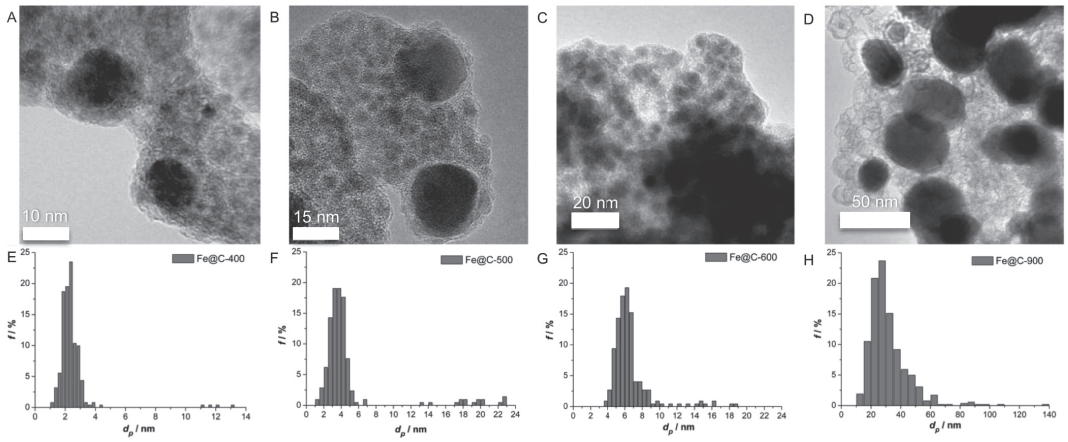

Figure 3.4 TEM and PSD of Fe@C-400 **A,E**; Fe@C-500 **B,F**; Fe@C-600 **C,G**; and Fe@C-900 **D,H**; indicating an increase in average particle size with increasing pyrolysis temperature. See **Table 3.1** for tabulated values of the average nanoparticle size of the histograms.

predominant phases is not visible. The complex nature of this region is demonstrated in **Figure A3.9B**, where linear combinations of metallic iron (α-Fe), hexagonal carbide (ε'-$Fe_{2.2}C$), Hägg carbide (χ-Fe_5C_2) and cementite (θ-Fe_3C) diffractions are plotted. Metallic iron and cementite can be identified due to the pronounced main-intensity diffractions of the (111) and (031) plane at 44.6˚ and 45.1˚ of α-Fe and θ-Fe_3C, respectively, and due to the isolated Bragg peaks at 48.7˚ and 49.3˚ of θ-Fe_3C. The presence of epsilon and Hägg Fe-carbides is tentative, for reasons of stability and overlap with previously assigned phases, including the minor diffraction of the γ-Fe_2O_3 (400) plane at 43.3˚. The Fe-carbide Bragg peaks can be unequivocally assigned for the sample pyrolyzed at 900 ˚C. The majority of the bulk Fe is clearly present as larger crystallites in the cementite phase, and a minor contribution can be assigned to metallic iron. Moreover, the pyrolysis at 900 ˚C has resulted in conversion of the pyrolytic amorphous carbon into nanocrystalline graphite, visualized by the diffraction of the C(001) plane at 26.2 ˚. Overall, there is a considerable effect of the temperature on the phase and size of the Fe nanoparticles. The effect on the size of the Fe nanoparticles is more comprehensible from TEM analysis (**Figure 3.4**). There is a successive increase in the average particle size of Fe as the temperature of pyrolysis increases. The samples pyrolyzed up to 600 ˚C show very narrow particle size distributions with average particle size between 2.3 to 6.0 nm (**Table 3.1**). Consequently, these values represent high dispersion up to 50%. The width of the particle size distribution (PSD) increases considerably at 900 ˚C and significant tailing towards higher particle size is visible. From the images of larger particles over the entire temperature range, the Fe phase seems to be encapsulated by a few nanolayers of a graphitic-type carbon shell (**Figure A3.10A**). This graphite layer coarsens with temperature, as the shell is clearly visible on micrographs from the Fe@C-900 sample (**Figure A3.10B and A3.10C**).

3.3.3 Catalytic performance of Fe@C catalysts

Figure 3.5A,B show the conversion profile (X_{CO}) and Fe time yield (*FTY*) of Fe@C catalysts during time-on-stream (*TOS*) under typical high-temperature Fischer-Tropsch operating conditions of 340 ˚C, 20 bar and equimolar syngas flow rates. The profiles are characterized by a successive increase in the conversion level, with an activation rate and time interval that strongly depend on the pyrolysis temperature. The *FTY* activity values are remarkable for Fe-based HTFT catalysts and moreover, the catalysts do not deactivate during the period of 80 h *TOS* studied. Among all catalysts, Fe@C-500 has the shortest activation time, reaching a steady state conversion level of 76% after ~30 h *TOS*. The materials synthesized at 400 and 600 ˚C reached similar levels of conversion after approximately 60 h *TOS*. Fe@C-900 did not reach steady state performance after 80 h *TOS*, showing a gradual increase in conversion from 35 to 55%. Figure 5c and 5d show the methane selectivity and the olefin to paraffin ratio (*O/P*) for C_2 hydrocarbons as a function of conversion level. Regardless the conversion level, Fe@C-400 and Fe@C-500 produce more methane than the materials synthesized at higher temperatures. At iso-conversion levels of 55%, the selectivity towards methane is 17% for Fe@C-400, and 13 and 12 % for Fe@-600 and Fe@C-900, respectively. Interestingly, the *FTY* of the Fe@C-400 surpasses the value of Fe@C-500 after 30 h *TOS* and indeed, its methane selectivity decreases below the value of Fe@C-500 for longer *TOS*. **Table 3.2** summarizes the activity, defined as *FTY*, chain growth probability α and product selectivities. After 80 h *TOS*, the activity decreased with the increase in pyrolysis temperature, similar reasoning is applicable for the methane selectivity. The product distribution on Fe@C follows the ASF distribution with α values that range from 0.43 to 0.55 after 80 h *TOS* (**Figure A3.11**), once more increasing with pyrolysis temperature. In addition, the effect of the pyrolysis temperature is clearly visible in the hydrocarbon product spectrum (**Figure A3.12**). However, the selectivity toward C_2-C_5 hydrocarbons remains constant, and the C_2-C_5 olefin to paraffin ratio does not follow a clear trend with pyrolysis temperature.

Table 3.2 Catalytic performance of Fe@C catalysts after 80h *TOS* operating under HTFT conditions of T = 340 ˚C, P = 20 bar, CO/H_2 = 1, and $GHSV$ = 30,000 h^{-1}.

Catalyst	X_{CO}	*FTY*	S_{CH4}	S_{CO2}	ΣC_2-C_5	ΣC_2-C_5=	α
	%	$mmol_{CO}g_{Fe}^{-1}s^{-1}$	C%	C%	C%	C%	-
Fe@C-400	74	0.38	15	47	30	16	0.00
Fe@C-500	76	0.36	15	46	29	14	0.06
Fe@C-600	74	0.31	14	46	30	13	0.06
Fe@C-900	53	0.19	13	45	30	17	0.01

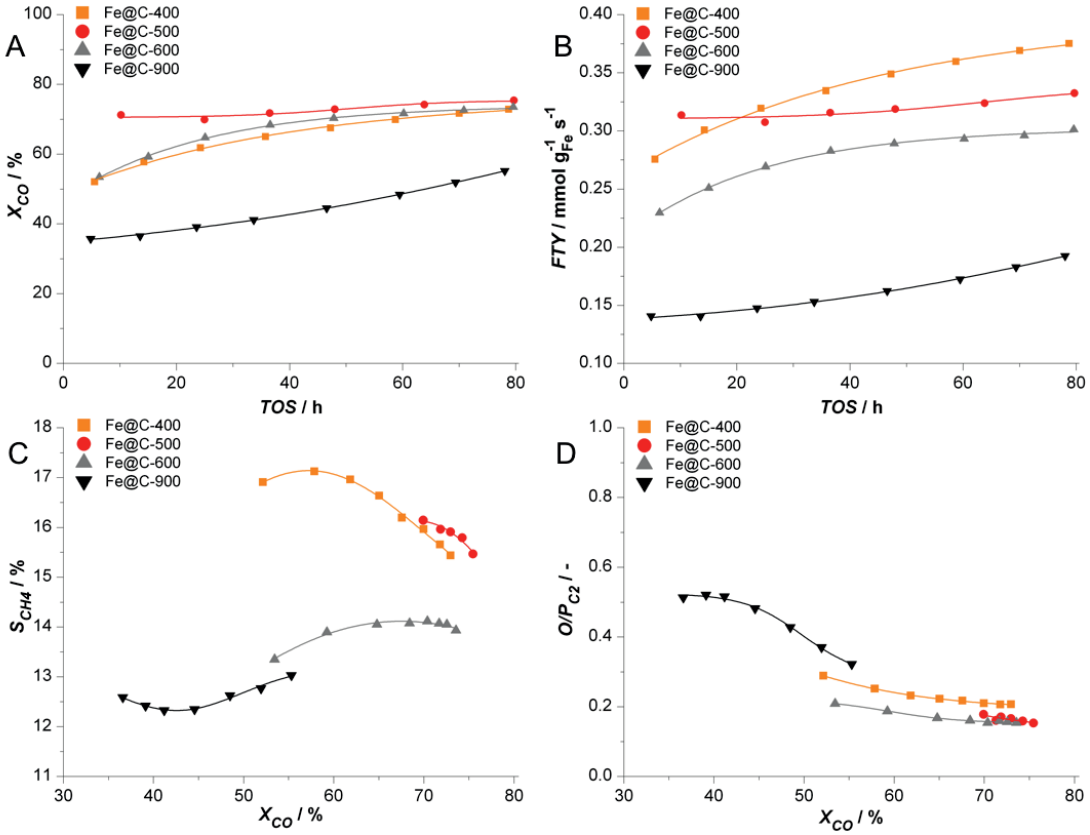

Figure 3.5 FTS performance of Fe@C catalysts under HTFT conditions (T = 340 ˚C, P = 20 bar, CO/H_2 = 1, $GHSV$ = 30,000 h^{-1}) displaying profiles of **A** CO conversion (X_{CO}), **B** Fe time yield (FTY), **C** methane selectivity (S_{CH4}), and **D** olefin to paraffin ratio (O/P) for C_2 hydrocarbons as a function of TOS **A,B** and X_{CO} **C,D**.

3.4 Discussion

The TGA, DRIFTS-MS, XAS and MAS studies show great resemblance in terms of structural changes over the temperature range studied. The combined analysis gives a better understanding in the process of Fe-BTC pyrolysis towards formation of Fe-based FTS catalysts. DRIFTS-MS and TGA analyses show that the commercial MOF contains impurities that are removed during the initial heating stage. In addition to water, DMF continuously evaporates up to temperatures of 300 ˚C, where the framework decomposition starts. In addition, desorption of these molecules reveals the presence of free acid in the MOF. The typical ν(O-H) vibrations at 3650 and 3570 cm^{-1} of hydration and hydroxylation of the CUS disapppear between 350 and 400 ˚C, indicating the destruction of the MOF network. This is in accordance with previously reported *in situ* XRD studies, showing the onset of framework destruction at 350 ˚C, and complete loss of crystallinity at 400 ˚C [53]. Linker

decomposition under inert atmosphere is characterized by decarboxylation, as large CO_2 contributions are obtained in the DRIFTS and MS analysis, while CO intensities are minor for both. Side-reactions between carboxylate moieties occur, possibly forming anhydride-functionalized compounds. The carboxylate stretch at 100 ˚C from 1720 to 1740 cm^{-1} can indicate esterification of free acid, but pronounced ν(C-O) vibrations from esters are absent. Most likely, the initial shift is caused by water and DMF removal, actually desolvating the free acid. Simultaneously, the formation of Fe nanoparticles occurs through reduced-oxide intermediates. In the *in situ* XANES experiments, the pre-edge doublet decreases energy splitting and centroid position, whereas the ratio between the first and second peaks increases. The decrease in symmetry may indicate the formation of a partially reduced oxide, Fe_3O_4. In this oxide, Fe(II) ions are located at octahedral sites, while Fe(III) species are distributed between octahedral and tetrahedral sites, thus justifying the appearance of an intense pre-edge feature [54]. The conversion to the Wüstite phase takes place at 450 ˚C and contributions from carbides are not ruled out [45]. Indeed, EXAFS analysis shows first shell Fe-C and second shell Fe-O bonds emerging at 400 ˚C at distances much different from the carboxylate distances found in the spectra of the MOF. The significant increase in Fe-Fe coordination numbers in higher shells demonstrates the formation of nanoparticles. The ratio of Wüstite and carbides at 450 ˚C was confirmed by Mössbauer spectroscopy at liquid He temperature, showing a prevalence of 73% FeO in addition to 27% Fe_xC. Interestingly, pyrolysis at 600 ˚C results in the full reduction of the Wüstite phase into α-Fe. The reduction of FeO to Fe at 570˚C has been reported, however, under a 5 vol% CO or H_2 atmosphere [55]. The MS results show that considerable amounts of CO are formed above 550 ˚C, and to a lesser extent H_2. Hence, the reducing environment created by pyrolysis products is sufficient to provoke the full reduction from FeO to Fe. Furthermore, the reduction is clearly visible in TGA where the 600 ˚C peaks corresponds to roughly 12% weight loss, in accordance with complete removal of oxygen from 27% FeO with balance Fe_3C (11.6 wt%). The additional loss of 10 wt% above temperatures of 700 ˚C can be explained by the gasification of the carbon matrix, possibly catalyzed by Fe species, producing a minor hydrogen evolution signal in the MS [56].

The Fe@C catalysts consist of Fe nanoparticles embedded in a carbonaceous matrix, of which the loading and carbide phase successively increase with pyrolysis temperature. The commercial Fe-BTC was found to possess a much lower porosity and associated surface area than the MIL-100(Fe) counterpart, ascribed to defects and free carboxylic acid groups. The pyrolysis process creates a mesoporous carbon with a very wide pore size distribution, though with roughly one third of the starting BET area. However, the microporosity of the Fe@C-400 is absent and its BET area is only 71 m^2 g^{-1}. From DRIFTS and TGA results, incomplete removal of the bulky pyrolysis products from the micropores is suspected. Thus, the sample was submerged in methanol and dried; after N_2-physisorption the BET area had increased more than 60%. Applying the same procedure to the Fe@C-900 sample did neither change the porosity nor the BET area. The long-range order of Fe

assessed by XRD showed a change of Fe-phase upon passivation. The highly dispersed Fe particles are very pyrophoric after *in situ* preparation, and passivation readily converts significant amounts of the Fe phases into γ-Fe_2O_3. The formation of the γ-Fe_2O_3 phase from Fe_3O_4 is reported to occur at temperatures below 100 ˚C, a local surface temperature that may be reached considering exotherms from oxidations (ΔH_f^0 ~ -800 kJ mol^{-1}) [57, 58]. The γ phase only converts to the α phase above 250 ˚C, indicating such temperatures were not reached during passivation [59]. Amongst the carbides, there seems to be a predominance of the cementite (θ-Fe_3C) phase. It is generally understood that this is the result of lattice matching of the carbide with the iron matrix, however, more recent work suggests that contributions of lattice vibration and anomalous magnetic ordering play an important role as well [60]. It is clear that for high temperatures the Fe@C catalysts exclusively form a cementite (θ-Fe_3C) phase. The TEM images confirm the nanocrystalline and monodisperse nature of the Fe particles and only from 600 ˚C onwards a slight tail in the particle size distribution (PSD) is observed. The PSD of Fe@C-900 displays pronounced tailing, in addition to the large average particle size. This effect is often obtained with highly mobile nanoparticles and is ascribed to sintering due to elevated temperatures [61]. Note that the Tammann temperature of iron lies just above 900 ˚C, indicating that at this point, the buildup of larger particles is favored at the expense of smaller ones [62]. The development of the carbon-shell structure depends on the pyrolysis temperature and likely plays a role in the stabilization of Fe nano-particles. Similar carbon encapsulation structures have been reported for composite iron materials prepared by pyrolysis of organic precursors such as Fe(II)-tripyridyl triazine [63].

In situ spectroscopy together with *ex situ* catalyst characterization demonstrate that the pyrolysis of Fe-BTC promotes the development of reduced Fe oxides and Fe carbide species. The pyrolysis temperature controls the distribution of oxides *vs* carbides as well as the Fe particle size, carbide type and porous structure of the resultant Fe@C material. **Figure 3.6A** summarizes the complex changes of the Fe nature as the pyrolysis temperature increases, whereas **Figure 3.6B** illustrates the changes in particle size and Fe phase as function of the pyrolysis temperature employed. The nature of the Fe species present after pyrolysis was found to significantly affect the development of carbide structures upon syngas exposure under Fischer-Tropsch conditions. *In situ* Mössbauer carried out on a reduced Fe@C sample pyrolyzed at 450 ˚C displayed that only the intermediate Fe_xC carbide was reduced to metallic Fe. Wüstite was not reduced in H_2 at 400 ˚C, in agreement with literature. After 5 h under HTFT conditions, the sample is composed of 53% of ε'-$Fe_{2.2}C$ with the balance Wüstite. The Fe@C-600 readily shows a contribution of 75% metallic Fe and just 25% intermediate Fe_xC carbide, and consecutively comprises 67% χ-Fe_5C_2 and 27% ε'-$Fe_{2.2}C$ after 5 h of HTFT. These controversial results can possibly be explained by looking at the correlation between particle size and C percentage in the carbide lattice. Because, thermodynamically, octahedral carbides like ε'-$Fe_{2.2}C$ transform into trigonal prismatic carbides such as χ-Fe_5C_2 above ~250 ˚C and into θ-Fe_3C above

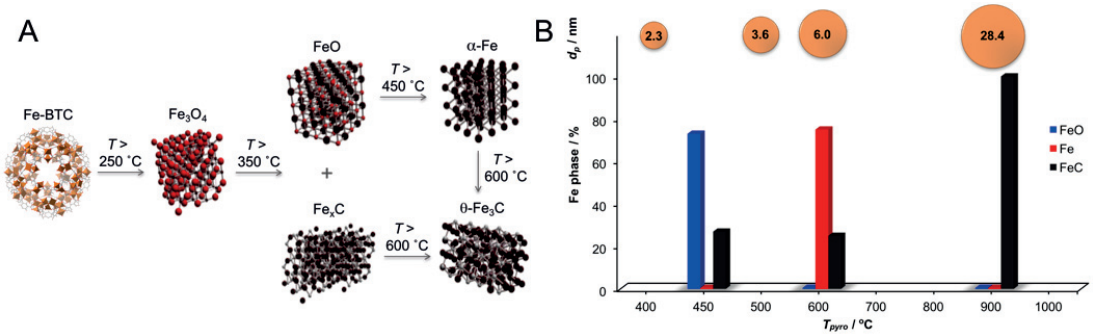

Figure 3.6 A Fe phase transformations during pyrolysis of Fe-BTC towards Fe@C and **B** Fe-phase distribution and average particle size of Fe@C catalysts after pyrolysis at different temperatures.

~350 ˚C through twinning, lowering strain and vibrational entropy [64, 65]. Moreover, it was postulated that the formation of octahedral carbides is entropically and kinetically unfavored [46]. However, kinetic limitations of C diffusion into the Fe lattice will have a far less pronounced effect on the C concentration in small particles with an average diameter between 2.3 and 3.6 nm than in particles of 6.0 nm. Therefore, it is suggested that both the FeO and Fe phase transform into ε'-$Fe_{2.2}C$ for the sample pyrolyzed at 450 ˚C. The Fe@C-600 sample follows the expected behavior as described above, transforming the Fe phase into χ-Fe_5C_2 while preserving the intermediate carbide. Nevertheless, entropic contributions may play an important role in acquiring the Fe carbide phase at the steady state operation, possibly converting epsilon carbide into Hägg carbides [66, 67]. No metallic iron is found in Fe@C under HTFT conditions, in agreement with other studies demonstrating that the Fe carbide phase prevails over metallic Fe under syngas exposure, since the activation energy for C diffusion is lower than the value for the FTS reaction [68, 69].

The changing nature of Fe with increasing pyrolysis temperature was found to have an important effect on the activity and activation behavior of the Fe@C samples. High activity under HTFT was obtained for all catalysts with an *FTY* up to 0.38 $mmol_{CO}\ g_{Fe}\ s^{-1}$, which is several times higher than for comparable Fe_5C_2@C systems reported [70]. Fe@C-500 showed very stable performance with short activation behavior. The product distribution was constant during the measured *TOS*, which may indicate that no major changes occurred in the particle size, electronic state, and carbidic structure of Fe. In the case of Fe@C-400 and Fe@C-600, both catalysts show very similar activation rates of 0.52% h^{-1} in the first 40 h *TOS*, stabilizing at 76% conversion after 60 h *TOS*. Among all the catalysts, Fe@C-900 showed the longest induction period and steady state was not yet achieved during the applied *TOS*. In terms of product distribution, for Fe@C-400, the methane selectivity continuously decreases reaching 14% after 80 h *TOS*. After this period, Fe@C-400 and Fe@C-500 have a virtually similar catalytic performance, and the interconversion of ε'-$Fe_{2.2}C$ into χ-Fe_5C_2 may explain these effects. Fe@C-600 showed a lower selectivity to methane when compared at iso-conversion

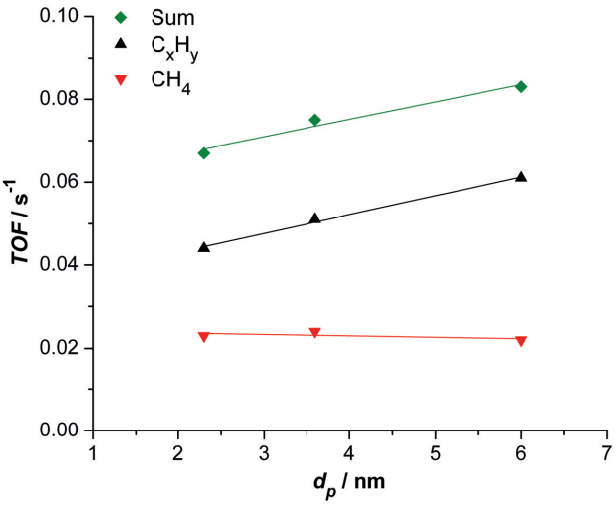

Figure 3.7 Initial *TOF* after 5 h HTFT experiments (*T* = 340 °C, *P* = 20 bar, CO/H_2 = 1, *GHSV* = 30,000 h^{-1}) as function of average particle size of Fe@C-400 (2.3 nm), Fe@C-500 (3.6 nm) and Fe@C-600 (6.0 nm).

levels with Fe@C-500 and Fe@C-400, which may be linked to particle size structure-sensitivity effects, like in previous studies [71]. Additional experiments at different space velocities and at similar X_{CO} and *TOS* may provide additional insight on the effect of pyrolysis temperature on the product distribution, but are beyond the scope of the present work. More detailed insight in structure-activity relations was obtained from turnover frequency (*TOF*) calculations. **Figure 3.7** displays the apparent *TOF* of Fe@C-400, Fe@C-500 and Fe@C-600 after 5 h *TOS*, showing higher apparent intrinsic catalytic activity of iron species with increasing pyrolysis temperature, whereas the *TOF* towards methane slightly decrease. Since the Fe-phase composition and particle size distribution are highly correlated and vary in all catalysts, it is difficult to speculate about the difference in activity of epsilon and Hägg carbides or to decouple the particle size and Fe-phase effect while the active phase is evolving during HTFT. However, the structure-sensitivity of the hydrocarbon selectivity during initial turnover is striking, indicating the importance of taking into account the development of the Fe-carbide phase next to particle size effects [71, 72]. The HTFT performance confirms that the intimate Fe-C interaction of the Fe@C materials plays an important role in the nature of the active sites of the catalyst.

3.5 Conclusions

In this Chapter, a combined *in situ* XAS, DRIFTS and Mössbauer study was performed together with *ex situ* catalyst characterization to elucidate the nature of Fe and C during the pyrolysis process of Fe-BTC as well as during Fischer-Tropsch synthesis. Fe-BTC is a prime precursor for obtaining highly active and stable FTS catalysts by means of pyrolysis. The commercial MOF is highly

hydrated and contains residual DMF and free carboxylic acid groups, resulting in lower surface area than its MIL-100(Fe) counterpart. During initial stage of pyrolysis, the Fe-BTC undergoes desolvation, whereas perturbation of the framework initiates at 250 ˚C. Structural breakdown follows at 350 ˚C under release of significant amounts of carbon dioxide. Simultaneously, the Fe(III) phase transforms to Fe(II) along a 150 ˚C temperature increase. Depending on the pyrolysis temperature, the FeO phase (73%) or α-Fe (75%) phase prevail at 450 or 600 ˚C, respectively. The θ-Fe_3C phase is dominant at 900 ˚C and the particle size drastically increases with these high temperatures near the Tammann temperature. The resulting catalysts contain high loadings of Fe between 34 and 54 wt% and the carbon matrix has a mesoporous nature comprising a wide pore size distribution. After syngas exposure, the highly dispersed Fe@C-400 comprises mainly ε'-$Fe_{2.2}C$ as main carbide phase, while pyrolysis at 600 ˚C promotes the development of Hägg carbides. The Fe@C-400, 500 and 600 catalysts were highly active under HTFT conditions (*FTY* = 0.31–0.38 $mmol_{CO}\, g_{Fe}\, s^{-1}$) and did not exhibit any deactivation during 80 h *TOS*. Their FTS performance showed similar initial *TOF* values, but quite different activation behavior and product distributions. In particular, the methane selectivity was minimized for the Fe@C-600, while maintaining similar olefin to paraffin ratio. Fe@C-900 displayed a very long induction period, and did not reach steady state conversion under the applied reaction conditions. Summarizing, it was demonstrated that it is possible to tune the iron loading, the particle size and the Fe-phase of resulting Fe@C catalysts by changing the pyrolysis temperature of Fe-BTC to obtain highly active and stable FTS catalysts.

References

[1] Conti, J.J., Holtberg, P.D., Diefenderfer, J.R., Napolitano, S.A., Schaal, A.M., Turnure, J.T., Westfall, L.D., Annual Energy Outlook, in, U.S. Department of Energy, Washington, DC, 2014, pp. 269.

[2] Stewart, L., Alboudwarej, H., Felix, J.J., Taylor, S., Badry, R., Bremner, C., Brough, B., Skeates, C., Baker, A., Palmer, D., Pattison, K., Beshry, M., Krawchuk, P., Brown, G., Calvo, R., Triana, J.A.C., Hathcock, R., Koerner, K., Hughes, T., Kundu, D., Cárdenas, J.L.d., West, C., *Oilfield Review*, 18 (**2006**) 34-53.

[3] Abdul-Hamid, O.S., Hamid, H.A.H., Odulaja, A., Fantini, A.-M., Hassani, H., Christodoulides, P., Bayer, C., Stöger, K., Kalirai, H., Moudassir, M., Sattar, M., Gredinger, A., Gutman, K., Lavnick, D., Mekerba, M., Arifin, Z., Starnegg, T., Annual Statistical Bulletin, in, OPEC, Vienna, Austria, 2014, pp. 112.

[4] Rostrup-Nielsen, J.R., *Catal. Today*, 21 (**1994**) 257-267.

[5] Sie, S.T., Krishna, R., *Appl. Catal., A*, 186 (**1999**) 55-70.

[6] Stranges, A.N., *A history of the fischer-tropsch synthesis in Germany 1926–45*, in: B.H. Davis, M.L. Occelli (Eds.) Stud. Surf. Sci. Catal., Elsevier, Amsterdam, **2007**, pp. 1-27.

[7] Sartipi, S., Parashar, K., Makkee, M., Gascon, J., Kapteijn, F., *Catal. Sci. Technol.*, 3 (**2013**) 572-575.

[8] Schulz, H., *Appl. Catal., A*, 186 (**1999**) 3-12.

[9] Dry, M.E., *Catal. Today*, 71 (**2002**) 227-241.

[10] Steynberg, A.P., Espinoza, R.L., Jager, B., Vosloo, A.C., *Appl. Catal., A*, 186 (**1999**) 41-54.

[11] Torres Galvis, H.M., de Jong, K.P., *ACS Catal.*, 3 (**2013**) 2130-2149.

[12] Dry, M.E., *Chapter 7 - FT catalysts*, in: S. André, D. Mark (Eds.) Stud. Surf. Sci. Catal., Elsevier, Amsterdam, **2004**, pp. 533-600.

[13] Li, S., Krishnamoorthy, S., Li, A., Meitzner, G.D., Iglesia, E., *J. Catal.*, 206 (**2002**) 202-217.

[14] Schulz, H., *Comparing Fischer-Tropsch synthesis on iron- and cobalt catalysts: The dynamics of structure and function*, in: B.H. Davis, M.L. Occelli (Eds.) Stud. Surf. Sci. Catal., Elsevier, Amsterdam, **2007**, pp. 177-199.

[15] Jager, B., Espinoza, R., *Catal. Today*, 23 (**1995**) 17-28.

[16] Gascon, J., Corma, A., Kapteijn, F., Llabrés i Xamena, F.X., *ACS Catal.*, 4 (**2013**) 361-378.

[17] Masoomi, M.Y., Morsali, A., *Coord. Chem. Rev.*, 256 (**2012**) 2921-2943.

[18] Wu, Y.-n., Zhou, M., Li, S., Li, Z., Li, J., Wu, B., Li, G., Li, F., Guan, X., *Small*, 10 (**2014**) 2927-2936.

[19] Cao, X., Zheng, B., Rui, X., Shi, W., Yan, Q., Zhang, H., *Angew. Chem. Int. Ed.*, 53 (**2014**) 1404-1409.

[20] Lee, H.J., Cho, W., Lim, E., Oh, M., *Chem. Commun.*, 50 (**2014**) 5476-5479.

[21] Shiva, K., Jayaramulu, K., Rajendra, H.B., Kumar Maji, T., Bhattacharyya, A.J., *Z. Anorg. Allg. Chem.*, 640 (**2014**) 1115-1118.

[22] Wu, A., Liu, D., Tong, L., Yu, L., Yang, H., *CrystEngComm*, 13 (**2011**) 876-882.

[23] Liu, D.-J., Goenaga, G., Ma, S., Yuan, S., Shui, J., *ESC Trans.*, 30 (**2011**) 97-104.

[24] Ma, S., Goenaga, G.A., Call, A.V., Liu, D.-J., *Chem. Eur. J.*, 17 (**2011**) 2063-2067.

[25] Zhao, D., Shui, J.-L., Chen, C., Chen, X., Reprogle, B.M., Wang, D., Liu, D.-J., *Chem. Sci.*, 3 (**2012**) 3200-3205.

[26] Xia, W., Mahmood, A., Zou, R., Xu, Q., *Energ. Environ. Sci.*, 8 (**2015**) 1837-1866.

[27] Yu, G., Sun, B., Pei, Y., Xie, S., Yan, S., Qiao, M., Fan, K., Zhang, X., Zong, B., *J. Am. Chem. Soc.*, 132 (**2010**) 935-937.

[28] Proietti, E., Jaouen, F., Lefèvre, M., Larouche, N., Tian, J., Herranz, J., Dodelet, J.-P., *Nat Commun*, 2 (**2011**) 416.

[29] Amali, A.J., Sun, J.-K., Xu, Q., *Chem. Commun.*, 50 (**2014**) 1519-1522.

[30] Jiang, H.-L., Liu, B., Lan, Y.-Q., Kuratani, K., Akita, T., Shioyama, H., Zong, F., Xu, Q., *J. Am. Chem. Soc.*, 133 (**2011**) 11854-11857.

[31] Liu, B., Shioyama, H., Akita, T., Xu, Q., *J. Am. Chem. Soc.*, 130 (**2008**) 5390-5391.

[32] Liu, B., Shioyama, H., Jiang, H., Zhang, X., Xu, Q., *Carbon*, 48 (**2010**) 456-463.

[33] Xu, G., Ding, B., Shen, L., Nie, P., Han, J., Zhang, X., *J. Mater. Chem. A*, 1 (**2013**) 4490-4496.

[34] deKrafft, K.E., Wang, C., Lin, W., *Adv. Mater.*, 24 (**2012**) 2014-2018.

[35] Santos, V.P., Wezendonk, T.A., Jaén, J.J.D., Dugulan, A.I., Nasalevich, M.A., Islam, H.-U., Chojecki, A., Sartipi, S., Sun, X., Hakeem, A.A., Koeken, A.C.J., Ruitenbeek, M., Davidian, T., Meima, G.R., Sankar, G., Kapteijn, F., Makkee, M., Gascon, J., *Nat Commun*, 6 (**2015**) 1-8.
[36] De Lange, M.F., Vlugt, T.J.H., Gascon, J., Kapteijn, F., *Microporous Mesoporous Mater.*, 200 (**2014**) 199-215.
[37] Edam, R., Mertens, V., Ribes, C., Beyer, S., Schmidt, E., Chojecki, A., Development of On-Line GC Method for High Throughput Fischer-Tropsch to Olefins Campaign, in, Dow Chemical, Terneuzen, 2010.
[38] Chojecki, A., Meima, G., Bashir, M., Khare, C., Ruitenbeek, M., High Throughput Campaign Fischer-Tropsch to Olefin. Part 1: Validation of the Experimental Setup. Catalytic Test Results over Fused Iron Catalysts, in, Dow Chemical, Terneuzen, 2011.
[39] Leclerc, H., Vimont, A., Lavalley, J.-C., Daturi, M., Wiersum, A.D., Llwellyn, P.L., Horcajada, P., Ferey, G., Serre, C., *PCCP*, 13 (**2011**) 11748-11756.
[40] Wuttke, S., Bazin, P., Vimont, A., Serre, C., Seo, Y.-K., Hwang, Y.K., Chang, J.-S., Férey, G., Daturi, M., *Chem. Eur. J.*, 18 (**2012**) 11959-11967.
[41] Vimont, A., Leclerc, H., Maugé, F., Daturi, M., Lavalley, J.-C., Surblé, S., Serre, C., Férey, G., *J. Phys. Chem. C*, 111 (**2007**) 383-388.
[42] Lohe, M.R., Rose, M., Kaskel, S., *Chem. Commun.*, (**2009**) 6056-6058.
[43] Lieb, A., Leclerc, H., Devic, T., Serre, C., Margiolaki, I., Mahjoubi, F., Lee, J.S., Vimont, A., Daturi, M., Chang, J.-S., *Microporous Mesoporous Mater.*, 157 (**2012**) 18-23.
[44] Sciortino, L., Alessi, A., Messina, F., Buscarino, G., Gelardi, F.M., *J. Phys. Chem. C*, 119 (**2015**) 7826-7830.
[45] de Smit, E., Beale, A.M., Nikitenko, S., Weckhuysen, B.M., *J. Catal.*, 262 (**2009**) 244-256.
[46] de Smit, E., Cinquini, F., Beale, A.M., Safonova, O.V., van Beek, W., Sautet, P., Weckhuysen, B.M., *J. Am. Chem. Soc.*, 132 (**2010**) 14928-14941.
[47] Horcajada, P., Surble, S., Serre, C., Hong, D.-Y., Seo, Y.-K., Chang, J.-S., Greneche, J.-M., Margiolaki, I., Ferey, G., *Chem. Commun.*, (**2007**) 2820-2822.
[48] Mitchell, L., Williamson, P., Ehrlichová, B., Anderson, A.E., Seymour, V.R., Ashbrook, S.E., Acerbi, N., Daniels, L.M., Walton, R.I., Clarke, M.L., Wright, P.A., *Chem. Eur. J.*, 20 17185-17197.
[49] McCammon, C.A., Price, D.C., *Phys. Chem. Miner.*, 11 250-254.
[50] Moura, F.C.C., Oliveira, G.C., Araujo, M.H., Ardisson, J.D., Macedo, W.A.A., Lago, R.M., *Appl. Catal., A*, 307 (**2006**) 195-204.
[51] Dhakshinamoorthy, A., Alvaro, M., Horcajada, P., Gibson, E., Vishnuvarthan, M., Vimont, A., Grenèche, J.-M., Serre, C., Daturi, M., Garcia, H., *ACS Catal.*, 2 (**2012**) 2060-2065.
[52] Seo, Y.-K., Yoon, J.W., Lee, J.S., Lee, U.H., Hwang, Y.K., Jun, C.-H., Horcajada, P., Serre, C., Chang, J.-S., *Microporous Mesoporous Mater.*, 157 (**2012**) 137-145.
[53] Vimont, A., Goupil, J.-M., Lavalley, J.-C., Daturi, M., Surblé, S., Serre, C., Millange, F., Férey, G., Audebrand, N., *J. Am. Chem. Soc.*, 128 (**2006**) 3218-3227.
[54] Piquer, C., Laguna-Marco, M.A., Roca, A.G., Boada, R., Guglieri, C., Chaboy, J., *J. Phys. Chem. C*, 118 (**2014**) 1332-1346.
[55] Jozwiak, W.K., Kaczmarek, E., Maniecki, T.P., Ignaczak, W., Maniukiewicz, W., *Appl. Catal., A*, 326 (**2007**) 17-27.
[56] Furimsky, E., Sears, P., Suzuki, T., *Energy & Fuels*, 2 (**1988**) 634-639.
[57] Jiao, F., Jumas, J.-C., Womes, M., Chadwick, A.V., Harrison, A., Bruce, P.G., *J. Am. Chem. Soc.*, 128 (**2006**) 12905-12909.
[58] Majzlan, J., Navrotsky, A., Schwertmann, U., *Geochim. Cosmochim. Acta*, 68 (**2004**) 1049-1059.
[59] Sahoo, S.K., Agarwal, K., Singh, A.K., Polke, B.G., Raha, K.C., *Int. J. Eng. Sci. Tech.*, 2 (**2010**) 118-126.
[60] Fang, C.M., Sluiter, M.H.F., van Huis, M.A., Ande, C.K., Zandbergen, H.W., *Phys. Rev. Lett.*, 105 (**2010**) 055503.
[61] Merkle, R., Maier, J., *Z. Anorg. Allg. Chem.*, 631 (**2005**) 1163-1166.
[62] Burgess, G.K., Melting points of the iron group elements by a new radiation method, in: S.W. Stratton (Ed.) Bulletin of the Bureau of Standards, National Institute of Standards and Technology (NIST), Gaithersburg, Maryland, 1907, pp. 345-355.

[63] Velázquez-Palenzuela, A., Zhang, L., Wang, L., Cabot, P.L., Brillas, E., Tsay, K., Zhang, J., *J. Phys. Chem. C*, 115 (**2011**) 12929-12940.
[64] Andersson, S., Hyde, B.G., *J. Solid State Chem.*, 9 (**1974**) 92-101.
[65] Nagakura, S., *J. Phys. Soc. Jpn.*, 14 (**1959**) 186-195.
[66] Dirand, M., Afqir, L., *Acta Metall.*, 31 (**1983**) 1089-1107.
[67] de Smit, E., Weckhuysen, B.M., *Chem. Soc. Rev.*, 37 (**2008**) 2758-2781.
[68] Niemantsverdriet, J.W., Van der Kraan, A.M., Van Dijk, W.L., Van der Baan, H.S., *J. Phys. Chem.*, 84 (**1980**) 3363-3370.
[69] Niemantsverdriet, J.W., van der Kraan, A.M., *J. Catal.*, 72 (**1981**) 385-388.
[70] Hong, S.Y., Chun, D.H., Yang, J.-I., Jung, H., Lee, H.-T., Hong, S., Jang, S., Lim, J.T., Kim, C.S., Park, J.C., *Nanoscale*, 7 (**2015**) 16616-16620.
[71] Torres Galvis, H.M., Bitter, J.H., Davidian, T., Ruitenbeek, M., Dugulan, A.I., de Jong, K.P., *J. Am. Chem. Soc.*, 134 (**2012**) 16207-16215.
[72] Shroff, M.D., Kalakkad, D.S., Coulter, K.E., Kohler, S.D., Harrington, M.S., Jackson, N.B., Sault, A.G., Datye, A.K., *J. Catal.*, 156 (**1995**) 185-207.

Appendix

3

Elucidating the Nature of Fe species during Pyrolysis of the Fe-BTC MOF into Highly Active and Stable Fischer-Tropsch Catalysts

A3.1 Experimental supplement

A3.1.1 XAS data processing

All the XAFS data were merged in *Horae Athena* and the exported file was further processed with *VIPER* software for normalisation and background subtraction. Subsequent detailed analysis was performed using EXCURVE software. Fe foil was used to extract the amplitude reduction factor. This value of 0.75 was fixed for the analysis of the remaining data sets. In the EXCURVE software, it is possible to include single-scattering paths of various shells without the need for a crystal structure, and refine until the best fit between experiment and theory is achieved. The model used for simulating the room temperature EXAFS spectrum of Fe-BTC was based on the crystallographic data reported by Horcajada *et al.* [1]. This method is particularly useful in very complex systems such as the one described here. The software allows estimation of the change in *R*-factor and, therefore, validates including additional shells. In addition, it is also possible to constrain two closely similar parameters to the same value. For example, in some cases the Fe-C and Fe-O are assumed to have similar Debye-Waller factors.

A3.1.2 Mössbauer measurements

The high-pressure Mössbauer *in situ* cell developed at Reactor Institute Delft is manufactured of stainless steel SS316L and capable of going up to 25 bar of gas mixtures at temperatures of 450 ˚C. It allows for combined Mössbauer spectroscopy in transmission mode and IR spectroscopy in DRIFT configuration. At the top of the cell a CVD diamond window is mounted, allowing the IR measurements, while a beryllium window is included at the bottom, having high permeability to the gamma rays used in Mössbauer spectroscopy. The sample is mounted inside the cell in holders containing graphite discs at the bottom and the cell is closed with gold plated metal C-rings. The gas flows through the catalyst bed from top to bottom, the inlet gas being preheated in the heating compartment. The cell can be mounted on transport tubes and cooled down to 4.2 K in a cryostat for low-temperature Mössbauer measurements. One Mössbauer spectrum was recorded each time at room temperature for 10-15 h until a satisfactory signal-to-noise ratio was achieved. Subsequently, the cell was cooled down using liquid He and the low temperature Mössbauer spectrum was recorded. The measurements at liquid He temperature were used for data deconvolution, however both spectra provided much qualitative input on the system studied. The Mössbauer spectra were fitted using the *Mosswinn* 4.0 program [2]. The high-pressure beryllium windows used in this cell contain 0.08% Fe impurity whose spectral contribution was fitted and removed from the final spectra. Experimental uncertainties in the isomer shift (*IS*) ± 0.01 mm s^{-1}; in the quadrupole splitting (*QS*) ± 0.01 mm s^{-1}; in the line width (Γ) ± 0.01 mm s^{-1}; in the hyperfine field ± 0.1 T; and in the spectral contribution ± 3%

A3.1.3 HR-TEM calculation of dispersion

The dispersion *D* (equation **A3.1**) is calculated as number of surface atoms N_s divided by the total amount of atoms N_t, excluding the agglomerate fraction beyond the Gauss distribution. From the particle analysis, we calculate a surface area *A* to volume ratio *V* by dividing the sum of the areas over the total volume of the particles counted. The surface density of Fe atoms (*n*) was calculated with the atom count from the main plane in XRD (110) of the BCC lattice with associated lattice constant (*a* = 2.856 Å). Avogadro's number N_A, molar mass M_m and bulk density ρ_{Fe} were used as found in Perry's handbook [3]. The dispersion, total particle count and agglomerate fraction for the Fe@C samples is given in **Table A3.0**.

$$D = \frac{N_s}{N_t} = \frac{A}{V}\ \frac{M_m\ n_{110}}{N_A\ \rho_{Fe}} \times 100\% \qquad (\mathbf{A3.1})$$

Table A3.1 Calculated dispersion and agglomerate fraction for the particle counts on HR-TEM analysis of Fe@C.

Catalyst	*D* / %	Particle counts / -	Agglomerate fraction / %
Fe@C-400	50	251	1.6
Fe@C-500	32	680	5.1
Fe@C-600	19	263	4.5
Fe@C-900	4	523	6.6

A3.1.4 Catalytic performance tests of Fe@C

CO conversion and carbon selectivity were defined by equations **A3.2** and **A3.3**, respectively, where X_{CO} stands for CO conversion, *F* indicates the molar flow, *S* is the carbon selectivity towards a product with *n* carbon atoms and *y* is the molar fraction of a hydrocarbon C*n* [4, 5]. Catalytic activity is expressed as iron time yield (*FTY*), defined as the number of CO moles converted to hydrocarbons per gram of iron per second. The carbon balance was satisfied by 95 ± 1% for all experiments. The apparent turnover frequency (*TOF*) was calculated for the catalysts pyrolyzed between 400-600 ˚C and was obtained from equation **A3.4**. Fe@C-900 was not considered in the *TOF* analysis because of the wide particle size distribution of the polydisperse particles and absent Mössbauer data for this catalyst. Gas hourly space velocity (*GHSV* = 30,000 h^{-1}) is defined as the ratio of the volumetric flow rate (STP) over the catalyst bed volume.

$$X_{CO} = \left(1 - \frac{C_{He,d,R} \cdot C_{CO,d,R}}{C_{He,d,blk} \cdot C_{CO,d,blk}}\right) \cdot 100\% \qquad \textbf{(A3.2)}$$

where $C_{He,d,blk}$, $C_{He,d,R}$, $C_{CO,d,blk}$, $C_{CO,d,R}$ are the concentrations determined by GC analysis of He in the blank, He in the diluted reactor effluent, CO in the blank, and CO in the diluted reactor effluent, respectively.

$$S_{Cn} = \frac{n \cdot \left(\frac{C_{Cn,d,R}}{C_{He,d,R}}\right)}{\left(\frac{C_{CO,d,blk}}{C_{He,d,blk}} - \frac{C_{CO,d,R}}{C_{He,d,R}}\right)} \cdot 100\% \qquad \textbf{(A3.3)}$$

where $C_{Cn,d,R}$ is the concentration the diluted reactor effluent determined be GC analysis of a product with n carbon atoms.

$$TOF = \frac{X_{CO}\ F_{CO}^{in}\ (1 - S_{CO_2})}{\frac{w_{Fe}}{M_m}\ D\ \varepsilon} \qquad \textbf{(A3.4)}$$

where X_{CO} is the carbon conversion, $F_{CO,in}$ the molar flow of CO in the inlet, S_{CO2} the selectivity towards CO_2, w_{Fe} the mass of Fe in the catalyst, M_m the molar mass of Fe, D the metal dispersion and ε is the fractional carburization of iron after exposure to syngas determined by Mössbauer spectroscopy.

A3.2 Results

A3.2.1 *In situ* characterization during pyrolysis and FTS

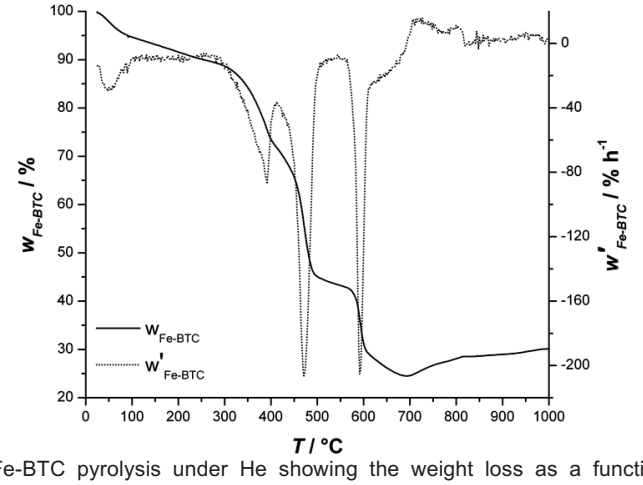

Figure A3.1 TGA of Fe-BTC pyrolysis under He showing the weight loss as a function of the pyrolysis temperature (*T*) applied, indicating three regions of large mass losses.

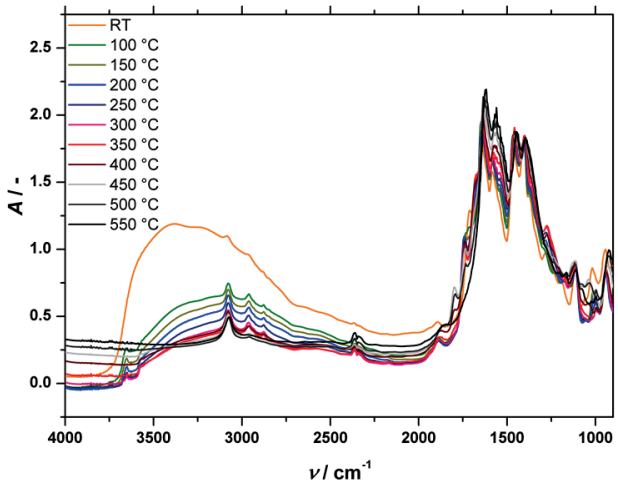

Figure A3.2 Full DRIFT spectra of Fe-BTC pyrolysis in He showing spectra obtained at set point temperature reached with 2 ˚C/min, showing the initial hydration of Fe-BTC, the release of free acid during pyrolysis and the formation of pyrolysis products such as CO_2.

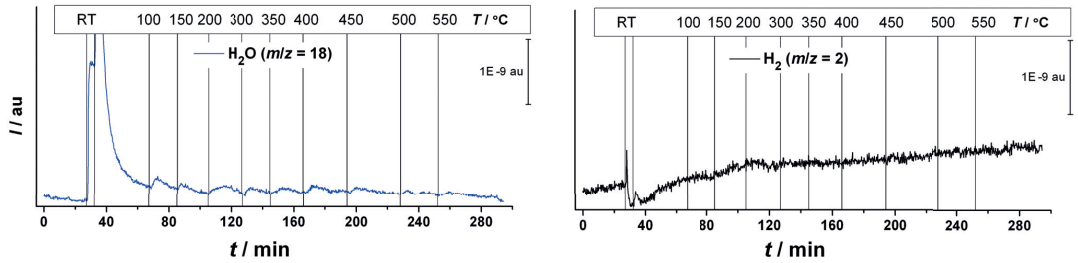

Figure A3.3 Mass spectra of effluent gas during Fe-BTC pyrolysis in He with indications when the temperature (*T*) was increased to the set-point value.

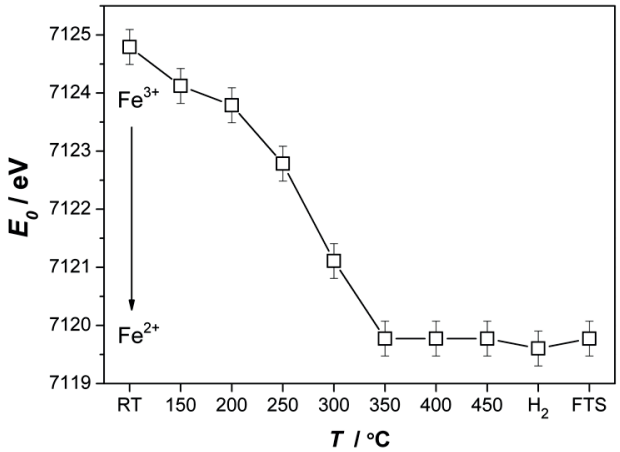

Figure A3.4 XANES-spectra derived edge energy positions (E_0) indicating a decrease in Fe oxidation state during pyrolysis, while maintaining that bulk oxidation state during reduction for 3 h in 10 vol% H_2 at 400 ˚C and during 5 h HTFT at 340 ˚C and 2 bar with CO/H_2 =1.

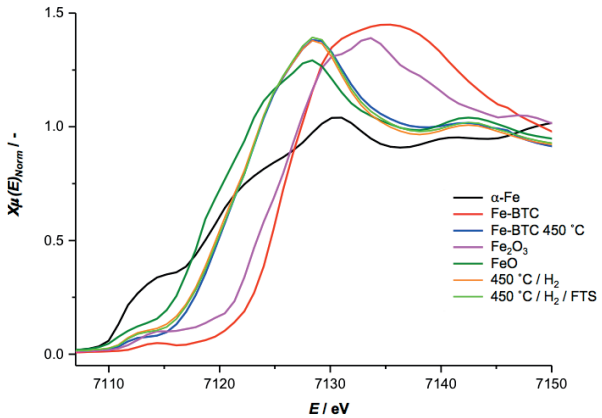

Figure A3.5 XANES of Fe-BTC, the pyrolyzed compound Fe@C, subsequently reduced and under HTFT conditions, together with the reference materials metallic iron, wüstite, and hematite, used for correlating data.

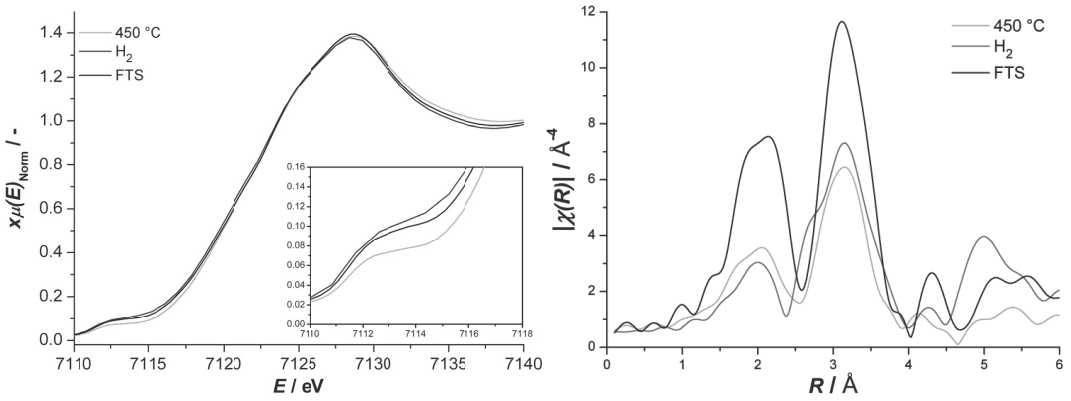

Figure A3.6 *In situ* XAS spectra of pyrolyzed Fe-BTC subsequently reduced in 10 vol% H_2 at 400 ˚C and 1 bar for 3 h and under HT-FTS at 340 ˚C and 2 bar after 5 h; showing the XANES with pre-edge insert and magnitude of the Fourier transformed EXAFS signal of the same experiment.

Table A3.2 EXAFS fitting results of the spectra recorded after pyrolysis in He at different temperatures and subsequent reduction in hydrogen for 3 h at 400 °C and 1 bar and exposure to syngas for 5 h at 340 °C and 2 bar using an equimolar CO/H_2 ratio and total flow rates of 20 cm^3_{STP} min^{-1}.

Temperature T / ˚C	Shell Number	Scatterer	Coordination Number N / -	Distance R / Å	Debye-Waller factor $\Delta\sigma^2$ / $Å^2$
RT	1	O	6	1.998	0.014
	2	C	4	2.958	0.019
	3	Fe	2	3.328	0.016
150	1	O	6.0	2.0	0.021
	2	C	3.6	2.967	0.026
	3	Fe	2.3	3.328	0.016
200	1	O	6.0	2.0	0.021
	2	C	3.0	2.964	0.026
	3	Fe	2.4	3.33	0.033
250	1	O	5.8	2.0	0.023
	2	C	2.6	2.974	0.027
	3	Fe	1.7	3.33	0.032
300	1	O	5.3	2.0	0.023
	2	C	2.3	3.01	0.029
	3	Fe	1.9	3.33	0.033
350	1	O	5.1	2.001	0.023
	2	C	2.0	2.97	0.031
	3	Fe	1.1	3.247	0.033
400	1	O	4.5	2.001	0.023
	2	C	1.7	3.0	0.033
	3	Fe	0.9	3.286	0.033
450	1	C	2.2	2.115	0.026
	2	O	2.3	2.250	0.026
	3	Fe	0.5	2.503	0.033
	4	Fe	4.0	3.055	0.033
	5	Fe	5.6	3.219	0.033
	6	Fe	2.4	3.407	0.034
400 / H_2	1	C	2.0	2.158	0.026
	2	O	2.1	2.287	0.026
	3	Fe	1.2	2.525	0.033
	4	Fe	3.0	3.045	0.033
	5	Fe	4.7	3.191	0.033
	6	Fe	1.7	3.357	0.034
340 / FTS	1	C	2.7	2.099	0.022
	2	O	2.5	2.194	0.023
	3	Fe	0.8	2.542	0.033
	4	Fe	8.8	3.089	0.033
	5	Fe	6.7	3.279	0.033
	6	Fe	2.9	3.510	0.034

Amplitude reduction factor S_0^2 = 0.75 was calculated from Fe foil standard was the same in all cases. Errors in N ± 10% and in R ± 0.02 Å.

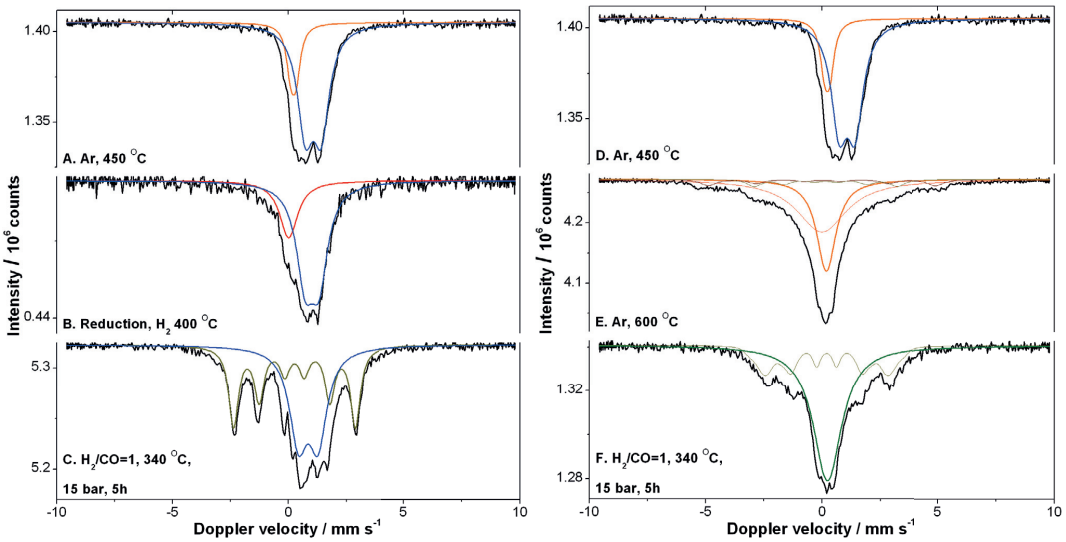

Figure A3.7 *In situ* Mössbauer spectra **A-F** measured at 300 K and accompanying fitting results of Fe-BTC pyrolyzed in Ar at temperatures up to 450 ˚C **A-C** and 600 ˚C **D-F**. The samples were subsequently exposed to 5 h HTFT conditions of 340 ˚C, 15 bar of CO/H_2=1.

Table A3.3 The Mössbauer fitted parameters of Fe-BTC sample treated at 450 °C.

Sample	*T* (K)	*IS* ($mm \cdot s^{-1}$)	*QS* ($mm \cdot s^{-1}$)	*Hyperfine field* (T)	*Γ* ($mm \cdot s^{-1}$)	*Phase*	*Spectral contribution* (%)
Fe-BTC	300	0.22	0.23	-	0.45	Fe^{3+} (SPM Fe_xC)	20
Ar, 450 °C		1.07	0.68	-	0.84	Fe^{2+}	80
Fe-BTC	4.2	0.26	0.02	24.4	1.45	Fe^{3+} (Fe_xC)	27
Ar, 450 °C		0.44	-	50.1	1.05	Fe^{3+} ($Fe_{1-x}O$ I)	13
		1.06	-	36.7	1.30	Fe^{2+} ($Fe_{1-x}O$ II)	26
		1.08	-1.40	39.9*	0.87	Fe^{2+} ($Fe_{1-x}O$ III)	27
		0.70	2.82	-	0.75	Fe^{2+}	7
Fe-BTC	300	0.01	-	-	0.90	Fe^{0} (SPM)	25
H_2, 400 °C		1.06	0.46	-	0.51	Fe^{2+}	75
Fe-BTC	4.2	0.01	-	34.5	0.40	Fe^{0}	24
H_2, 400 °C		0.56	-	51.1	0.75	Fe^{3+} ($Fe_{1-x}O$ I)	5
		0.98	-0.27	35.5*	1.07	Fe^{2+} ($Fe_{1-x}O$ II)	60
		0.95	3.35	-	1.22	Fe^{2+}	11
Fe-BTC	300	0.26	-	16.3	0.51	ϵ'-$Fe_{2.2}C$	49
H_2/CO=1, 340		0.85	0.84	-	0.94	Fe^{2+}	51

°C, 15 bar, 5 h							
Fe-BTC	4.2	0.23	0.10	18.5	0.49	ε'-$Fe_{2.2}C$	53
H_2/CO=1		0.23	-0.04	24.2	0.54	Fe^{3+} (Fe_xC)	7
340 °C,		0.54	-	51.2	0.75	Fe^{3+} ($Fe_{1-x}O$ I)	5
15 bar, 5 h		1.09	-0.68	35.6*	1.07	Fe^{2+} ($Fe_{1-x}O$ II)	35

Table A3.4 The Mössbauer fitted parameters of Fe-BTC sample treated at 450 °C.

Sample	*T (K)*	*IS ($mm \cdot s^{-1}$)*	*QS ($mm \cdot s^{-1}$)*	*Hyperfine field (T)*	*Γ ($mm \cdot s^{-1}$)*	*Phase*	*Spectral contribution (%)*
Fe-BTC	300	0.01	-	-	2.60	Fe^0 (SPM)	51
Ar, 600 °C		0.01	-	30.5	0.85	Fe^0	8
		0.18	-	-	1.02	Fe^{3+} (SPM Fe_xC)	33
		0.16	-	19.1	0.75	Fe^{3+} (Fe_xC)	8
Fe-BTC	4.2	0.01	-	34.5	0.47	Fe^0	75
Ar, 600 °C		0.19	-	23.9*	0.98	Fe^{3+} (Fe_xC)	25
Fe-BTC	300	0.23	0.05	-	1.49	Fe^{3+} (SPM Fe_xC)	69
H_2/CO=1		0.19	-	16.8*	0.36	Fe^{3+} (Fe_xC)	31
340 °C,							
15 bar, 5 h							
Fe-BTC	4.2	0.24	-	18.6	0.46	ε'-$Fe_{2.2}C$	27
H_2/CO=1		0.24	-	25.5	0.77	χ-Fe_5C_2 (I)	33
340 °C,		0.19	-	21.0	0.77	χ-Fe_5C_2 (II)	21
15 bar, 5 h		0.22	-	13.2	0.77	χ-Fe_5C_2 (III)	13
		0.14	0.92	-	0.37	Fe^{3+}	6

A3.2.2 Characterization of Fe@C catalysts

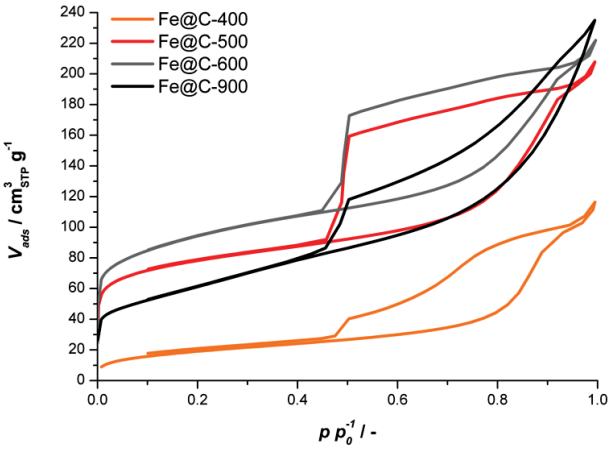

Figure A3.8 N_2 physisorption at 77 K of Fe@C catalysts degassed at 175 ˚C for 16 h displaying the formation of mesoporous carbon with varying porosity upon pyrolysis of the microporous Fe-BTC.

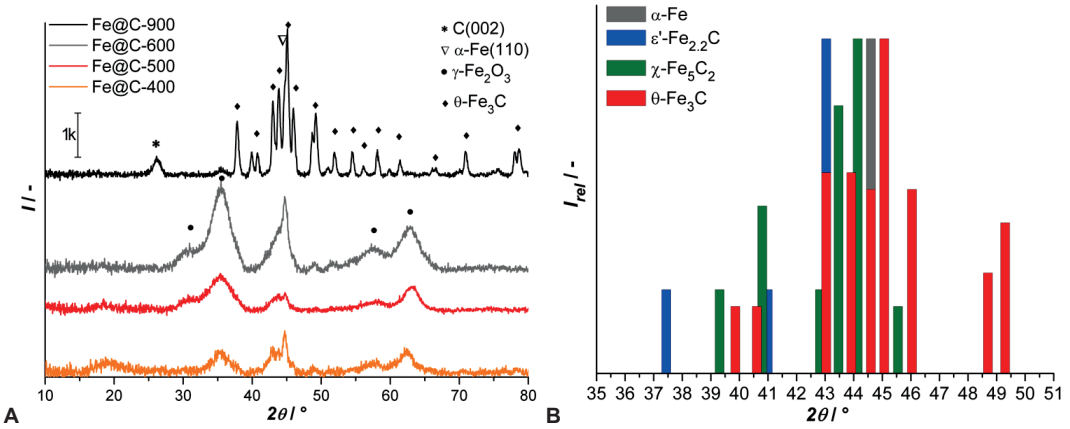

Figure A3.9 XRD of Fe@C catalysts after 2 h passivation in 5 vol% O_2 and prior to loading into FTS reactors, showing **A** the contributions of multiple Fe phases, and **B** the linear combination of theoretical diffraction intensities in the congested Fe-carbide region between 35-50˚.

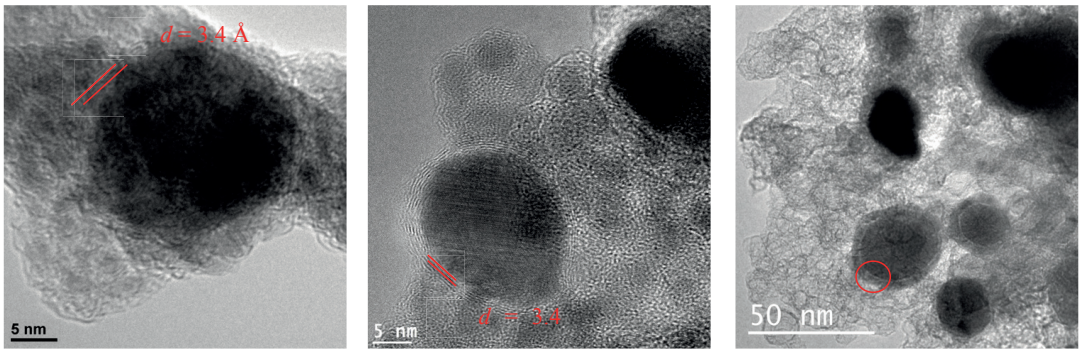

Figure A3.10 TEM images of agglomerates on (*from left to right*) Fe@C-400, Fe@C-500, and Fe@C-900 showing a graphitic shell (d = 3.4 Å) encapsulating the Fe nanoparticles, with a coarsening layer upon temperature increase.

A3.2.3 Catalytic performance of Fe@C catalysts

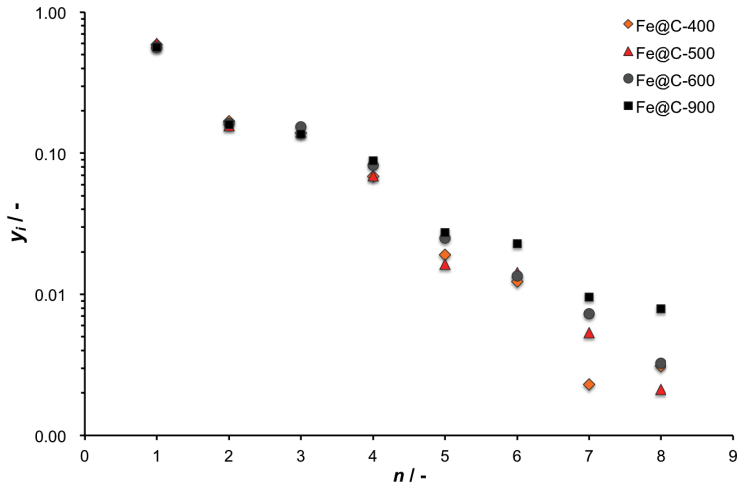

Figure A3.11 ASF plots for Fe@C-400, 500, 600, and 900 at 80 h *TOS* under HT-FTS conditions (T = 340 ˚C, P = 20 bar, CO/H_2 = 1, *GHSV* = 30,000 h^{-1}). The chain growth probability α (0.43-0.55) was calculated for the range C_3-C_8, indicative for low-α HTFT conditions.

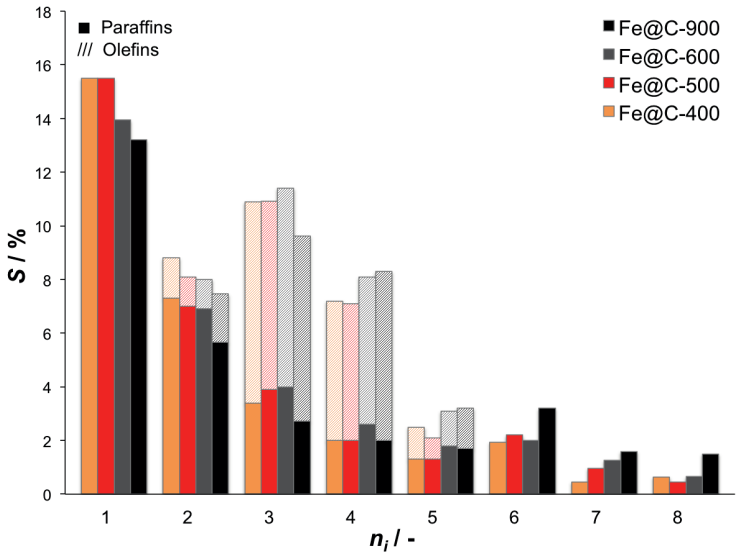

Figure A3.12 Product selectivity (*S*, carbon based) for Fe@C-400, 500, 600 and 900 at 80 h *TOS* under HTFT conditions (*T* = 340 ˚C, *P* = 20 bar, CO/H_2 = 1, *GHSV* = 30,000 h^{-1}) showing paraffins (*solid*) and olefins (*hatched*). Olefins and paraffins are not distinguished from C_6 onwards.

References

[1] Horcajada, P., Surble, S., Serre, C., Hong, D.-Y., Seo, Y.-K., Chang, J.-S., Greneche, J.-M., Margiolaki, I., Ferey, G., *Chem. Commun.*, (**2007**) 2820-2822.

[2] Klencsár, Z., *Nucl. Instrum. Methods Phys. Res., Sect. B*, 129 (**1997**) 527-533.

[3] Green, D.W., Perry, R.H., *Perry's Chemical Engineers' Handbook, Eighth Edition*, McGraw-Hill Professional, **2007**.

[4] Chojecki, A., Meima, G., Bashir, M., Khare, C., Ruitenbeek, M., High Throughput Campaign Fischer-Tropsch to Olefin. Part 1: Validation of the Experimental Setup. Catalytic Test Results over Fused Iron Catalysts, in, CRI-2011-777, Dow Chemical, Terneuzen, 2011.

[5] Edam, R., Mertens, V., Ribes, C., Beyer, S., Schmidt, E., Chojecki, A., Development of On-Line GC Method for High Throughput Fischer-Tropsch to Olefins Campaign, in, CRI-2010-1011, Dow Chemical, Terneuzen, 2010.

Chapter

4

Structural and elemental influence from various MOFs on the performance of Fe@C catalysts for Fischer-Tropsch synthesis

The structure and elementary composition of various commercial Fe-based MOFs used as precursors for Fischer-Tropsch synthesis (FTS) catalysts have a large influence on the high-temperature FTS activity and selectivity of the resulting Fe on carbon composites. The selected Fe-MOF topologies (MIL-68, MIL-88A, MIL-100, MIL-101, MIL-127, and Fe-BTC) differ from each other in terms of porosity, surface area, Fe and heteroatom content, crystal density and thermal stability. They are reengineered towards FTS catalysts by means of a simple pyrolysis at 500 °C under N_2 atmosphere and afterward characterized in terms of porosity, crystallite phase, bulk and surface Fe content, Fe nanoparticle size and oxidation state. The Fe loading (36-46 wt%) and nanoparticle size (3.6-6.8 nm) of the obtained catalysts are directly related to the elementary composition and porosity of the initial MOFs. Furthermore, the carbonization leads to similar surface areas for the C matrix (S_{BET} between 570-670 $m^2\ g^{-1}$), whereas the pore width distribution is completely different for the various MOFs. The high catalytic performance (*FTY* in the range of $1.9\text{-}4.6 \cdot 10^{-4}$ $mol_{CO}\ g^{-1}_{Fe}\ s^{-1}$) of the resulting materials could be correlated to the Fe particle size and corresponding surface area, and only minor deactivation was found for the N-containing catalysts. Elemental analysis of the catalysts containing deliberately added promotors and inherent impurities from the commercial MOFs revealed the subtle interplay between Fe particle size and complex catalyst composition in order to obtain high activity and stability next to a low CH_4 selectivity.

This chapter is based on the following publication:

T.A. Wezendonk, Q.S.E. Warringa, V.P. Santos, A. Chojecki, M. Ruitenbeek, G. Meima, M. Makkee, F. Kapteijn and J. Gascon ***Faraday Discuss.***, 2017, 197, 225-242.

4.1 Introduction

Fischer-Tropsch synthesis (FTS) is a process that catalytically converts syngas, a mixture of CO and H_2, towards longer chain hydrocarbon products such as gasoline, diesel and plastics precursors. The FTS process was designed nearly a century ago to cope with the limitations in petroleum feedstock, allowing the production of fuels and chemicals from coal, natural gas and biomass [1, 2]. Currently, several large plants worldwide operate the FTS process through syngas obtained from steam methane reforming or coal gasification [3-6]. Fast-growing worldwide energy consumption and conventional oil reserve challenges provide a continuous drive to develop improved catalysts for the FTS process.

Since a few years, metal-organic frameworks (MOFs) have emerged from the deep waters of scientific research and have been proposed increasingly as heterogeneous catalysts for many applications, such as Knoevenagel condensation, “click” chemistry, selective hydrogenations, Friedländer coupling, electrocatalysis and photocatalysis [7]. However, it was recently demonstrated that MOFs are not only potent catalysts in their final form, but they also serve the purpose as excellent precursors for high-temperature Fischer-Tropsch (HTFT) catalysts [8]. The concept of the synthesis technique is a simple pyrolysis, heat treatment in an inert atmosphere, which carbonizes the MOF towards embedded metal nanoparticles in a porous C matrix (M@C). The resulting nanoparticle-carbon composites possess outstanding properties for application in electrodes, electrocatalysts and H_2/CO_2 adsorbents [9-13]; these materials amongst many others have been comprehensively reviewed [14]. Recent investigations into MOF-derived catalysts for FTS by the group of Wang confirmed the high potential of the Fe@C system using the MIL-88B topology as catalyst precursor [15]. Recently, an in-depth study of the nature of the Fe species during pyrolysis and subsequent FTS reaction was reported by our group, elucidating the carbonization mechanism of the commercial Fe-BTC MOF with the MIL-100 topology [16]. *In situ* DRIFTS-MS and XAS applied during the pyrolysis process revealed the decarboxylation of the framework and auto-reduction of the Fe^{3+} species towards active Fe carbide. *In situ* Mössbauer emission spectroscopy and HR-TEM allowed for the correlation of the pyrolysis temperature and the Fe nanoparticle size and showed the evolution of the Hägg carbide phase depending on the particle size as the FTS reaction progressed.

Herein, the relation between MOF topology and the activity and selectivity under HTFT are determined in order to optimize the Fe@C catalyst. By systematically varying the structure and elemental composition prior to pyrolysis, understanding is gained into the transformation of the framework towards an active Fe@C catalyst. The commercially available Fe-MOFs selected in this study (MIL-68, MIL-88A, MIL-100, MIL-127, MIL-101-NH_2 and Fe-BTC) comprise carboxylate linkers that differ both in size and connectivity, in addition to heteroatoms such as N. Therefore, the MOFs show large differences in porosity, thermal stability and heteroatom content, summarized in **Table 4.1** and **Figure 4.1**. The size of the biggest voids within these structures ranges from 6 to 34 Å with

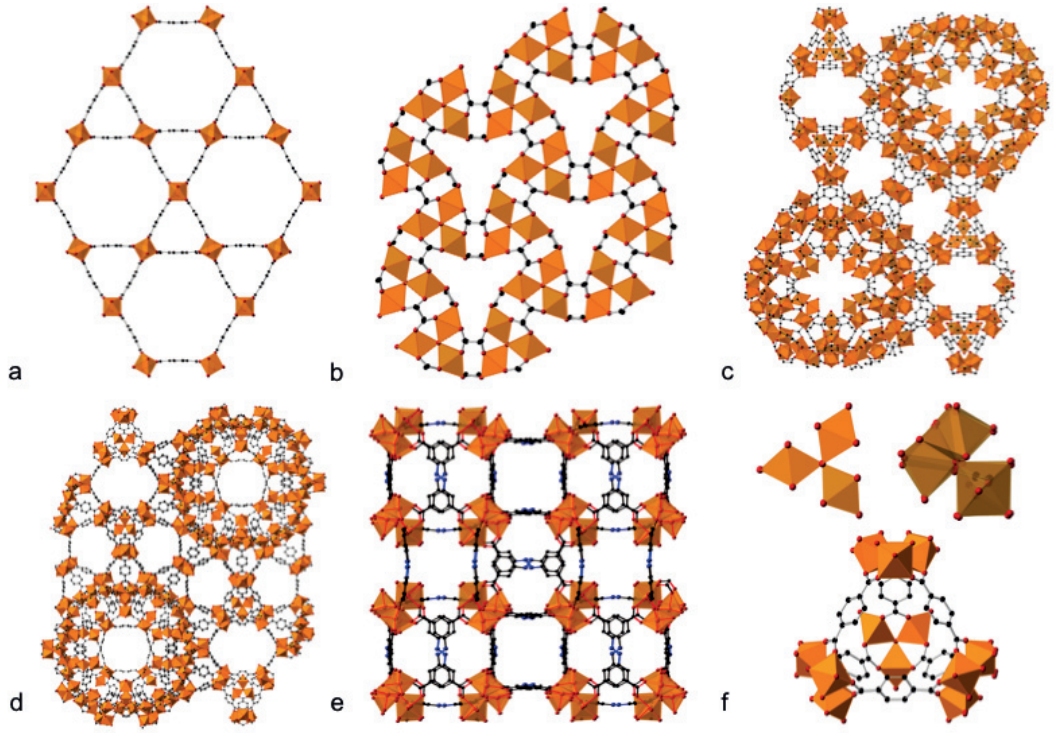

Figure 4.1 Selected Fe-MOF topologies: a) MIL-68 b) MIL-88A C) MIL-100 d) MIL-101 e) MIL-127 and f) the configuration of Fe trimers and super tetrahedra present in the different structures.

Table 4.1 Fe-MOF properties taken from reported literature studies [17-31], comprising BET area (S_{BET}), Fe loading (w_{Fe}), calculated crystal density (ρ_{crys}), pore diameter (d_{pore}) and decomposition temperature in air (T_d).

Fe-based MOF	S_{BET} $m^2\ g^{-1}$	w_{Fe} %	ρ_{crys} $g\ cm^{-3}$	d_{pore} Å	T_d °C
MIL-68	355	23.6	0.87	6-16	290
MIL-88A	40	26.2	1.55	6	195
MIL-100	2150	25.8	0.69	25-29	300
MIL-101-NH_2	4100	22.5	0.62	29-34	320
MIL-127	1400	21.3	0.97	6-10	360
F300 Fe-BTC	1040	25	na	22	295

corresponding BET areas between 40-4100 m^2 g^{-1}. The thermal stability in air, depending on the strength of the metal-ligand interaction, varies between 200-360 ˚C. The use of commercial MOFs is a deliberate choice, as to promote a route toward industrial catalyst manufacturing. Several MOF producers exist nowadays (e.g. MOF Technologies, NuMat Technologies, theMOFcompany, all spin-off companies from academia [32-35]), each using different manufacturing technologies, bearing an aspect that is to be investigated. Prices of MOFs are expected to come down and more focus on industrial scale production increases the chances on industrial implementation of MOFs.

4.2 Experimental

4.2.1 Synthesis

The Fe-based MOFs used in this research were commercially acquired from BASF (Basolite F300®) and from MOFTECH (MIL-68, MIL-88A, MIL-100, MIL-101-NH_2 and MIL-127). They were used without further purification in both the pyrolysis and characterization. Pyrolysis of the MOFs was performed in a quartz tubular reactor (*L* = 1.0 m x ID = 5.0 cm) located horizontally in a ceramic fiber oven (Carbolite, Sheffield) where between 50-100 mg of the MOF was placed in a ceramic crucible and subjected to heat treatment in a nitrogen atmosphere (150 cm^3 min^{-1}_{STP}, gas hourly space velocity 4.5 h^{-1}). The pyrolysis temperature was fixed at 500 ˚C, the ramp rate and dwell time were set to 2 ˚C min^{-1} and 8 h, respectively. Before exposure to ambient conditions each material was passivated at room temperature using a stream of 5 vol% O_2 in N_2 for 2 h. The synthesized catalysts are denoted herein as “Fe@C-X”, with X representing the MOF used as catalyst precursor. Incipient wetness impregnation (IWI) was carried out with a 50:50 vol% methanol/water solution in which K_2CO_3 was dissolved. The amount dissolved is determined by the iron loading of the sample with molar ratio K/Fe = 0.0226, aiming at 0.6 wt% of K loading. The IWI volume used is 1.0 cm^3 g^{-1} and is pipetted onto the sample. After careful mixing, the sample is put in an ultrasonic bath for 90 min and dried in N_2 atmosphere for 4 h at 250 ˚C. K-promoted samples are denoted as KFe@C-X, where K is added to distinguish the promoted samples.

4.2.2 Characterization

Thermogravimetric analysis (TGA) was performed on a Mettler Toledo TGA/SDTA1 with sample robot (TSO 801RO) and gas control (TSO 800GC1). The temperature was linearly increased from 25 to 1000 ˚C at a heating rate of 5 ˚C min^{-1} under air flow. The Fe loading of the carbon-matrix catalysts was calculated using the Fe_2O_3 phase residual mass.

Powder X-ray diffraction (PXRD) was performed with a Bruker D8 Advance diffractometer in Bragg-Brentano geometry with Co *Kα* radiation and a Lynxeye position sensitive detector. The slit used was

a Divergence slit V12. The scatter screen height was 5 mm with 45 kV at 40 mA. Data was analysed by Bruker software Diffrac.EVA version 4.0.

N_2-physisorption was performed on a Micromeritics Tristar II at 77 K to determine the textural properties of compounds. All samples were evacuated at 175 ˚C for 16 h prior to measurement. Data analysis was performed with Microactive software V3.00. The BET area was determined by direct fitting of points in the P/P_0 = 0.05-0.15 domain, constraining the upper boundary of the relative pressure window using the two-point BET method [36]. Total pore volume was measured at P/P_0 = 0.95 where no inter-particle condensation occurred, the external surface area and microporous volume were determined by the *t*-method, obtaining a linear fit in the De Boer thickness of at least 10 data points.

Elemental analysis was carried out with inductively coupled plasma optical emission spectroscopy (ICP-OES) instrumentation. First, samples underwent destruction in a closed flask under high temperature and pressure. C was measured with a CHNOS-Analyzer from Elementar; Fe has been measured after an acidic destruction with an Analyst 200 AAS from Perkin Elmer. About 5 mg of sample was used per element measured.

X-ray photoelectron spectroscopy (XPS) measurements were performed on a K-alpha Thermo Fisher Scientific spectrometer using a monochromated Al *Kα* X-ray source. The measurements were carried out using point analysis with auto-height signal optimization, with each point having a spot size of 300 micron at ambient temperature and chamber pressure of about 10^{-8} mbar. A flood gun was used for charge compensation. All the spectra measured were corrected by setting the reference binding energy of C*1s* at 284.8 ± 0.025 eV. The electron energy analyzer was operated with pass energy of 200 eV and 0.25 eV energy spacing for the survey spectrum, and pass energy of 50 eV and 0.1 eV energy spacing for the high-resolution spectrum was used. Each spectrum reported is the statistic average of 10 measured scans. The spectra were analyzed and processed using Thermo Avantage v5.903 software (Thermo Fisher Scientific). Smart background subtraction, derived from the Shirley background, was used over the peak width. By applying full width integration over the core-level signals and using tabulated atomic sensitivity factors (ASF), relative atomic contributions on the surface were calculated.

Scanning electron microscope (SEM) images and energy dispersive X-ray (EDX) spectra of the samples were recorded by a JEOL JSM-7500F field emission scanning electron microscope equipped with a Noran System Six spectral imaging system and a 30mm^2 Novar detector. For SEM, an acceleration of 5 kV was used with a spot size of 20-50 nm. For EDX, the acceleration was increased to 20 kV and scanning times of 5 min are used to determine chemical composition. Elemental mapping was performed with similar settings employing a mapping time of approximately 15 min.

High-resolution transmission electron micrographs (HRTEM) were collected on a JEOL model JEM-2010 working at 200 kV with a LaB_6 filament. It reaches a resolution between layers of 0.14 nm and between points of 0.25 nm. It is equipped with an Orius 831 camera from Gatan. Ethanol suspensions containing the samples were deposited onto a Au grid covered with lacey carbon and left to dry in air prior to measuring.

4.2.1 Catalytic testing

The catalyst performance tests were conducted in the high-pressure reactor assembly module-I (HPRAM-I) system at the Dow Chemical Company. It consists of 48 reactors that can be operated simultaneously at various process conditions, gas feed systems, exit modules with flow splitters, and gas chromatograph analyzers (Siemens Maxum-II). For activity testing, ~10 mg (20 mm^3) of fresh catalyst with the particle size of 177–420 μm was diluted with 100 mm^3 SiC particles of similar size range. First, samples were activated *in situ* in a 90/10 vol% H_2/He mixture at 425 ˚C for 3 h under 3 bar followed by cooling to 340 ˚C under N_2 flow at the same pressure. After increasing the pressure to the process set point of 20 bar, a 10 cm^3 min^{-1}_{STP} flow consisting of CO 45 vol%, H_2 45 vol% and He 10 vol% was introduced. These operating conditions are hereby referred to as high-temperature Fischer-Tropsch (HTFT) conditions. Catalytic activity is expressed as Fe time yield (*FTY*), defined as the number of moles of CO converted to hydrocarbons per gram of Fe per second, and as area time yield (*ATY*), moles of CO converted to hydrocarbons per surface area of Fe particles per second. CO conversion and carbon selectivity are defined by **Equations 4.1 and 4.2**, respectively, where X_{CO} stands for CO conversion, *F* indicates the molar flow, *S* is the carbon selectivity towards a product with *n* carbon atoms and *y* is the molar fraction of a hydrocarbon C*n*.

$$X_{CO} = \left(1 - \frac{C_{He,d,R} \cdot C_{CO,d,R}}{C_{He,d,blk} \cdot C_{CO,d,blk}}\right) \qquad \textbf{4.1}$$

where $C_{He,d,blk}$, $C_{He,d,R}$, $C_{CO,d,blk}$, $C_{CO,d,R}$ are the concentrations determined by GC analysis of He in the blank, He in the diluted reactor effluent, CO in the blank, and CO in the diluted reactor effluent, respectively.

$$S_{Cn} = \frac{n \cdot \left(\frac{C_{Cn,d,R}}{C_{He,d,R}}\right)}{\left(\frac{C_{CO,d,blk}}{C_{He,d,blk}} - \frac{C_{CO,d,R}}{C_{He,d,R}}\right)} \qquad \textbf{4.2}$$

where $C_{Cn,d,R}$ is the concentration the diluted reactor effluent determined be GC analysis of a product with *n* carbon atoms.

4.3 Results

4.3.1 Characterization of MOF precursors

N_2 physisorption at 77 K, TGA and XRD confirmed the presence of MIL-68 [19, 26, 29], MIL-88A [24, 25, 30], MIL-100 [21, 22, 27], MIL-101 [17, 20, 31], and MIL-127 [18, 23, 28] (**Table A4.1, Figure A4.1 and Figure A4.2**). XRD of the F300 Fe-BTC MOF revealed a very low degree of crystallinity, but the MIL-100 topology was confirmed since the isotherm contained an additional step in the micropore regime corresponding to the large cages in the MTN-type framework [21, 22]. This behaviour was more pronounced in the MIL-100 sample, and values for porosity exceeded the F300 as well. As reported, MIL-88A heavily contracts upon degassing and thus, a near-zero N_2 uptake was found [24, 29]. In general, no significant deviation from literature values was found.

4.3.2 Characterization of Fe@C catalysts

4.3.2.1 Texture of C matrix and crystalline Fe phases

N_2 physisorption at 77 K of the Fe@C materials showed highly microporous catalysts with significant contributions of mesopores and external surface area (**Table 4.2 and Figure 4.2A**). To estimate the porosity of the C matrix, these values were normalized on the C content correcting for the Fe mass assuming a Fe_2O_3 phase (**Table 4.2**). The resulting BET areas are closely aligned, with the lowest value of 570 $m^2\ g^{-1}$ for the low-crystalline starting MOF Fe-BTC. It is clear that the coordinated solvent molecules located in the intra-framework sites (MIL-68, MIL-88A) are released during the carbonization, liberating the MOF porosity. In the specific case of MIL-88A, which is not porous prior to pyrolysis, the pore volume is increased to 0.47 $cm^3\ g^{-1}$ of C matrix with corresponding BET area of 655 $m^2\ g^{-1}$. This is an impressive result, especially keeping in mind that these values are one third of carbonized ZIF-8 at 800 ˚C [10]. Although values derived from the BJH pore size distribution have to be taken as merely qualitative, clear trends can be obtained from this analysis (**Figure A4.3**). The MIL-68 derived material, Fe@C-MIL68, contains most of its pore volume in large meso-macropores of around 50 nm in size, whereas for the Fe@C-MIL100 and -127 well-defined mesopores exist in a narrow distribution between 10-20 nm in addition to the micropores. XRD results demonstrated that nanocrystalline Fe oxides (γ-Fe_2O_3) were formed for Fe@C-MIL68, -88, -100 and -F300 after passivation of the material (**Figure 4.2B**). However, the diffraction pattern of Fe@C-MIL127 revealed the presence of a single Fe carbide phase (cementite), without Fe oxide phases present. MIL-127 possesses the lowest amount of Fe, although the C/Fe ratio is similar to that of MIL-68 and MIL-$101NH_2$, suggesting that either the N functionality or the high decomposition temperature play a role in the carburization of Fe during pyrolysis.

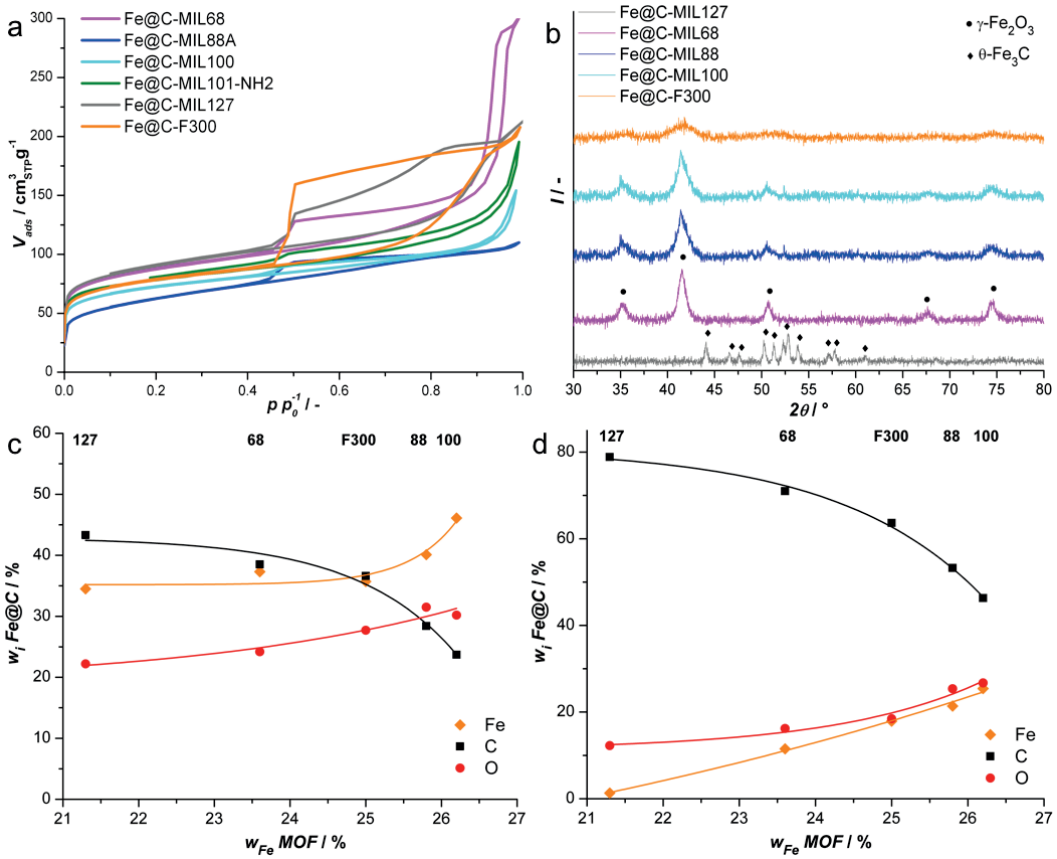

Figure 4.2 A Nitrogen uptake at 77 K per gram of Fe@C catalyst and **B** XRD of the Fe@C catalysts, indicating the presence of nanosized γ-Fe_2O_3 and θ-Fe_3C phases present after passivation **C** Bulk and **D** surface Fe@C catalyst composition as function of Fe loading of parent MOF calculated from ICP and XPS, respectively.

4.3.2.2 Bulk and surface Fe loading

TGA and ICP analyses were performed to determine the bulk Fe loading of the pyrolyzed MOFs, establishing values between 36-46 wt% of Fe (**Table 4.2 and Figure A4.4**). Both techniques suggest a nonlinear relation between the Fe loading of Fe@C and initial Fe-MOF loading. Only Fe@C-MIL100 shows an unexpectedly large deviation between TGA and ICP results, indicating that non-C impurities can be present. Elemental analysis of Fe and C allowed for the calculation of the remainder phase, assumed as O (**Figure 4.2C**). By accounting for the Fe loading and associated O content as Fe_2O_3, the C/O ratio of the matrix was calculated in order to estimate the degree of carbonization (**Table 4.2**). Remarkably, for all the different MOFs, except for MIL-127, the mass balance of the leaving groups is CO_2 + $(H_2)O$, indicating a very similar degree of carbonization. On

the other hand, the decomposition mass balance for MIL-127 suggests the release of only 2 (H_2)O and no CO_2 upon carbonization, thus confirming the higher C content in this particular pyrolyzed MOF. Furthermore, the C/O/N ratio suggests that either the N=N bond is maintained, or scission followed by incorporation into the C has taken place. XPS analysis showed that the encapsulation of Fe by the C matrix varied greatly between 45-96% (**Figure 4.2D**) and that the Fe content at the exposed Fe@C surface is a linear function of the Fe loading of the MOF. Interestingly, the surface of Fe@C-MIL127 consists almost exclusively of N-functionalized C, with only 1.3 wt% Fe on the surface. Fe@C-MIL100 and -F300 contain nearly the same fraction of Fe on the surface, in addition to a very similar bulk Fe loading.

4.3.2.3 Fe oxidation state and C matrix functionalization

Fe core-level XPS spectra illustrated that the Fe surface consists mainly of Fe_2O_3, as witnessed by the binding energy of 710.9 eV for the $2p_{3/2}$ peak and multiplet splitting with satellite features due to the high spin Fe^{3+} phase (**Figure A4.5A**) [37]. These findings indicate that the θ-Fe_3C phase of Fe@C-MIL127 is covered by a protective oxide layer, most likely formed during the passivation of the sample, implying that the Fe surface is at least partially accessible. The XPS survey spectra were used to calculate the degree of O-functionalization of the C surface by accounting for the Fe loading and accompanied O content (**Figure 4.2D and Figure A4.5B**). The catalysts are divided into high- and low degree of O- functionalized carbons, with Fe@C-MIL88 and -100 containing between 23 and 26 O atoms per 100 C atoms, and Fe@C-MIL68, -127 and -F300 only 11 to 13 O atoms per 100 C atoms. Additionally, the surface of the C matrix of Fe@C-MIL127 was found to contain 9 N atoms per 100 C atoms, and 3 contributions could be distinguished from the N core-level spectra. The binding energies of the peaks are located at 398.7, 399.4 and 400.4 eV, demonstrating the presence pyrrolic, pyridinc and graphitic N species [38, 39]. The surface N content was even higher in comparison to the bulk value, 7.1 wt% versus 5.6 wt%, respectively. Furthermore, the survey spectra exposed the

Table 4.2 Fe@C properties determined by ICP (Fe loading, w_{Fe} and O-functionalization of C, C/O), XPS (Fe surface/bulk ratio *Fe/Fe S/B*), N_2-physisorption (BET area, S_{BET}) and HR-TEM (average particle diameter, d_{Fe}).

Catalyst	S_{BET}	w_{Fe}	*C/O* (bulk)	*Fe/Fe (S/B)*	d_{Fe}
	$m^2\ g^{-1}{}_C$	%	-	%	nm
Fe@C-MIL68	675	37.3	6.9	31	6.8
Fe@C-MIL88A	655	46.1	3.3	55	5.9
Fe@C-MIL100	610	38.1	2.8	53	4.2
Fe@C-MIL101NH_2	635	39.8	na	na	4.2
Fe@C-MIL127	585	34.5	3.9-0.5N	4	4.3
Fe@C-F300	570	35.7	4.2	50	3.6

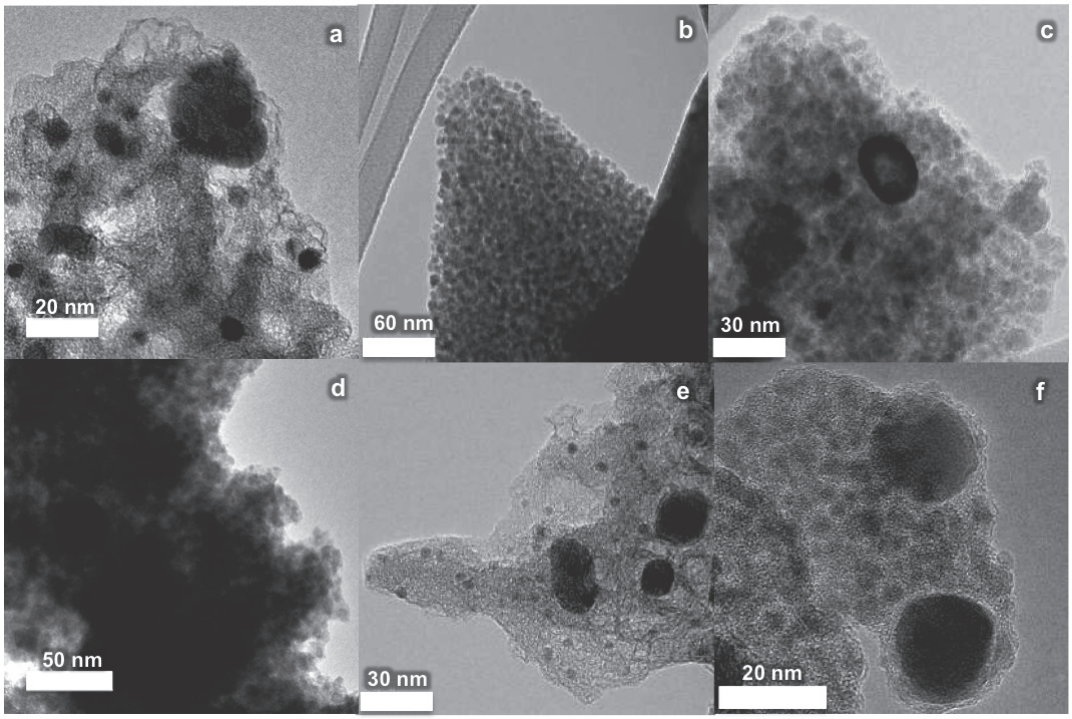

Figure 4.3 TEM images of **A** Fe@C-MIL68, **B** Fe@C-MIL88, **C** Fe@C-MIL100, **D** Fe@C-MIL101NH_2, **E** Fe@C-MIL127 and **F** Fe@C-F300. Small Fe nanoparticles (medium contrast spheres) can be distinguished from the carbonaceous matrix (higher transmission), and are often accompanied by a number of agglomerates (large spheres). The high dispersion is still visible in larger fragments where several layers of particles overlap.

presence of impurities in addition to the expected Fe, C, O and N contributions. Additional N signals were obtained from the spectra of Fe@C-MIL68 and -100, but were below 0.5 wt%. Both Fe@C-MIL88 and -127 contained significant amounts of Cl (1.5 and 1.0 wt%, resp.), possibly originating from the $FeCl_3$ reactant in the synthesis process. Fe@C-MIL100 contained a large amount of Cr and Mo surface impurities (both 2.8 wt%), which explains the large deviation between the Fe loading obtained from ICP and that calculated from TGA analysis (~7 wt%). The higher bulk content of these metal impurities suggests that they are not encapsulated by C, affirming the origin of the impurities in the MOF synthesis.

4.3.2.4 Morphology and Fe particle size

SEM analysis illustrates the conservation of the MOF morphology after pyrolysis, showing large differences in the crystallinity and grain size (**Figure A4.6**). However, the maximum size of the crystallites did not exceed a few micrometer, and thus no diffusion limitations are expected in the HTFT performance of the various Fe@C catalysts. TEM images (**Figure 4.3 and Figure A4.7**) were

analysed to calculate the average Fe nanoparticle size (**Table 4.2**) and to generate particle size distributions (PSD) of the Fe@C catalysts (**Figure A4.8**). The average particle size, excluding the agglomerate fraction, was estimated between 3.6-6.8 nm. The PSDs show that the majority of the particles are below 10 nm, implying a homogeneous carbonization of the framework towards the embedded Fe@C system. No dependence of the Fe loading on the Fe particle size exists, much contrary to conventional catalyst synthesis routes.

4.3.2.5 K-promotion of Fe@C catalysts

Elemental analysis confirmed that the targeted promotor loading of 0.6 wt% K was obtained for the Fe@C catalysts values varying from 0.53 to 0.59 wt%. EDX mapping confirmed the high dispersion of the promotor throughout the bulk phase of the catalysts. K*2p* core-level contributions were confirmed in the tail of the C*1s* core-level XPS spectra.

4.3.3 Catalytic Testing of Fe@C catalysts

4.3.3.1 Unpromoted Fe@C catalyst performance

Previous results had shown improved activity and product selectivity for K-promoted Fe@C catalysts [8], however, three unpromoted samples were tested in HTFT as well; Fe@C-MIL88, -101NH_2 and -F300 (**Figure 4.4 and Table 4.3**). Although Fe@C-MIL101NH_2 showed the highest activity after 20 h (X_{CO} = 72.6%), a linear deactivation rate resulted in the lowest CO conversion after 80 h. Fe@C-MIL88 and -F300 displayed an activation period over 50 h after which the CO conversion levels

Table 4.3 Catalytic performance of unpromoted and K-promoted Fe@C catalysts. Reactions were carried out at 340 ˚C, 20 bar, H_2/CO = 1 and employing a space velocity of 15 $cm^3_{syngas}\ g^{-1}_{cat}\ s^{-1}$. Product analysis of the unpromoted and promoted catalysts was carried out at steady state conversion after 80 h time on stream (*TOS*).

Catalyst	X_{CO}	*FTY*	S_{CH4}	S_{CO2}	α
	%	$10^{-4}\ mol_{CO}\ g^{-1}_{Fe}\ s^{-1}$	%	%	-
Fe@C-MIL88	66	2.59	11.6	46	0.54
Fe@C-MIL101NH_2	65	2.90	17.2	47	0.43
Fe@C-F300	76	3.73	14.0	47	0.48
KFe@C-MIL68	41.1	1.86	9.4	55	0.60
KFe@C-MIL88A	71.3	2.62	12.7	49	0.58
KFe@C-MIL100	94.9	4.23	10.0	47	0.56
KFe@C-MIL127	89.5	4.46	15.0	49	0.65
KFe@C-F300	91.7	4.59	7.8	47	0.59

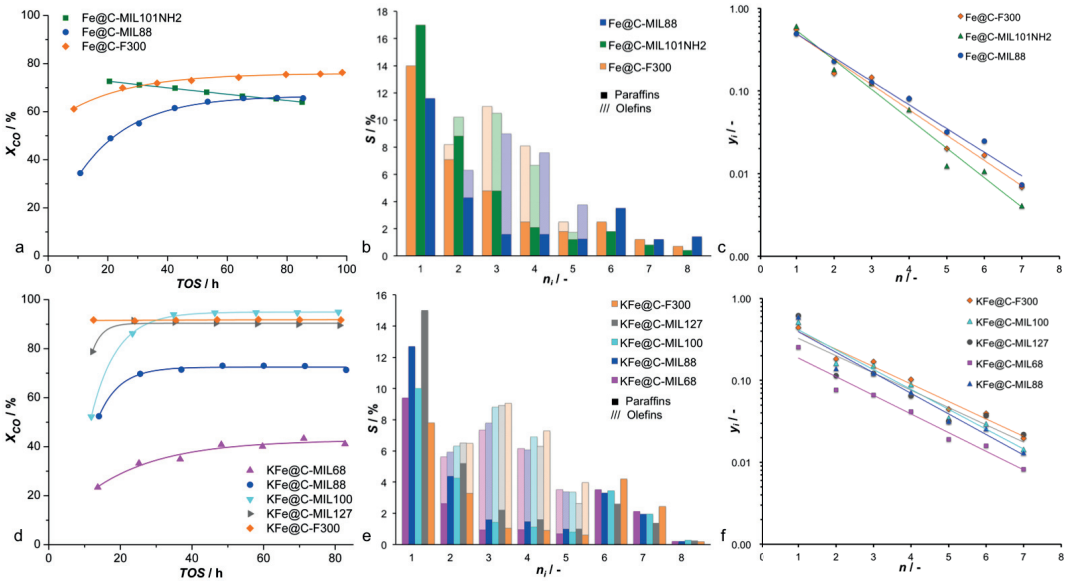

Figure 4.4 HTFT performance of **A-C** unpromoted and **D-F** K-promoted Fe@C catalysts, displaying CO conversion levels versus time on stream, C-based selectivity with product distributions and Anderson-Schulz-Flory plots to assess the chain growth probability. Reactions were carried out at 340 ˚C, 20 bar, H_2/CO = 1 and employing a space velocity of 15 $cm^3_{syngas}\ g^{-1}_{cat}\ s^{-1}$. Product analysis of the unpromoted and promoted catalysts was carried out at steady state conversion after 80 h time on stream (*TOS*). Paraffin and olefin selectivity is lumped from C_6 onward.

stabilized. Fe@C-MIL88 exhibited lower CH_4 selectivity levels than Fe@C-F300, whereas Fe@C-MIL101NH_2 reached a value over 17%. This catalyst additionally produced the lowest O/P ratios over the entire product slate, combined with the lowest value for the chain growth probability (α = 0.43). These results are indicative of increased hydrogenation, possibly by enhanced readsorption of unsaturated hydrocarbons by the N-functionalized C. The enhanced hydrogenation might also explain the significant deactivation, as CO methanation is far more exothermic than Fischer-Tropsch ASF-type hydrocarbon production (ΔH_f^0 = -247 kJ/mol_{CO} *vs* -177 kJ/mol_{CO} for α = 0.5, resp. [40, 41]). Fe@C-MIL88 displayed the highest α-value of 0.54, while Fe@C-F300 obtained the highest activity of $3.78 \cdot 10^{-4}$ $mol_{CO}\ g^{-1}_{Fe}\ s^{-1}$.

4.3.3.2 K-promoted Fe@C catalyst performance

In general, and in good agreement with the literature [42, 43], the potassium promotion of the catalysts resulted in a significant increase in CO conversion, decrease in methane selectivity, increased O/P ratios and higher values for α in the HTFT experiments (**Figure 4.4 and Table 4.3**). However, large differences in the CO conversion levels for the different KFe@C catalysts are

observed, as KFe@C-MIL68 and -88 convert significantly less CO and consequently, their *FTY* values are the lowest. KFe@C-MIL100 and -F300 display very similar CO conversion and *FTY*, though KFe@C-MIL100 exhibits slightly higher methane selectivity. The activation periods of KFe@C vary between 0 to 50 h, with a trend toward longer activation for the catalysts with lower activity. Again, the catalyst with N- functionalization exhibits deactivation, however, to a much smaller extent compared to the unpromoted Fe@C-MIL101NH_2 (1.9% vs 8.9%). Remarkably, the KFe@C-MIL127 catalyst shows the highest methane selectivity combined with the highest value for alpha, implying some deviation from ideal ASF behaviour and suggesting the presence of Fe sites with enhanced hydrogenation activity. KFe@C-F300 combines the highest *FTY* with the lowest CH_4 selectivity while operating at very high conversion levels, indicating its performance does not suffer from higher local hydrogen concentrations due to limiting CO reactant depletion or diffusion limitations.

4.4 Discussion

4.4.1 Characterization of Fe@C catalysts

Key in this work was examining the influence of the MOFs on the Fe@C formation in terms of the C matrix properties and Fe nanoparticle size, as it would allow for the formulation of structure-activity relations to the Fischer-Tropsch synthesis. The porosity and surface area are very similar when transforming the values to per gram of C matrix. These results indicate a comparable pyrolysis behaviour, implying that the framework in itself does not have an effect on the resulting porosity, and that other factors like temperature and duration of pyrolysis influence the properties of the C matrix. These claims are supported by the limited porosity and surface area by pyrolysis of MIL-88A for just 1 h, obtaining a BET area of 115 m^2 g^{-1}, only half of the value reported in this work [44]. The similar pyrolysis behaviour for the Fe@C catalysts was confirmed by analysing the degree of carbonization, calculated from C/O ratios of the C matrix, indicating one molecule of CO_2 is removed from the framework next to an additional O molecule, assumed to be in the form of a water molecule. In previous work, it was shown that the structure collapse by initial decarboxylation is followed by carboxylate side reactions, supposedly forming anhydride species as intermediates towards more graphite-like structures [16]. Additionally, higher C/O ratios were found on the surface than in the bulk, suggesting that surface C is more prone to releasing O from its structure. The presence of graphitic shells on the surface of the Fe nanoparticles, witnessed in HR-TEM, suggest that Fe plays an important role in the carbonization process by scavenging O from the C matrix. Such C morphology control and graphitization have been illustrated previously in Fe-MOF pyrolysis [45]. These generalizations seem valid for Fe carboxylates, but extrapolation to non-carboxylate MOF with different metal-ligand interaction is speculative. The average Fe nanoparticle size obtained from the Fe-MOF pyrolysis is not a function of the Fe loading, but seems to be related to the structure and porosity of the original MOF precursor. A trend towards smaller Fe nanoparticles is visible with

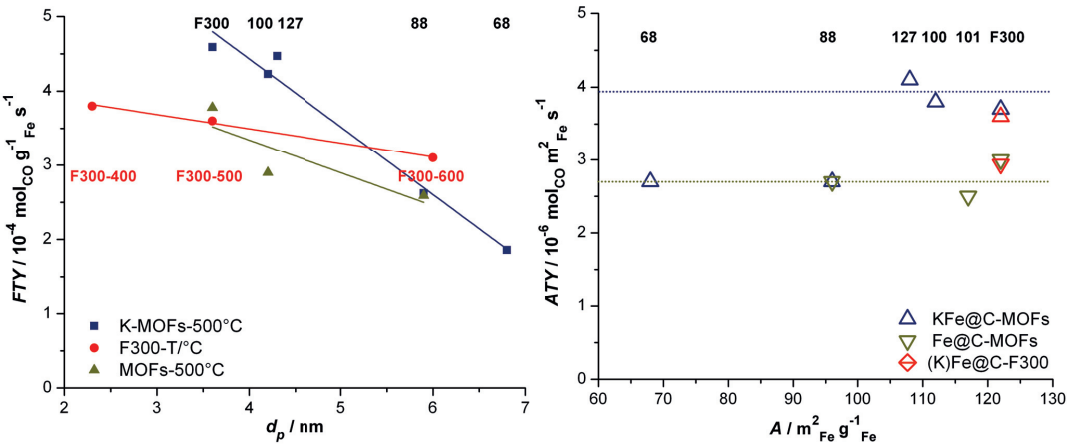

Figure 4.5 A Correlation between Fe nanoparticle size and catalytic activity normalized for the Fe mass (*FTY),* including data from Fe@C-F300 synthesized at different temperatures [16] and **B** catalytic activity normalized for the Fe surface area (*ATY*) of several Fe@C catalysts [8].

increasing pore volume and surface area (**Figure A4.9**). Shorter nearest-neighbour distances of Fe clusters may very well play a role in the formation of larger Fe nanoparticles, as is clearly observed for the highly contracted and non-porous MIL-88A, having an average nanoparticle size of 5.9 nm. An additional factor at play is the decomposition temperature, being the lowest for MIL-68 and -88A, forming the largest Fe nanoparticles.

4.4.2 Catalytic testing of Fe@C catalysts

The activity of Fe@C catalysts displayed a linear dependence to the size of the Fe nanoparticles (**Figure 4.5A**). For the unpromoted samples, the particle size effect on the activity was less pronounced than for the promoted samples, in line with previously reported *FTY* values for a similar range of particle sizes produced by pyrolysis of F300 Fe-BTC at different temperatures [16]. These findings indicate that particle size is the key factor in Fe@C catalyst design, and this effect is even more pronounced in the K-promoted samples. The surface specific activity, or area time yield (*ATY*), provides clearer insight into the relative catalytic activity of the different samples. All unpromoted Fe@C show similar performance, whereas higher *ATY* are obtained for the promoted catalysts (**Figure 4.5B**). The exceptions to this trend are the KFe@C-MIL68 and -88, which display *ATY* similar to that of unpromoted catalysts. From these results, together with the identical *O/P* ratios (C_3-C_4 = 0.8 and C_5 = 0.7 for both) and even slightly higher methane selectivity than that observed for the unpromoted Fe@C-MIL88, it is concluded that K promotion in these samples is not effective as in the other cases. Furthermore, we suspect that the lower Fe surface area of KFe@C-MIL68 results in K overpromotion, giving rise to some CO disproportionation (S_{CO2} = 55%) [46]. In general, the alkali

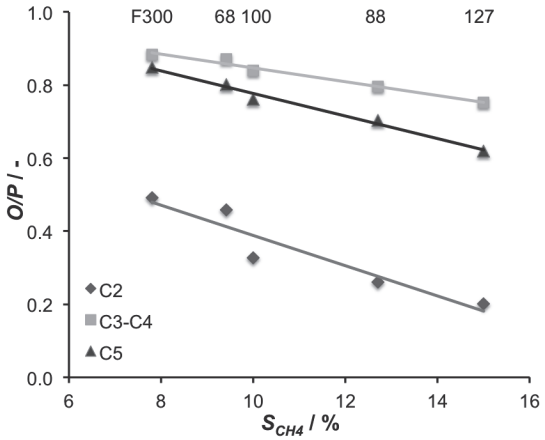

Figure 4.6 Correlation of the hydrogenation ability of KFe@C catalysts displaying olefin to paraffin ratio (*O/P*) and methane selectivity (S_{CH4}).

promotion resulted in decreased hydrogenation ability of KFe@C catalysts, showing a linear correlation toward far higher *O/P* ratios, and additionally, providing much higher activity (**Figure 4.6**). To put into perspective, the productivity of lower olefins as chemicals precursors is maximized with the best KFe@C catalysts, obtaining 50-90% of olefins in the C_2-C_5 range with CO_2-free selectivity over 53% without showing deactivation after 80 h. As discussed, deactivation was only observed for N-functionalized Fe@C catalysts, although this apparent relationship seems somewhat counterintuitive. For example, in studies on Fe/CNT for use as FTS catalysts, N-functionalization is often used to enhance the anchoring of Fe particles in the CNTs, thus increasing their activity and stability [47, 48]. Furthermore, the increased addition of N groups to the support often decreases the

Table 4.5 Average values for 100 x 100 micron EDX mapping studies on large grains of KFe@C catalysts.

X/Fe mol%	KFe@C-MIL68	KFe@C-MIL88A	KFe@C-MIL100	KFe@C-MIL127	KFe@C-F300
K/Fe	2.10	2.18	1.57	1.73	1.97
Cl/Fe		2.34		4.79	
Cr/Fe			5.58		
Mo/Fe			2.40		
N/Fe				73.2	
S/Fe					0.85
Cu/Fe					0.85
Mn/Fe					1.55

CH_4 selectivity in FTS over these N-doped carbons [49]. Therefore, EDX mapping of large grains of catalysts (approximately 100 x 100 micron) was performed on the samples that contained impurities in the XPS spectra (**Table 4.5, Figure A4.10 and Figure A4.11**). EDX results confirmed the K loading obtained by ICP analysis and showed the high dispersion of the alkali, and additionally confirmed bulk impurities for KFe@C-MIL88, -100, -127 and -F300. The EDX analysis of KFe@C-MIL88 and -127 contained 0.5 and 1.0 wt% of highly dispersed Cl. The EDX mapping for KFe@C-MIL100 displayed that large amounts (4.9 wt% total) of Cr and Mo were located in agglomerates, most likely in the form of bulk metal oxides. Interestingly, the KFe@C-F300 catalyst with the highest activity and lowest CH_4 selectivity contained Cu, Mn and S in amounts known as optimum for promoting FTS activity and selectivity [42, 43, 50-53]. Minute amounts of S are reported to titrate the active sites for hydrogenation, increasing the O/P ratio and activity, but unaffecting the alpha value [50, 51]. Additionally, increased activity from S promotion was shown by DFT calculations to originate from a decrease in the Fe-CO bond strength [53]. Cu is reported to increase the reduction of Fe_2O_3 by a combination of textural and H_2 spillover effects, and promotes the reaction rates in FTS and WGS [42, 54]. Apparently, it is the exact combination of the abovementioned promotors that distinguishes KFe@C-F300 as the best catalyst tested in this study.

4.5 Conclusions

In the preparation of FTS catalysts through the MOF mediated synthesis approach, the structure and elementary composition of the MOF play a key role on the FTS activity and selectivity of the resulting Fe on C composites. On one hand, the exact composition of the linker seems to play a small role in the surface area of the resulting C matrix (S_{BET} between 570-670 $m^2\ g^{-1}$). On the other hand, pore size distribution and average Fe particle size of the final catalysts are highly dependent on the original topology. All Fe@C samples prepared following this approach displayed outstanding activities in HTFT, especially after promotion with K (*FTY* in the range of 1.9-4.6 $\cdot 10^{-4}$ $mol_{CO}\ g^{-1}_{Fe}\ s^{-1}$). The obtained activities correlate well with the surface of the Fe particles, though the *ATY* of KFe@C-MIL-68 and -88 revealed that K promotion did not improve their activity. When it comes to selectivity to short chain olefins and catalyst deactivation, our results highlight the importance of impurities and the presence of other heteroatoms in the original MOF precursor. The use of linkers containing N resulted in less stable catalysts, while an optimum final composition is obtained when the commercial Fe-BTC MOF is used as precursor. In addition to added K, the presence of traces of S, Mn and Cu, most likely originating from its synthesis conditions, result in a lower hydrogenation activity and decreased Fe-CO bond strength. The combined effects result in decreased methane selectivity, increased O/P ratio and increased activity. Altogether, our results further demonstrate the complexity of FTS and the potential of commercial MOFs for the preparation of a new generation of catalysts able to fulfil most of the requirements of this challenging reaction.

References

[1] Schulz, H., *Appl. Catal., A*, 186 (**1999**) 3-12.
[2] Stranges, A.N., *A history of the fischer-tropsch synthesis in Germany 1926–45*, in: B.H. Davis, M.L. Occelli (Eds.) Stud. Surf. Sci. Catal., Elsevier, Amsterdam, **2007**, pp. 1-27.
[3] Dry, M.E., *Catal. Today*, 71 (**2002**) 227-241.
[4] Rostrup-Nielsen, J.R., *Catal. Today*, 18 (**1993**) 305-324.
[5] Rostrup-Nielsen, J.R., *Catal. Today*, 21 (**1994**) 257-267.
[6] Steynberg, A.P., Espinoza, R.L., Jager, B., Vosloo, A.C., *Appl. Catal., A*, 186 (**1999**) 41-54.
[7] Gascon, J., Corma, A., Kapteijn, F., Llabrés i Xamena, F.X., *ACS Catal.*, 4 (**2013**) 361-378.
[8] Santos, V.P., Wezendonk, T.A., Jaén, J.J.D., Dugulan, A.I., Nasalevich, M.A., Islam, H.-U., Chojecki, A., Sartipi, S., Sun, X., Hakeem, A.A., Koeken, A.C.J., Ruitenbeek, M., Davidian, T., Meima, G.R., Sankar, G., Kapteijn, F., Makkee, M., Gascon, J., *Nat Commun*, 6 (**2015**) 1-8.
[9] Chen, Y.-Z., Wang, C., Wu, Z.-Y., Xiong, Y., Xu, Q., Yu, S.-H., Jiang, H.-L., *Adv. Mater.*, 27 (**2015**) 5010-5016.
[10] Jiang, H.-L., Liu, B., Lan, Y.-Q., Kuratani, K., Akita, T., Shioyama, H., Zong, F., Xu, Q., *J. Am. Chem. Soc.*, 133 (**2011**) 11854-11857.
[11] Kim, T.K., Lee, K.J., Cheon, J.Y., Lee, J.H., Joo, S.H., Moon, H.R., *J. Am. Chem. Soc.*, 135 (**2013**) 8940-8946.
[12] Lee, J.H., Moon, B., Kim, T.K., Jeoung, S., Moon, H.R., *Dalton Trans.*, 44 (**2015**) 15130-15134.
[13] Lee, K.J., Kim, T.-H., Kim, T.K., Lee, J.H., Song, H.-K., Moon, H.R., *J. Mater. Chem. A*, 2 (**2014**) 14393-14400.
[14] Shen, K., Chen, X., Chen, J., Li, Y., *ACS Catal.*, 6 (**2016**) 5887-5903.
[15] An, B., Cheng, K., Wang, C., Wang, Y., Lin, W., *ACS Catal.*, 6 (**2016**) 3610-3618.
[16] Wezendonk, T.A., Santos, V.P., Nasalevich, M.A., Warringa, Q.S.E., Dugulan, A.I., Chojecki, A., Koeken, A.C.J., Ruitenbeek, M., Meima, G., Islam, H.-U., Sankar, G., Makkee, M., Kapteijn, F., Gascon, J., *ACS Catal.*, 6 (**2016**) 3236-3247.
[17] Bauer, S., Serre, C., Devic, T., Horcajada, P., Marrot, J., Férey, G., Stock, N., *Inorg. Chem.*, 47 (**2008**) 7568-7576.
[18] Chevreau, H., Permyakova, A., Nouar, F., Fabry, P., Livage, C., Ragon, F., Garcia-Marquez, A., Devic, T., Steunou, N., Serre, C., Horcajada, P., *CrystEngComm*, 18 (**2016**) 4094-4101.
[19] Fateeva, A., Horcajada, P., Devic, T., Serre, C., Marrot, J., Grenèche, J.-M., Morcrette, M., Tarascon, J.-M., Maurin, G., Férey, G., *Eur. J. Inorg. Chem.*, 2010 (**2010**) 3789-3794.
[20] Férey, G., Mellot-Draznieks, C., Serre, C., Millange, F., Dutour, J., Surblé, S., Margiolaki, I., *Science*, 309 (**2005**) 2040.
[21] Férey, G., Serre, C., Mellot-Draznieks, C., Millange, F., Surblé, S., Dutour, J., Margiolaki, I., *Angew. Chem. Int. Ed.*, 43 (**2004**) 6296-6301.
[22] Horcajada, P., Surble, S., Serre, C., Hong, D.-Y., Seo, Y.-K., Chang, J.-S., Greneche, J.-M., Margiolaki, I., Ferey, G., *Chem. Commun.*, (**2007**) 2820-2822.
[23] Liu, Y., Eubank, J.F., Cairns, A.J., Eckert, J., Kravtsov, V.C., Luebke, R., Eddaoudi, M., *Angew. Chem. Int. Ed.*, 46 (**2007**) 3278-3283.
[24] Mellot-Draznieks, C., Serre, C., Surblé, S., Audebrand, N., Férey, G., *J. Am. Chem. Soc.*, 127 (**2005**) 16273-16278.
[25] Serre, C., Millange, F., Surblé, S., Férey, G., *Angew. Chem. Int. Ed.*, 43 (**2004**) 6285-6289.
[26] Volkringer, C., Meddouri, M., Loiseau, T., Guillou, N., Marrot, J., Férey, G., Haouas, M., Taulelle, F., Audebrand, N., Latroche, M., *Inorg. Chem.*, 47 (**2008**) 11892-11901.
[27] Volkringer, C., Popov, D., Loiseau, T., Férey, G., Burghammer, M., Riekel, C., Haouas, M., Taulelle, F., *Chem. Mater.*, 21 (**2009**) 5695-5697.
[28] Cunha, D., Ben Yahia, M., Hall, S., Miller, S.R., Chevreau, H., Elkaïm, E., Maurin, G., Horcajada, P., Serre, C., *Chem. Mater.*, 25 (**2013**) 2767-2776.
[29] Serre, C., Mellot-Draznieks, C., Surblé, S., Audebrand, N., Filinchuk, Y., Férey, G., *Science*, 315 (**2007**) 1828.

[30] Surble, S., Serre, C., Mellot-Draznieks, C., Millange, F., Ferey, G., *Chem. Commun.*, (**2006**) 284-286.
[31] Taylor-Pashow, K.M.L., Rocca, J.D., Xie, Z., Tran, S., Lin, W., *J. Am. Chem. Soc.*, 131 (**2009**) 14261-14263.
[32] Crawford, D., Casaban, J., Haydon, R., Giri, N., McNally, T., James, S.L., *Chem. Sci.*, 6 (**2015**) 1645-1649.
[33] Crawford, D.E., Casaban, J., *Adv. Mater.*, 28 (**2016**) 5747-5754.
[34] Taddei, M., Steitz, D.A., van Bokhoven, J.A., Ranocchiari, M., *Chem. Eur. J.*, 22 (**2016**) 3245-3249.
[35] Wilmer, C.E., Leaf, M., Lee, C.Y., Farha, O.K., Hauser, B.G., Hupp, J.T., Snurr, R.Q., *Nat Chem*, 4 (**2012**) 83-89.
[36] De Lange, M.F., Vlugt, T.J.H., Gascon, J., Kapteijn, F., *Microporous Mesoporous Mater.*, 200 (**2014**) 199-215.
[37] Biesinger, M.C., Payne, B.P., Grosvenor, A.P., Lau, L.W.M., Gerson, A.R., Smart, R.S.C., *Appl. Surf. Sci.*, 257 (**2011**) 2717-2730.
[38] Kapteijn, F., Moulijn, J.A., Matzner, S., Boehm, H.P., *Carbon*, 37 (**1999**) 1143-1150.
[39] Pels, J.R., Kapteijn, F., Moulijn, J.A., Zhu, Q., Thomas, K.M., *Carbon*, 33 (**1995**) 1641-1653.
[40] Chaumette, P., Verdon, C., Boucot, P., *Top. Catal.*, 2 (**1995**) 301-311.
[41] Mills, G.A., Steffgen, F.W., *Catalysis Reviews*, 8 (**1974**) 159-210.
[42] Bukur, D.B., Mukesh, D., Patel, S.A., *Ind. Eng. Chem. Res.*, 29 (**1990**) 194-204.
[43] Li, S., Li, A., Krishnamoorthy, S., Iglesia, E., *Catal. Lett.*, 77 (**2001**) 197-205.
[44] Li, Y., Zhou, Y.-X., Ma, X., Jiang, H.-L., *Chem. Commun.*, 52 (**2016**) 4199-4202.
[45] Li, Q., Xu, P., Gao, W., Ma, S., Zhang, G., Cao, R., Cho, J., Wang, H.-L., Wu, G., *Adv. Mater.*, 26 (**2014**) 1378-1386.
[46] Kapteijn, F., Moulijn, J.A., *J. Chem. Soc., Chem. Commun.*, (**1984**) 278-279.
[47] Lu, J., Yang, L., Xu, B., Wu, Q., Zhang, D., Yuan, S., Zhai, Y., Wang, X., Fan, Y., Hu, Z., *ACS Catal.*, 4 (**2014**) 613-621.
[48] Schulte, H.J., Graf, B., Xia, W., Muhler, M., *ChemCatChem*, 4 (**2012**) 350-355.
[49] Xiong, H., Moyo, M., Motchelaho, M.A., Tetana, Z.N., Dube, S.M.A., Jewell, L.L., Coville, N.J., *J. Catal.*, 311 (**2014**) 80-87.
[50] Bromfield, T.C., Coville, N.J., *Appl. Catal., A*, 186 (**1999**) 297-307.
[51] Torres Galvis, H.M., Koeken, A.C.J., Bitter, J.H., Davidian, T., Ruitenbeek, M., Dugulan, A.I., de Jong, K.P., *J. Catal.*, 303 (**2013**) 22-30.
[52] van Dijk, W.L., Niemantsverdriet, J.W., van dar Kraan, A.M., van der Baan, H.S., *Appl. Catal.*, 2 (**1982**) 273-288.
[53] Cheng, J., Hu, P., Ellis, P., French, S., Kelly, G., Lok, C.M., *J. Phys. Chem. C*, 114 (**2010**) 1085-1093.
[54] de Smit, E., de Groot, F.M.F., Blume, R., Havecker, M., Knop-Gericke, A., Weckhuysen, B.M., *PCCP*, 12 (**2010**) 667-680.

Annex

4

Structural and elemental influence from various MOFs on the performance of Fe@C catalysts for Fischer-Tropsch synthesis

A4.1 Supplement to Results

A4.1.1 Characterization of MOF precursors

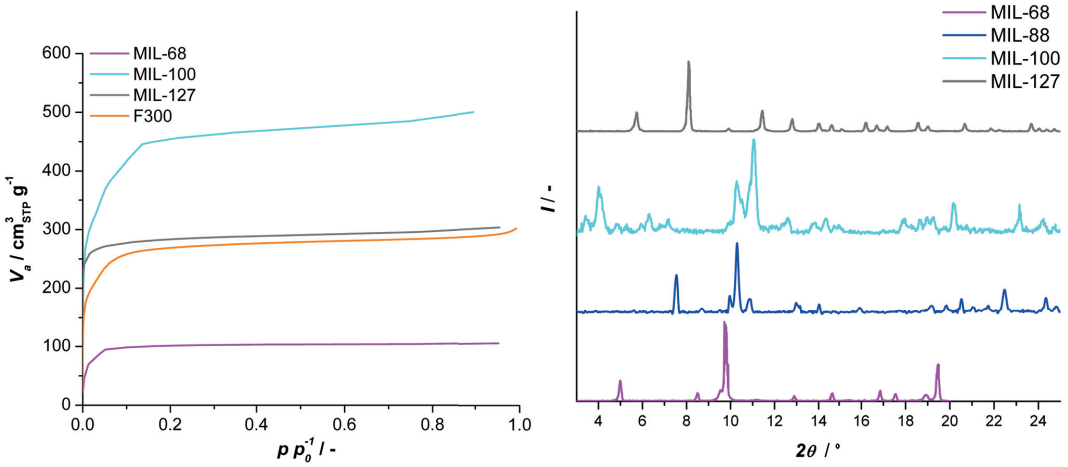

Figure A4.1 A N_2 physisorption at 77 K and **B** PXRD patterns for the various MOFs. Isotherm shapes and diffraction patterns match with literature [1-12].

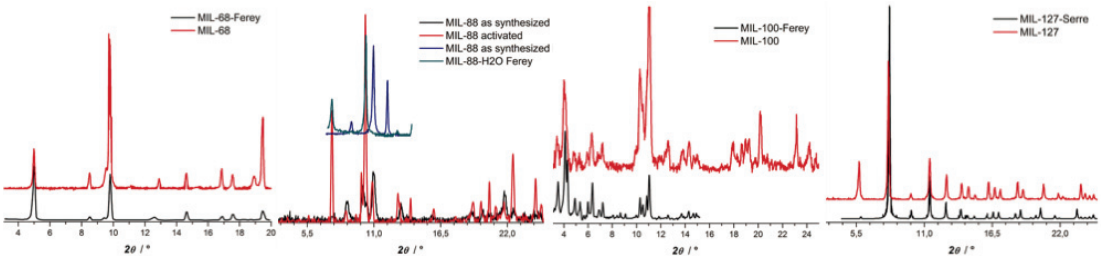

Figure A4.2 Comparison of the diffraction angle and relative intensity for the various MOFs and reported XRD patterns from literature.

Table A4.1 N_2 physisorption calculations for the various MOFs, comprising BET area (S_{BET}) and total pore volume (V_p). Values agree with reported BET area and pore volume in literature.

Fe-based MOF	S_{BET} / m^2 g^{-1}	V_p / cm^3 g^{-1}
MIL-68	400	0.16
MIL-100	1777	0.99
MIL-127	1131	0.47
F300	1021	0.45

A4.3.2 Characterization of Fe@C catalysts

Table A4.2 Data of N_2 physisorption per gram of catalyst, without taking into account the high Fe_2O_3 loading of the Fe@C materials.

Catalyst	S_{BET} $m^2\ g^{-1}$	S_{Ext} $m^2\ g^{-1}$	V_P $cm^3\ g^{-1}$	V_μ $cm^3\ g^{-1}$
Fe@C-MIL68	314	161	0.28	0.06
Fe@C-MIL88A	224	163	0.16	0.03
Fe@C-MIL100	260	136	0.18	0.06
Fe@C-MIL127	323	172	0.30	0.06
Fe@C-MIL101NH_2	283	120	0.25	0.07
Fe@C-F300	280	140	0.29	0.06

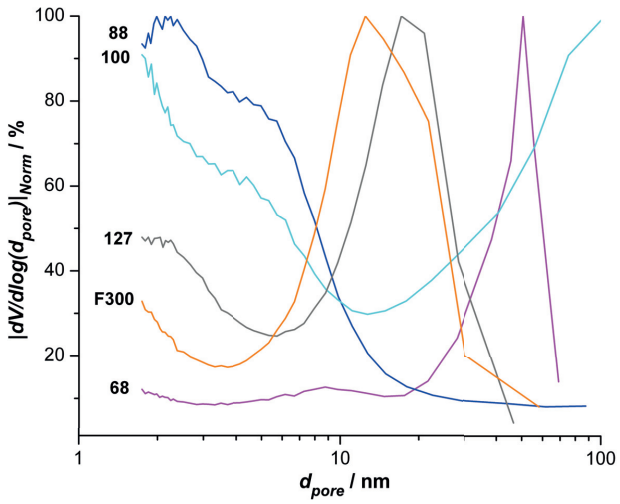

Figure A4.3 BJH transformation of isotherms displaying the normalized pore size distribution of Fe@C catalysts.

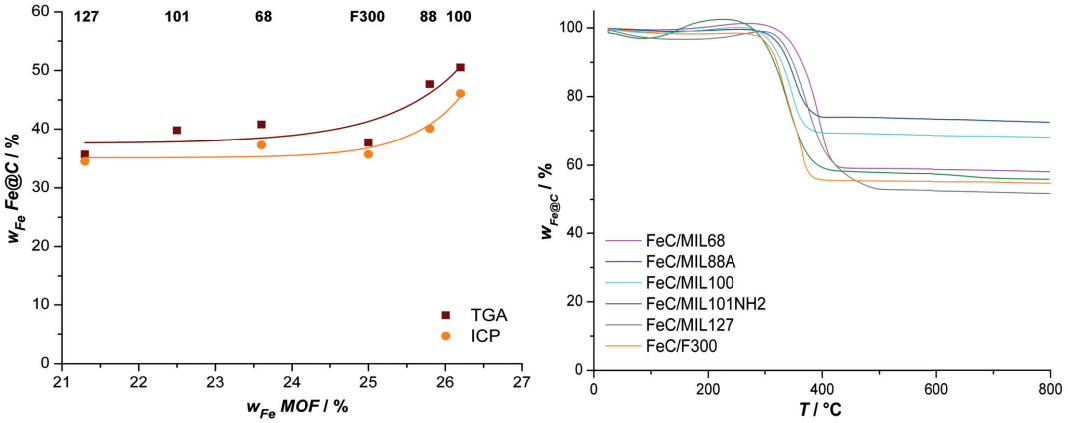

Figure A4.4 A TGA and ICP analysis showing the non-linear relation between Fe loading in the MOF and in the resulting Fe@C catalyst and **B** TGA profiles of Fe@C catalysts in air.

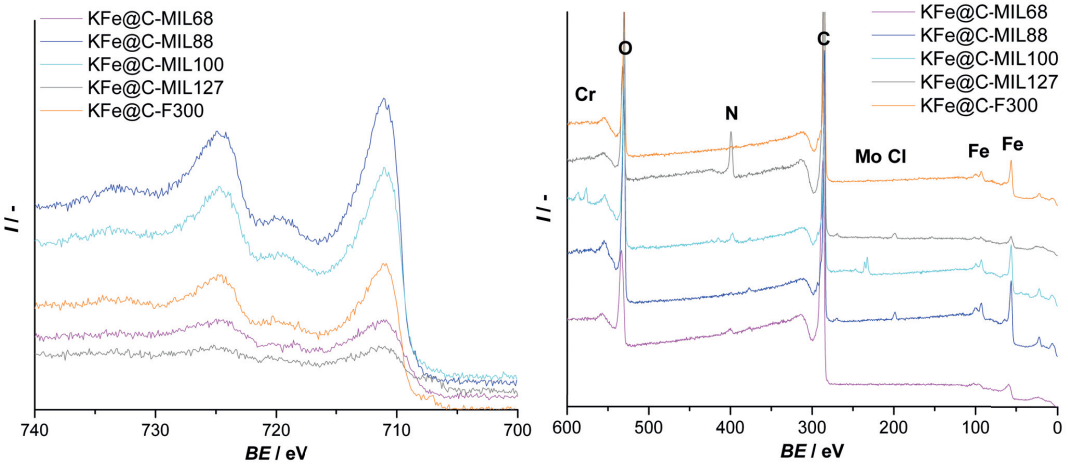

Figure A4.5 A Core-level Fe*2p* spectra for passivated catalysts and **B** their associated survey spectra displaying surface impurities.

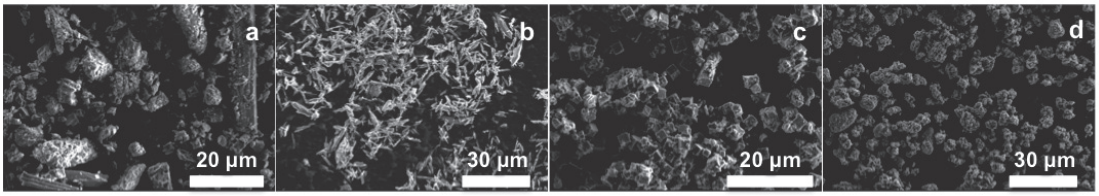

Figure A4.6 SEM images of pyrolyzed MOFs **A** Fe@C-MIL68, **B** Fe@C-MIL88, **C** Fe@C-MIL127 and **D** Fe@C-F300.

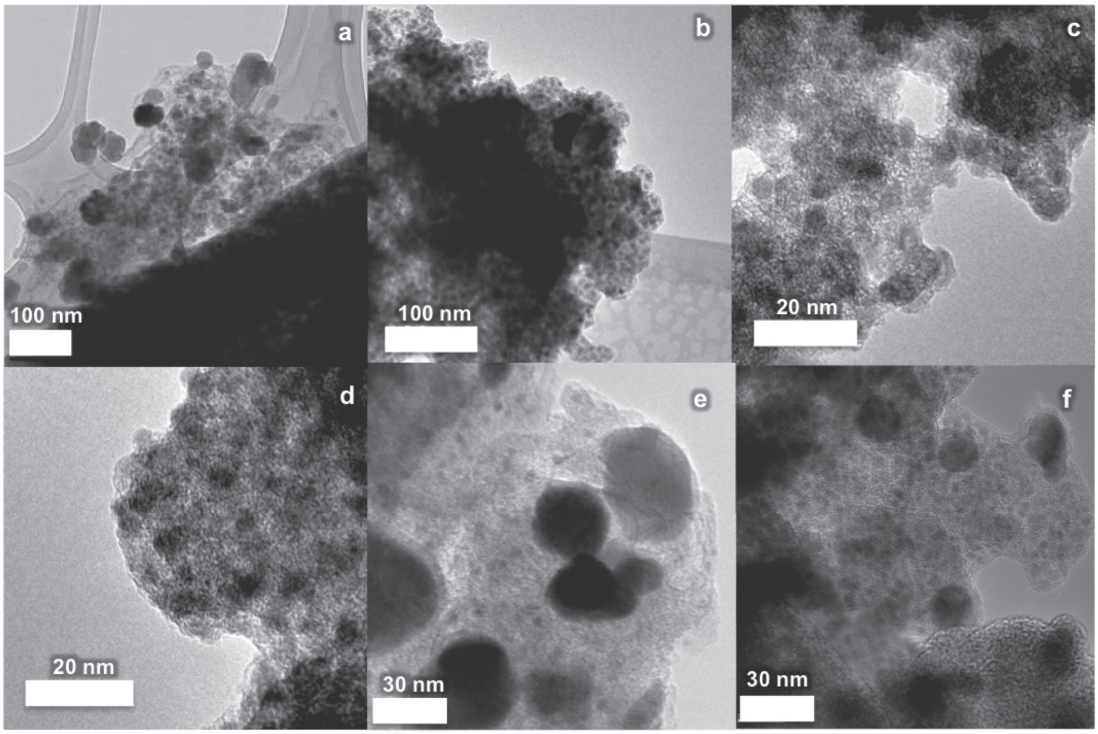

Figure A4.7 Additional TEM images of **A** Fe@C-MIL68, **B** Fe@C-MIL88, **C** Fe@C-MIL100, **D** Fe@C-MIL101NH2, **E** Fe@C-MIL127 and **F** Fe@C-F300.

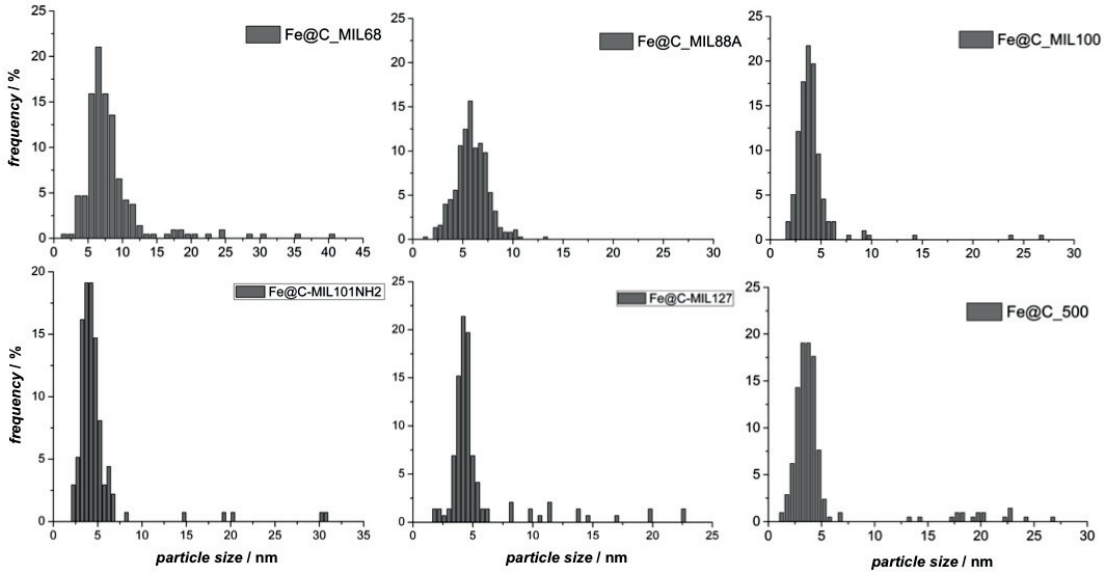

Figure A4.8 Particle size distribution determined by TEM in the Fe@C catalysts derived from different MOFs by pyrolysis at 500 ˚C.

A4.4 Supplement to Discussion

A4.4.1 Characterization of Fe@C catalysts

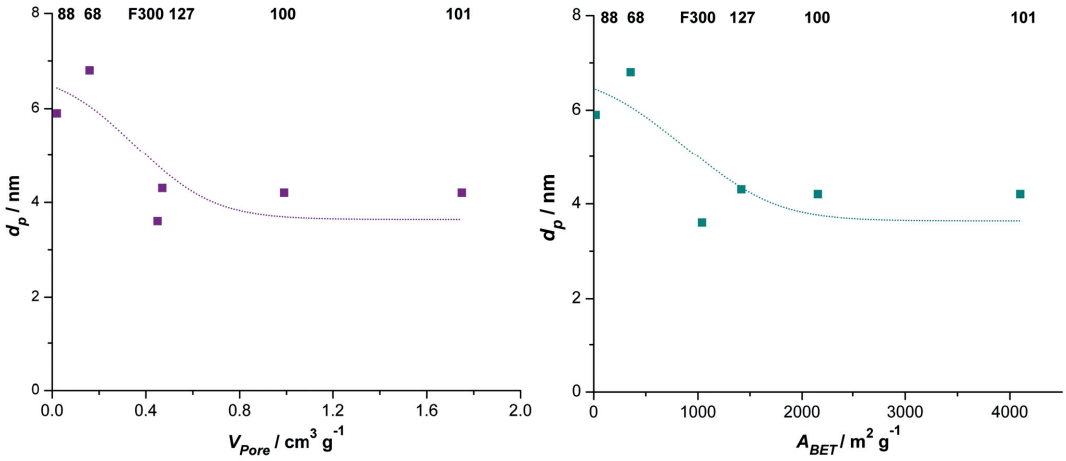

Figure A4.9 Relation between the average Fe particle size and the pore volume **A** and BET area **B** for the Fe@C catalysts derived from the various Fe-MIL-X typologies (X= 88, 68, 127, 100 and 101) and Fe-BTC F300.

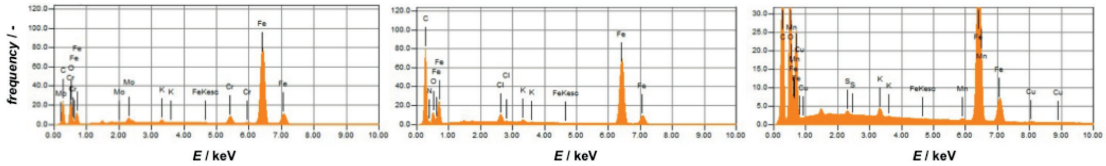

Figure A4.10 Elemental analysis from EDX spectra for *left*) KFe@C-MIL100, *middle*) KFe@C-MIL127 and *right*) KFe@C-F300 catalysts showing impurities in the bulk phase.

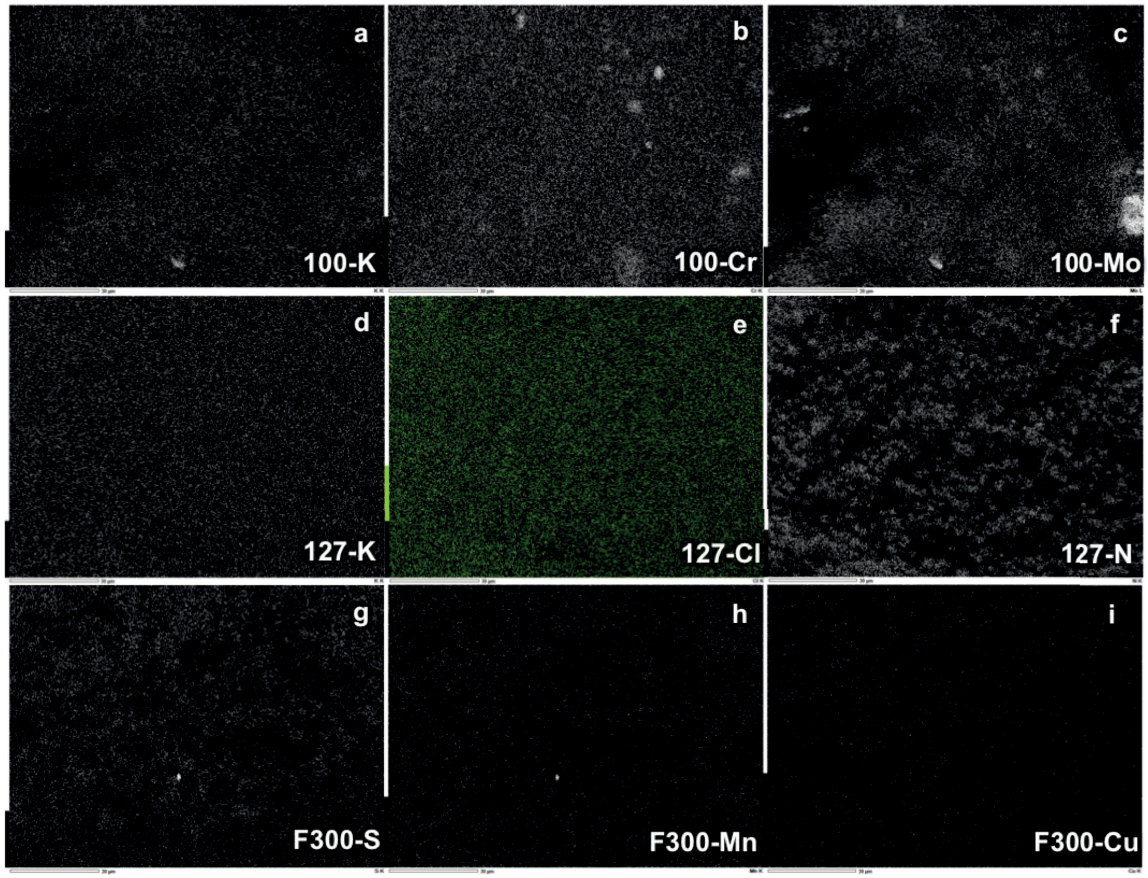

Figure A4.11 EDX mapping images of KFe@C-MIL100 a) KFe@C-MIL127 b) and KFe@C-F300 c), clearly showing agglomeration of metal impurities in the Fe@C-MIL100 sample and dispersed elements in the others.

References

[1] Bauer, S., Serre, C., Devic, T., Horcajada, P., Marrot, J., Férey, G., Stock, N., *Inorg. Chem.*, 47 (**2008**) 7568-7576.

[2] Chevreau, H., Permyakova, A., Nouar, F., Fabry, P., Livage, C., Ragon, F., Garcia-Marquez, A., Devic, T., Steunou, N., Serre, C., Horcajada, P., *CrystEngComm*, 18 (**2016**) 4094-4101.

[3] Fateeva, A., Horcajada, P., Devic, T., Serre, C., Marrot, J., Grenèche, J.-M., Morcrette, M., Tarascon, J.-M., Maurin, G., Férey, G., *Eur. J. Inorg. Chem.*, 2010 (**2010**) 3789-3794.

[4] Férey, G., Mellot-Draznieks, C., Serre, C., Millange, F., Dutour, J., Surblé, S., Margiolaki, I., *Science*, 309 (**2005**) 2040.

[5] Férey, G., Serre, C., Mellot-Draznieks, C., Millange, F., Surblé, S., Dutour, J., Margiolaki, I., *Angew. Chem. Int. Ed.*, 43 (**2004**) 6296-6301.

[6] Horcajada, P., Surble, S., Serre, C., Hong, D.-Y., Seo, Y.-K., Chang, J.-S., Greneche, J.-M., Margiolaki, I., Ferey, G., *Chem. Commun.*, (**2007**) 2820-2822.

[7] Liu, Y., Eubank, J.F., Cairns, A.J., Eckert, J., Kravtsov, V.C., Luebke, R., Eddaoudi, M., *Angew. Chem. Int. Ed.*, 46 (**2007**) 3278-3283.

[8] Mellot-Draznieks, C., Serre, C., Surblé, S., Audebrand, N., Férey, G., *J. Am. Chem. Soc.*, 127 (**2005**) 16273-16278.

[9] Serre, C., Millange, F., Surblé, S., Férey, G., *Angew. Chem. Int. Ed.*, 43 (**2004**) 6285-6289.

[10] Volkringer, C., Meddouri, M., Loiseau, T., Guillou, N., Marrot, J., Férey, G., Haouas, M., Taulelle, F., Audebrand, N., Latroche, M., *Inorg. Chem.*, 47 (**2008**) 11892-11901.

[11] Volkringer, C., Popov, D., Loiseau, T., Férey, G., Burghammer, M., Riekel, C., Haouas, M., Taulelle, F., *Chem. Mater.*, 21 (**2009**) 5695-5697.

[12] Cunha, D., Ben Yahia, M., Hall, S., Miller, S.R., Chevreau, H., Elkaïm, E., Maurin, G., Horcajada, P., Serre, C., *Chem. Mater.*, 25 (**2013**) 2767-2776.

Chapter

5

Controlled Formation of Iron Carbides and their Performance in Fischer-Tropsch Synthesis

Iron carbides are unmistakably associated with the active phase for Fischer-Tropsch synthesis (FTS). The formation of these carbides is highly dependent on the catalyst formulation, the activation method and the operational conditions. Because of this highly dynamic behavior, studies on active phase performance often lack the direct correlation between catalyst performance and iron carbide phase. For the above reasons, an extensive *in situ* Mössbauer spectroscopy study on highly dispersed Fe@C MOF-derived catalysts was coupled to their FTS performance testing. The preparation of Fe@C catalysts allows control over the active phase formation and therefore provides an ideal model system to study the iron carbide performance. Reduction of fresh Fe@C followed by low-temperature Fischer-Tropsch (LTFT) conditions resulted in the formation of the ε'-$Fe_{2.2}C$, whereas carburization of the fresh catalysts under high-temperature Fischer-Tropsch (HTFT) resulted in the formation of χ-Fe_5C_2. The both catalysts were thereafter subjected to LTFT performance testing, while maintaining a similar degree of carburization and Debye temperature. Furthermore, the different activation methods did not alter other important catalyst properties, as pre- and post-reaction transmission electron microscopy (TEM) characterization confirmed that the iron nanoparticle dispersion was preserved. It is concluded that the activity of χ-Fe_5C_2 and ε'-$Fe_{2.2}C$ is virtually identical, whilst a significant increase in the hydrogenation ability of ε'-$Fe_{2.2}C$ is found. The absence of these differences under subsequent HTFT experiments, where χ-Fe_5C_2 is the dominating phase, is a strong indication that the iron carbide phase is responsible for the differences in selectivity.

This chapter is based on the following publication:

T.A. Wezendonk, X. Sun, A.I. Dugulan, A.J.F. van Hoof, E.J.M. Hensen, F. Kapteijn and J. Gascon, ***J. Catal.*** *Submitted*.

5.1 Introduction

In the early years surrounding the discovery of the atmospheric-pressure synthesis, Fischer postulated that the primary step before hydrogen addition is the carbon monoxide dissociation, and thus, the formation of carbides as intermediate compounds in the reaction [1, 2]. Cobalt, nickel and iron, three metals that display FTS activity, react at 200 ˚C with carbon monoxide to form carbides, and carbon balances of synthesis reactions and product analysis of the decomposition of spent catalysts indicated that carbides were formed during the synthesis [3]. At this time, catalyst characterization techniques were still emerging, as only fifteen years had passed since the Nobel Prize in Physics was awarded to the Braggs for their work on X-ray diffraction (XRD), and it would be another five before Brunauer and Emmett started publishing on Van der Waals adsorption isotherms. The first iron-phase characterization studies were performed on the high-temperature Fischer-Tropsch (HTFT) catalyst, fused bulk iron catalysts with low surface area, where the iron phase was resolved by magnetization experiments [4]. The temperature-dependent magnetic moments allowed for quantification of the iron phase during FTS, and showed that, after complete reduction, iron was converted in magnetite and Hägg carbide (around 45 % and 50 %, resp.) with small amounts of metallic iron remaining. The composition of the catalyst changed, as the magnetite phase gradually increased during operation, whereas the Hägg carbide phase decreased and was oxidized and interconverted to another iron carbide phase [5]. This fundamental view on the dynamics of iron catalysts has not changed much up to date.

The discovery of Mössbauer absorption spectroscopy and the further development of XRD allowed the characterization of small iron nanoparticles on supported catalysts, and several iron carbides were identified over the years [6-18]. In addition, the application of X-ray photoelectron spectroscopy (XPS) and X-ray absorption spectroscopy (XANES/EXAFS) further stimulated the studies into FTS carbide-phase formation. The carbide phases found in literature associated with FTS are ε-Fe_2C, ε'-$Fe_{2.2}C$, Fe_7C_3, χ-Fe_5C_2, and θ-Fe_3C, however, generally, the monoclinic Hägg carbide (χ-Fe_5C_2) and hexagonal closed packed carbide (ε'-$Fe_{2.2}C$) are the predominant carbide phases found. Debate emerged regarding activity and selectivity of the different iron carbides, now that it became more widely accepted that carbides are the active phase. Thus, many studies have focused on the activation of fresh catalysts in order to optimize their performance and establish the iron phases [19-42]. Particularly, Mössbauer studies coupled with catalytic tests provide good insight into the effect of the activation protocol and operational regime on the carbide phase. However, the focus of these papers was often limited; either the differences in the evolution of the active phase were investigated or the performance of the catalysts acquired through different activation protocols was reported. Hence, the main conclusion usually derived is that one activation method is preferred over the other, for a wide variety of reasons, and that a coexistence of carbide phases could be obtained. Therefore, it is not possible to uniquely determine key performance indicators such as activity and selectivity

inherent to a specific iron carbide phase. To properly quantify their intrinsic activity and distinguish the iron carbides, one would need to find a very robust catalyst that can withstand the different activation regimes to maintain identical reducibility, degree of carburization, and catalytic stability.

The discovery and development of a new type of iron catalyst produced through the decomposition of highly porous, crystalline, and dispersed iron clusters in carbon matrices, or metal-organic frameworks (MOFs) was recently reported by our group [43-45]. The Fe@C catalysts have a high loading of monodispersed nanoparticles and show high degree of carburization during *in situ* Mössbauer experiments following the MOF pyrolysis (**Table 5.1**). Moreover, the resulting Fe@C catalysts display exceptional activity and stability under high temperature Fischer-Tropsch (HTFT) conditions due to the embedding of iron in the carbon matrix formed after MOF decomposition. These catalysts provide an ideal model system because of the control over the particle size and iron phase by tuning the degree of carbonization through the pyrolysis temperature [45]. With increasing particle size, a higher the ratio of χ-Fe_5C_2 over ε'-$Fe_{2.2}C$ is found in Mössbauer spectroscopy experiments. Additionally, *in situ* Mössbauer experiments following the Fe-BTC pyrolysis and its carburization confirmed that ε'-$Fe_{2.2}C$ is indeed a stable phase under the HTFT conditions for particles below roughly 3 nm. However, after reduction and subsequent activation under HTFT, controlling and isolating the hexagonal carbide phases under HTFT is tedious. The low carbon chemical potential under HTFT does not allow the formation of single phase ε'-$Fe_{2.2}C$ when starting from the fully oxidized iron nanoparticles.

In this Chapter, the previous HTFT work and abundant literature data on iron catalyst activation are applied to produce single-phase iron carbides in order to compare their performance at steady state operation over 100 h. To demonstrate the intrinsic carbide performance, χ-Fe_5C_2 and ε'-$Fe_{2.2}C$ phases are prepared from the same MOF-derived Fe@C catalysts using syngas activation and hydrogen reduction followed by low-temperature Fischer-Tropsch (LTFT) experiments. The catalyst phase during activation and LTFT is derived from *in situ* Mössbauer spectroscopy and the activation and LTFT experiments are carried out in parallel in fixed-bed reactor operation, both starting from catalysts produced by pyrolysis of the same MOF at 500 and 600 °C (hereafter Fe@C-500 and Fe@C-600, respectively). TEM analysis of the fresh and spent catalysts is performed to ensure proper structure-activity relations are obtained by maintaining nanoparticle dispersion. The detailed carbide-phase characterization enables an extrapolation of the results in terms of activity and selectivity toward the HTFT regime, and as such establishes a comprehensive overview. While this study does not aim to elucidate the active sites and intermediates present on the highly dynamic surface of the bulk carbide phases, it unequivocally demonstrates the effect of the carbide bulk phase on the activity and selectivity of the catalysts.

Table 5.1 Fe@C catalyst characterization* after passivation; T_{pyro} denotes the pyrolysis temperature in ˚C.

T_{pyro} / ˚C	w_{Fe} / %	d_p / nm	γ-Fe_2O_3 / %	Fe/C_{surf} / -	S_{BET} / m^2 g^{-1}	V_P / cm^3 g^{-1}
500	37.8	3.6	95	0.021	281	0.30
600	43.8	6.0	92	0.016	339	0.32

*Iron loading in wt% (w_{Fe}), average iron nanoparticle size (d_p), percentage of bulk iron oxide phase (γ-Fe_2O_3), iron to carbon ratio on the surface (Fe/C_{surf}), BET area (S_{BET}) and total pore volume (V_P) per gram of catalyst.

5.2 Experimental

Fe@C-500 and Fe@C-600 were synthesized by our earlier reported MOF mediated synthesis approach [43-45], where approximately 1.0 g of as-received Fe-BTC Basolite F300 was placed inside a crucible and subjected to pyrolysis at 500 or 600 ˚C for 8 h in a horizontally located quartz tubular reactor under a nitrogen gas hourly space velocity of 4.5 h^{-1}. The resulting nanoparticles were passivated in 5 % oxygen in nitrogen at room temperature as they were extremely prone to oxidation, witnessed by a conversion over 92 % of the reduced iron phase into maghemite (γ-Fe_2O_3). The following key experimental procedures are addressed in a concise manner to display the similarities in the characterization and testing. For full technical details, the reader is referred to **Annex 5** and references therein. The catalytic performance tests (**Figure A5.1**) [46] and *in situ* Mössbauer experiments (**Figure A5.2**) [45] were carried out in stainless steel tubular reactors of 4 mm and 15 mm internal diameter, respectively. The catalysts were pretreated either by atmospheric hydrogen reduction or pressurized syngas activation, denoted herein as reduction and carburization, respectively. Reduction comprises feeding pure hydrogen at an atmospheric pressure while ramping the temperature to 400 ˚C at a rate of 2 ˚C min^{-1}, allowing reduction for 3 h at a space velocity based on catalyst weight (*WHSV*) of approximately 90 dm^3_{H2} g_{Fe}^{-1} h^{-1}. The activated catalyst is cooled down to FTS reaction temperature of 230 ˚C under hydrogen flow. The pressure was subsequently increased to 20 bar, and carbon monoxide introduction followed during a period of 1 h to obtain a H_2/CO ratio of unity with a *WHSV* of 55 $dm^3_{H2/CO}$ g_{Fe}^{-1} h^{-1}. Carburization comprises feeding equimolar syngas at 15 bar while ramping the temperature to 340 ˚C at a rate of 2 ˚C min^{-1}, effectively carburizing the catalyst for a period of 140 h at a *WHSV* of 120 $dm^3_{H2/CO}$ g_{Fe}^{-1} h^{-1}. The activated catalyst is cooled down to FTS reaction temperature of 230 ˚C under syngas flow. The pressure was subsequently increased to 20 bar and the *WHSV* decreased to 55 $dm^3_{H2/CO}$ g_{Fe}^{-1} h^{-1}. The weight hourly space velocities for activation and FTS were increased by a factor 2.0 for the *in situ* Mössbauer cell to overcome the inherent dimensional mismatch in the internal diameter. With increased space velocities, a better approximation to plug flow behavior through the wider tubular

reactor can be achieved, which also diminishes adverse effects otherwise caused by higher partial pressures of water and carbon dioxide due to the lower superficial gas velocity. Differential reactor operation and isothermal conditions were ensured for the two experimental techniques, aiming at conversion levels between 5-15 % under LTFT conditions. Spent catalysts from the performance tests were passivated for a period of 3 h in the abovementioned quartz tubular reactor by flowing 5 % oxygen in nitrogen at room temperature through the packed beds inside their stainless-steel tubes. Transmission ^{57}Fe Mössbauer spectra were collected at 300 K and 4.2 K with a sinusoidal velocity spectrometer using a ^{57}Co(Rh) source and velocity calibration was carried out using an α-Fe foil, the resulting Mössbauer spectra were fitted using the Mosswinn 4.0 program [47]. Debye temperatures were calculated using a Levenberg-Marquardt fitting algorithm of the Lamb-Mössbauer factor [48, 49], using the Debye model approximation. TEM imaging was carried out on passivated catalysts prepared on a well-conducting copper grid with a support of lacey carbon and an additional 2 nm carbon film. The images were acquired on a CryoTitan at room temperature operated at 300 kV and equipped with a field emission gun using a Gatan 2k×2k CCD camera. The structures of the carbon matrix from the catalyst and the carbon grid of the TEM showed distinct differences.

5.3 Results and Discussion

5.3.1 *In situ* Mössbauer Absorption Spectroscopy

A first glance on the room temperature spectra of the fresh Fe@C-500 catalyst (**Figure A5.3, Table A5.1**) indicates the presence of very small iron nanoparticles, readily established by TEM and XRD data. At an isomer shift of 0.31 mm s^{-1} and an average magnetization of zero [23], it is calculated that over 90% is present as superparamagnetic iron oxide nanoparticles below 4.0 nm [45]. Under cryogenic temperatures (**Figure A5.3, Table A5.1**), the contributions of the tetrahedral and octahedral sites of maghemite (γ-Fe_2O_3) are distinguished, next to a large contribution of unresolved iron oxides with an average hyperfine field of 48.4 T resulting from different particle sizes [21]. As carburization initiates under HTFT conditions, the iron oxides are gradually reduced towards carbides and nonstoichiometric oxides over time, as can be seen from the spectra taken after 24 h and 96 h (**Figure A5.4, Table A5.2**). The room temperature spectra are most clear in displaying the trend of carbide phase growth and change in the nature of the oxide. The oxide exhibits an isomer shift of 1.06 mm s^{-1}, much larger than the oxide of the fresh catalyst. At cryogenic temperatures, the three iron cation sites of nonstoichiometric and iron-deficient wüstite can now be unambiguously assigned (**Figure 5.1A**) [50]. The mixed valence of the iron phase originates from the variable occupancy of octahedral and tetrahedral sites [51], and as such, the relative ratio of the three sites can vary between certain boundaries [52]. The co-existence of the Hägg carbide phase was determined from three overlapping sextuplets with lower magnetic fields of 25.6, 21.2 and 11.1 T [20, 53]. The spectra originate from the three different sites in the χ- Fe_5C_2 lattice, where the carbon atom is in the center

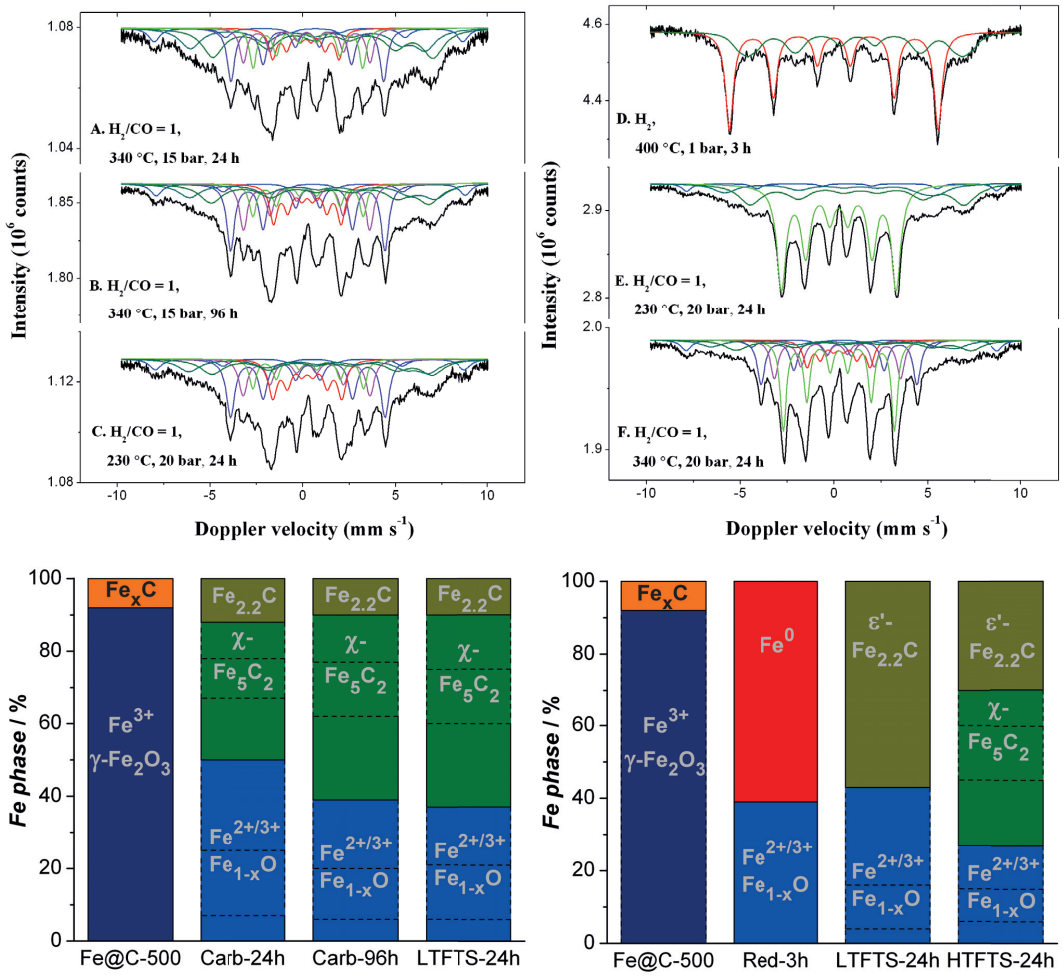

Figure 5.1 Mössbauer spectra of Fe@C-500 measured at 4.2 K after carburization (A,B) and subsequent LTFT conditions (C), and after reduction (D), subsequent LTFT conditions (E) and additional HTFT (F). The bar graphs represent the spectral contributions of iron phases determined by the relative absorption areas.

of triangle-based prism containing six iron atoms [20]. After 24 h under HTFT conditions, exactly half of the iron oxide has been converted into carbide, and carburization into χ-Fe_5C_2 continuously increases in time (**Figure 5.1B**). In addition to the Hägg carbide phase, a minor contribution of hexagonal iron carbide was found, but the spectral contribution of this phase decreased rather than increased. After 96 h of *in situ* carburization, 63 ± 3 % of the iron phase has carburized into Hägg carbide, and then levels off when switching to LTFT conditions (**Figure 5.1C**). The degree of carburization remains virtually unchanged (64 ± 3 %) after 24 h under LTFT conditions (**Table A5.3**).

The hydrogen treatment of Fe@C-500 at 400 ˚C renders a clear degree of reduction in the sample (**Figure 5.1D, Figure A5.4**). The sextuplet observed at 4.2 K, without relative isomer shift and a hyperfine field around 34.6 T, is typically assigned to ferrite (α-Fe) [21, 54]. The measurements at room temperature reveal that half of the metallic iron contributions originate from a poorly resolved signal around the central region, indicating that a large amount of the nanoparticles is present as very small superparamagnetic species. The remainder of the iron phase contains contributions from Fe^{2+} and Fe^{3+}, which are attributed to the wüstite phase ($Fe_{1-x}O$). Hence, the degree of reduction under hydrogen atmosphere after 3 h at 400 ˚C can be estimated to 61 % (**Table A5.3**). The spectra obtained at room temperature after 24 h of LTFT are of a different nature. It seems however, that the oxide phase has not undergone much change, as it maintains an identical isomer shift and only a slight change in the quadrupole splitting is observed (**Figure A5.4, Table A5.2**). The cryogenic measurements confirm the presence of the three $Fe_{1-x}O$ spectra, with isomer shifts between 0.56 and 1.33 mm s^{-1} and significant quadrupole splitting, values that are much different from the initial Fe_2O_3 phase (**Table A5.3**). Moreover, the metallic iron contribution has disappeared completely and turned into hexagonal iron carbide (ε'-$Fe_{2.2}C$), as a sextuplet with a significant isomer shift of 0.24 mm s^{-1} and much lower hyperfine field of 19.0 T has been measured [22, 26, 55]. Comparison of the spectral contributions of the both phases confirm that the metallic iron has been fully converted to single-phase hexagonal iron carbide, as 61 ± 3 % ε'-carbide is obtained compared to 57 ± 3 % metallic iron (**Figure 5.1E**).

Additionally, *in situ* reduction was carried out for the Fe@C-600 sample, to establish whether differences in activation are obtained due to the larger nanoparticle size of 6 nm compared to 3.6 nm of Fe@C-500. Following reduction at 400 ˚C, the degree of reduction of Fe@C-600 was found very similar to Fe@C-500, with 56 % somewhat lower than 61 % for the latter (**Figure A5.5**). Nonetheless, the steady-state carbide phase contribution of the catalyst with 6.0 nm iron nanoparticles was remarkably higher, with an ε'-$Fe_{2.2}C$ spectral contribution of 68 %, compared to 59 % for 3.6 nm iron nanoparticles. In addition to the ε'-$Fe_{2.2}C$ phase, the larger particles rendered the onset of a secondary carbide phase. Even though the overlap greatly hindered the fitting procedure, additional sextuplets at 4.2 K could be assigned at isomer shifts between 0.18-0.22 mm s^{-1}, while a magnetic field of 25.9 T was obtained for the sextuplet with the highest isomer shift, indicative of the presence of χ-Fe_5C_2 (**Table A5.4**) However, the room temperature spectra provided a hyperfine field value of 23 T, which can be ascribed to ε-Fe_2C (**Table A5.5**). The crude fit provided a value of 11 ± 3 % spectral contribution of this tentative phase after 24 h of LTFT under 20 bar equimolar syngas. Nevertheless, the comparison of the spectral contributions of Fe@C-500 and Fe@C-600 after LTFT shows that the ε'-$Fe_{2.2}C$ is produced on the two reduced catalysts comprising different particle sizes (**Figure A5.6 and Table 5.2**). The spectra of the Fe@C-500 catalyst obtained after 24 h under HTFT conditions, following the LTFT measurements, demonstrate the evolution of the Hägg carbide at the

Table 5.2 Mössbauer derived iron carbide phases from Fe@C catalysts under reduction or carburization activation, balance of iron phase is wüstite $Fe_{1-x}O$.

Fe@C	Activation[a]	LTFT[b]
500-Red	60% α-Fe	59% ε'-$Fe_{2.2}C$
500-Carb	54% χ-Fe_5C_2, 9% ε'-$Fe_{2.2}C$	56% χ-Fe_5C_2, 8% ε'-$Fe_{2.2}C$
600-Red	56% α-Fe	68% ε'-$Fe_{2.2}C$, 11% χ-Fe_5C_2*

Data obtained from Mössbauer spectroscopy at 4.2 K after [a] reduction or carburization treatment, 3 h under atmospheric hydrogen at 400 ˚C and 96 h under 15 bar equimolar H_2/CO, respectively, and [b] after 24 h low temperature Fischer-Tropsch synthesis conditions of 20 bar equimolar H_2/CO at 230 ˚C. * Tentative.

expense of both the hexagonal carbide and oxide phase (**Figure 5.1F**). The cryogenic temperature measurements show the additional contributions of the three sites of Hägg carbide at higher velocities, and the relative spectral contribution of 43 % indicates that over 50 % of the ε'-$Fe_{2.2}C$ is converted to χ-Fe_5C_2 (**Table A5.3**). In addition, the HTFT conditions also carburize part of the oxide phase, about 27 % of spectral contribution from wüstite is present after 24 h of HTFT, indicating that 37% of $Fe_{1-x}O$ is converted toward χ-Fe_5C_2. A very similar trend is obtained for the HTFT measurements of Fe@C-600 subsequently after the LTFT reaction, where 32 % of the spectral area is assigned to ε'-$Fe_{2.2}C$ and 38 % to χ-Fe_5C_2. This phase transition is in sharp contrast to the stable Hägg carbide phase under LTFT conditions, which is obtained after carburization under HTFT conditions. It is notable that the resulting coexistence of carbide phases of these reduced and interconverted catalysts under HTFT is very similar to the spectral composition of *in situ* experiments on reduced Fe@C-600 that was directly exposed to HTFT conditions [45]. The 75 % metallic iron was transformed into 27 % ε'-$Fe_{2.2}C$ and 67 % χ-Fe_5C_2 after just 5 h under equimolar syngas at 340 ˚C and 15 bar. Even though single-phase carbides could not be synthesized through the abovementioned protocol, these results together with the associated catalytic data under HTFT further deepen the discussion on the activity and stability of iron carbides in the Fischer-Tropsch performance testing section.

The abovementioned measurements demonstrate that carbide-phase interconversion is related to the change in FTS conditions. As the temperature is increased over 100 ˚C, the FTS kinetics are increased by an order of magnitude. The higher temperature and increased conversion result in a much lower carbon chemical potential, and therefore, the thermodynamically stable state is the Hägg carbide. Indeed, significant ε'-$Fe_{2.2}C$ carbide interconversion is measured which is associated with

carbon diffusion through the lattice and crystal deformation. Therefore, both the rate and degree of interconversion may very well be dependent on the particle size and degree of carburization of the initial iron nanoparticle. However, no significant difference was observed in the degree of carburization for Fe@C-500 and 600, while the interconversion toward χ-Fe_5C_2 phase was slightly more pronounced on the former catalyst (**Figure A5.6**). Hence, it is likely that either a metastable equilibrium was achieved, or that the incremental interconversion in the deeper crystallite layers is kinetically limited by the diffusion of carbon. The trend of the developing surface carbide phase is in agreement with the carburization experiments on the fresh catalysts, where the oxide phase is gradually converted toward Hägg carbide over a period of many hours. Thus, the carburization kinetics of iron oxide, with respect to metallic iron, are several orders of magnitude slower.

In addition to the elucidation of the iron phases, the Mössbauer measurements at different temperatures enabled the calculation of the Debye temperatures for the various iron phases (**Figure 5.2**). The Debye temperature is, by approximation, proportional to the density of atoms per volume considered [56]. It is therefore considered a measure for the bond strength of the metal within the surrounding lattice and in traditional view, related to the hardness of a crystal. The logic of this interpretation is reflected by remarkably low Debye temperatures in the range of 45-170 K for highly porous MOFs and coordination polymers, in which the metal atoms are localized in molecular clusters of ionic character. The metal-metal distance and their spatial distribution greatly influence the Debye temperature, as these parameters direct the number density of the structure. The increase in the Debye temperature of Zn-MOF-74 compared to Zn-MOF-5, 170 K against 102 K, respectively, is explained by the far longer and flexible linker in the latter framework and the resulting increase in separation of the metal clusters [57, 58]. The same trend holds for MOFs comprising other metals and linkers as structural building blocks. The large-cage Gd-NBDC MOF consists of diatomic gadolinium units connected through six amino-benzenedicarboxylate linkers with Gd-Gd distances of 4.1 Å in the cluster and far larger three-dimensional spacing in the range of 10.5-12.1 Å [59]. On the other hand, the dense gadolinium-formate MOF is built up of continuous chains of nine-coordinated gadolinium ions bridged by three shared oxygen atoms of the formate ligands, resulting in Gd-Gd distances of 4.0 Å in the chains and 6.2 Å through the linkers [60]. Not surprisingly, the Debye temperature of Gd-NBDC of 45 K is far lower than the value of 168 K obtained for the Gd-formate MOF. These Debye temperatures, however, are in sharp contrast with conventional metals and metal oxides, as the values for bulk compounds are considerably higher. In the case of ferrite and magnetite these values increase to about 420-476 and 505-588 K, respectively [61-63]. The Debye temperature is therefore a good indication for the degree of interaction between the atoms in the different phases under consideration.

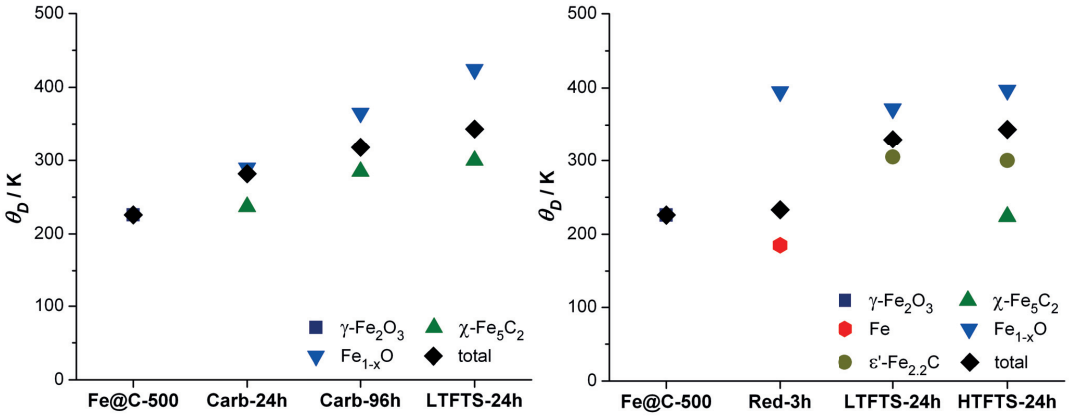

Figure 5.2 Debye temperatures of the iron phases in carburized Fe@C-500 and reduced Fe@C-500, following activation and FTS conditions.

Hence, the values of 226 K and 238 K for the fresh Fe@C-500 and Fe@C-600 catalysts are quite striking (**Table A5.6**). These Debye temperatures represent a very diffuse, perhaps even quasi-crystalline, system of iron oxide nanoparticles that is clearly derived from the atomically dispersed iron of the MOF precursor. The subsequent carburization of the Fe@C-500 catalyst produces the χ-Fe_5C_2 carbide phase, and its Debye temperature gradually increases over time to 300 K after 24 h of LTFT reaction (**Figure 5.2**). The reduction of Fe@C-500 leads to the formation of metallic iron with an even lower Debye temperature than the starting oxide of 185 K, whereas the value for wüstite reaches 395 K. The decrease in Debye temperature of metallic iron with respect to the initial oxide, in addition to the large difference between the two Debye temperatures and moreover, the large variation in the ratio to which extent bulk phase behavior value is achieved (41 ± 3 % for Fe and 76 ± 4 % for $Fe_{1-x}O$ [64]), indicates that metallic iron is formed as a surface layer on top of the iron oxide that possibly segregates in part from the bulk (**Figure 5.2**). The following exposure to LTFT conditions resulted in the formation of ε'-$Fe_{2.2}C$ carbide with a Debye temperature of 305 K, while only minor change was observed in $Fe_{1-x}O$. The Debye temperatures of the two types of iron carbides in Fe@C calculated from Mössbauer spectroscopy are nearly one third lower than theoretical estimates for bulk carbide crystals [65]. Hence, the lower bond strengths associated with a decrease in the Debye temperatures suggest a higher presence of crystal defects or lower coordination sites, related to the presence of surface atoms. Comparison of the two Debye temperatures and the degree of carburization for the two activation methods, 300 K for 56 % χ-Fe_5C_2 and 305 K for 59 % ε'-$Fe_{2.2}C$, thus demonstrate that two fundamentally different, though very similar, iron carbide phases have been produced.

5.3.2 Fischer-Tropsch Synthesis

The catalytic experiments were carried out in a fixed-bed reactor system under quasi-differential conditions in the same way as the Mössbauer experiments. The results of the catalytic tests are displayed in **Figure 5.3 and Table 5.3**, where the conversion, activity and selectivity profiles of the catalysts activated by two different methods are plotted alongside. The carburized catalysts show significant induction period during the first 70 h until reaching steady state, and similarly, changes are observed in the selectivity profiles of these catalysts. The methane selectivity drops under the initial 10 % at values between 8 and 9 %, and even though possibly correlated to the conversion levels, the effect is not as profound as the 60 % increase in activity. Similar marginal differences are found in the carbon dioxide selectivity. The initial values around 7 % are indicative of low water-gas shift activity, to be expected at these low temperatures, and they increase only little to 8.2 % for Fe@C-500 and 9.2 % for Fe@C-600 (**Table 5.3**). These carburized catalysts display an activity of 4.02 and $3.59 \cdot 10^{-5}$ mol_{CO} g_{Fe}^{-1} s^{-1}, respectively, after 115 h of LTFT. The reduced samples reach steady-state conversion readily after the first sampling interval, maintaining identical activity and selectivity profiles during 119 h reaction time. In contrast to the outstanding stability of reduced Fe@C-500 over the entire time on stream, the Fe@C-600 catalyst initially shows slight deactivation but stabilizes and also reaches steady-state operation. The selectivity of Fe@C-600 toward methane and carbon dioxide is however, very similar to the initial values. After 100 h, both catalysts show constant activity and selectivity to methane and carbon dioxide, indicating that no further reduction or carburization of the iron phase is taking place.

The observation that the carburization of α-Fe toward ε'-$Fe_{2.2}C$ takes place within the hour, is in agreement with the carbon diffusion prevalence in the iron lattice over FTS kinetics on the surface, as the carburization kinetics of ferrite are in the order of catalytic turnover numbers [27, 40]. The conversion levels obtained after one hour are maintained even after 100 h, indicative of a highly stable catalyst absent from sintering and inactive carbon deposition. The Mössbauer data after 24 h LTFT indicates that the hexagonal iron carbide is a very stable phase under the applied high carbon chemical potential, and moreover, that it can be obtained only by carburizing very small metallic iron nanoparticles. The conversion data during 140 h carburization (**Figure 5.4**) demonstrates that the increase in conversion is parallel to the carburization of the fresh catalyst toward χ-Fe_5C_2. The notable resemblance of the shapes indicates that carburization of iron oxide under HTFT conditions is very slow and that the equilibrium phase is reached much later than in the carburization of metallic iron, as the reaction rate reaches steady state after 140 h. Moreover, the shape of the conversion profile and degree of carburization suggest that the surface carbide acts as a gateway, moving the dissociated carbon down into the bulk of the iron oxide particle. Therefore, the rate of diffusion controls the rate of reaction by modifying the active site density by effectively lowering the surface

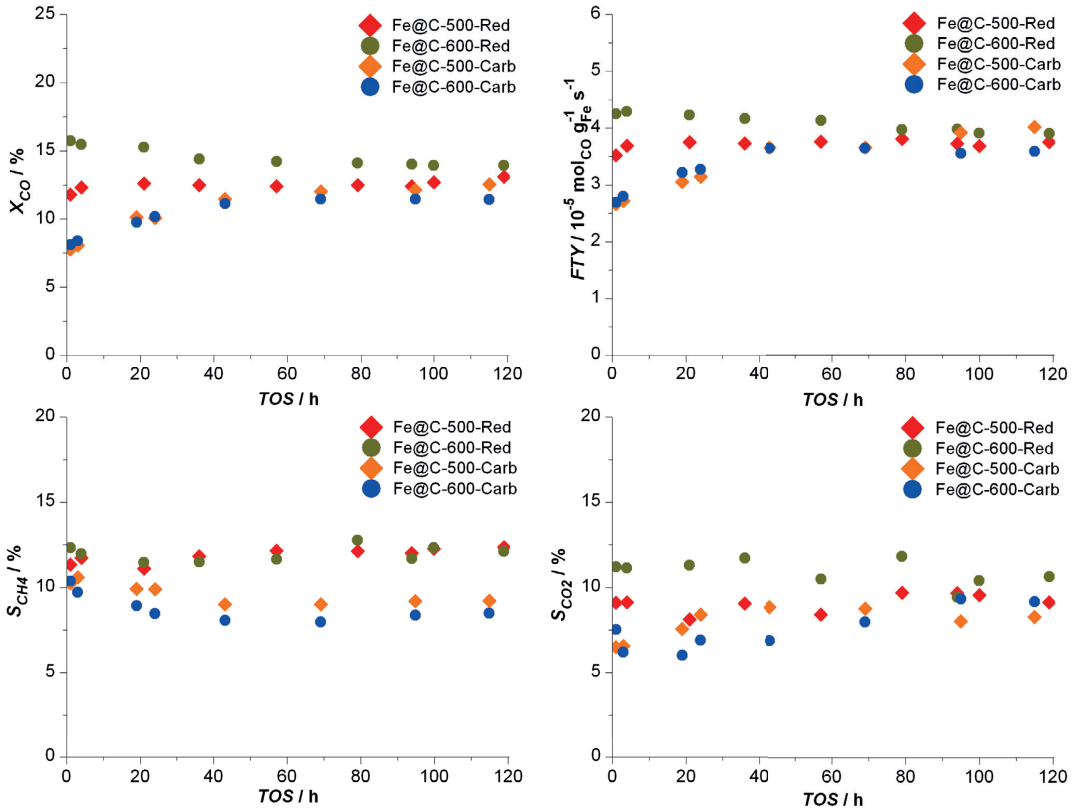

Figure 5.3 Fe@C-500 and Fe@C-600 catalytic testing results under LTFT conditions (230 ˚C, 20 bar, H_2/CO = 1, *WHSV* = 55 $dm^3_{H2/CO}$ g_{Fe}^{-1} h^{-1}, displaying the conversion profiles (X_{CO}), iron time yield (*FTY*), methane selectivity (S_{CH4}) and carbon dioxide selectivity (S_{CO2}).

Table 5.3 Catalytic performance of reduced and carburized Fe@C under LTFT conditions of 230 ˚C, 20 bar, H_2/CO = 1, *WHSV* = 55 $dm^3_{H2/CO}$ g_{Fe}^{-1} h^{-1}, product selectivities obtained between 94-99 h time on stream.

Fe@C	X_{CO} / %	*FTY* / [*]	S_{CH4} / C%	S_{CO2} / C%	S_{C2-C4} / C%	S_{C5+} / C%	α / -
500-Carb	12.5	4.02	9.2	8.2	23.3	59.3	0.72
600-Carb	11.4	3.59	8.5	9.2	22.0	60.3	0.71
500-Red	13.1	3.75	12.4	9.1	27.6	50.9	0.68
600-Red	13.9	3.90	12.1	10.6	28.2	49.1	0.67

* *FTY*, iron time yield, catalytic activity expressed as 10^{-5} mol carbon monoxide converted to hydrocarbon products per gram of iron per second, explicitly excluding carbon dioxide selectivity.

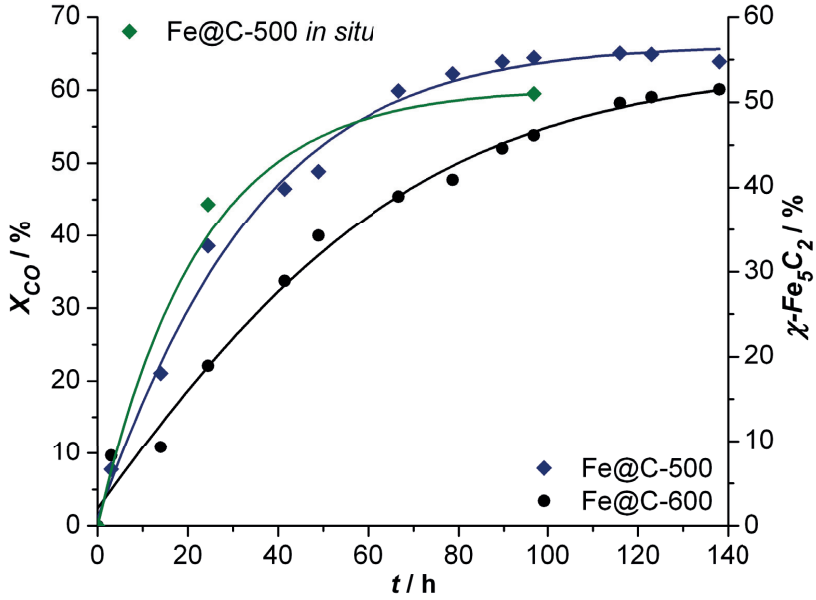

Figure 5.4 Conversion profiles obtained during catalytic testing of Fe@C-500 and -600 while carburizing the fresh catalysts under 340 ˚C, 15 bar, H_2/CO = 1, plotted alongside the spectral contribution of Hägg carbide of Fe@C-500 during carburization under identical conditions in the *in situ* Mössbauer cell.

carbide concentration. The process of reaching constant rates of reaction and degree of carburization is increased with two orders of magnitude over the iron oxides compared to metallic iron catalysts.

The dimension of the activity was casted into moles of carbon monoxide converted toward hydrocarbon products per hour, in order to compare the Fe@C results to both iron and cobalt literature values (**Table A5.7**). The activity of Fe@C catalysts at 230 ˚C is very impressive in view of the range of lower values obtained at higher temperatures for different iron catalysts. The majority of the iron catalysts remain below the activity values reported for Fe@C up to temperatures of 260-270 ˚C, where the activity increases up to a twofold for iron catalysts supported on silica and carbon nanotubes. These results demonstrate that the dispersion of iron is by far better achieved and maintained on large surface-area supports with little metal-support interaction, of which MOF-derived catalysts are the perfect example. The exception to this trend in activity and temperature is a recently reported skeletal iron catalyst, derived from an iron-alumina template that is subsequently alkali leached. The high dispersion and accessibility of the iron nanoparticles and the lower operation temperature of 200 ˚C render the formation of ε-Fe_2C. The activity of this catalyst is slightly lower, however, direct comparison is not applicable to this batch operational mode with an initial pressure of 50 bar with conversions calculated relative to the starting pressure of 30 bar (**Scheme A5.1**) [66]. The Fe@C activity compared to cobalt catalysts is similar or slightly worse, as several outliers to

higher activity are obtained for cobalt in the temperature range of 190-240 ˚C. Nevertheless, it is noteworthy that the activity of stable iron catalysts is comparable to well-dispersed cobalt catalysts.

The comparison of the Fe@C catalysts to iron supported on carbon-nanotubes under similar LTFT conditions (220 ˚C, 25 bar and H_2/CO = 2 and X_{CO} = 5-15 %) yields quite an analogous product slate. A carbon dioxide selectivity between 6.9-19.5 %, a C_3-C_7 alpha around 0.64-0.67, and an olefin content in the range of 40-70 % are in good agreement with our results [67]. Studies on coprecipitated iron-zinc catalysts impregnated with Cu, K, and Ru under LTFT conditions similar to the present research (235 ˚C, 21.4 bar and H_2/CO = 2 and X_{CO} = 13-16 %) demonstrate that extensive promotion can greatly increase the chain growth probability, decreasing the methane selectivity below 3 % and increasing the C_{5+} selectivity above 85 % [68]. The significant improvement in long-chain hydrocarbon selectivity has to be interpreted in terms of fundamental changes in physiochemical properties, rather than minor changes in hydrogenation ability from a different active carbide phase. These profoundly promoted iron catalysts comprise an even higher wax selectivity than conventional cobalt supported on zirconia-alumina catalysts, which achieve a methane selectivity of 7.9 %, C_2-C_4 selectivity of 13.7 % and a C_{5+} selectivity of 78.4 % under comparable LTFT conditions (240 ˚C, 20.7 bar, H_2/CO = 1) [69]. It is remarkable that both the FTS and WGS rates over the Fe@C catalysts under LTFT conditions are nearly identical as those over Co@C catalysts derived from ZIF-67 and MOF-74 (**Table A5.7**). However, the Fe@C methane selectivity of ~10 % is superior to the ~20 % of the cobalt catalysts [70]. The increased hydrogenation ability may however, be partially explained by the higher partial pressure of hydrogen (30 bar and H_2/CO = 2 against 20 bar and H_2/CO = 1), as C_{5+} selectivity is limited to 65 % in comparison to 60 % for the Fe@C counterpart. These results confirm that iron-based catalysts are exceptionally versatile and that highly dispersed samples can challenge the performance of cobalt-based catalysts.

The high stability of the catalytic performance is likely related to the nature of the Fe@C catalyst, comprising a high degree of Fe-C interaction through its matrix that stabilizes the iron carbide phase and apparently, does not allow sintering or migration of iron clusters. Furthermore, the catalysts do not suffer from high partial pressures of water or carbon dioxide under these differential conditions at low conversion. Above critical ratios of the partial pressure of water over hydrogen (pH_2O/pH_2) and carbon dioxide over carbon monoxide (pCO_2/pCO), as derived by O'Brien *et al.* [36], the reaction conditions yield an atmosphere where iron oxide is the thermodynamic stable phase. However, those calculations were most likely performed using the thermodynamic equilibria values at 1000 K from the original book [71], shown by recalculation in **Scheme A5.2**. At relevant reaction conditions around 500 K, the values for $-\log(pO_2)$ are a factor of 2.5 higher, resulting in pH_2O/pH_2 and pCO_2/pCO ratios several orders of magnitude larger than reported. Therefore, determining the surface concentrations of water and carbon dioxide would describe the tendency of the iron phase to oxidize more realistically. However, the importance of the WGS ability on iron catalysts is underlined,

as the log(pH_2O/pH_2) value of iron is far higher than for cobalt catalysts, confirming that iron is inherently more prone to oxidation by water than cobalt catalysts. The same calculation for the ratio pCO_2/pCO demonstrates that carbon dioxide is a substantially less oxidizing molecule than water, enhancing the catalyst stability when iron is WGS active.

The result that perhaps attracts the most attention is the methane selectivity of the reduced Fe@C samples, which is significantly higher than that of the carburized Fe@C samples. The analysis at iso-conversion levels allows for a qualitative comparison of the methane selectivity between the two activation methods for the same catalysts: ~9 % methane for carburized samples compared to ~12% methane for the reduced catalysts (**Table 5.3**). On the contrary, the activity of all catalysts is nearly equal after reaching steady-state operation. Comparing the Fe@C-500 activity under reduction and carburization, the difference is below 8 %, and for the Fe@C-600 it is below 9 %. The product distribution furthermore underlines the difference between selectivities of the carburized and reduced Fe@C catalysts. Though the calculated values for the chain growth probability are very alike, it seems that the decrease in methane selectivity for the carburized samples is related to an increase in long-chain hydrocarbon selectivity (**Table 5.3**). While the methane selectivity is about 25 % lower than for the reduced samples, the relative increase in C_2-C_4 is ~21 % and in C_{5+} is ~20 %. The bar graphs for the carbon selectivity in **Figure A5.7** additionally demonstrate the trend toward an increase in long-chain hydrocarbon selectivity for the carburized samples. This trend in selectivity suggests that the overall hydrogenation ability of the carburized catalysts is lower than that of the reduced samples. Comparison to the theoretical Flory and Schulz distributions plotted in **Figure A5.8** displays that alpha values of 0.7 ± 0.05, in line with the accuracy of the calculated values from FTS experiments, indeed correspond to a methane selectivity between 7-13 %. The CO_2-free methane selectivities for the four experiments are in agreement with the theoretical values, though the carburized samples comprising methane selectivities between 9-10 % correspond more to alpha equal or larger to 0.7, whereas the reduced samples with methane selectivities around 13.5 % are more in the range of alpha equal or below 0.65. Additionally, the CO_2-free C_2-C_4 selectivities for all samples in the range of 24.2-31.5 % are notably lower than the theoretical values, suggesting marginally higher alpha values around 0.75 for reduced samples and 0.8 for carburized samples. Comparable differences in selectivity for reduced and carburized precipitated iron catalysts were obtained by Bukur *et al.* in both fixed bed and slurry phase FTS experiments [34, 38]. For reduced samples, the methane selectivity was higher while a lower C_{5+} selectivity was obtained in comparison to carburized catalysts. The authors postulated that the surface hydrogen concentration is higher on reduced catalysts, as ferrite would possess a larger number of sites for hydrogen adsorption or enhanced hydrogen dissociation ability, therefore altering the occupation of elemental hydrogen. Hence, carburization indeed leads to increased long-chain hydrocarbon selectivity in comparison to reduction possibly by decreasing the hydrogenation ability of the surface.

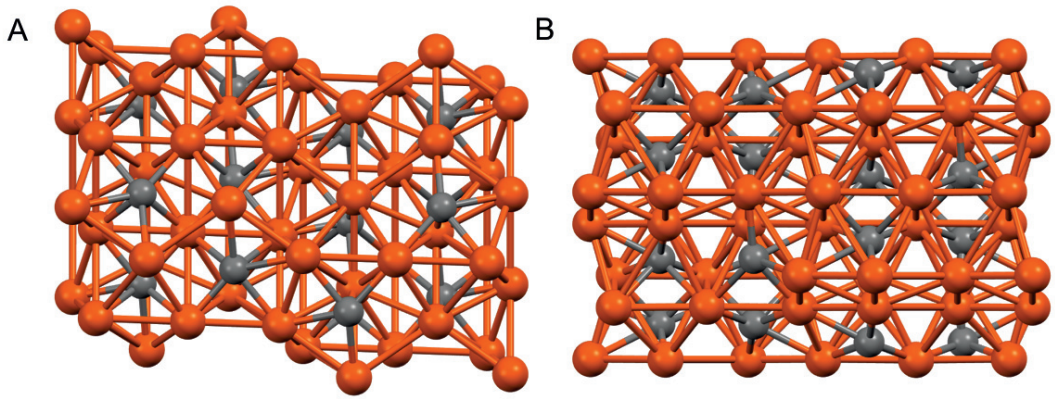

Figure 5.5 Crystallographic structures of **A** hexagonal carbide ε'-$Fe_{2.2}C$ and **B** Hägg carbide χ-Fe_5C_2 viewed along the c-axis. Iron atoms are depicted as orange spheres and carbon atoms as grey spheres [17, 72]

The key question remains why the product selectivity of the two carbide phases in Fe@C is different. Closely examining the structure of the carbides, it is observed that ε'-$Fe_{2.2}C$ comprises a moderately higher atomic carbon to iron ratio of 0.45 compared to 0.4 for χ-Fe_5C_2, and the interstitial occupation of the carbon atoms is quite different (**Figure 5.5**). The carbon atoms in the hexagonal lattice of ε'-$Fe_{2.2}C$ are located in the octahedral site, whereas the carbon in monoclinic χ-Fe_5C_2 is located in the trigonal prismatic interstice. This could suggest that a different active site might be built on the surface of the carbide, which possesses different electron density or exposed crystal facets. The hydrogenation ability might therefore be altered, rendering differences in the adsorption-desorption strengths or in the reaction intermediate stabilization through a different kinetic pathway. However, keeping in mind that the equal levels of activity obtained in this study suggest that the number density of these active sites is controlled by the nanoparticle size and that the nature of the active sites must be rather similar. These conclusions coincide with DFT studies on different iron carbide surfaces, demonstrating that different Hägg carbide surfaces comprise very similar surface energies [73]. Larger differences between the adsorption energy of CO exist on vacancy sites and alternative sites on the χ-Fe_5C_2 surface, indicating that stepped and corrugated surfaces play an important role in adsorption and activation of carbon monoxide on iron carbide surfaces [74]. Furthermore, carbon monoxide adsorption on sites comprising more iron atoms displays progressively weakening of the CO bond with increasing number of bonds to iron atoms, suggesting the type of carbide can play a role in performance [75]. Therefore, the formation of unique iron carbide surface sites may result in intrinsic selectivity differences giving rise to a notable 25 % change in hydrogenation ability. However, at this stage, it is not confirmed nor rejected that other factors than the iron nature are at play.

Differences in selectivity between hydrogen-reduced and syngas-carburized iron catalysts are not unknown for iron catalysts [76]. However, where early Ruhrchemie studies report identical behavior in selectivity for hydrogen-reduced and syngas-carburized iron catalysts compared to Fe@C catalysts in this work, no conclusive characterization for iron dispersion, deactivation, and iron phases was reported to interpret the results with regard to the iron carbide phase [77]. Elaborate work by Bukur *et al.* on the effect of pretreatment conditions on the catalytic performance iron catalysts confirmed the abovementioned results [34]. The hydrogen-reduced catalysts comprised higher overall hydrogenation ability than carburized catalysts, witnessed by an increased methane production and decreased C_{5+} selectivity. Mössbauer characterization of the spent catalysts showed that ε'-$Fe_{2.2}C$ was the dominant phase for the reduced catalysts, obtaining values between 57 % and 95 % of hexagonal carbide. The dominant phase of the carburized samples was Hägg carbide, with values ranging between 65 % and 94 % of χ-Fe_5C_2. Whilst these results coincide with the present study, most of the samples drawn from the reactor displayed mixtures of several carbides and oxides. Furthermore, severe deactivation of the carburized samples and overall integral reactor operation with large variation in conversion over time resulted in large differences between catalyst composition and carbide phases, not allowing for an unequivocal correlation between the iron carbide phase and selectivity. Nevertheless, a more general effect of the activation method on the catalyst selectivity was established, as it was postulated that differences in selectivity originate from the change in relative hydrogen coverage obtained after reduction and carburization. The formation of metallic iron would be key to promote higher hydrogen coverage on the iron catalyst surface. The increasing coverage for hydrogen would increase stability during FTS, as less inactive carbon is deactivating the catalytic surface.

To display the subtlety of intrinsic iron carbide performance quantification, HTFT performance results of reduced Fe@C catalysts are plotted alongside those of carburized samples, where activation is directly followed by HTFT reaction conditions (**Figure 5.6**). Both the activity and selectivity of the carburized and reduced catalysts are indistinguishable under HTFT (**Table A5.8**). From the abovementioned Mössbauer analysis, it is found that Fe@C-600 carburization and HTFT after 24 h produces 30 % of ε'-$Fe_{2.2}C$ and 43 % of χ-Fe_5C_2, whereas reduction of Fe@C-600 and subsequent HTFT produces 27 % of ε'-$Fe_{2.2}C$ and 67 % of χ-Fe_5C_2 after just 5 h under equal HTFT conditions. Hence, irrespective of the activation method, the HTFT conditions result in a coexistence of carbide phases in the Fe@C catalysts. The performance results for these catalysts are unmistakably identical, now with the Hägg carbide as the dominant phase. The Debye temperature of 224 K for the Hägg carbide formed on the reduced Fe@C-500 catalyst (**Figure 5.2**) resembles the value for the fresh Fe@C-500 which is carburized under HTFT for 24 h. Additionally, half of the ε'-$Fe_{2.2}C$ carbide phase of reduced Fe@C-500 is converted to χ-Fe_5C_2 under HTFT conditions, and the carburization toward Hägg carbide from the oxide phase is confirmed as well. This interconversion indicates that

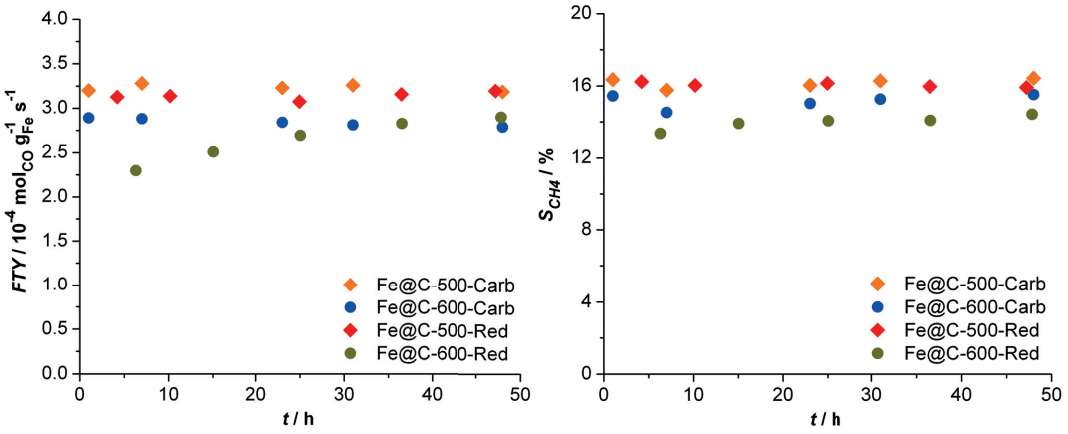

Figure 5.6 Fe@C-500 and Fe@C-600 catalytic testing results under HTFT conditions (340 ˚C, 20 bar, H_2/CO = 1, *WHSV* = 120 $dm^3_{H2/CO}$ g_{Fe}^{-1} h^{-1}, displaying the iron time yield (*FTY*) and methane selectivity (S_{CH4}).

the carbon chemical potential of the HTFT conditions dictates the sole formation of χ-Fe_5C_2 on the iron surface, rendering the identical performance on both catalysts now evident. The combined analysis of the two FTS temperature regimes underlines the importance of the controlled carbide phase formation and appropriate operating conditions to enable comparison of activity and selectivity. These results provide a firm basis to assign the difference in methane and long-chain hydrocarbon selectivity to the single-phase presence of ε'-$Fe_{2.2}C$ and χ-Fe_5C_2.

5.3.3 Transmission Electron Microscopy

In order to rule out differences in iron carbide phases and catalytic performance originating from changes in the iron dispersion, TEM analysis is reported for the fresh and spent catalysts (**Figure 5.7 and Figure A5.10**). Both the fresh and spent catalysts were extremely prone to oxidation, as no carbide phases were detected after exposure to 5 % oxygen in helium at room temperature. Both fresh and spent samples are characterized by a high density of spherical particles placed randomly throughout the carbon matrix. The small iron nanoparticles possess remarkably low contrast compared to the carbon matrix, in addition to the absence of lattice fringes or clear crystallite domains. Quantitative analysis established the average particle size of the fresh Fe@C-500 at 3.6 nm, obtaining a unimodal normal distribution for the monodisperse iron (**Figure A5.9A**). Because of the pyrolysis temperature effect, as extensively investigated previously, the particle size of Fe@C-600 increased to an average of 6.0 nm (**Table 5.4**). In addition to the high dispersion, the two catalysts comprise a very low degree of agglomerates, as only 5 % of the particles is present in size above 10 nm. Lattice fringes are only visible on the larger nanoparticles at the edges of the catalyst grains, where values of 0.246 nm and 0.207 nm are calculated for Fe@C-500, and 0.236 nm and

0.196 nm for Fe@C-600. These spacings correspond to the 311 and 400 plane of γ-Fe_2O_3, respectively, confirming the oxidized nature of the fresh samples. The electron diffraction patterns of the bulk phase show very weak and broad rings of polycrystalline iron oxides, likely because of the small average particle size of the sample (**Figure A5.11A**). Micrographs of the somewhat larger particles on the outskirts of the carbon matrix clearly show the presence of graphitic shells around the particles.

The spent analysis of the both the carburized and reduced samples show that the dispersion is very well maintained. Micrographs contain a high density of isolated nanoparticles with low contrast to the carbon matrix. Carburization of the Fe@C-500 and -600 catalysts at 340 ˚C for 140 h and additional LTFT for 100 h produces iron nanoparticles with average size of 4.2 nm and 6.5 nm, respectively (**Table 5.4**). Compared to 3.6 nm and 6.0 nm for the fresh samples, these results are indicative of very stable catalysts, suffering from only minor particle growth during operation. Moreover, only the outskirts of the catalyst grains display particle growth, while in the bulk of the catalysts there is virtually no difference between the fresh and spent particles (**Figure A5.10B**). The high stability can be explained by the homogenous embedding of the iron nanoparticles in the carbon matrix, effectively eliminating severe sintering effects like particle migration and coalescence. Though the particle size distributions show that monodispersion is maintained, the width of the curves has broadened (**Figure A5.9B,E**). Additionally, the curves display a positive skew and are consequently better represented by a log normal fit, in contrast to the Gaussian curves of the fresh samples. These characteristics suggest that Ostwald ripening is the sintering mechanism that produces the minor increase in particle size distribution [78]. However, the typical behavior of enhanced sintering on smaller nanoparticles is applicable to the Fe@C catalysts as well, as the increase in average particle size was more profound on Fe@C-500 than on Fe@C-600 regardless of the activation protocol [79].

Reduction of Fe@C500 and -600 catalysts and subsequent LTFT reaction for 100 h produces very similar particle size distributions, yet comprising slightly larger average sizes: 4.4 nm and 6.9 nm, respectively (**Table 5.4**). No additional differences between reduced and carburized samples are observed from the images, except for a small increase in the average particle size of the reduced catalyst. Moreover, the extraction of the modal value from the histograms, i.e., the most frequent particle size disregarding the skew in the log normal distributions, confirms identical particle sizes for the different activation methods (**Figure A5.9C,F**). Furthermore, the electron diffraction patterns of spent samples are quite diffuse like the fresh samples, where the polycrystalline γ-Fe_2O_3 phase is now identified due of the presence of four diffraction rings with corresponding *d*-spacing (**Figure A5.11B**). Additionally, the very small number of bright spots present in the ring pattern confirm that agglomeration is effectively hindered on Fe@C catalysts. Thus, the iron dispersion was maintained after activation and prolonged hours of FTS operation, without a substantial increase in average

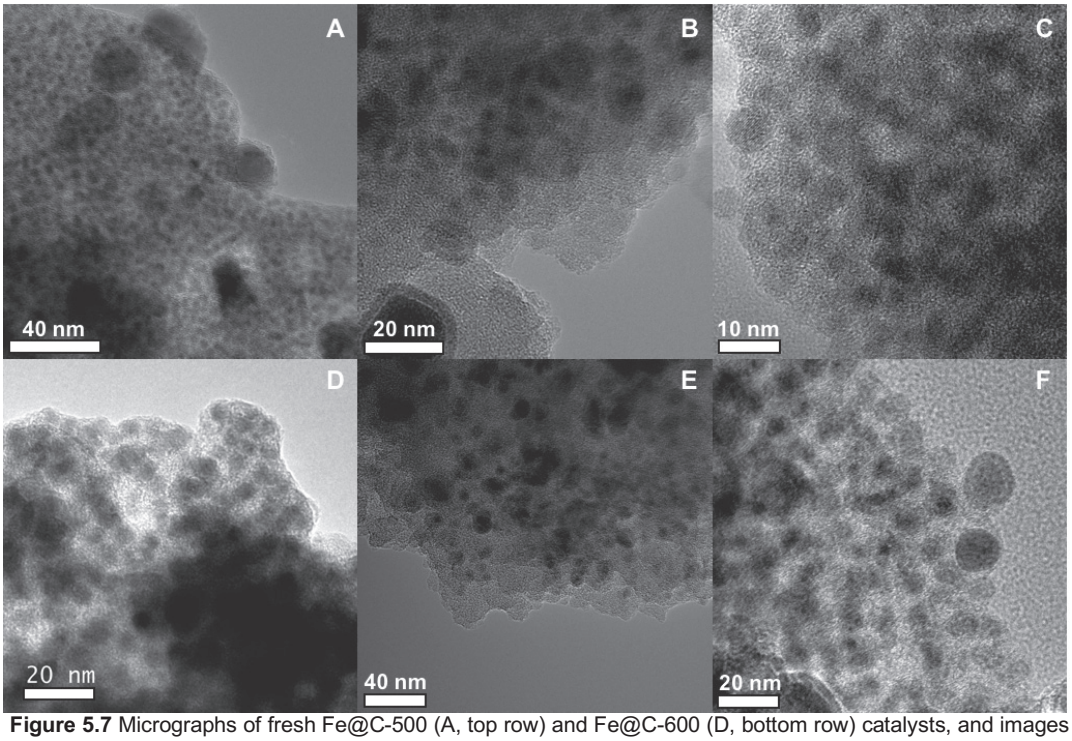

Figure 5.7 Micrographs of fresh Fe@C-500 (A, top row) and Fe@C-600 (D, bottom row) catalysts, and images of spent catalysts after 140 h carburization and 120 h LTFT (B,E) and after 3 h reduction and 120 h LTFT (C,F) under different magnification. The small iron nanoparticles embedded in the carbon matrix are visible as low-contrast dark circles, in comparison to the lighter carbon matrix.

particle size. This profound stability allows measuring intrinsic activity and selectivity without the effects of differences in catalytic surface area and particle morphology effects.

Table 5.4 Average particle size of pre- and post-reaction Fe@C catalysts after 120 h LTFT reaction using different activation procedures.

Catalyst	Fresh	Carburized		Reduced	
	Average / nm	Average / nm	Mode / nm	Average / nm	Mode / nm
Fe@C-500	3.6 ± 0.1 nm	4.2 ± 0.3	4.0 ± 0.5	4.4 ± 0.5	4.0 ± 0.5
Fe@C-600	6.0 ± 0.2 nm	6.5 ± 0.5	7.0 ± 0.5	6.9 ± 0.5	7.0 ± 0.5

Differences in selectivity arising from the change in relative coverage because of particle size effects can be investigated looking at the catalytic performance of the Fe@C-500 and Fe@C-600. The latter comprises a much larger average particle size of the spent catalysts between 6.5-6.9 nm compared to the smaller average particle size of spent Fe@C-500 between 4.2-4.4 nm. Isotopic labelling studies on Fe-CNT under HTFT conditions display that higher CH_x coverages and lower H coverages on Hägg carbides are found for increasing particles sizes [80]. However, the difference in hydrocarbon selectivity was only visible with a change in activation method for both catalysts comprising different particle size (**Figure 5.3 and Table 5.3**). Hence, it is concluded that the variation in product selectivity is associated with the difference in iron carbide phase, effectively ruling out particle size effects.

5.4 Conclusions

In this work, Fe@C catalysts were used to produce single-phase iron carbides in a controlled manner for their performance assessment in Fischer-Tropsch synthesis. Postulates from literature indicating that supported, highly-dispersed iron catalysts are needed to stabilize a high degree of carbon incorporation into the lattice are confirmed, as single phase ε'-$Fe_{2.2}C$ and χ-Fe_5C_2 were synthesized from 3.6 nm iron nanoparticles. Fe@C catalysts that are reduced and carburized render the formation of hexagonal ε'-$Fe_{2.2}C$ and Hägg χ-Fe_5C_2 carbide under LTFT, respectively, with a similar degree of carburization, particle size and stability. Thus, the different activation methods provided control over the iron phase under steady-state LTFT, whereas other physiochemical properties were not altered. It is found that ε'-$Fe_{2.2}C$ and χ-Fe_5C_2 possess equal catalytic activity in the particle size range of 3.6-6.0 nm, however, between the two activation methods there is a clear difference in selectivity. The increased hydrogenation ability of the ε'-$Fe_{2.2}C$ iron phase, demonstrated by a higher methane selectivity and lower C_{5+} selectivity, indicates that there are deviations in the surface chemistry of the two carbides. These deviations originate either from intrinsic differences of the surface sites formed on the two types of iron carbides, or are related to the differences in relative coverage of hydrogen and carbon following the activation procedure. The activity of Fe@C catalysts under LTFT at 230 ˚C is noteworthy, as other iron catalysts remain below Fe@C activity values up to operating temperatures of 260-270 ˚C. The necessity of LTFT operation to maintain single-phase ε'-$Fe_{2.2}C$ carbide was verified with additional experiments of Fe@C under HTFT conditions, causing interconversion of ε'-$Fe_{2.2}C$ into a mixture of χ-Fe_5C_2 and ε'-$Fe_{2.2}C$ under the lower carbon chemical potential conditions. A similar coexistence of iron carbide phases was obtained for directly carburized catalysts, and comparison under HTFT resulted identical activity and selectivity for both reduced and carburized Fe@C catalysts. Spent catalysts of the LTFT performance tests were examined by TEM and confirmed that the high iron dispersion was maintained, demonstrating the absence of sintering phenomena that cause formation of large inactive iron clusters and interconversion of iron carbide

phases. The retained dispersion furthermore confirms that the difference in catalyst selectivity is only obtained by the different activation methods for both catalysts with similar particle size. Hence, it is concluded that the variation in product selectivity is likely associated to the different iron carbide phases.

References

[1] Fischer, F., Tropsch, H., *Brennst.-Chem.*, 7 (**1926**) 97.
[2] Fischer, F., Tropsch, H., *Brennst.-Chem.*, 11 (**1930**) 489.
[3] Fischer, F., Tropsch, H., *Ges. Abh. Kenntn. Kohle*, 10 (**1930**) 313.
[4] Pichler, H., Kruger, E., *Brennstoff-Chemie*, 47 (**1966**) 368.
[5] Malan, O.G., Louw, J.D., Ferreira, L.C., *Brennst.-Chem.*, 42 (**1961**) 209-212.
[6] Barton, G.H., Gale, B., *Acta Crystallogr.*, 17 (**1964**) 1460-1462.
[7] Eckstrom, H.C., Adcock, W.A., *J. Am. Chem. Soc.*, 72 (**1950**) 1042-1043.
[8] Fasiska, E.J., Jeffrey, G.A., *Acta Crystallogr.*, 19 (**1965**) 463-471.
[9] Hägg, G., *Z. Kristallogr.*, 89 (**1934**) 92.
[10] Hofer, L.J.E., Cohn, E.M., Peebles, W.C., *J. Am. Chem. Soc.*, 71 (**1949**) 189-195.
[11] Hofmann, U., Groll, E., *Z. Anorg. Allg. Chem.*, 191 (**1930**) 414-428.
[12] Senateur, J.P., Fruchart, R., Michel, A., *Compt. Rend.*, 255 (**1962**) 1615.
[13] Herbstein, F.H., Snyman, J.A., *Inorg. Chem.*, 3 (**1964**) 894-896.
[14] Ron, M., Mathalone, Z., *Physical Review B*, 4 (**1971**) 774-777.
[15] Mitchell, J.J., *J. Chem. Phys.*, 21 (**1953**) 1153-1159.
[16] Pichler, H., Merkel, H., *Brennst.-Chem.*, 31 (**1950**) 33-42.
[17] Nagakura, S., *J. Phys. Soc. Jpn.*, 14 (**1959**) 186-195.
[18] Mitchell, J.J., *The Journal of Chemical Physics*, 21 (**1953**) 1153-1159.
[19] Shultz, J.F., Hall, W.K., Seligman, B., Anderson, R.B., *J. Am. Chem. Soc.*, 77 (**1955**) 213-221.
[20] Bernas, H., Campbell, I.A., Fruchart, R., *J. Phys. Chem. Solids*, 28 (**1967**) 17-24.
[21] Amelse, J.A., Butt, J.B., Schwartz, L.H., *J. Phys. Chem.*, 82 (**1978**) 558-563.
[22] Raupp, G.B., Delgass, W.N., *J. Catal.*, 58 (**1979**) 348-360.
[23] Raupp, G.B., Delgass, W.N., *J. Catal.*, 58 (**1979**) 337-347.
[24] Raupp, G.B., Delgass, W.N., *J. Catal.*, 58 (**1979**) 361-369.
[25] Schäfer-Stahl, H., *Angew. Chem. Int. Ed.*, 19 (**1980**) 729-731.
[26] Niemantsverdriet, J.W., Van der Kraan, A.M., Van Dijk, W.L., Van der Baan, H.S., *J. Phys. Chem.*, 84 (**1980**) 3363-3370.
[27] Niemantsverdriet, J.W., van der Kraan, A.M., *J. Catal.*, 72 (**1981**) 385-388.
[28] Jung, H.J., Vannice, M.A., Mulay, L.N., Stanfield, R.M., Delgass, W.N., *J. Catal.*, 76 (**1982**) 208-224.
[29] Jung, H.J., Walker, P.L., Vannice, A., *J. Catal.*, 75 (**1982**) 416-422.
[30] Reymond, J.P., Mériaudeau, P., Teichner, S.J., *J. Catal.*, 75 (**1982**) 39-48.
[31] Blanchard, F., Reymond, J.P., Pommier, B., Teichner, S.J., *J. Mol. Catal.*, 17 (**1982**) 171-181.
[32] Kuivila, C.S., Stair, P.C., Butt, J.B., *J. Catal.*, 118 (**1989**) 299-311.
[33] Dictor, R.A., Bell, A.T., *J. Catal.*, 97 (**1986**) 121-136.
[34] Bukur, D.B., Koranne, M., Lang, X., Rao, K.R.P.M., Huffman, G.P., *Appl. Catal., A*, 126 (**1995**) 85-113.
[35] Shroff, M.D., Kalakkad, D.S., Coulter, K.E., Kohler, S.D., Harrington, M.S., Jackson, N.B., Sault, A.G., Datye, A.K., *J. Catal.*, 156 (**1995**) 185-207.
[36] O'Brien, R.J., Xu, L., Spicer, R.L., Davis, B.H., *Energy & Fuels*, 10 (**1996**) 921-926.
[37] Herreyre, S., Gadelle, P., Moral, P., Millet, J.M.M., *J. Phys. Chem. Solids*, 58 (**1997**) 1539-1545.
[38] Bukur, D.B., Lang, X., Ding, Y., *Appl. Catal., A*, 186 (**1999**) 255-275.
[39] Li, S., O'Brien, R.J., Meitzner, G.D., Hamdeh, H., Davis, B.H., Iglesia, E., *Appl. Catal., A*, 219 (**2001**) 215-222.
[40] Li, S., Ding, W., Meitzner, G.D., Iglesia, E., *J. Phys. Chem. B*, 106 (**2002**) 85-91.
[41] Hao, Q., Bai, L., Xiang, H., Li, Y., *J. Nat. Gas Chem.*, 18 (**2009**) 429-435.
[42] de Smit, E., Cinquini, F., Beale, A.M., Safonova, O.V., van Beek, W., Sautet, P., Weckhuysen, B.M., *J. Am. Chem. Soc.*, 132 (**2010**) 14928-14941.
[43] Santos, V.P., Wezendonk, T.A., Jaén, J.J.D., Dugulan, A.I., Nasalevich, M.A., Islam, H.-U., Chojecki, A., Sartipi, S., Sun, X., Hakeem, A.A., Koeken, A.C.J., Ruitenbeek, M., Davidian, T., Meima, G.R., Sankar, G., Kapteijn, F., Makkee, M., Gascon, J., *Nat Commun*, 6 (**2015**) 1-8.

[44] Wezendonk, T., Warringa, Q.S.E., Da Costa Oliveira Santos Silva, V., Chojecki, A., Ruitenbeek, M., Meima, G., Makkee, M., Kapteijn, F., Gascon, J., *Faraday Discuss.*, (**2016**).
[45] Wezendonk, T.A., Santos, V.P., Nasalevich, M.A., Warringa, Q.S.E., Dugulan, A.I., Chojecki, A., Koeken, A.C.J., Ruitenbeek, M., Meima, G., Islam, H.-U., Sankar, G., Makkee, M., Kapteijn, F., Gascon, J., *ACS Catal.*, 6 (**2016**) 3236-3247.
[46] Sartipi, S., Jansma, H., Bosma, D., Boshuizen, B., Makkee, M., Gascon, J., Kapteijn, F., *Rev. Sci. Instrum.*, 84 (**2013**) 124101.
[47] Klencsár, Z., *Nucl. Instrum. Methods Phys. Res., Sect. B*, 129 (**1997**) 527-533.
[48] Alves Jr, N., Caetano, E.P., Rodríguez, V.P., Baggio-Saitovitch, E., Determination of Debye Temperature from Mössbauer Data, in, Centro Brasileiro de Pesquisas Fisicas (CBPF), 1995.
[49] De Grave, E., Verbeeck, A.E., Chambaere, D.G., *Phys. Lett. A*, 107 (**1985**) 181-184.
[50] McCammon, C.A., Price, D.C., *Phys. Chem. Miner.*, 11 250-254.
[51] Hazen, R.M., Jeanloz, R., *Rev. Geophys.*, 22 (**1984**) 37-46.
[52] Bauer, E., Pianelli, A., *Mater. Res. Bull.*, 15 (**1980**) 177-188.
[53] Le Caer, G., Dubois, J.M., Senateur, J.P., *J. Solid State Chem.*, 19 (**1976**) 19-28.
[54] Barinov, V.A., Tsurin, V.A., Kazantsev, V.A., Surikov, V.T., *Phys. Met. Metallography*, 115 (**2014**) 53-68.
[55] Amelse, J.A., Schwartz, L.H., Butt, J.B., *J. Catal.*, 72 (**1981**) 95-110.
[56] Van Sciver, S.W., *Low-Temperature Materials Properties*, in: S.W. Van Sciver (Ed.) Helium Cryogenics, Springer New York, New York, NY, **2012**, pp. 17-58.
[57] Canepa, P., Tan, K., Du, Y., Lu, H., Chabal, Y.J., Thonhauser, T., *J. Mater. Chem. A*, 3 (**2015**) 986-995.
[58] Huang, B.L., McGaughey, A.J.H., Kaviany, M., *Int. J. Heat Mass Transf.*, 50 (**2007**) 393-404.
[59] Lorusso, G., Palacios, M.A., Nichol, G.S., Brechin, E.K., Roubeau, O., Evangelisti, M., *Chem. Commun.*, 48 (**2012**) 7592-7594.
[60] Lorusso, G., Sharples, J.W., Palacios, E., Roubeau, O., Brechin, E.K., Sessoli, R., Rossin, A., Tuna, F., McInnes, E.J.L., Collison, D., Evangelisti, M., *Adv. Mater.*, 25 (**2013**) 4653-4656.
[61] Fe3O4: heat capacity, Debye temperature: Datasheet from Landolt-Börnstein - Group III Condensed Matter · Volume 41D: "Non-Tetrahedrally Bonded Binary Compounds II" SpringerMaterials, in: P. Villars (Ed.), Springer-Verlag Berlin Heidelberg.
[62] Fe rt m Debye/Einstein temperature: Datasheet from “Pauling File Multinaries Edition – 2012" SpringerMaterials, in: P. Villars (Ed.), Springer-Verlag Berlin Heidelberg; Material Phases Data System (MPDS), Switzerland; and National Institute for Materials Science (NIMS), Japan.
[63] Fe3O4 lt rhom Debye/Einstein temperature: Datasheet from "Pauling File Multinaries Edition – 2012" SpringerMaterials, in: P. Villars (Ed.), Springer-Verlag Berlin Heidelberg; Material Phases Data System (MPDS), Switzerland; and National Institute for Materials Science (NIMS), Japan.
[64] FeO (Fe(1-x)O): elastic moduli, Debye temperature: Datasheet from Landolt-Börnstein - Group III Condensed Matter · Volume 41D: "Non-Tetrahedrally Bonded Binary Compounds II" SpringerMaterials, in: O. Madelung, U. Rössler, M. Schulz (Eds.), Springer-Verlag Berlin Heidelberg.
[65] Guillermet, A.F., Grimvall, G., *J. Phys. Chem. Solids*, 53 (**1992**) 105-125.
[66] Xu, K., Sun, B., Lin, J., Wen, W., Pei, Y., Yan, S., Qiao, M., Zhang, X., Zong, B., *Nat Commun*, 5 (**2014**).
[67] van Steen, E., Prinsloo, F.F., *Catal. Today*, 71 (**2002**) 327-334.
[68] Li, S., Krishnamoorthy, S., Li, A., Meitzner, G.D., Iglesia, E., *J. Catal.*, 206 (**2002**) 202-217.
[69] Withers, H.P., Eliezer, K.F., Mitchell, J.W., *Ind. Eng. Chem. Res.*, 29 (**1990**) 1807-1814.
[70] Qiu, B., Yang, C., Guo, W., Xu, Y., Liang, Z., Ma, D., Zou, R., *J. Mater. Chem. A*, 5 (**2017**) 8081-8086.
[71] Reed, T.B., *Free Energy of Formation of Binary Compounds: An Atlas of Charts for High-Temperature Chemical Calculations*, MIT Press, Cambridge, MA, **1971**.
[72] Retief, J.J., *Powder Diffr.*, 14 (**2013**) 130-132.
[73] Steynberg, P.J., Berg, J.A.v.d., Rensburg, W.J.v., *J. Phys.: Condens. Matter*, 20 (**2008**) 064238.
[74] Petersen, M.A., van den Berg, J.-A., van Rensburg, W.J., *J. Phys. Chem. C*, 114 (**2010**) 7863-7879.
[75] Sorescu, D.C., *J. Phys. Chem. C*, 113 (**2009**) 9256-9274.
[76] Anderson, R.B., *Catalysis*, in: P.H. Emmett (Ed.), Van Nostrand-Reinhold, New York, **1956**, pp. 29.
[77] Storch, H.H., Golumbic, N., Anderson, R.B., *The Fischer-Tropsch and Related Syntheses*, John Wiley & Sons, Inc., New York, **1951**.
[78] Hansen, T.W., DeLaRiva, A.T., Challa, S.R., Datye, A.K., *Acc. Chem. Res.*, 46 (**2013**) 1720-1730.

[79] Torres Galvis, H.M., Bitter, J.H., Davidian, T., Ruitenbeek, M., Dugulan, A.I., de Jong, K.P., *J. Am. Chem. Soc.*, 134 (**2012**) 16207-16215.
[80] Xie, J., Yang, J., Dugulan, A.I., Holmen, A., Chen, D., de Jong, K.P., Louwerse, M.J., *ACS Catal.*, 6 (**2016**) 3147-3157.

Annex

5

Controlled Formation of Iron Carbides and their Performance in Fischer-Tropsch Synthesis

A5.1 Experimental

FTS experiments were performed in a six-flow fixed-bed microreactor setup designed in the Catalysis Engineering group of TU Delft [1]. The reactor consists of five heating blocks with separate temperature controllers to ensure a flat isothermal zone along the reactor inserts with inner diameter of 4 mm (Figure S1). In order to stabilize the process pressure at high conversion levels, a trace of inert gas (N_2) was injected downstream the reactor to each flow. The nitrogen gas was used as an internal standard for the online gas analysis. Between 130-150 mg of fresh catalyst particles of sieve fraction 100-250 micron were mixed with SiC of the same size and diluted three times on volume after which the packing was loaded onto quartz wool plugs in the reactor inserts. Samples were first activated *in situ* by 80 cm^3_{STP} min^{-1} of H_2 at 400 ˚C for 3 h under atmospheric pressure followed by cooling down to 230 ˚C under H_2 flow. After increasing the pressure to the process value of 20 bar, the total flow was reduced to 50 cm^3_{STP} min^{-1} and CO was gradually introduced to the feed stream in order to reach its final concentration (H_2/CO = 1) in 1 h. A rate of 2 ˚C min^{-1} was applied for all the heating/cooling steps. Permanent gases as well as light hydrocarbons in the gas phase were analyzed online by a Compact GC (Interscience), equipped with three columns and detectors in parallel, applying He as carrier gas. In the first column (Carboxen 1010, 10 m × 0.32 mm) N_2, CO, CH_4 and CO_2 were separated at 60 ˚C and analyzed by TCD. In the second column (Al_2O_3/KCl, 10 m × 0.32 mm) and FID detection, separation between all C_1–C_5 components was achieved at 160 ˚C. In the third column (RTx-1 0.5µm, 15 m × 0.32 mm) C_5–C_{10} hydrocarbons were separated at 80 ˚C and analyzed by FID. After steady-state catalytic behavior was obtained, selectivity data were collected and the carbon balance was satisfied by 100 ± 5%. CO conversion, carbon selectivity and molar fraction of each product were defined by equations (1), (2) and (3), respectively, where X_{CO} stands for CO conversion, F indicates the molar flow, S is the carbon selectivity of a product with n carbon number and y is its molar fraction. Alpha was determined through the exponential of the slope of the Anderson-Schulz-Flory [2] (ASF) natural logarithmic plot in the C_3-C_7 range. Catalytic activity is expressed as iron time yield (*FTY*), defined as the number of CO moles converted to hydrocarbons per gram of iron per second.

$$X_{CO} = \frac{F_{in,CO} - F_{out,CO}}{F_{in,CO}} \times 100 \qquad (1), \qquad S_{Cn} = \frac{nF_{Cn}}{F_{CO_2} + \sum_{n=1}^{N} nF_{Cn}} \times 100 \qquad (2), \qquad y_{Cn} = \frac{F_{Cn}}{\sum_{n=1}^{N} F_{Cn}} \qquad (3)$$

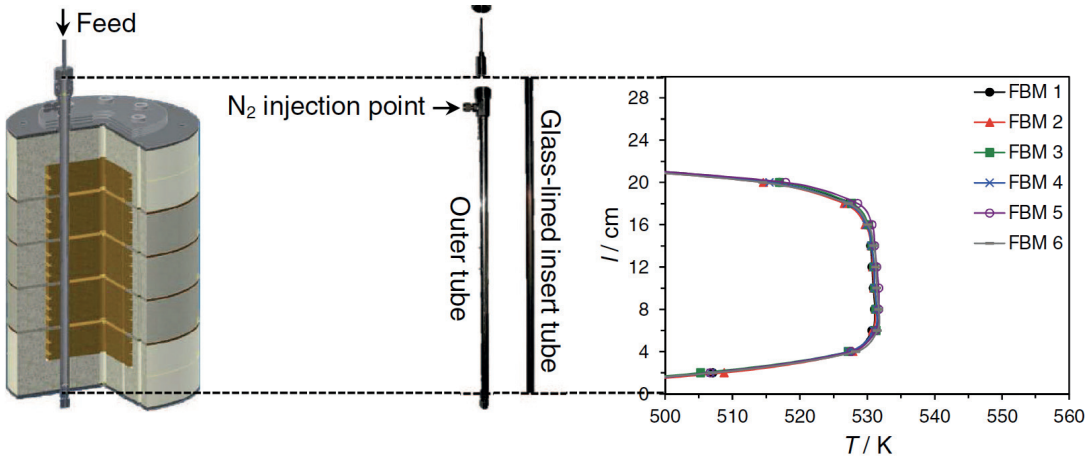

Figure A5.1 Schematic figure of the five heated zones of the fixed-bed microreactor, reactor insert and housing. Temperature profiles of the six fixed-bed microreactors (FBM 1–6) at 260 ˚C indicate the isothermal region is located in the middle three grey zones.

Transmission ^{57}Fe Mössbauer spectra were collected at 300 K and 4.2 K with a sinusoidal velocity spectrometer using a ^{57}Co(Rh) source. Velocity calibration was carried out using an α-Fe foil. The source and the absorbing samples were kept at the same temperature during the measurements, ensuring no center shift is observed while measuring under a different temperature. The high-pressure Mössbauer in situ cell developed at Reactor Institute Delft is manufactured of stainless steel SS316L and capable of going up to 25 bar of gas mixtures at temperatures of 450 ˚C (Figure S2). It allows for combined Mössbauer spectroscopy in transmission mode and IR spectroscopy in DRIFT configuration. At the top of the cell a CVD diamond window is mounted, allowing the IR measurements, while a beryllium window is included at the bottom, having high permeability to the gamma rays used in Mössbauer spectroscopy (Figure S2). The sample is mounted inside the cell in holders containing graphite discs at the bottom and the cell is closed with gold plated metal C-rings. The gas flows through the catalyst bed from top to bottom, the inlet gas being preheated in the heating compartment. The cell can be mounted on transport tubes and cooled down to 4.2 K in a cryostat for low-temperature Mössbauer measurements. One Mössbauer spectrum was recorded each time at room temperature for 10-15 h until a satisfactory signal-to-noise ratio was achieved. Subsequently, the cell was cooled down using liquid He and the low temperature Mössbauer spectrum was recorded. The high-pressure beryllium windows used in this cell contain 0.08% Fe impurity whose spectral contribution was fitted and removed from the final spectra. The data deconvolution of the measurements at liquid He temperature are reported in the main text, however, both spectra provided much qualitative input on the system studied. For example, an apparent absence of magnetization at room temperature is a result of a rapidly fluctuating magnetization vector due to the decoupled magnetization from the iron lattice [3], indicating the presence of very small

nanoparticles. The Mössbauer spectra at both temperatures were fitted using the Mosswinn 4.0 program [4]. Experimental uncertainties in the isomer shift (*IS*) ± 0.01 mm s^{-1}; in the quadrupole splitting (*QS*) ± 0.01 mm s^{-1}; in the line width (Γ) ± 0.01 mm s^{-1}; in the hyperfine field ± 0.1 T; Debye temperature: Θ_D ± 10 K; and in the spectral contribution ± 3 %. An asterisk * denotes a distribution of hyperfine fields was measured, and the average magnetization is reported. Debye temperatures were calculated using a Levenberg-Marquardt fitting algorithm of the Lamb-Mössbauer factor (*W*) [5, 6], using the Debye model. The temperature dependent absorption areas are proportional to the recoilless fraction of Mössbauer atoms (f) [7].

$$f = \exp(-2W) \qquad 2W = \frac{-6E_R}{k_B\Theta_D}\left\{\frac{1}{4} + \left(\frac{T}{\Theta_D}\right)^2 \int_0^{x_D} \frac{x\,dx}{e^x - 1}\right\} \qquad x_D \equiv \Theta_D/T$$

The f-factor comprises a Debye function with E_R the recoil energy of a Mössbauer atom, k_B the Boltzmann constant, and Θ_D the Debye temperature. The absorption areas measured at 4.2 K and 300 K were used to determine the Debye temperature of the different iron phases, anharmonicity of the lattice vibrations were not taken into account. The Debye temperature is characteristic to a particular material and by approximation through the Debye model, and in theory, is proportional to the number density of atoms per volume considered [8].

$$\Theta_D = \frac{hc}{2\pi k_B}\left(6\pi^2 \frac{N}{V}\right)^{1/3}$$

where *c* is the speed of sound in the material, *N* is the number of moles and *V* is the volume.

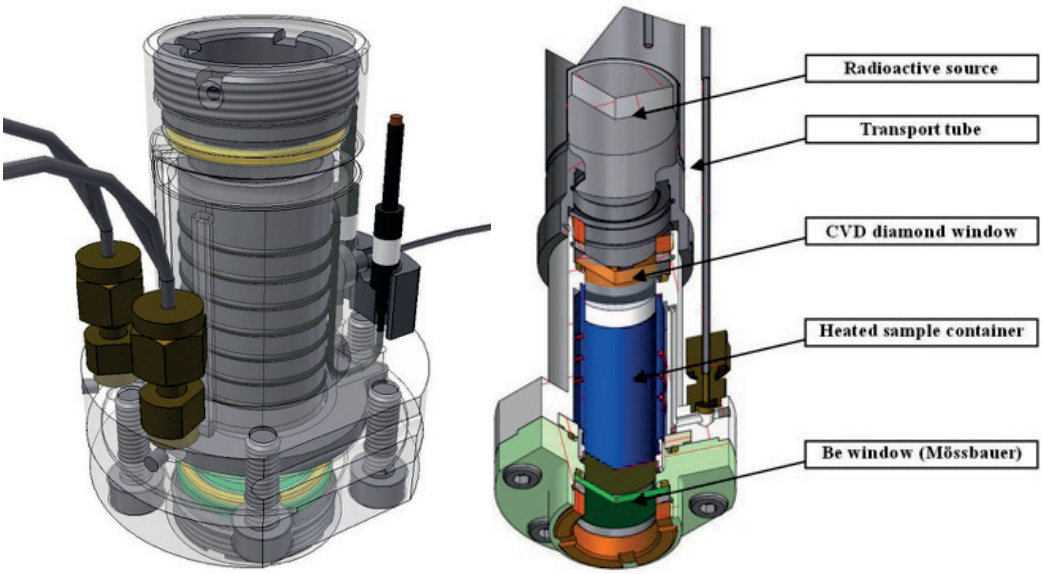

Figure A5.2 Mössbauer high-pressure *in situ* cell exterior (left) and interior (right).

A5.2 Results and Discussion

A5.2.1 Mössbauer Spectroscopy

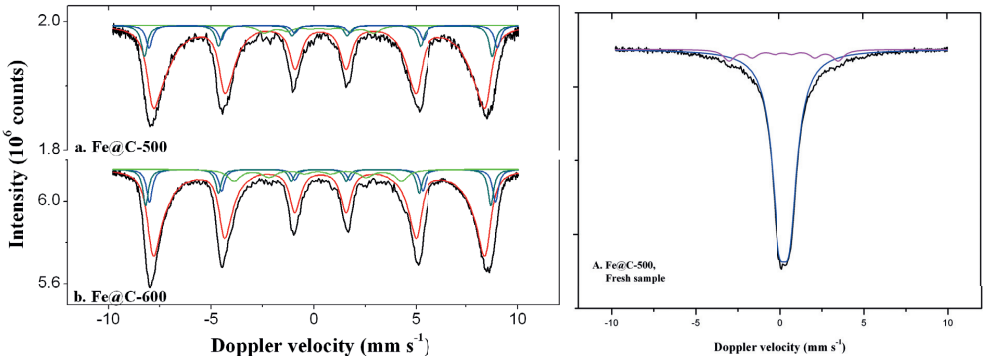

Figure A5.3 Fresh Fe@C-500 (a) and Fe@C-600 (b) Mössbauer spectra at 4.2 K and the room temperature spectrum of Fe@C-500 (A).

Table A5.1 The Mössbauer fitted parameters of Fresh Fe@C-500 and Fe@C-600 at liquid He and room temperature.

Catalyst Mössbauer temperature	*IS* (mm·s^{-1})	*QS* (mm·s^{-1})	*Hyperfine field* (T)	*Γ* (mm·s^{-1})	*Phase*	*Spectral contribution* (%)
Fe@C-500	0.27	-0.03	52.9	0.36	Fe^{3+}	11
T = 4.2 K	0.45	0.08	53.0	0.36	Fe^{3+}	7
	0.31	-0.03	48.4*	0.62	Fe^{3+}	77
	0.25	-	16.5	0.76	Fe_xC	5
Fe@C-600	0.25	0.01	52.5	0.32	Fe^{3+}	11
T = 4.2 K	0.43	0.05	52.6	0.33	Fe^{3+}	10
	0.31	-0.03	48.7*	0.58	Fe^{3+}	71
	0.19	-	25.1	0.76	θ-Fe_3C	8
Fe@C-500	0.25	-	20.5	0.80	Fe_xC	10
T = 300 K	0.31	0.66	-	1.12	Fe^{3+}	90

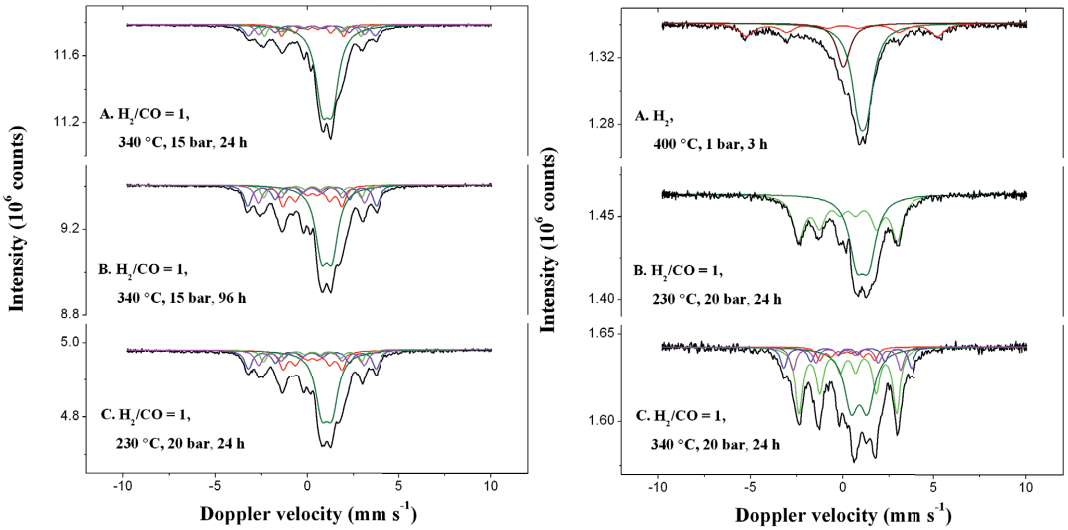

Figure A5.4 Room temperature Mössbauer spectra of carburized (left) Fe@C-500 after 24 h (A) and 96 h (B) and the activated catalyst under LTFT conditions (C), reduced (right) Fe@C-500 catalyst (A) and the under LTFT conditions (B) and subsequent HTFT conditions (C).

Table A5.2 The Mössbauer fitted parameters of Fe@C-500 under different treatments measured at room temperature.

Catalyst Treatment	*IS* ($mm \cdot s^{-1}$)	*QS* ($mm \cdot s^{-1}$)	*Hyperfine field* (T)	*Γ* ($mm \cdot s^{-1}$)	*Phase*	*Spectral contribution* (%)
Fe@C-500 $H_2/CO=1$ 340 °C, 15 bar, 24 h	0.26	-	16.3	0.35	ϵ'-$Fe_{2.2}C$	9
	0.24	-	21.4	0.52	χ-Fe_5C_2 (I)	12
	0.23	-	17.8	0.46	χ-Fe_5C_2 (II)	10
	0.27	-	10.5	0.36	χ-Fe_5C_2 (III)	9
	1.06	0.56	-	0.83	Fe^{2+}	60
Fe@C-500 $H_2/CO=1$ 340 °C, 15 bar, 96 h	0.27	-	16.4	0.40	ϵ'-$Fe_{2.2}C$	9
	0.26	-	21.7	0.48	χ-Fe_5C_2 (I)	17
	0.22	-	17.9	0.48	χ-Fe_5C_2 (II)	15
	0.26	-	10.0	0.48	χ-Fe_5C_2 (III)	17
	1.04	0.59	-	0.79	Fe^{2+}	42
Fe@C-500 $H_2/CO=1$ 230 °C, 20 bar, 24 h	0.26	-	16.4	0.40	ϵ'-$Fe_{2.2}C$	9
	0.26	-	21.6	0.49	χ-Fe_5C_2 (I)	18
	0.22	-	17.7	0.49	χ-Fe_5C_2 (II)	14
	0.27	-	10.0	0.49	χ-Fe_5C_2 (III)	17
	1.04	0.56	-	0.82	Fe^{2+}	42

Fe@C-500 H_2, 400 °C, 3h	0.01	-	-	0.86	Fe^0 (SPM)	18
	0.01	-	32.5	0.97	Fe^0	23
	1.06	0.44	-	0.94	Fe^{2+}	59
Fe@C-500 H_2/CO=1 240 °C, 20 bar, 24 h	0.27	-	16.6	0.74	ϵ'-$Fe_{2.2}C$	54
	1.06	0.65	-	0.97	Fe^{2+}	46
Fe@C-500 H_2/CO=1 340 °C, 20 bar, 24 h	0.26	-	16.5	0.48	ϵ'-$Fe_{2.2}C$	39
	0.25	-	21.6	0.41	χ-Fe_5C_2 (I)	11
	0.21	-	18.2	0.41	χ-Fe_5C_2 (II)	12
	0.22	-	9.3	0.41	χ-Fe_5C_2 (III)	6
	0.88	0.89	-	0.92	Fe^{2+}	32

Table A5.3 The Mössbauer fitted parameters of Fe@C-500 under different treatments measured at 4.2 K.

Catalyst Treatment	*IS* (mm·s^{-1})	*QS* (mm·s^{-1})	*Hyperfine field* (T)	*Γ* (mm·s^{-1})	*Phase*	*Spectral contribution* (%)
Fe@C-500 H_2/CO=1 340 °C, 20 bar, 24 h	0.27	-	18.4	0.44	ϵ'-$Fe_{2.2}C$	12
	0.24	-	25.6	0.48	χ-Fe_5C_2 (I)	17
	0.20	-	21.2	0.47	χ-Fe_5C_2 (II)	11
	0.16	-	11.1	0.48	χ-Fe_5C_2 (III)	10
	0.50	-0.33	51.9	0.73	Fe^{3+} ($Fe_{1-x}O$ I)	7
	0.93	-1.33	39.4	1.37	Fe^{2+} ($Fe_{1-x}O$ II)	18
	1.32	-0.46	36.9	1.37	Fe^{2+} ($Fe_{1-x}O$ III)	25
Fe@C-500 H_2/CO=1 340 °C, 20 bar, 96 h	0.27	-	18.5	0.45	ϵ'-$Fe_{2.2}C$	10
	0.26	-	25.9	0.49	χ-Fe_5C_2 (I)	23
	0.20	-	21.2	0.49	χ-Fe_5C_2 (II)	15
	0.23	-	11.3	0.49	χ-Fe_5C_2 (III)	13
	0.50	-0.10	51.9	0.73	Fe^{3+} ($Fe_{1-x}O$ I)	6
	1.17	-1.35	41.1	1.47	Fe^{2+} ($Fe_{1-x}O$ II)	14
	1.29	-0.72	36.5	1.47	Fe^{2+} ($Fe_{1-x}O$ III)	19
Fe@C-500 H_2/CO=1 230 °C, 20 bar, 24 h	0.28	-	18.6	0.43	ϵ'-$Fe_{2.2}C$	9
	0.26	-	25.9	0.54	χ-Fe_5C_2 (I)	23
	0.20	-	21.3	0.54	χ-Fe_5C_2 (II)	15
	0.23	-	11.6	0.54	χ-Fe_5C_2 (III)	15
	0.46	-0.13	51.9	0.80	Fe^{3+} ($Fe_{1-x}O$ I)	7
	1.05	-1.46	40.2	1.47	Fe^{2+} ($Fe_{1-x}O$ II)	15
	1.33	-0.58	36.9	1.47	Fe^{2+} ($Fe_{1-x}O$ III)	16

Fe@C-500 H_2, 400 °C, 3h	0.01	-	34.6	0.51	Fe^0	61
	1.19	-0.14	35.8*	0.84	Fe^{2+}	39
Fe@C-500 H_2/CO=1 240 °C, 20 bar, 24 h	0.24	-	19.0	0.59	ϵ'-$Fe_{2.2}C$	57
	0.56	-0.26	51.6	0.60	Fe^{3+} ($Fe_{1-x}O$ I)	4
	0.61	-1.57	35.2	1.47	Fe^{2+} ($Fe_{1-x}O$ II)	12
	1.33	-0.19	35.4	1.47	Fe^{2+} ($Fe_{1-x}O$ III)	27
Fe@C-500 H_2/CO=1 340 °C, 20 bar, 24 h	0.25	-	18.4	0.39	ϵ'-$Fe_{2.2}C$	30
	0.26	-	25.8	0.48	χ-Fe_5C_2 (I)	18
	0.18	-	20.9	0.48	χ-Fe_5C_2 (II)	15
	0.23	-	10.5	0.48	χ-Fe_5C_2 (III)	10
	0.42	-	51.6	0.67	Fe^{3+} ($Fe_{1-x}O$ I)	6
	0.88	-1.78	40.7	1.47	Fe^{2+} ($Fe_{1-x}O$ II)	9
	1.30	-0.54	38.9	1.47	Fe^{2+} ($Fe_{1-x}O$ III)	12

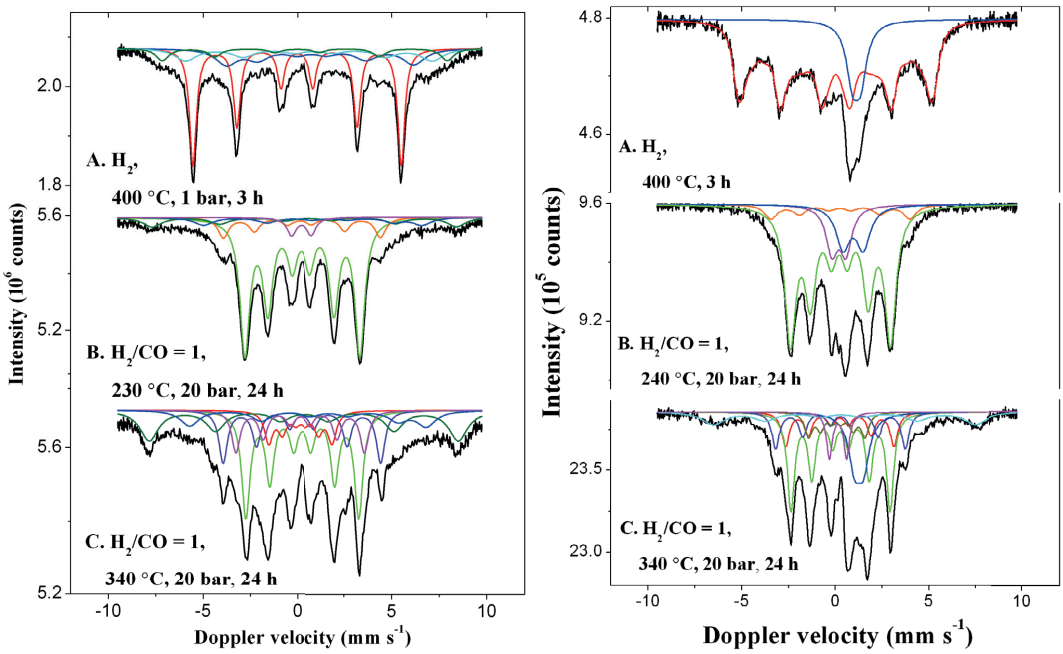

Figure A5.5 Mössbauer spectra of Fe@C-600 measured at 4.2 K (left) and room temperature (right), showing the catalyst after reduction (A), under LTFT (B) and under subsequent HTFT (C).

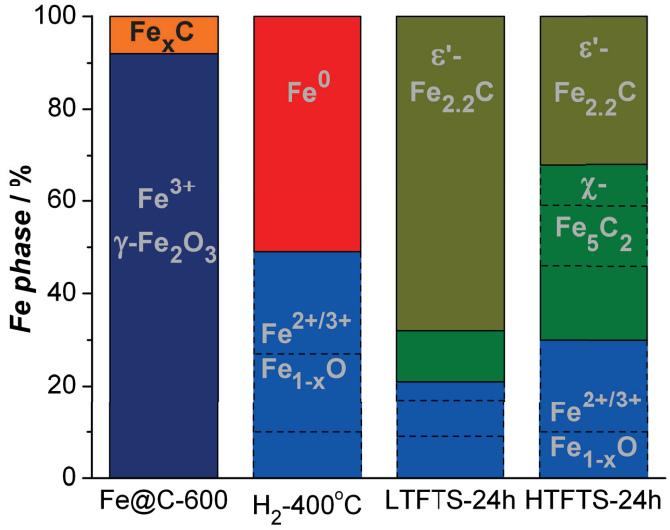

Figure A5.6 Bar graph of Fe@C-600 under reduction treatment, representing the spectral contributions of the iron phases determined by the relative absorption areas.

Table A5.4 The Mössbauer fitted parameters of Fe@C-600 under different treatments measured at 4.2 K.

Catalyst Treatment	*IS* (mm·s^{-1})	*QS* (mm·s^{-1})	*Hyperfine field* (T)	*Γ* (mm·s^{-1})	*Phase*	*Spectral contribution* (%)
Fe@C-600	0.01	-	34.3	0.44	Fe^{0}	51
H_2, 400 °C, 3h	0.19	0.40	46.9	0.82	Fe^{3+}	10
	0.75	-0.28	40.6	1.39	Fe^{2+}	17
	0.98	0.43	30.9	1.39	Fe^{2+}	22
Fe@C-600	0.23	-	19.1	0.62	ϵ'-$Fe_{2.2}C$	68
H_2/CO=1	0.18	0.12	25.9	0.68	ϵ -Fe_3C*	11
230 °C,	0.22	1.10	-	0.59	Fe_xC	4
20 bar, 24 h	0.45	-0.19	50.0	1.17	Fe^{3+}	9
	1.28	-0.92	36.0	1.17	Fe^{2+}	8
Fe@C-600	0.27	-	18.7	0.53	ϵ'-$Fe_{2.2}C$	32
H_2/CO=1	0.24	-	26.0	0.53	χ-Fe_5C_2 (I)	16
340 °C,	0.15	-	21.2	0.53	χ-Fe_5C_2 (II)	13
20 bar, 24 h	0.17	-	10.6	0.53	χ-Fe_5C_2 (III)	9
	0.36	-0.06	50.8	1.18	Fe^{3+}	20
	1.13	-1.15	39.0	1.18	Fe^{2+}	10

* Tentative assignment of the carbide phase

Table A5.5 The Mössbauer fitted parameters of Fe@C-600 under different treatments measured at 300 K.

Catalyst Treatment	*IS* (mm·s^{-1})	*QS* (mm·s^{-1})	*Hyperfine field* (T)	*Γ* (mm·s^{-1})	*Phase*	*Spectral contribution* (%)
Fe@C-600	0.01	-	24.4**	0.61	Fe^0	85
H_2, 400 °C, 3h	1.13	0.44	-	0.78	Fe^{2+}	15
Fe@C-600	0.24	-	16.6	0.71	ϵ'-$Fe_{2.2}C$	67
H_2/CO=1	0.26	0.03	23.0	0.83	ϵ -Fe_3C	8
230 °C,	0.19	0.75	-	0.75	Fe_xC	13
20 bar, 24 h	0.95	1.08	-	0.89	Fe^{2+}	12
Fe@C-600	0.27	-	16.5	0.48	ϵ'-$Fe_{2.2}C$	34
H_2/CO=1	0.26	-	21.5	0.48	χ-Fe_5C_2 (I)	13
340 °C,	0.22	-	17.9	0.48	χ-Fe_5C_2 (II)	12
20 bar, 24 h	0.14	-	9.4	0.48	χ-Fe_5C_2 (III)	8
	0.15	0.89	-	0.30	Fe_xC	6
	0.40	0.14	43.4	1.48	Fe^{3+}	13
	1.20	0.51	-	0.78	Fe^{2+}	14

* Tentative assignment of the carbide phase. ** Average magnetic field.

Table A5.6 Debye temperatures of Fe@C-500 during carburization and LTFT (left) and reduction, LTFT and HTFT (right).

Catalyst Treatment	*Phase*	Θ_D (K)
Fe@C-500	χ-Fe_5C_2 (I)	237
H_2/CO=1	$Fe_{1-x}O$	290
340 °C,		
15 bar, 24 h	total	282
Fe@C-500	χ-Fe_5C_2 (I)	285
H_2/CO=1	$Fe_{1-x}O$	365
340 °C,		
15 bar, 96 h	total	318
Fe@C-500	χ-Fe_5C_2 (I)	300
H_2/CO=1	$Fe_{1-x}O$	424
230 °C,		
20 bar, 24 h	total	343

Catalyst Treatment	*Phase*	Θ_D (K)
Fe@C-500	Fe^0	185
H_2, 400 °C,	$Fe_{1-x}O$	395
3h	total	233
Fe@C-500	ϵ'-$Fe_{2.2}C$	305
H_2/CO=1	$Fe_{1-x}O$	372
240 °C,		
20 bar, 24 h	total	330
Fe@C-500	ϵ'-$Fe_{2.2}C$	300
H_2/CO=1	χ-Fe_5C_2 (I)	224
340 °C,	$Fe_{1-x}O$	397
20 bar, 24 h	total	344

A5.2.2 Fischer Tropsch Synthesis

Table A5.7 LTFTS activity of Fe@C expressed in metal time yield, mol CO per mol metal per hour, compared to other studies.

Catalyst	*FTY* / molCO $molFe^{-1}$ h^{-1}	*T* / ˚C	*P* / bar	H_2/CO	Literature value	Literature units	Reference
Fe@C-500 C	8.1	230	20	1	4.02	10^{-5} mol_{CO} g_{Fe}^{-1} s^{-1}	This study
Fe@C-600	7.2	230	20	1	3.59	10^{-5} mol_{CO} g_{Fe}^{-1} s^{-1}	This study
Fe-Cu-CNT	2.2	220	25	1.66	3.3	$mmol_{CO}$ g_{cat}^{-1} h^{-1}	Van Steen 2002 [9]
Fe-Cu-K-CNT	0.3	220	25	1.66	1.2	$mmol_{CO}$ g_{cat}^{-1} h^{-1}	Van Steen 2002 [9]
Fe-Cu-CNT	1.2	220	25	1.66	1.8	$mmol_{CO}$ g_{cat}^{-1} h^{-1}	Van Steen 2002 [9]
Fe-Cu-K	0.2	250	1	0.7	0.6	μmol_{CO} g_{cat}^{-1} s^{-1}	Shroff 1995 [10]
Fe–Zn–K	1.5	235	21.4	2	1.5	mol_{CO} mol_{Fe}^{-1} h^{-1}	Li & Iglesia 2002 [11]
Fe–Zn–K–Cu	2.8	235	21.4	2	2.8	mol_{CO} mol_{Fe}^{-1} h^{-1}	Li & Iglesia 2002 [11]
Fe–Zn–K–Ru	6.0	235	21.4	2	6	mol_{CO} mol_{Fe}^{-1} h^{-1}	Li & Iglesia 2002 [11]
Fe-Si-Cu-K	1.6	230	13.1	0.7	*		O'Brien & Davis 1997 [12]
Fe-Si-K	1.0	230	13.1	0.7	*		O'Brien & Davis 1997[12]
Fused Fe	0.4	235	14.8	1	*		Zimmerman & Bukur 1989 [13]
Fused Fe	0.6	235	15.4	1	*		Zimmerman & Bukur 1989 [13]
Fused Fe	0.8	235	14.8	1	*		Zimmerman & Bukur 1989 [13]
Fe/SiO_2	4.0	250	10	1	2	mol_{CO} g_{cat}^{-1} s^{-1}	Xu & Bartholomew 2003 [14]
$Fe-Pt/SiO_2$	4.2	250	10	1	2.1	mol_{CO} g_{cat}^{-1} s^{-1}	Xu & Bartholomew 2003 [14]

Fe-Si-K	5.5	270	13.1	0.7	*		O'Brien & Davis 1996 [15]
Fe/AlSi	11	260	21	0.66	77	$mmol_{CO}\ g_{cat}^{-1}\ h^{-1}$	Keyvanloo & Bartholomew 2014 [16]
Fe-CNT	11	275	8	0.5	56.81	$\mu mol_{CO}\ g_{Fe}^{-1}\ s^{-1}$	Bahome & Coville 2005 [17]
Fe-CNT-K	12	275	8	0.5	58.9	$\mu mol_{CO}\ g_{Fe}^{-1}\ s^{-1}$	Bahome & Coville 2005 [17]
Fe-CNT-Cu	12	275	8	0.5	60.5	$\mu mol_{CO}\ g_{Fe}^{-1}\ s^{-1}$	Bahome & Coville 2005 [17]
Fe-Si	15	270	13.1	0.67	0.275	$mol_{CO}\ g_{Fe}^{-1}\ h^{-1}$	Ngantsoue-Hoc & Davis 2002 [18]
Fe-Si-Na	14	270	13.1	0.67	0.25	$mol_{CO}\ g_{Fe}^{-1}\ h^{-1}$	Ngantsoue-Hoc & Davis 2002 [18]
Fe-Si-K	10	270	13.1	0.67	0.18	$mol_{CO}\ g_{Fe}^{-1}\ h^{-1}$	Ngantsoue-Hoc & Davis 2002 [18]
RQ Fe	71	200	30	2	71	$mol_{CO}\ mol_{Fe}^{-1}\ h^{-1}$**	Xu & Qiao 2014 [19]**
RQ Fe	1.9-7.1	200	50→30	2	---	$mol_{CO}\ mol_{Fe}^{-1}\ h^{-1}$	Xu & Qiao 2014 [19]

** activity calculations from initial rate in batch reactor; recalculated with average *FTY* over t = 5, 10, 20 and 30 min, see Scheme A5.1.

Catalyst	*CTY* / molCO $molCo^{-1}\ h^{-1}$	*T* / ˚C	*P* / bar	H_2/CO	Literature values	Literature units	Reference
Co/Al_2O_3	23	190	9.9	2	1.1	$10^{-4}\ mol_{CO}\ g_{Co}^{-1}\ s^{-1}$	Fischer & Claeys 2013 [20]
Co/Zr-SiO_2	3.6	200	20	2.1	10	$10^{-4}\ mol_{CO}\ mol_{Co}^{-1}\ s^{-1}$	Iglesia 1992 [21]
Co/Al_2O_3	2.5	200	20	2.1	6.9	$10^{-4}\ mol_{CO}\ mol_{Co}^{-1}\ s^{-1}$	Iglesia 1992 [21]
Co/TiO_2	5.5	200	20	2.1	15.3	$10^{-4}\ mol_{CO}\ mol_{Co}^{-1}\ s^{-1}$	Iglesia 1992 [21]
Co/SiO_2	7.3	200	20	2.1	20.2	$10^{-4}\ mol_{CO}\ mol_{Co}^{-1}\ s^{-1}$	Iglesia 1992 [21]
Co-CNF	1.4	220	1	2	0.64	$10^{-5}\ mol_{CO}\ g_{Co}^{-1}\ s^{-1}$	Bezemer & De Jong 2006 [22]
Co-CNF	2.6	220	1	2	1.24	$10^{-5}\ mol_{CO}\ g_{Co}^{-1}\ s^{-1}$	Bezemer & De Jong 2006 [22]

Co-SiO_2	0.7	220	1	2	0.35	10^{-5} mol_{CO} g_{Co}^{-1} s^{-1}	Bezemer & De Jong 2006 [22]
Co-SiO_2	2.8	220	1	2	1.31	10^{-5} mol_{CO} g_{Co}^{-1} s^{-1}	Bezemer & De Jong 2006 [22]
Co-CNF	5.0	210	35	2	2.37	10^{-5} mol_{CO} g_{Co}^{-1} s^{-1}	Bezemer & De Jong 2006 [23]
Co-CNF	7.8	210	35	2	3.7	10^{-5} mol_{CO} g_{Co}^{-1} s^{-1}	Bezemer & De Jong 2006 [23]
Co-CNF	9.2	210	35	2	4.35	10^{-5} mol_{CO} g_{Co}^{-1} s^{-1}	Bezemer & De Jong 2006 [23]
Co/SiO_2	14	220	20	2	6.5	10^{-5} mol_{CO} g_{Co}^{-1} s^{-1}	Munnik & De Jong 2014 [24]
Co-Pt/SiO_2	19	220	20	2	8.9	10^{-5} mol_{CO} g_{Co}^{-1} s^{-1}	Munnik & De Jong 2014 [24]
Co@NC-550	6.7	230	30	2	*		Qiu & Ma 2017 [25]
Co@C-550	12	230	30	2	*		Qiu & Ma 2017 [25]
Co/H-ZSM5	27	240	15	1	4.5	10^{2} mol_{CO} kg_{Co}^{-1} h^{-1}	Sartipi & Kapteijn 2014 [26]
Co/SiO_2	15	240	15	1	2.5	10^{2} mol_{CO} kg_{Co}^{-1} h^{-1}	Sartipi & Kapteijn 2014 [26]
Co-Zr-Al_2O_3	5.4	240	20.7	1	0.09	mol_{CO} mol_{Co}^{-1} min^{-1}	Withers 1990 [27]
Co-Zr-Al_2O_3	17	240	20.7	1	0.29	mol_{CO} mol_{Co}^{-1} min^{-1}	Withers 1990 [27]

*Recalculations based on carbon monoxide conversion, carbon dioxide selectivity, space velocity, catalyst weight, and iron or cobalt loading.

Iron			*Feed*	*Product*	*Activity*
	X_{CO} / -	S_{CO2} / -	L_{CO} g_{Fe}^{-1} h^{-1}	L_{CO} g_{Fe}^{-1} h^{-1}	mol_{CO} mol_{Fe}^{-1} h^{-1}
O'Brien & Davis 1997 [12]	0.62	0.45	1.82	0.62	1.6
	0.38	0.4	1.82	0.42	1.0
Zimmerman & Bukur 1989 [13]	0.52	0.43	0.54	0.16	0.4
	0.73	0.4	0.53	0.23	0.6
	0.79	0.435	0.68	0.31	0.8
O'Brien & Davis 1996 [15]	0.84	0.46	4.86	2.2	5.49

Cobalt			*Feed*	*Product*	*Activity*
	X_{CO} / -	Co wt%	L_{CO} g_{Co}^{-1} h^{-1}	L_{CO} g_{Co}^{-1} h^{-1}	mol_{CO} mol_{Co}^{-1} h^{-1}
Qiu & Ma 2017 [25]	0.10	0.30	25.3	2.5	6.7
	0.30	0.52	14.6	4.4	11.5

Scheme A5.1 RQ-Fe batch reactor recalculations *doi:10.1038/ncomms6783*

Using ideal gas law to estimate pressure increase from temperature increase

T / K	*P* / bar	H_2/CO	P_{CO} / bar	
288	30	2	10	initial conditions
473	49.3	2	16.42	reaction conditions

T / K	*P* / bar	H_2/CO	$d(P_{CO})$ / bar	final conditions
473	30	2	6.42	

Using CO partial pressure and reactor volume minus PEG to estimate mol CO

$d(P_{CO})$ / bar	V_{Rx} / cm^3	V_{PEG} / cm^3	V_{gas} / cm^3	n_{CO} / mol	n_{CO} / mol
6.42	50	20	30	0.0049	4.9

Using Supplementary Figure 5 to estimate mol of CO converted per unit time

t / min	*t* / h	X_{CO} / %	$d(n_{CO})$ / mmol
5	0.08	54	2.65
10	0.17	71	3.48
20	0.33	82	4.02
30	0.50	87	4.26

Using mol CO converted with given mol Fe of catalyst to calculate activity *FTY*

t / h	*FTY* / mol_{CO}^{-1} mol_{Fe} h^{-1}	n_{Fe} / mmol
0.08	7.1	4.48
0.17	4.7	
0.33	2.7	
0.50	1.9	

Calculating total turnover of CO on Fe from 27 cycles of 30 min

cycles	n_{CO} per cycle	total CO turnover / mol	total n_{CO}/n_{Fe} turnover / mol_{CO} mol_{Fe}^{-1}
27	0.0049	0.13	**29.5**

Calculating total turnover of CO on Fe from Fe@C: 230 C, 20 bar, H_2/CO=1, 120 h

t / h	Q_{CO} / cm^3 min^{-1}	V_{CO} / dm^3	n_{CO} / mol	X_{CO} / %	n_{CO} converted / mol
120	25	180	8.04	12.5	1.00

m_{Fe} / g	n_{Fe} / mol	total n_{CO}/n_{Fe} turnover / mol_{CO} mol_{Fe}^{-1}
0.056	0.0010	**1002**

Comparing the turnover ratio and stability on Fe@C and RQ-Fe

Fe@C / RQ-Fe turnover ratio	Stability Fe@C at 120 h	RQ-Fe deactivation over 27 cycles
34	***X*CO from 7.5 to 12.5%**	***X*CO from 78% to 62%**

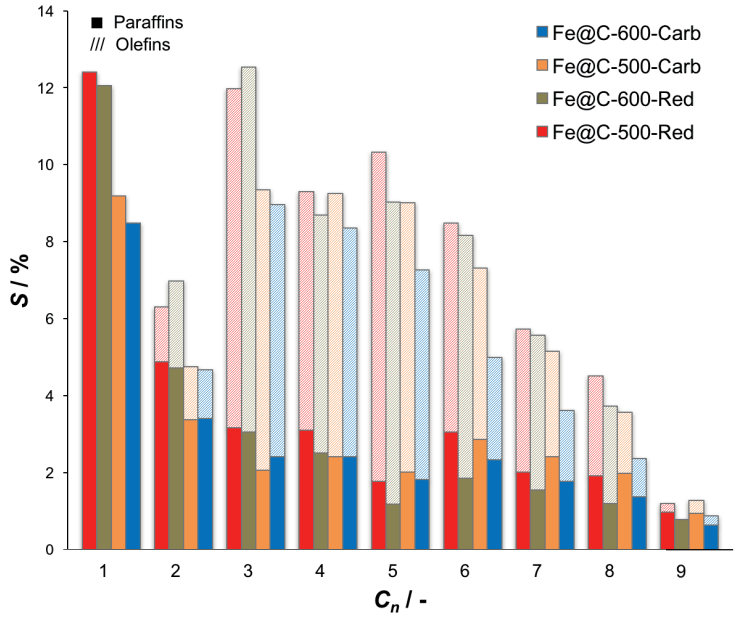

Figure A5.7 Product distribution on carburized and reduced Fe@C catalysts, displaying the carbon selectivity versus carbon number. LTFTS conditions are 230 ˚C, 20 bar, H_2/CO = 1, *WHSV* = 55 $dm^3_{H2/CO}\ g_{Fe}^{-1}\ h^{-1}$, product selectivities obtained between 94-99 h time on stream.

Table A5.8 Results of Fe@C catalytic tests activated through carburization or reduction under HTFT conditions of 340 ˚C, 20 bar, H_2/CO = 1, *WHSV* = 120 $dm^3_{H2/CO}\ g_{Fe}^{-1}\ h^{-1}$, product selectivities obtained between 47-48 h time on stream.

Fe@C	X_{CO} / %	*FTY* / [*]	S_{CH4} / C%	S_{CO2} / C%	α / -
500-Carb	78.6	3.18	16.4	46.5	0.48
600-Carb	66.7	2.78	15.5	42.6	0.49
500-Red	72.9	3.19	15.9	46.0	0.44
600-Red	70.4	2.89	14.4	44.0	0.46

* *FTY*, iron time yield, catalytic activity expressed as 10^{-4} mol carbon monoxide converted to hydrocarbon products per gram of iron per second, explicitly excluding carbon dioxide selectivity.

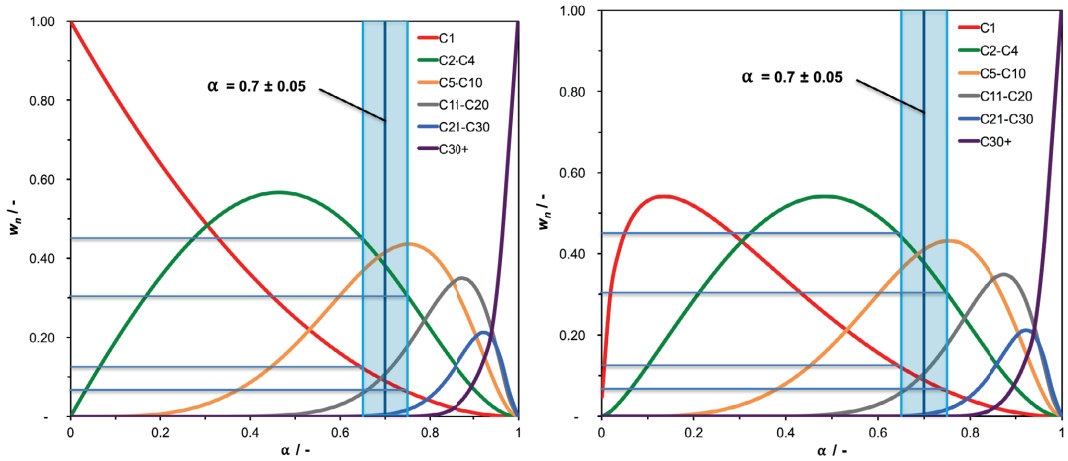

Figure A5.8 Flory [28] (left) and Schulz [29] (right) distribution of different carbon numbers and their sums in the hydrocarbon products, highlighted at alpha of 0.7, displaying variation in hydrocarbon selectivity is possible within the accuracy of measurement. The function values of the Flory (4) and Schulz (5) distribution are identical above alpha around 0.5 [30].

$$W_n = (1-\alpha)^2\, n\alpha^{n-1} \qquad (4)$$

$$W_n = (\ln^2\alpha) n\alpha^n \qquad (5)$$

A5.2.3 Transmission electron microscopy

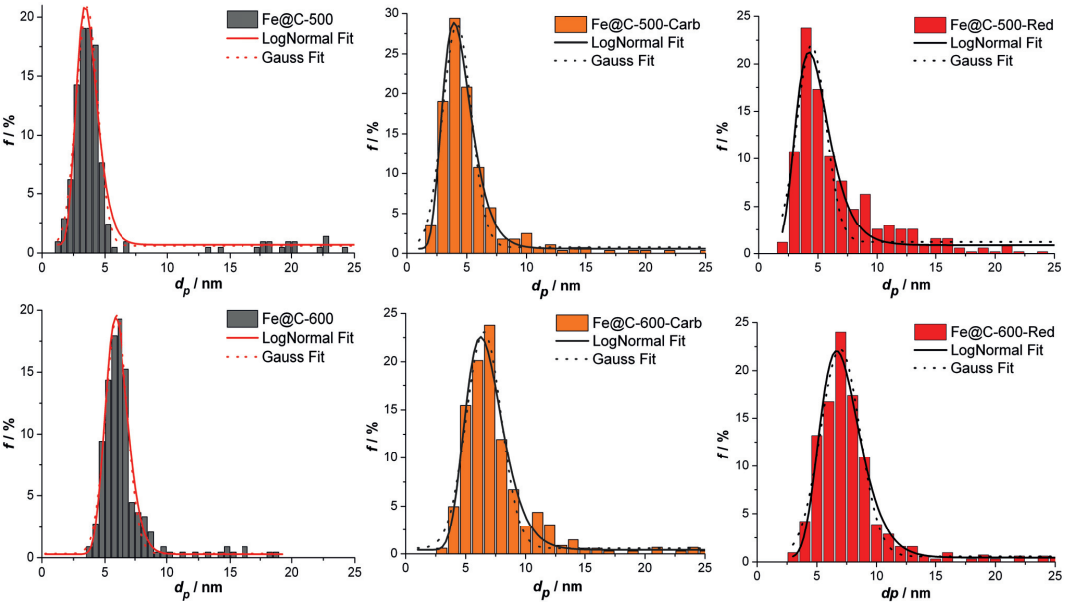

Figure A5.9 Particle size distributions of fresh and spent Fe@C catalysts for different activation methods including histogram fitting with Gaussian and LogNormal distribution.

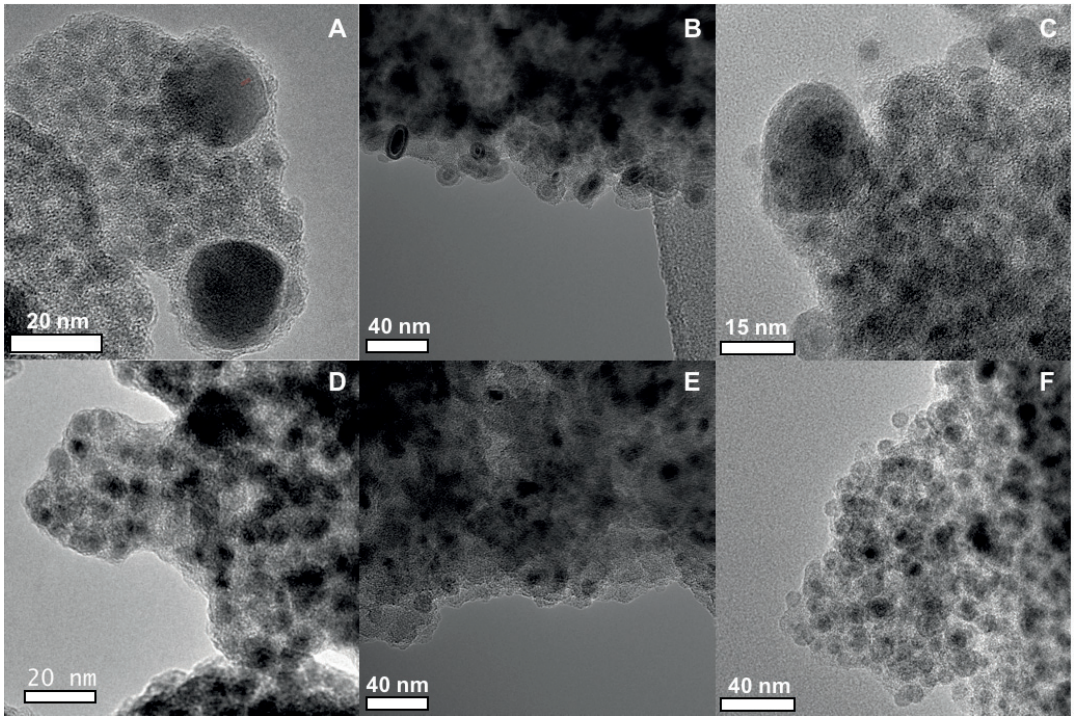

Figure A5.10 Additional micrographs of fresh Fe@C-500 (A, top row) and Fe@C-600 (D, bottom row) catalysts, and images of spent catalysts after 140 h carburization and 120 h LTFT (B,E) and after 3 h reduction and 120 h LTFT (C,F) under different magnification. The small iron nanoparticles embedded in the carbon matrix are visible as low-contrast dark circles, in comparison to the lighter carbon matrix.

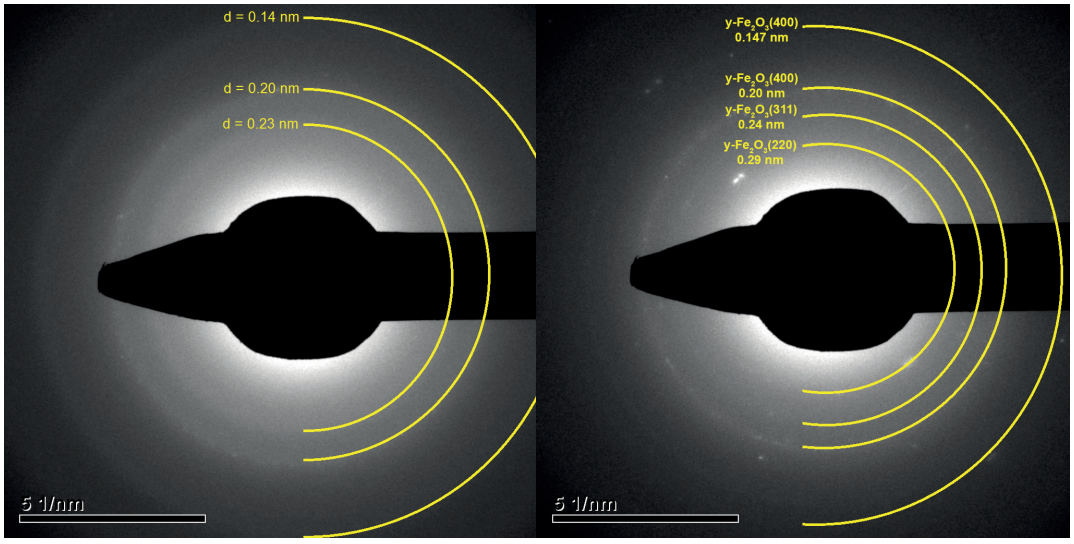

Figure A5.11 Examples of selected area electron diffraction of fresh (left) and spent (right) Fe@C-600 catalyst.

Scheme A5.2 Thermodynamic metal / metal oxide phase equilibria under oxidizing atmosphere according to T.B. Reed, 1971 [31].

Calculate for pH2O/pH2 under LTFT and HTFT temperatures

log(pO2) = 2log(F) + Gf(H2O)/2.303/RT **F = pH2O/pH2**

-log(pO2)	F	Gf(H2O) / kcal mol^{-1}	T / K	R / kcal mol^{-1} K^{-1}
49	0.03	-106	503	0.001987
46	0.5	-106	503	
40	0.03	-103	613	
37	0.5	-103	613	

Value -log(PO2) for first decrease in Fe toward FeO = ~21, does not get near at 500-600 K

Calculate for pCO2/pCO under LTFT and HTFT temperatures

-log(pO2)	F	Gf(CO2) / kcal mol^{-1}	T / K	R / kcal mol^{-1} K^{-1}
49	2.8	-114	503	0.001987
48	5	-114	503	
38	2.8	-110	613	
38	5	-110	613	

Value -log(PO2) for first decrease in Fe toward FeO = ~21, does not get near at 500-600 K

Check value pO for O'Brien [15] at 1000 K given in table 2 on page 67: oxygen affinity of metals*

*pO = -log(pO2) for oxygen in equilibrium at 1000 K

-log(pO2)	F	Gf(H2O) / kcal mol^{-1}	T / K	R / kcal mol^{-1} K^{-1}
23	**0.03**	-92	**1000**	0.001987

Value -log(PO2) for first decrease in Fe toward FeO = ~21, value approximately in agreement

Check Wezendonk (this work) with value of T.B. Reed in table 2 on page 67: oxygen affinity of metals

T.B. Reed [31]

F=1000	T=1000 K	**-LOG(PO2) = 13.6**

Wezendonk (this work)

-LOG(PO2)	F	Gf(H2O)	T / K	R / kcal mol^{-1} K^{-1}
14.1	1000	-92	1000	0.001987

Obtained values for pO are virtually identical.

References

[1] S. Sartipi, H. Jansma, D. Bosma, B. Boshuizen, M. Makkee, J. Gascon, F. Kapteijn, *Rev. Sci. Instrum.*, 84 (**2013**) 124101.
[2] R.A. Friedel, R.B. Anderson, *J. Am. Chem. Soc.*, 72 (**1950**) 1212-1215.
[3] J.W. Niemantsverdriet, *Spectroscopy in Catalysis*, Wiley-VCH, **2007**.
[4] Z. Klencsár, *Nucl. Instrum. Methods Phys. Res., Sect. B*, 129 (**1997**) 527-533.
[5] N. Alves Jr, E.P. Caetano, V.P. Rodríguez, E. Baggio-Saitovitch, Determination of Debye Temperature from Mössbauer Data, in, Centro Brasileiro de Pesquisas Fisicas (CBPF), 1995.
[6] E. De Grave, A.E. Verbeeck, D.G. Chambaere, *Phys. Lett. A*, 107 (**1985**) 181-184.
[7] K. Mahesh, *physica status solidi (b)*, 61 (**1974**) 695-700.
[8] S.W. Van Sciver, *Low-Temperature Materials Properties*, in: S.W. Van Sciver (Ed.) Helium Cryogenics, Springer New York, New York, NY, **2012**, pp. 17-58.
[9] E. van Steen, F.F. Prinsloo, *Catal. Today*, 71 (**2002**) 327-334.
[10] M.D. Shroff, D.S. Kalakkad, K.E. Coulter, S.D. Kohler, M.S. Harrington, N.B. Jackson, A.G. Sault, A.K. Datye, *J. Catal.*, 156 (**1995**) 185-207.
[11] S. Li, A. Li, S. Krishnamoorthy, E. Iglesia, *Catal. Lett.*, 77 (**2001**) 197-205.
[12] R.J. O'Brien, L. Xu, R.L. Spicer, S. Bao, D.R. Milburn, B.H. Davis, *Catal. Today*, 36 (**1997**) 325-334.
[13] W.H. Zimmerman, J.A. Rossin, D.B. Bukur, *Ind. Eng. Chem. Res.*, 28 (**1989**) 406-413.
[14] J. Xu, C.H. Bartholomew, J. Sudweeks, D.L. Eggett, *Top. Catal.*, 26 (**2003**) 55-71.
[15] R.J. O'Brien, L. Xu, R.L. Spicer, B.H. Davis, *Energy & Fuels*, 10 (**1996**) 921-926.
[16] K. Keyvanloo, M.K. Mardkhe, T.M. Alam, C.H. Bartholomew, B.F. Woodfield, W.C. Hecker, *ACS Catal.*, 4 (**2014**) 1071-1077.
[17] M.C. Bahome, L.L. Jewell, D. Hildebrandt, D. Glasser, N.J. Coville, *Appl. Catal., A*, 287 (**2005**) 60-67.
[18] W. Ngantsoue-Hoc, Y. Zhang, R.J. O'Brien, M. Luo, B.H. Davis, *Appl. Catal., A*, 236 (**2002**) 77-89.
[19] K. Xu, B. Sun, J. Lin, W. Wen, Y. Pei, S. Yan, M. Qiao, X. Zhang, B. Zong, *Nat Commun*, 5 (**2014**).
[20] N. Fischer, E. van Steen, M. Claeys, *J. Catal.*, 299 (**2013**) 67-80.
[21] E. Iglesia, S.L. Soled, R.A. Fiato, *J. Catal.*, 137 (**1992**) 212-224.
[22] G.L. Bezemer, P.B. Radstake, U. Falke, H. Oosterbeek, H.P.C.E. Kuipers, A.J. van Dillen, K.P. de Jong, *J. Catal.*, 237 (**2006**) 152-161.
[23] G.L. Bezemer, J.H. Bitter, H.P.C.E. Kuipers, H. Oosterbeek, J.E. Holewijn, X. Xu, F. Kapteijn, A.J. van Dillen, K.P. de Jong, *J. Am. Chem. Soc.*, 128 (**2006**) 3956-3964.
[24] P. Munnik, P.E. de Jongh, K.P. de Jong, *J. Am. Chem. Soc.*, 136 (**2014**) 7333-7340.
[25] B. Qiu, C. Yang, W. Guo, Y. Xu, Z. Liang, D. Ma, R. Zou, *J. Mater. Chem. A*, 5 (**2017**) 8081-8086.
[26] S. Sartipi, M. Alberts, V.P. Santos, M. Nasalevich, J. Gascon, F. Kapteijn, *ChemCatChem*, 6 (**2014**) 142-151.
[27] H.P. Withers, K.F. Eliezer, J.W. Mitchell, *Ind. Eng. Chem. Res.*, 29 (**1990**) 1807-1814.
[28] P.J. Flory, *J. Am. Chem. Soc.*, 58 (**1936**) 1877-1885.
[29] G.V. Schulz, *Z. Phys. Chem.*, 32B (**1936**) 27.
[30] G. Henrici-Olivé, S. Olivé, *Angew. Chem. Int. Ed.*, 15 (**1976**) 136-141.
[31] T.B. Reed, *Free Energy of Formation of Binary Compounds: An Atlas of Charts for High-Temperature Chemical Calculations*, MIT Press, Cambridge, MA, **1971**.

Chapter

6

Summary and Outlook

Fischer-Tropsch synthesis (FTS) is an industrial-scale process for the production of fuels and chemicals from non-petroleum feedstocks, and it has a long history of technological research and development. Metal-organic frameworks (MOFs) are a class of synthetic porous crystalline materials that are currently under research for their use in electronics and semiconductors, chemical sensing, gas adsorption and separation, and heterogeneous catalysis. This thesis brought together these worlds of nanotechnology research and industrial catalysis through the use of MOFs as precursor for advanced catalytic materials in the FTS process. In this chapter, the research and development efforts concerning the novel MOF-based synthesis method and the fundamental studies on the active phase of iron during FTS are summarized. Additionally, the current research on Fe@C catalysts is discussed and an outlook on future research goals will be provided.

6.1 Summary

Fischer-Tropsch synthesis (FTS), the industrial production of fuels and chemicals from non-petroleum feedstock over heterogeneous catalysts, already has a long history, but the increased demand for oil-derived products render it an even more interesting branch for catalyst development. This thesis brought together the worlds of novel nanotechnology and industrial catalysis, utilizing structures as catalysts in Fischer-Tropsch synthesis that had not been identified as catalysts themselves until recently. The thesis focused on the development of the MOF mediated synthesis (MOFMS), and particularly, on understanding the function of the MOF in the process of converting it into an active catalyst for iron-based FTS. In addition to the elucidation of the pyrolysis process, we determined how the MOF properties affect the resulting catalyst, and whether further spatial isolation of the iron clusters could improve the activity and stability of the produced catalysts. We confirmed that iron carbides are the active phase of iron-based Fischer-Tropsch synthesis and discovered that catalyst formulation and activation had a major impact on the produced iron carbide phases. Therefore, we used the Fe@C catalysts as a model system to quantify the performance of the obtained iron carbide phases.

The two main challenges of iron-based Fischer-Tropsch synthesis are to acquire more active and stable catalysts, due to inherent lower activity of iron compared to cobalt and a number of phenomena leading to increased deactivation. In addition, we mentioned that development of new and highly active catalysts is limited to these stability issues under FTS conditions, and thus, the challenge may indeed be formulated as more stable *and then additionally* more active. Fortunately, the development of Fe@C catalysts results in both higher activity and stability due to the unique spatial confinement of iron that is obtained through the decomposition of the MOF structure. On one hand, it renders a high monodispersion of iron nanoparticles at very high loadings, resulting in iron time yields that outperform many industrial and laboratory catalysts. On the other hand, the embedding of these iron nanoparticles in the carbon matrix through the pyrolysis treatment ensures an effective spatial isolation and inhibits sintering and agglomeration of the iron phase. In addition, the iron in the carbon matrix undergoes a high degree of carburization and does not convert to inactive oxide during FTS. The Fe@C family of catalysts is furthermore an amazing model system for studying the effects of the iron carbide phases under FTS, as it allows the control over dispersion, loading, and degree of reduction after synthesis, and the control over iron carbide phase, degree of carburization and stability during FTS.

This thesis was divided in five main chapters, in which **Chapter 1** served as introductory reading for the background of MOFMS in the context of FTS, highlighting the relevance of MOFMS as universal synthesis method for advanced heterogeneous catalysts and the challenges in both research and performance of current iron-based FTS for the production of fuels and chemicals from non-petroleum feedstock. In the first part of **Chapter 1**, we establish the black-box view on MOFMS comprising a

decomposition of the framework followed by carbothermal reduction of the iron clusters due to changes in standard free energy of formation in the temperature range applied during the pyrolysis. The resulting materials are already used as heterogeneous catalysts in various fields, but the conversion of the MOF toward catalyst was not well understood. While many improved values for catalytic performance indicators are reported, a fundamental study with aim to understand the conversion of Fe-MOFs into catalysts was lacking, nor was the use of several MOFs reported to unravel the relation between MOF and catalyst. Hence, we conducted studies to understand the MOF decomposition toward an active catalyst including *in situ* pyrolysis experiments and applying various Fe-MOFs as precursors for FTS performance testing. The development of Fe@C catalysts eventually led to answering fundamental questions on the performance of iron carbides in FTS. In early experiments, we reported a clear particle size dependence correlation with the type of iron carbide formed, and realized that the Fe@C system might allow control over the formation of carbides through the activation method whilst maintaining identical physiochemical properties. The second part of **Chapter 1** therefore reviews much of the work on iron-catalyst activation methods, producing various iron carbides as active phase, and we establish the relation between activation conditions, iron particle size, FTS conditions and the obtained iron carbide phase. The main conclusion from the abovementioned literature study is that a high dispersion of iron is key to obtain iron carbide phases other than Hägg carbide (χ-Fe_5C_2), whereas it is both increasingly difficult to synthesize these catalysts as well to maintain their stability under operation. Whenever hexagonal carbides (ε'-$Fe_{2.2}C$) were produced, supported catalysts were used with low loading to produce highly dispersed and well-anchored iron nanoparticles. However, the stabilization through strong metal support interaction would result in decreased reducibility, yielding incomparable catalytic system in terms of iron carbide phase. Nevertheless, the large volume of activation studies comprising thorough catalyst characterization and *in situ* spectroscopy allowed for establishing activation methods for the controlled formation of ε'-$Fe_{2.2}C$ and χ-Fe_5C_2.

In **Chapter 2** of this thesis, we have reported the design of new iron-based FTS catalysts through a novel synthesis method MOF mediated synthesis (MOFMS). We employed the commercially available Fe-BTC as precursor, additionally changing the iron loading by impregnation of furfuryl alcohol (FA) into the MOF. Heat treatment of the MOF at 500 ˚C in an inert atmosphere resulted in the formation of the 38-Fe@C composite with high iron loading and dispersion, displaying exceptional activity and stability in FTS. Moreover, the polymerization of FA into furan resins prior to decomposition of the MOF structure increased the isolation of the iron clusters, thus resulting in increased nanoparticle dispersion at the costs of iron loading. The activity of these catalysts increased with decreasing particle size, whereas no difference in stability of the catalysts was found. We arrived to the conclusion that the iron phase of the obtained nanoparticles does not alter the activity after reduction and carburization, but is merely a result of the increased proximity of carbon

from the furan resin. In absence of FA, oxidized nanoparticles were obtained after passivation of the metallic iron, due to their very small average size, whereas the cementite (θ-Fe_3C) nanoparticles derived from FA inclusion were more resistant to bulk oxidation. Moreover, the equal stability measured for all catalysts demonstrated that the structural decomposition and the carbothermal reduction readily established maximum encapsulation, thus providing the stability during catalytic testing. This statement was rationalized with virtual identical values for iron-to-carbon surface ratios obtained for the passivated catalysts. In addition to the exceptional stability of Fe@C, the performance comparison between both industrial and laboratory catalysts showed that the high dispersion resulted in remarkable active catalysts that outperformed many of the corresponding catalysts. The productivity of Fe@C was further improved by potassium promotion, decreasing undesired methane formation together with an increase in olefin selectivity and CO conversion.

In **Chapter 3** of this thesis, we fundamentally investigated the conversion of the Fe-BTC towards Fe@C by *in situ* X-ray absorption and Mössbauer spectroscopy, revealing that the MOF decomposition encompasses many intermediate iron phases. Starting from the Fe(III) oxo-clusters, the pyrolysis formed mixtures of several iron carbides and a Wüstite phase. The carbothermal reduction was witnessed through the emission of carbon dioxide and carbon monoxide, where the decarboxylation was found the main route for oxygen removal. After activation of the iron phase by hydrogen reduction, the Wüstite was fully converted to metallic iron and thus, upon syngas exposure created highly active Hägg carbides. The system showed no deactivation, attributed to the unique spatial confinement witnessed through XPS and TEM. The resulting catalyst combined a high iron loading and dispersion of which over 95% can be transformed into the active phase, resulting in the highest reported values for iron-based FTS activity. Hence, the spatial confinement created by the porous carbon matrix on one hand allows for a nearly full transformation into active phase and on the other hand prevents the metal nanoparticles from sintering even under high-temperature FTS. In addition, we concluded that the pyrolysis temperature allowed for combined tuning of the iron phase, loading, dispersion, and thus catalytic activity of the resulting Fe@C material. Relatively low pyrolysis temperatures of 400 ˚C, very close to the structural decomposition temperature, resulted in the highest iron dispersion and corresponding catalytic activity. The higher the pyrolysis temperature, the lower the obtained dispersion. The increasing pyrolysis temperature also enlarged the degree of reduction of the iron phase under pyrolysis. Highly dispersed nanoparticles were obtained at pyrolysis temperatures up to 600 ˚C, which did not display much difference in catalytic performance. However, a pyrolysis temperature of 900 ˚C created such large cementite nanoparticles that only small parts of the surface were oxidized, and the low dispersion resulted in the lowest activity for the catalysts.

In **Chapter 4** of this thesis, we further investigated the effect of the MOF precursor using different MOFs while employing fixed pyrolysis conditions. Under equal pyrolysis conditions, the different

MOFs undergo a similar degree of carbonization of the framework. High surface-area carbons are created from every MOF, though the pore size distribution of the resulting carbon matrix is very different from one MOF to the other. The iron nanoparticle size of the Fe@C catalysts is related to the porosity and cluster proximity of the parent MOF, as the highest dispersions were obtained when pyrolyzing the MOFs with the most extensive microporous surface areas and pore diameters. These results confirm that the spatial distribution of the MOF is key to produce catalysts with high dispersion and loading. The improved catalytic FTS performance could be related to a higher surface area of the iron nanoparticles, indicating the beneficial combination of dispersion and loading with regard to the activity of the Fe@C catalysts. Optimal hydrocarbon selectivity comprising low methane production could be obtained with potassium promotion, and moreover, all the K-promoted Fe@C catalysts did not display deactivation while operating at high conversions. Additionally, the alkali promotion increased the intrinsic activity of the Fe@C catalysts with highest dispersion, but this effect was not observed for the samples with lowest dispersion. The presence of Cu, Mn and S impurities retained from the MOF synthesis are thought to further enhance the selectivity to desired hydrocarbon products.

In **Chapter 5** of this thesis, a fundamental study on the role of iron carbides in FTS demonstrated similarities and differences in catalytic performance of two different iron carbide phases. The single-phase hexagonal ε'-$Fe_{2.2}C$ and Hägg χ-Fe_5C_2 iron carbides could be produced through different activation procedures, where ε'-$Fe_{2.2}C$ was produced after hydrogen reduction under low-temperature Fischer-Tropsch (LTFT) conditions, and χ-Fe_5C_2 was obtained after carburization under high-temperature Fischer-Tropsch (HTFT) conditions. *In situ* Mössbauer spectroscopy under the exact conditions as the catalytic performance testing demonstrated that the iron carbide phases were preserved under LTFT conditions, and that the degree of carburization and Debye temperature (traditionally a measure for the crystallite hardness, herein related to the development of the surface phase compared to its bulk phase characteristics) of the two different iron carbides was nearly equal. From the results of the catalytic performance tests under LTFT conditions, it is concluded that the intrinsic activity of the two carbide phases is virtually identical, whereas significant differences in the product distribution of the carbides are existent. The increased hydrogenation ability of the ε'-$Fe_{2.2}C$ iron phase, demonstrated by a higher methane selectivity and lower C_{5+} selectivity, indicates that there are deviations in the surface chemistry of the two carbides. These deviations originate either from intrinsic differences on the surface sites formed on the two types of iron carbides, or are related to the differences in relative coverage of hydrogen and carbon following the activation procedure. The activity of Fe@C catalysts under LTFT at 230 ˚C is noteworthy, as other iron catalysts exhibit lower activity values than Fe@C up to operating temperatures of 260-270 ˚C. Spent catalysts of the LTFT performance tests were examined by TEM and confirmed that the high iron dispersion was maintained, demonstrating the absence of sintering phenomena that cause formation of large

inactive iron clusters and interconversion of iron carbide phases. The retained dispersion furthermore confirms that the effect on the catalyst selectivity is only obtained through to the different activation procedures of both catalysts with similar particle size. Furthermore, the difference in selectivity between reduced and carburized catalysts disappeared when the temperature was increased to 340 ˚C. Under the lower carbon chemical potential of HTFT conditions, the Hägg carbide becomes the dominant surface phase, rendering identical performance of both catalysts. Hence, it is concluded that the variation in product selectivity is associated with the different iron carbide phases.

6.2 Evaluative Remarks

MOFs have found their way into catalysis in a very elegant way. By out-of-the-box thinking, these beautiful porous crystals with lively colours have been converted into the most active and stable iron-based FTS catalysts reported until this day. It is important to recognize that the later reported control over formulation, in-depth fundamental studies and following review papers would not have been reported would it not have been for the sheer curiosity of scientists from day one. In addition, that curiosity was always accompanied by a firm drive to face the challenges in iron-based FTS that were demonstrated so many times, in so many excellent ways [1].

The key of MOFMS is the continuous iron-cluster separation originating from the MOF topology. With the idea in mind to *freeze* the structure of the MOF, and apply it in FTS, the MOFMS was born. When the first crucible with Fe@C exited the pyrolysis furnace and nearly caught fire, we learned two things: one, we are dealing with highly pyrophoric iron nanoparticles; and two, we should passivate the samples. The cluster isolation, or spatial segregation of iron nanoparticle precursors, was found to further increase when adding carbon precursor in the void space between the iron clusters. These results agree with the traditional inverse correlation between loading and dispersion, but in this particular case, the distance between iron nanoparticles is controlled by the MOF topology and the deposited carbon precursor, not just by the concentration of mobile nanoparticle precursors in traditional synthesis methods. Nevertheless, the increased dispersion and resulting catalytic activity per gram of iron was at the cost of the loading, and consequently, studies were performed whether one could alter the dispersion and loading by the degree of carbonization through pyrolysis temperature. It is clear that the pyrolysis temperature greatly affects the dispersion, but also loading. The increased pyrolysis temperatures enhance the particle size by a combination of the increased degree of carbonization and increased mobility, both a result of thermal effects. As those elevated temperatures are not applied after pyrolysis in catalytic performance tests, there is no potential for the particles to further sinter. The encapsulation of the iron nanoparticles, or embedding, can be viewed in a more traditional manner as anchoring of nanoparticles in a zeolite-like confinement. Larger particles are only created at temperatures far above the decomposition temperature of the

MOF, as the significantly enhanced carbothermal reduction results in a lower degree of spacing by loss of the carbon matrix.

The abovementioned iron cluster separation can be altered by the use of different MOFs, where large pore MOFs with staggering BET areas represent the increased spatial segregation and thus increased cluster isolation. The different spatial distributions of iron nanoparticles obtained by altering the MOF topology can be visualised by the work of Prieto *et al.*, who display that the sintering behaviour of copper nanoparticles in close proximity is more severe than the growth phenomena on widely spaced particles [2]. The formation of the large clusters with lower chemical potential at the expense of smaller particles is a direct thermodynamic consequence, as the driving force is the reduction of the total surface energy of the system [3]. The trend of increasing nanoparticle size on MOF-mediated catalysts with increasing temperatures follows these thermodynamic predictions quite well, indicating that the Tammann and Hüttig temperature effectively delimit the temperature range of MOFMS when aiming for small nanoparticles. For example, unpublished data on Cu-MOF pyrolysis reveals that much higher heating rates and lower pyrolysis temperatures are necessary to obtain a reasonable dispersion for catalytic application. When realizing that the melting point of copper is nearly 500 ˚C lower than that of iron, these results are not surprising. However, it does spur the discussion to what the optimum design parameters for Fe-MOFs are in order to obtain maximum dispersion and consequent FTS activity.

The elucidation of the MOF pyrolysis demonstrated that the formation and anchoring of the nanoparticles initiates when structural collapse takes place, and consequently, MOFs with low decomposition temperature would be favoured. In addition, large-pore MOF topologies with increased iron cluster separation are desired over dense MOFs with interconnected clusters. However, the modest selection of topologies and linkers did not allow complete insight into the relation between the nature of the MOF and the resulting iron dispersion of Fe@C catalysts, as complete deconvolution of all characterization parameters was beyond the bounds of possibility. Moreover, the large pore structures were found more rigid than their denser counterparts under consideration, further intertwining the targeted parameters. Therefore, the MOF mediated synthesis method will need to evolve from the trial-and-error-based crystal engineering and coordination chemistry, to a fully integrated material design and application method. Research questions regarding topology may very well be answered with the help of pioneering researchers in the field of isoreticular chemistry. The MOF topology can be expanded with changing the linker length, increasing the cluster spacing, whilst maintaining an identical topology [4, 5]. In a similar manner can polymer-MOFs be used to further investigate the increased iron cluster isolation obtained with pre-pyrolysis carbon infusion, where the ordered structure and maintained topology are a clear advantage to the uncontrolled addition of FA [6]. In addition to enhanced control over the iron cluster isolation, is the use of polymers particularly interesting for creating millimetre-sized shaped granules

with increased mechanical stability [7]. Furthermore, the specific framework type may be chosen based on functional material discovery by the combination of computational crystal structure prediction and property predictions [8]. This approach is in sharp contrast to the current selection of topology, which is based on values of MOF characterization, implying that a possibly tedious synthesis route may be necessary prior to the evaluation of its properties. Hence, the current discoveries in the MOF field may contribute to the development of the MOFMS into a more mature synthesis method.

In addition to producing highly active and stable catalysts, the MOFMS has provided catalysts that can render single-phase iron carbides to assess their performance. Although the iron carbide phases had been investigated with *in situ* Mössbauer experiments while varying the iron nanoparticle size, the real control over the size and carbide phase was demonstrated with varying the activation method. The control over the iron carbide phase and dispersion allowed the unequivocal measurement of identical activity of the two carbide phases hexagonal ε'-$Fe_{2.2}C$ and Hägg χ-Fe_5C_2. These findings are in contrast with claims of a preferred iron carbide phase with maximum activity [9]. The results indicate that the activity and stability of iron catalysts are not dominated by a unique active-phase composition, but that the performance originates from the initial physiochemical composition and its effective conversion toward an active FTS catalyst under reaction conditions. Thus, it is paramount that the iron surface can be carburized without the loss of dispersion. The difference in selectivity, attributed to an increase in hydrogen ability of the reduced ε'-$Fe_{2.2}C$ catalyst, is still a topic of discussion. It is unsure whether these differences arise from changes in the intrinsic surface sites or that the relative hydrogen and carbon coverage is significantly altered by one activation method over the other. It must be noted, that the change in relative coverage can also be the result of a changes in intrinsic surface sites. Current efforts are aimed at finding clever ways to design experiments that can accept or reject one of these arguments. The work on LTFT is continued at the moment as well, as noteworthy performance at 230 ˚C was achieved, and currently under 210 ˚C. Given that the fundamental study under LTFT was not focused on optimal catalyst formulation, there is still much room for improvement in activity and selectivity.

In short, by the work carried out in this thesis, we have gained lots of insight into the novel MOMFS method for heterogeneous catalyst synthesis. It has led to the development of highly active and stable catalysts under both HTFT and LTFT conditions, and to further understanding of the fundamentals of iron carbide phases in FTS in general. As in any research project, more questions than answers have surfaced along the road and this thesis will certainly not be the end of our efforts.

6.3 Current Investigations and Outlook

Owing to their high activity and stability, Fe@C catalysts are a fascinating research topic in the field of FTS. Much of the work in this thesis has been focused on the elucidation and application of the

catalyst synthesis method MOFMS, and therefore, a desire for better understanding of the catalytic behaviour of Fe@C catalysts remains. For that reason, a parametric study including kinetic data analysis has been carried out in the HTFT regime. The fitting of these datasets to a model of Ojeda *et al.* [10] comprising H-assisted and unassisted CO dissociation, is currently being finalized. Our specific aim is to properly assess the behaviour with regard to selectivity, i.e., hydrocarbon selectivity according to Schulz-Flory distributions, olefin-to-paraffin ratios related to space time and water-gas shift activity compared to FTS activity. The selection of the model was aided with results from steady-state isotopic transient kinetic analysis (SSITKA), performed at the NTNU in Trondheim. We aim to perform additional transient isotopic studies under realistic FTS conditions to provide insight in the coverage of hydrogen and carbon on the catalytic surface, and reveal mechanistic information such as the degree of isotope insertion into the hydrocarbon products.

The opportunity that Fe@C catalysts create coincides with inherent challenges to the operation of highly active CO dissociation catalysts. Iron catalysts are known for the large differences in density during reduction and activation and the possibility of iron phase segregation [11]. Additionally, forces exerted on the catalyst grains due to rapid carburization and carbon deposition during steady state operation may result in particle break-up and reactor fouling. Therefore, it is of the highest importance to fixed-bed reactor operation that the grains are properly pelletized or granulated with binder material. As pelletization of these pyrolytic carbons is highly inefficient and often results in particle break-up readily during reactor loading, a study was performed on pre-pyrolysis polymer addition to the parent MOF. The shaping of these pellets was investigated, taking into account the iron loading and carbon porosity of the granules after pyrolysis. Only some of the tested polymers could generate the desired dispersion, loading and porosity, and importantly, the catalytic activity of these Fe@C-polymer catalysts was not compromised and allowed for over hundred hours of stable operation. We are subjecting these formulated Fe@C catalysts to tensile compression strength experiments, to assess the improvement in mechanical stability from polymer addition.

Last, but certainly not least, is the often-heard argument that MOFs must be way too expensive to use as a template for catalyst synthesis. In our view, such reasoning should be carefully addressed with estimations on the added value of products compared to the feedstock, to properly amount for the capital and operational expenditure of an envisioned process including costs for catalyst inventory. However, since such types of cost estimations may be a project on its own [12], we limit ourselves to the pricing of commercial scale MOF production, to reveal its incremental costs to other bulk chemicals. Fe-BTC can be readily synthesized at room temperature and atmospheric pressure in an aqueous solution of pH 11, using NaOH to dissolve the trimesic acid. Iron chloride is then subsequently added dropwise and the resulting solid is washed with water and dried with ethanol. The produced Fe-BTC comprises better porosity than the Basolite F300 Fe-BTC produced by BASF [13]. The major share of the costs for this synthesis route are from the trimesic acid. Chinese and Indian suppliers provide bulk quotations for the MOF linker between 10-20 USD/kg, whereas ferric

chloride, caustic soda and ethyl alcohol are easily acquired between 0.2-1.5 USD/kg, 0.3-0.7 USD/kg, and 0.4-1.8 USD/kg, respectively. As the molar ratio of the reaction mixture is 1.5 $FeCl_3$: 1.0 BTC : 3.0 NaOH [13], a rough estimate for the raw materials price is about 25 USD/kg. We believe that such prices will not hold back the use of MOFMS for the production of exquisite heterogeneous catalysts.

References

[1] Torres Galvis, H.M., Bitter, J.H., Davidian, T., Ruitenbeek, M., Dugulan, A.I., de Jong, K.P., *J. Am. Chem. Soc.*, 134 (**2012**) 16207-16215.
[2] Prieto, G., Zečević, J., Friedrich, H., de Jong, K.P., de Jongh, P.E., *Nat Mater*, 12 (**2013**) 34-39.
[3] Wynblatt, P., Gjostein, N.A., *Prog. Solid State Chem.*, 9 (**1975**) 21-58.
[4] Slater, A.G., Little, M.A., Pulido, A., Chong, S.Y., Holden, D., Chen, L., Morgan, C., Wu, X., Cheng, G., Clowes, R., Briggs, M.E., Hasell, T., Jelfs, K.E., Day, G.M., Cooper, A.I., 9 (**2016**) 17.
[5] Pachfule, P., Garai, B., Banerjee, R., *Inorg. Chem.*, 55 (**2016**) 7200-7205.
[6] Zhang, Z., Nguyen, H.T.H., Miller, S.A., Cohen, S.M., *Angew. Chem. Int. Ed.*, 54 (**2015**) 6152-6157.
[7] Schukraft, G.E.M., Ayala, S., Dick, B.L., Cohen, S.M., *Chem. Commun.*, 53 (**2017**) 10684-10687.
[8] Pulido, A., Chen, L., Kaczorowski, T., Holden, D., Little, M.A., Chong, S.Y., Slater, B.J., McMahon, D.P., Bonillo, B., Stackhouse, C.J., Stephenson, A., Kane, C.M., Clowes, R., Hasell, T., Cooper, A.I., Day, G.M., *Nature*, 543 (**2017**) 657-664.
[9] Xu, K., Sun, B., Lin, J., Wen, W., Pei, Y., Yan, S., Qiao, M., Zhang, X., Zong, B., *Nat Commun*, 5 (**2014**).
[10] Ojeda, M., Nabar, R., Nilekar, A.U., Ishikawa, A., Mavrikakis, M., Iglesia, E., *J. Catal.*, 272 (**2010**) 287-297.
[11] Shroff, M.D., Kalakkad, D.S., Coulter, K.E., Kohler, S.D., Harrington, M.S., Jackson, N.B., Sault, A.G., Datye, A.K., *J. Catal.*, 156 (**1995**) 185-207.
[12] Serra-Crespo, P., Wezendonk, T.A., Bach-Samario, C., Sundar, N., Verouden, K., Zweemer, M., Gascon, J., Berg, H.v.d., Kapteijn, F., *Chemical Engineering & Technology*, 38 (**2015**) 1183-1194.
[13] Sanchez-Sanchez, M., de Asua, I., Ruano, D., Diaz, K., *Crystal Growth & Design*, 15 (**2015**) 4498-4506.

517547-L-sub01-bw-Wezendonk
Processed on: 20-2-2018

Chapter

6

Samenvatting en Vooruitblik

Fischer-Tropsch synthese (FTS) is een proces op industriële schaal voor de productie van brandstoffen en chemicaliën vanuit grondstoffen anders dan ruwe olie, en het heeft reeds een lange geschiedenis van technologisch onderzoek en ontwikkeling. Metaal-organische raamwerken (Metal-organic frameworks, *MOFs*) zijn een groep van synthetische, poreuze, kristallijne materialen welke momenteel worden onderzocht voor het gebruik in elektronica, halfgeleiders, chemische sensoren, gasadsorptie en –scheiding, en heterogene katalyse. In dit proefschrift zijn deze werelden van het nanotechnologisch onderzoek en industriële katalyse samengebracht in het gebruik van MOFs als precursor voor geavanceerde katalytische materialen in het FTS-proces. In dit hoofdstuk worden de resultaten samengevat van de ontwikkeling van deze nieuwe synthesemethode, en de fundamentele studies gepresenteerd naar de actieve fase van ijzer gedurende het Fischer-Tropsch proces. Ook wordt het huidige onderzoek naar de Fe@C-katalysatoren bediscussieerd en wordt er een vooruitblik gegeven op de toekomstige onderzoeksdoelen.

6.2.1 Samenvatting

Fischer-Tropsch synthese (FTS) is de industriële productie van brandstoffen en chemicaliën met behulp van heterogene katalysatoren vanuit synthesegas, dat geproduceerd kan worden uit grondstoffen anders dan ruwe olie. Het heeft reeds een lange geschiedenis, maar de stijgende vraag naar producten afgeleid van ruwe olie maken dat het een zeer interessante tak is voor katalysatorontwikkeling. In dit proefschrift zijn de werelden van nanotechnologie en industriële katalyse samengebracht door gebruik te maken van nieuwe chemische structuren als precursor voor katalysatoren in FTS, materialen welke zelf nog niet zo lang waren geïdentificeerd als katalysatoren. In dit onderzoek heb ik me toegelegd op de ontwikkeling van de *MOF mediated synthesis* (MOFMS), de synthese van katalysatoren middels het gebruik van MOFs als precursor, en in het bijzonder op het blootleggen van de functie van de MOF in het proces waarbij deze wordt omgezet in de actieve ijzerkatalysator voor toepassing in het FTS-proces. Naast het inzichtelijk maken van het pyrolyseproces is bepaald hoe de MOF-eigenschappen de structuur van de uiteindelijke katalysator beïnvloeden, en of verdere ruimtelijke isolatie van de ijzerclusters de activiteit en stabiliteit van de katalysatoren ten goede komt. Er is bevestigd dat ijzercarbides de actieve fase zijn voor ijzerkatalysatoren in FTS, en gevonden dat de formulering en activeringsprocedure van de katalysatoren van grote invloed is op de resulterende ijzercarbide-fase. Om bovengenoemde redenen zijn de Fe@C-katalysatoren gebruikt als modelsysteem om de prestaties van de ijzercarbide-fases te kwantificeren.

De twee voornaamste uitdagingen bij het gebruik van ijzerkatalysatoren in Fischer-Tropsch synthese zijn om een hogere activiteit en een goede stabiliteit te behalen. IJzerkatalysatoren hebben een lagere intrinsieke activiteit dan kobaltkatalysatoren en kunnen door het gebruik op hoge temperatuur onderhevig zijn aan snelle deactivering. Bovendien is de ontwikkeling van nieuwe, zeer actieve katalysatoren beperkt tot het overwinnen van deze stabiliteitsproblemen, en er mag om die reden gezegd worden dat de voornaamste uitdaging van ijzerkatalysatoren het behalen van een hoge stabiliteit is. Tot ons genoegen heeft de ontwikkeling van Fe@C-katalysatoren geleid tot zowel een hogere activiteit als een goede stabiliteit, dankzij de hoge dispersie en omhullende bescherming van de ijzerdeeltjes wat wordt verkregen door de ontleding van de MOF-structuur. Enerzijds wordt een hoge lading ijzer verkregen, vergezeld met een zeer hoge dispersie van de nanodeeltjes, dat leidt tot een activiteit die vele industriële en laboratoriumkatalysatoren overtreft. Anderzijds verzekert het insluiten van de ijzer nanodeeltjes in een poreuze koolstofmatrix de ruimtelijke isolatie die de agglomeratie van de ijzerfase tegenhoudt. Daarbij komt dat het ijzer in de koolstofmatrix een hoge mate van carburizering ondergaat gedurende FTS en niet wordt omgezet naar inactieve oxides. Fe@C-katalysatoren vanuit de MOF mediated synthesis zijn daarmee een uitermate geschikt modelsysteem om het effect van de ijzercarbide fase te bestuderen, omdat de synthesemethode de

controle toelaat over de dispersie, belading, en mate van reductie van de katalysatoren, naast de controle over de ijzercarbide fase en mate van carburizering gedurende FTS.

Het onderzoek in dit proefschrift is beschreven in vijf hoofdstukken, waar **hoofdstuk 1** dient ter introductie van de MOFMS in de context van FTS. Hierin wordt de relevantie van MOFMS belicht als universele synthesemethode voor geavanceerde heterogene katalysatoren, alsmede de uitdagingen in het onderzoek naar verbeterde prestaties van ijzerkatalysatoren voor de productie van brandstoffen en chemicaliën uit synthesegas vanuit grondstoffen anders dan ruwe olie. In de eerste sectie van hoofdstuk 1 wordt de *black-box* visie op MOFMS gepresenteerd als de ontleding van de MOF gevolgd door de carbothermische reductie van de ijzerclusters bij de hoge temperatuur van de pyrolyse. Enkele van deze materialen werden reeds gebruikt als heterogene katalysator, maar de omzetting van de MOF naar katalysator was niet afdoende begrepen. Ondanks de betere katalytische prestaties ontbrak het fundamentele inzicht in de omzetting van ijzer-MOFs naar katalysator, en het verband tussen de MOF en katalysator. Daarom zijn *in situ* pyrolyse studies uitgevoerd met verschillende ijzer-MOFs als precursor om deze omzetting naar actieve Fe@C-katalysator te begrijpen en hun prestaties in FTS vast te leggen. We vonden een duidelijke correlatie tussen de deeltjesgrootte en het type ijzercarbide dat werd gevormd, wat ook bepaald werd door de activeringsmethode, met behoud van de fysico-chemische eigenschappen. In het tweede deel van **hoofdstuk 1** worden daarom veel studies omtrent ijzerkatalysator-activering geëvalueerd, waarin verscheidene ijzercarbides als actieve fase worden beschreven. In dit overzicht worden verbanden gelegd tussen de activeringscondities, deeltjesgrootte van ijzer, FTS-condities en de resulterende ijzercarbide fasen. De voornaamste conclusie uit bovengenoemde literatuurstudie is dat een hoge dispersie van ijzerdeeltjes de sleutel is om andere ijzercarbidefases te verkrijgen dan het Hägg carbide (χ-Fe_5C_2), en dat de synthese en stabiliteit van deze soorten ijzercarbiden niet triviaal zijn. Wanneer hexagonale carbides (ε'-$Fe_{2.2}C$) aanwezig waren, werden gedragen katalysatoren gebruikt met lage ijzerbelading om een hoge dispersie en goed verankerde nanodeeltjes te creëren. Echter, in enkele gevallen leidde de stabilisatie van de nanodeeltjes door een sterke metaal-drager interactie tot een verlaagde reductiegraad. Dit resulteert in niet-vergelijkbare katalytische systemen in termen van de productie van de ijzercarbide fasen. Desalniettemin zorgde het grote volume aan activeringsstudies met zeer degelijke katalysatorkarakterisering en *in situ* spectroscopische analyse voor het vaststellen van activeringsmethoden voor de gecontroleerde vorming van ε'-$Fe_{2.2}C$ en χ-Fe_5C_2, de meest geclaimde actieve fases in FTS over ijzerkatalysatoren.

In **hoofdstuk 2** van dit proefschrift is het ontwerp van nieuwe ijzerkatalysatoren voor FTS middels de *MOF mediated synthesis* (MOFMS) beschreven. De commercieel verkrijgbare Fe-BTC MOF is hierin gebruikt als precursor voor katalysatorsynthese, en daarnaast is de ijzerbelading gevarieerd door het impregneren van de MOF met furfuryl alcohol (FA). Een warmtebehandeling van de MOF op 500 ˚C in een inerte atmosfeer resulteerde in vorming van de 38-Fe@C-katalysator met hoge ijzerbelading

en –dispersie, welke een uitzonderlijke activiteit en stabiliteit in FTS vertoonde. Bovendien verhoogde de polymerisatie van FA in polyfurfuryl alcohol (PFA), voorafgaand aan de decompositie van de MOF-structuur, in een toegenomen dispersie van de nanodeeltjes ten koste van de ijzerbelading. De activiteit van deze katalysatoren nam toe met afnemende deeltjesgrootte, terwijl geen effect op de stabiliteit werd waargenomen. De verhoging van de activiteit werd niet toegeschreven aan de aanwezigheid van een andere ijzerfase na synthese, deze is slechts het gevolg van het verhoogde koolstofgehalte afkomstig van het gebruik van FA. Zonder FA werden volledig geoxideerde nanodeeltjes verkregen na de passiveringsbehandeling van het metallische ijzer; de cementiet (θ-Fe_3C) nanodeeltjes verkregen de FA-toevoeging bleken beter bestand tegen bulkoxidatie. De gelijke stabiliteit van alle katalysatoren geeft aan dat de decompositie en carbothermische reductie reeds in een optimale inkapseling resulteert. Deze verklaring wordt gesteund door de vrijwel identieke waarden voor de ijzer-tot-koolstof verhouding aan het oppervlak van de gepassiveerde katalysatoren. Naast de uitzonderlijke stabiliteit laat een vergelijking met zowel industriële als laboratoriumkatalysatoren zien dat de hoge dispersie en ijzerbelading van Fe@C opmerkelijk actieve katalysatoren oplevert die de prestaties van vele andere overtreffen. De Fe@C-katalysatoren konden verder verbeterd worden door promotering met kalium, waardoor ongewenste methaanvorming werd verminderd en tegelijk een verhoogde olefineselectiviteit en koolmonoxideconversie werd verkregen.

In **hoofdstuk 3** van dit proefschrift is het fundamentele onderzoek beschreven naar de omzetting van Fe-BTC naar Fe@C door middel van *in situ* Röntgen-absorptie en Mössbauer spectroscopie, waarin aangetoond werd dat in het MOF-ontledingsproduct vele tussenliggende ijzerfasen kunnen ontstaan. Tijdens de pyrolyse worden de Fe(III) oxo-clusters van de MOF naar verscheidene mengsels van ijzercarbides en ijzeroxides (Wüstiet) omgezet. Het effect van de carbothermische reductie was goed zichtbaar dankzij de emissie van koolstofdioxide en koolstofmonoxide, waarbij decarboxylering de hoofdroute voor zuurstofeliminatie bleek. De activering van de ijzerfase door waterstofreductie resulteerde in een complete conversie van de ijzeroxidefasen naar metallisch ijzer, dat na blootstelling aan het synthesegas in actieve Hägg carbides werd omgezet. Er werd geen deactivering van de katalysator gemeten dankzij de unieke ruimtelijke isolering van de ijzerdeeltjes, zoals aangetoond door XPS- en TEM-analyse. Door de combinatie van een hoge ijzerbelading en dispersie in de Fe@C-katalysator kan meer dan 95% van de ijzerfase worden omgezet naar de actieve carbidefase, resulterend in de hoogst gerapporteerde waarden voor FTS-activiteit van ijzerkatalysatoren. De ruimtelijke core-shell structuur die gevormd is met een kern van een ijzerhoudende fase ingekapseld door een poreuze koolstoflaag maakt enerzijds de bijna volledige transformatie van ijzer naar de actieve fase mogelijk, en anderzijds voorkomt het de deactivering van de ijzer nanodeeltjes onder hoge-temperatuur FTS. Door variatie van de pyrolysetemperatuur kan de controle over ijzerfase, lading, dispersie en zodoende de katalytische activiteit verkregen worden. Voor een relatief lage pyrolysetemperatuur van 400 ˚C, dichtbij de ontledingstemperatuur van de

MOF-structuur, werd de hoogste ijzerdispersie en bijbehorende activiteit behaald. Hoe hoger de pyrolysetemperatuur, hoe lager de verkregen dispersie. Een verhoogde pyrolysetemperatuur vergrootte ook de reductiegraad van de ijzerfase. Nanodeeltjes en hoge dispersie werden verkregen tot pyrolysetemperaturen tot 600 ˚C, waar redelijk kleine verschillen in katalytische prestatie werden behaald. Echter, voor een pyrolysetemperatuur van 900 ˚C werden zulke grote cementiet nanodeeltjes gecreëerd dat dit voor deze lage dispersie resulteerde in de laagst gemeten activiteit van de Fe@C-katalysatoren.

In **hoofdstuk 4** van dit proefschrift is verder onderzoek beschreven naar het effect van verschilende MOFs als precursor voor identieke pyrolysecondities. De MOFs ondergaan dan een vergelijkbare mate van carbonisering van de structuur. Materialen met een hoog oppervlak worden verkregen uit iedere MOF, hoewel de poriegroottedistributie verschilt van de ene MOF op de andere. De ijzer nanodeeltjesgrootte van de Fe@C-katalysatoren bleek gerelateerd aan de porositeit van en de ijzercluster-nabijheid in de MOF, aangezien de hoogste dispersies werden behaald met pyrolyse van de MOFs met de grootste microporeuze oppervlakte en porie-diameter. Deze resultaten bevestigen dat de ruimtelijke verdeling van de MOF de sleutel is tot het produceren van katalysatoren met hoge dispersie en lading. De FTS-activiteiten konden worden gerelateerd aan het oppervlak van de nanodeeltjes, wat aangeeft dat er een gunstige combinatie is van dispersie en belading met betrekking tot de activiteit. De optimale selectiviteit naar koolwaterstoffen met lage methaanproductie kon worden behaald met kaliumpromotie. Bovendien vertoonden deze K-gepromoteerde Fe@C-katalysatoren geen deactivering gedurende operatie op hoge conversieniveaus. De alkalipromotie verhoogde de intrinsieke activiteit van de Fe@C-katalysatoren met de hoogste dispersie, maar niet die van de monsters met de laagste dispersie. De Cu-, Mn-, en S-onzuiverheden in sommige monsters, overblijfselen uit de MOF-synthese, worden er verder van verdacht de selectiviteit te beïnvloeden.

In **hoofdstuk 5** van dit proefschrift wordt een fundamentele studie gepresenteerd naar de rol van ijzercarbides in FTS waarin de overeenkomsten en verschillen in katalytische prestaties worden gedemonstreerd. Geïsoleerde fasen van hexagonaal ε'-$Fe_{2.2}C$ en Hägg χ-Fe_5C_2 ijzercarbiden werden geproduceerd door verschillende activeringsprocedures, waarbij ε'-$Fe_{2.2}C$ werd verkregen na waterstofreductie en lage-temperatuur FTS-condities (LTFT), terwijl χ-Fe_5C_2 werd verkregen na carburisering onder hoge-temperatuur FTS-condities (HTFT). *In situ* Mössbauer spectroscopische analyse van de katalysatoren onder exact identieke condities demonstreerde dat de ijzercarbide fases intact bleven onder LTFT-condities, en dat de mate van carburisering en de Debye temperatuur (traditioneel een mate voor de kristalhardheid, hierin gerelateerd aan de ontwikkeling van de oppervlaktefase ten opzichte van bulkfase karakteristieken) van de twee verschillende carbides vrijwel gelijk waren. LTFT-activiteitstesten lieten een vrijwel identieke intrinsieke activiteit van de twee carbide fasen zien, maar significante verschillen in de productdistributie. De verhoogde

hydrogeneringsactiviteit van de ε'-$Fe_{2.2}C$ ijzerfase, blijkend uit een hogere methaanselectiviteit en lage C_{5+} selectiviteit, duidt op intrinsieke verschillen aan het katalytische oppervlak (*sites*) van de twee types ijzercarbide. Dit kan resulteren in verschillen in relatieve bezetting van waterstof en koolstof op het katalytisch oppervlak na de activeringsprocedure. De activiteit van Fe@C-katalysatoren onder LTFT-condities op 230 ˚C is noemenswaardig, daar andere ijzerkatalysatoren een vele malen lagere activiteit vertonen dan Fe@C. TEM-analyse van gebruikte LTFT-katalysatoren bevestigden behoud van de hoge ijzerdispersie en verklaarden daarmee de afwezigheid van deactivering. Het behoud van dispersie bevestigt ook dat het verschil in selectiviteit alleen is verkregen door het verschil in activeringsmethode en dus ijzercarbide fase. Dit verschil in selectiviteit voor de twee ijzercarbide fasen is ook gemeten bij Fe@C-katalysatoren met andere deeltjesgrootte. Bovendien verdween dit verschil in selectiviteit wanneer de FTS-temperatuur werd verhoogd naar 340 ˚C. Onder de HTFT-condities is het Hägg carbide de dominante oppervlaktefase, wat resulteert in volledig identieke prestaties van beide katalysatoren. Om die reden is geconcludeerd dat het verschil in productselectiviteit is geassocieerd met de verschillende ijzercarbide fasen.

6.2.2 Evaluatie

MOFs zijn op een elegante manier verzeild geraakt in de katalyse. Dankzij een *out-of-the-box* denkwijze zijn deze prachtige poreuze kristallen met levendige kleuren omgezet naar een van de meest actieve en stabiele ijzerkatalysatoren voor FTS. Het is belangrijk om te erkennen dat de daaropvolgende fundamentele studies omtrent de controle over de formulering en de literatuurstudies over de methode zelf, niet zouden zijn gepubliceerd zonder de nieuwsgierigheid van wetenschappers vanaf dag één. Bovendien ging deze nieuwsgierigheid altijd vergezeld van een zekere gedrevenheid om de uitdagingen van ijzerkatalystoren in FTS aan te gaan, die reeds zo vaak op zoveel uitstekende manieren zijn gerapporteerd [1].

De sleutel tot de MOFMS is de ruimtelijke ijzerclusterscheiding in de MOF-topologie. Met het idee in ons hoofd om de structuur te bevriezen, en het daarna toe te passen in FTS, was het idee van de MOFMS geboren. Toen het eerste verbrandingsschaaltje met Fe@C de pyrolysereactor uitkwam en bijna vlam vatte, leerden we twee dingen: één, we hebben hier te maken met extreem pyrofore ijzer nanodeeltjes; en twee, we moeten de monsters passiveren. De clusterisolatie, of ruimtelijke scheiding van het ijzer in de precursors, bleek verder te vergroten wanneer een koolstofbron in de lege ruimte tussen de clusters werd aangebracht. De resultaten zijn in overeenstemming met de traditionele inverse correlatie tussen lading en dispersie. Maar in dit specifieke geval is de afstand tussen de ijzer nanodeeltjes vooraf bepaald door de MOF-topologie en de aangebrachte koolstofbron, niet zozeer door de concentratie van mobiele nanodeeltjes-precursors zoals in traditionele synthesemethoden. Desalniettemin gaat de verhoogde dispersie en resulterende katalytische activiteit ten koste van de belading, en zodoende werden studies uitgevoerd om vast te

stellen of de dispersie en lading beïnvloed kon worden door de mate van carbonisering door het veranderen van de pyrolysetemperatuur. Het is duidelijk dat de pyrolysetemperatuur inderdaad van grote invloed is op de lading en dispersie, dankzij het gecombineerde effect van verhoogde lading en ijzermobiliteit bij hogere temperaturen. Omdat tijdens de katalytische prestatietesten lagere temperaturen dan de pyrolysetemperaturen gebruikt worden, is er geen neiging voor de deeltjes om verder te agglomereren. Het insluiten van de ijzer nanodeeltjes, of de inkapseling in de koolstofdrager, kan met een meer traditionele blik ook bekeken worden als een manier van het verankeren van de nanodeeltjes in een zeoliet-achtige omhulling. De grotere nanodeeltjes worden allen gecreëerd bij temperaturen ver boven de decompositietemperatuur van de MOF, waar significante verhoging van de carbothermische reductie resulteert in een lagere mate van ijzerisolatie door het verlies van koolstof.

De hierboven genoemde ijzerclusterscheiding kan worden veranderd door het gebruik van verschillende MOFs, waar MOFs met grote poriën en enorme oppervlakte de representatie zijn van een verhoogde ruimtelijke scheiding en dus verhoogde ijzerclusterisolatie. De verschillende ruimtelijke distributie van de ijzer nanodeeltjes verkregen door het veranderen van de MOF-topologie kan gevisualiseerd worden met behulp van het werk van Prieto *et al.* Zij tonen aan dat de *sintering* van koper nanodeeltjes in dichte nabijheid van elkaar veel hoger is dan wanneer de deeltjes een grote ruimtelijke scheiding hebben [2]. De vorming van grotere clusters met een lagere chemische potentiaal ten koste van de kleinere deeltjes is een directe thermodynamische consequentie, daar de drijvende kracht de reductie van de totale oppervlakte-energie van het systeem is [3]. De trend van de toenemende deeltjesgrootte van katalysatoren die op hogere temperaturen zijn gesynthetiseerd, volgt deze thermodynamische voorspelling zeer goed. Dit bevestigt dat de Tammann en Hüttig temperatuur effectief de grenzen aangeven van het temperatuurbereik van de MOFMS wanneer men tot doel heeft het fabriceren van kleine nanodeeltjes. Bijvoorbeeld, onze ongepubliceerde data over Cu-MOF pyrolyse laat zien dat een hogere opwarmsnelheid noodzakelijk is voor het verkrijgen van een redelijke dispersie voor katalytische toepassing. Wanneer het besef komt dat het smeltpunt van koper bijna 500 ˚C lager ligt dan dat van ijzer en geen carbides vormt, zijn deze resultaten niet geheel een verrassing. Maar, het stimuleert wel de discussie over wat de optimale ontwerpparameters zijn voor Fe-MOFs zodat maximale dispersie en FTS-activiteit kan worden behaald.

De studie van de MOF-pyrolyse demonstreerde dat de vorming en verankering van de nanodeeltjes begint wanneer de structuur begint uiteen te vallen, wat zou betekenen dat MOFs met een lage decompositietemperatuur de meest gunstige zijn. Daarbij komt dat de MOF-topologiën met zeer grote poriën en verhoogde ijzerclusterscheiding de voorkeur hebben boven de MOFs met hoge dichtheden en onderling verbonden ijzerclusters. Toch moeten we concluderen dat de beperkte selectie van topologieën en verschillende linkers ons niet in staat stelden om volledig inzicht te

verkrijgen over de relatie tussen de aard van de MOF en de resulterende ijzerdispersie in Fe@C-katalysatoren. Bovendien waren de MOF-structuren met grote poriën vele malen meer rigide dan de tegenhangers met hogere dichtheid, wat zorgde voor verdere verstrengeling van de te onderzoeken parameters. Om die reden zal de MOF mediated synthesis verder ontwikkeld moeten worden, om vanuit een *trial-and-error*-type ontwikkelingsmethode naar een volledig geïntegreerde methode van materiaalontwerp en toepassing te gaan. Onderzoeksvragen omtrent de topologie zouden beantwoord kunnen worden met de hulp van de pioniers in het veld van *isoreticular chemistry*. De MOF-topologie kan verder uitgebreid worden door gebruik te maken van langere linkerlengtes in de MOF, om zo de clusterscheiding te verhogen, terwijl een identieke topologie behouden blijft [4, 5]. Op eenzelfde manier kunnen polymeer-MOFs gebruikt worden om verder uit te zoeken wat een verhoogde ijzerclusterisolatie kan betekenen, met het voordeel dat een beter geordende structuur en behouden topologie meer inzicht geven dan de ongecontroleerde toevoeging van koolstofbronnen zoals FA [6]. Naast de verhoogde controle over de ijzerclusterisolatie, is het gebruik van polymeren specifiek interessant voor het maken van granulaten met de afmeting van enkele millimeters, om zodoende de mechanische stabiliteit te bevorderen [7]. De keuze voor een specifiek MOF-type kan ook gebaseerd worden op data uit functionele materiaalontdekking door kristalstructuur-voorspellingen en eigenschappenvoorspellingen [8]. Deze aanpak staat in schril contrast met de huidige selectieprocedure van de topologie, gebaseerd op waardes van de MOF-karakterisering, wat betekent dat extensieve syntheserouten moeten worden bewandeld voordat de eigenschappen kunnen worden geanalyseerd. De huidige ontdekkingen in het veld van MOFs zouden kunnen bijdragen aan de ontwikkeling van de MOFMS tot een meer volwassen synthesemethode.

Naast het creëren van zeer actieve en stabiele katalysatoren voorzag de MOFMS ons ook van katalysatoren die verscheidene ijzercarbide fases konden produceren, zodat hun prestaties konden worden onderzocht. Hoewel de ijzercarbide fasen onderzocht waren met *in situ* Mössbauer experimenten terwijl de deeltjesgrootte werd gevarieerd, bracht de activeringsmethode echte controle over de ijzercarbide fase. De controle over de ijzercarbide fase en daarbij constante dispersie maakte de eenduidige bepaling mogelijk van een identieke activiteit van de twee carbide fases hexagonaal ε'-$Fe_{2.2}C$ en Hägg χ-Fe_5C_2. Deze bevindingen staan in contrast met claims over een voorkeur van de ijzercarbide fase met maximale activiteit [9]. De resultaten wijzen uit dat de activiteit en stabiliteit van ijzerkatalysatoren niet gedomineerd worden door een unieke samenstelling van de actieve fase, maar dat de prestatie afkomstig is van de initiële physico-chemische eigenschappen van de katalysator en de effectieve omzetting naar een actieve FTS-katalysator onder reactiecondities. Het is daarom van het voornaamste belang dat het ijzeroppervlak gecarburiseerd kan worden zonder dat de dispersie verloren gaat. Het verschil in selectiviteit, toegeschreven aan een verhoogd hydrogeneringsvermogen van de ε'-$Fe_{2.2}C$ katalysator, blijft onderdeel van discussie. We zijn niet verzekerd dat deze verandering voortvloeit uit verschillen in het intrinsieke katalytische

oppervlak, of dat relatieve bezetting van waterstof en koolstof significant gewijzigd wordt van de ene op de andere activeringsmethode. Het verschil in relatieve bezetting kan ook het resultaat zijn van een verandering in het intrinsieke katalytische oppervlak. Huidige inspanningen gericht op het vinden van slimme experimenten zodat een van deze argumenten geaccepteerd of verworpen kan worden. Het werk aan de LTFT wordt ook voortgezet, met de noemenswaardige activiteit op 230 ˚C, en op dit moment ook op 210 ˚C. Gezien het feit dat de fundamentele studie onder LTFT-condities niet gericht was op de optimale katalysatorformulering, blijft er ruimte voor verbetering in activiteit en selectiviteit.

Samenvattend, door het werk uitgevoerd in dit proefschrift, is er veel inzicht verkregen in de nieuwe MOFMS-methode voor heterogene katalysatorsynthese. Het heeft geleid tot de ontwikkeling van zeer actieve en stabiele ijzerkatalysatoren onder zowel HTFT als LTFT-condities, en tot verder begrip van de ijzercarbide fases in FTS in het algemeen. Zoals in ieder onderzoeksproject, zijn er meer vragen dan antwoorden bij gekomen op de weg naar dit proefschrift, en het zal daarom zeker niet het einde van onze inspanningen zijn.

6.2.3 Huidig onderzoek en vooruitblik

Dankzij hun hoge activiteit en stabiliteit zijn Fe@C-katalysatoren een fascinerend onderzoeksonderwerp in het veld van FTS. Veel van het werk in dit proefschrift heeft zich gericht op de opheldering en toepassing van de katalysatorsynthesemethode MOFMS, en daarom blijft de wens bestaan om een beter begrip in het katalytisch gedrag van Fe@C te verkrijgen. Om die reden is een parametrische studie inclusief kinetische data-analyse uitgevoerd in het HTFT-regime. De datasets zijn gefit aan een model van Ojeda *et al.* [10], met als basis de H-geassisteerde en ongeassisteerde CO dissociatie. Ons specifiek doel is om op een juiste manier het gedrag van de selectiviteit te benaderen, bestaande uit koolwaterstofselectiviteit volgens de Schulz-Flory distributies, olefine-tot-paraffine verhoudingen gerelateerd aan de verblijftijd, de *water-gas shift* activiteit en de FTS-activiteit. De keuze voor het model was gestaafd met resultaten van een *steady-state isotopic transient kinetic analysis* (SSITKA) studie, uitgevoerd aan de NTNU in Trondheim. Ons doel is om aanvullende experimenten uit te voeren onder realistische FTS-condities om meer inzicht te verkrijgen in de bezetting van waterstof en koolstof op het katalytisch oppervlak, om zodoende mechanistische informatie af te leiden zoals de mate van isotoop-insertie in de koolwaterstofproducten.

De kansen die gecreëerd worden door de Fe@C-katalysatoren gaan hand in hand met de inherente uitdagingen van zeer actieve CO-dissociatie katalysatoren. IJzerkatalysatoren staan bekend om de grote verschillen in dichtheid die gevormd worden gedurende de reductie en activering, waarin de kans bestaat op ijzerfase-segregatie [11]. Daarbovenop komen de krachten die uitgeoefend worden op de katalysatorkorrels door snelle carburizering en overdadige koolstofafzetting, wat ook gedurende *steady-state* operatie kan resulteren in desintegratie van de deeltjes en uiteindelijk kan

leiden tot reactorfalen. Het is daarom van groot belang voor gepakt-bed reactoroperatie dat de katalysatorkorrels goed zijn gepelletiseerd of gegranuleerd met een bindermateriaal. Omdat het pelletiseren van deze pyrolytische koolstofmaterialen zeer lastig is en vaak al resulteert in desintegratie van de deeltjes gedurende het laden van de reactoren, is er onderzoek gedaan naar het toevoegen van polymeer aan de oorspronkelijke MOF. De vorming van deze pellets is onderzocht, waarbij is gelet op de ijzerbelading en porositeit van het koolstofdragermateriaal na de pyrolyse. Alleen enkele van de geteste polymeren leverden de gewenste dispersie, lading en porositeit, waar het voornaamste doel was om de katalytische activiteit en stabiliteit te behouden gedurende honderden uren van reactoroperatie. De Fe@C-composieten zijn aan compressiesterkte testen blootgesteld om de verbetering in mechanische stabiliteit door het gebruik van polymeertoevoeging te kwantificeren.

Tenslotte, is er het vaak gehoorde argument dat MOFs veel te duur zouden zijn om te gebruiken als precursor voor katalysatorsynthese. Wij vinden dat een dergelijke stelling met zorg moet worden benaderd, waarin de toegevoegde waarde van de producten in vergelijking tot de grondstoffen moet worden afgeschat. Zodoende kan ook een goede schatting voor het kapitaal en operationele kosten van een proces worden gemaakt, inclusief de kosten voor de katalysator. Maar, aangezien dergelijke kostschattingen een project op zichzelf zijn [12], beperken we ons hier tot het beprijzen van MOF-productie op commerciële schaal, om te laten zien dat de kosten in vergelijking met andere bulk chemicaliën slechts marginaal stijgen. Fe-BTC kan op kamertemperatuur en atmosferische druk worden gesynthetiseerd in een waterige oplossing met een pH van 11, waarbij gebruikt wordt gemaakt van NaOH om het trimesinezuur op te lossen. IJzerchloride wordt hierop druppelsgewijs toegevoegd en de resulterende stof kan worden gewassen met water en worden gedroogd met alcohol. Het op bovengenoemde manier geproduceerde Fe-BTC beschikt over een betere porositeit dan Basolite F300 geproduceerd door BASF [13]. Het grootste deel van de kosten voor deze syntheseroute komen van het trimesinezuur, met de systematische naam 1,3,5-benzeentricarbonzuur. Chinese en Indische leveranciers schrijven bulkoffertes voor deze MOF-linker uit tussen 10-20 USD/kg, terwijl ijzerchloride, natriumhydroxide en ethanol makkelijk verkrijgbaar zijn tussen 0.2-1.5 USD/kg, 0.3-0.7 USD/kg, en 0.4-1.8 USD/kg, respectievelijk. Omdat de molaire ratio van het reactiemengsel 1.5 $FeCl_3$: 1.0 BTC : 3.0 NaOH is [13], kan een ruwe schatting van de grondstofkosten van 25 USD/kg worden gemaakt. Wij blijven van mening dat zulke prijzen het gebruik van MOFMS voor de productie van voortreffelijke heterogene katalysatoren niet zal tegenhouden.

Literatuur

[1] Torres Galvis, H.M., Bitter, J.H., Davidian, T., Ruitenbeek, M., Dugulan, A.I., de Jong, K.P., *J. Am. Chem. Soc.*, 134 (**2012**) 16207-16215.
[2] Prieto, G., Zečević, J., Friedrich, H., de Jong, K.P., de Jongh, P.E., *Nat Mater*, 12 (**2013**) 34-39.
[3] Wynblatt, P., Gjostein, N.A., *Prog. Solid State Chem.*, 9 (**1975**) 21-58.
[4] Slater, A.G., Little, M.A., Pulido, A., Chong, S.Y., Holden, D., Chen, L., Morgan, C., Wu, X., Cheng, G., Clowes, R., Briggs, M.E., Hasell, T., Jelfs, K.E., Day, G.M., Cooper, A.I., 9 (**2016**) 17.
[5] Pachfule, P., Garai, B., Banerjee, R., *Inorg. Chem.*, 55 (**2016**) 7200-7205.
[6] Zhang, Z., Nguyen, H.T.H., Miller, S.A., Cohen, S.M., *Angew. Chem. Int. Ed.*, 54 (**2015**) 6152-6157.
[7] Schukraft, G.E.M., Ayala, S., Dick, B.L., Cohen, S.M., *Chem. Commun.*, 53 (**2017**) 10684-10687.
[8] Pulido, A., Chen, L., Kaczorowski, T., Holden, D., Little, M.A., Chong, S.Y., Slater, B.J., McMahon, D.P., Bonillo, B., Stackhouse, C.J., Stephenson, A., Kane, C.M., Clowes, R., Hasell, T., Cooper, A.I., Day, G.M., *Nature*, 543 (**2017**) 657-664.
[9] Xu, K., Sun, B., Lin, J., Wen, W., Pei, Y., Yan, S., Qiao, M., Zhang, X., Zong, B., *Nat Commun*, 5 (**2014**).
[10] Ojeda, M., Nabar, R., Nilekar, A.U., Ishikawa, A., Mavrikakis, M., Iglesia, E., *J. Catal.*, 272 (**2010**) 287-297.
[11] Shroff, M.D., Kalakkad, D.S., Coulter, K.E., Kohler, S.D., Harrington, M.S., Jackson, N.B., Sault, A.G., Datye, A.K., *J. Catal.*, 156 (**1995**) 185-207.
[12] Serra-Crespo, P., Wezendonk, T.A., Bach-Samario, C., Sundar, N., Verouden, K., Zweemer, M., Gascon, J., Berg, H.v.d., Kapteijn, F., *Chemical Engineering & Technology*, 38 (**2015**) 1183-1194.
[13] Sanchez-Sanchez, M., de Asua, I., Ruano, D., Diaz, K., *Crystal Growth & Design*, 15 (**2015**) 4498-4506.

Chapter

6

Acknowledgements

Four years have passed since I found myself having a discussion with professors Jorge Gascon and Freek Kapteijn about the possibilities of a position as PhD student in the Catalysis Engineering group. However, even before, Jorge has been my focal point during the courses at the TU Delft, and he has always showed tremendous interest and involvement. The same goes for Freek, a very committed internship coordinator and keen on teaching data treatment of reaction kinetics. These dedicated professors became my promotors and for that reason, they deserve my gratitude.

Jorge, thank you for teaching me everything that I have asked you for. You have an endless drive toward research and the gathering of knowledge, and you are eager to jump to a totally different subject just by enthusiasm. I have learned a lot from the way you structure research and the manuscripts that follow. Thank you for your trust, letting me present our work everywhere in the world. Finally, thanks for the movies that killed the time during synchrotron nights. Freek, thank you for your never-ending critique during the lunch and group meetings. You really took the time to assess my findings, made sure that I had done it in a correct way and let me rethink my analysis to improve it. I really enjoyed your guidance on the catalyst-shaping project, your monolith-enthusiasm and experience was very welcome. The persistence you have on investigating true kinetics and elementary steps was much appreciated in this combined material science – heterogeneous catalysis project. Finally, thanks for letting every professor in Cape Town believe that I was your taxi driver. A very warm thank you to you Michiel Makkee, though not my co-promotor, he very well may have been. Thank you for including reality, feasibility, technical readiness levels and *schotelgetallen* into the equation. You have always provided industrial and critical insight to my thesis, and I do hope that you can live with the result of these four years. As much as to many other professors and professionals in the field, my gratitude goes out to my committee members. Thank you for your remarks and ultra-fast response time, I am sure contacting Guinness would establish a world-record time of committee formation. Thank you to all the researchers that I have met during the conferences around the world, who were willing to discuss my work and provide me with relevant and sometimes completely new information. Monique, congratulations on your position and I wish you all the best in the years to come. Patricia, thanks for teaching me so much on TEM analysis and lattice fringes in particular, I very much liked meeting you again in South Africa.

A special thanks to the people from Dow Chemical in Terneuzen, and to Vera, Adam and Matthijs in particular. Vera, when I first met you, you became my MSc thesis supervisor, and thanks to you, my interest for catalysis research grew to a maximum. Thank you for jump-starting my PhD with your lead on the first manuscript. I have fully enjoyed our continued collaboration during these four years and I hope you read this dissertation with some pride and joy. Adam, thank you for your work in this project and the input it provided to this thesis. It was nice meeting you again in Denver. Matthijs, thank you for your highly valuable input to the *ACS Catal* manuscript and taking so much time working through it. I would also like to acknowledge professors Krijn de Jong and Emiel Hensen for the fruitful discussions and collaborations on the MOF mediated synthesis projects together with Xiaohui. Your insight provided much input to our successive work. Iulian, thank you for our endless discussion on Mössbauer data and signal analysis. I am amazed by the facilities in your laboratory and the way you provide data to the whole of The Netherlands and beyond. I hope my work has helped you to a more extensive collaboration with the Catalysis Engineering group. Enrique, and also Sole, thanks for collaborating and having such great times together.

Harrie, Bart, Lila, Willy, en ook Kevin, hartelijk bedankt voor al jullie inspanning. Wellicht zorgde mijn wetenschappelijke nieuwsgierigheid zo nu en dan voor een aantal ongewenste aanpassingen in de opstellingen, ik hoop dat jullie gelukkig zijn met de vooruitgang die ik heb geboekt en de gerealiseerde resultaten. Harrie, koning ad-hoc en hertog veelzijdig, nooit te beroerd om iets te doen, altijd vrolijk, meneer ik-kan-er-wél-bij, je bent echt een geweldige technicus. Ik hoop dat je nog vele jaren kan genieten van deze baan en dat er maar nog veel collega's en promovendi leuke uitdagingen voor je kunnen creëren in de altijd veranderlijke wetenschappelijke omgeving. Bart, de heer *Tee-Pee-Ar*, *Tee-Gee-Aa*, en nog veel meer, held van het onderhoud en nog meer van de vervanging (sorry voor mijn decompositie-troep): zoals vaker gezegd, Rome is niet in één dag gebouwd, maar jij was er zeker vanaf het begin bij. Bedankt voor al je geduld en eindeloze aansporing. Liliana, Miss Baron, so nice to have had you on board this team. I highly value your experience on many setups and your hands-on mentality. The way you got the SIMDIST running really displayed your potential and power to work with both professors and research staff. Willy, ik heb het eerder gehad over Guinness records. Ik weet zeker dat jij de laagste-afschrijving-op-apparatuur met twee vingers in je neus haalt. Jouw protocollen, informatieverschaffing en handhaving zijn een onmisbare spil in een goed functionerend lab. Kevin, veel dank voor het tuben van de manifold voor de hogedruk reactor en voor het delen van je ervaring met dit soort opstellingen en specifiek de gaschromatograaf. Dat je nog maar vaak van het snowboarden mag genieten. Els en Caroline, bedankt voor al jullie hulp met het plannen van alle afspraken, de reminders voor belangrijke zaken, het verwerken van alle documenten van studenten, de hulp bij de boekingen van

buitenlandreizen, en interesse in mijn project. Sorry dat ik jullie moest belasten met al die pakketjes versturen. Ben, Bart, Duco, en Wiel, bedankt voor jullie hulp bij het instrueren en/of analyseren van mijn zwarte poeders. Hoewel mijn *Faraday Discussions* paper nog weinig geciteerd is, is dit toch echt het werk waarin ik jullie allemaal hartelijk heb bedankt. Iedereen in de BHV-groep, bedankt voor de opleiding en ervaring, met stip Tonny Schuit voor de begeleiding in het hogedruk lab.

Catalysis Engineering! My lord, what a time we have had. Some professors have come, others have gone, but we always stayed true to our task. Whatever that task was, and whatever problems we faced while doing so. Lide, thanks for helping me with the FTS setup while running so many hours, and your critical opinion on data gathering and catalyst synthesis. You are truly a smart and ambitious professor-to-be and I am delighted that you are effectively supporting me to defend my thesis. Maria José, thank you for collaborating with me on various projects from methane conversion and syngas chemistry, to the hours in the PT2 course. Xiaohui, you have become a highly esteemed colleague and I have enjoyed working together. Thanks for sharing so much of your culture with me, I really had fun showing you my country and the Dutch habits. You are also one hell of a travel mate abroad. Xuerui, Xinlei, and Xiaohui, thanks for visiting us here near the windmills, Sofie loves the Delft Nijntje you gave her. Filipe and Ágí, thanks for being amazing office buddies! Beba, thanks for teaching me to combine hard work with whisky, of course, not at the same time. Alma, always so friendly and joyful, thanks for sharing all your chemistry knowledge with me. Jara, thanks for the laughs and showing everybody how scheduling works. Yixiao, great work on the TAP and thanks for the discussions on isotopic labelling studies. Ina, miss perseverance, I am sure that methane is going to crack on you eventually. Robert, the last PhD to remain in the old building, good luck holding the fortress. Edu, thanks for the energizing spirit you are! Dima, I highly appreciate your teaching sessions on XPS and your friendly ways. Russian chocolate rocks! Fran, thanks for teaching me the fundamentals of electrochemistry, you are welcome for that Denver-beer in Amsterdam. Irina and Arthur, thanks for the dinners we shared from Prague to Jeddah, hope to see you soon again. Nastya, thanks for your great work on our many collaborations and even more amazing work on holding down Maarten. Anahid and Mohammed, thanks for your care when my car was totalled and for being such warm persons in general. To all the colleagues in the new building – sorry I was always in the old one: Meixia, Adrian, Constantino, Riming, Guanna, and thanks to all the others with whom I have spent time in the lab; Hao, Jose, Sina, Abrar, Rupali, Martijn, Sumit, Thais, Philip, Elena, Alexey, Alla, Rob, Mario, Tania, Maxim, Emmanuel, Jorrit, Oscar, Jan, Yuvraj, Damla, Canan, Jana, Pablo, Sonia, the list just goes on… Special thanks to all students, BSc and MSc, Krijn, Evelien, Liam, Daniel, Vivian, Ishika, Marius, Stephane, Bob and Christian, for your hard work and believing in my ideas.

Boys, deze is voor jullie. Zuipen op de boot, grappen tijdens het koken, Paulaners in de kroeg, de bar in de brand bij de chupi's, potjes jassen in de zon, lekker brak zitten zeiken op elkaar, in één woord: geweldig. Dank voor de post-studietijd studietijd. Dat mijn brakke bek op het porselein maar lang onze groepsapp-foto mag zijn. De vrouw die in één adem genoemd hoort te worden met koken, biertjes, zeilen en natuurlijk de Ald Wal: Margje. Bedankt dat je altijd klaarstaat voor serieuze en minder serieuze gesprekken. Kelvin! Van Backstreet Boy naar Best Man. Bedankt voor al het relativeren, de gesprekken over de bank, over de chemische sector, over waar kansen liggen, en over wat mooie auto's zijn. Gertje, mijn collega-PhDer, tante Birgit. Het echte werk begon waarschijnlijk in Brussel met de kerstboom in de lift. Maar we hebben niet stil gezeten sindsdien. Echt helemaal top dat we samen ons eigen onderzoeksplan hebben gesmeed en daar nog een cover uit hebben gehaald ook. Bosboom, Marloe en Boob zullen beamen dat Frankrijk een AZG-tje wordt. Bedankt voor jullie amazing pizza-skills met Sofie. Guus, Yvo, Ed, zonder jullie is het nooit meer hetzelfde, bedankt voor alle etentjes en drankjes, de gezelligheid, en dat jullie me weer op tijd op de trein zetten naar Nicole. Miguel y Paola, gracias por seguir siendo amigos y que todavía tenemos grandes momentos juntos. The best comes unexpected. Thanks for joining my defense party! Eli, bedankt voor je luisterend oor tijdens je PhD-tijd en de discussies nadien, we houden de etentjes samen erin. Koot en Karlijn bedankt dat jullie wanneer mogelijk altijd even langskomen voor koffie of lunch, jullie zijn altijd welkom. Conrad, Cor, bedankt voor je intens ongevoelige en soms botte, maar goudeerlijke opmerkingen. Sander en Mauro, bedankt voor het altijd weer laten herleven van de tijd in Den Haag. Sharina, Jelle, Marc, Lies, Mark, Luus, Eva, Michael, Karlijn, Jacob, bedankt voor de gezelligheid en dat jullie zulke goede vrienden voor Nicole zijn. We praten te veel over België deel 2, laten we dat vooral snel doen.

Pap en mam. Bedankt dat jullie er altijd voor me zijn, alles voor me hebben geregeld, kantelpunten bij me hebben aangekaart, overal met me mee naar toe zijn gegaan, me veel hebben geleerd, alles hebben bekostigd, en uit liefde hebben gegeven. Onze gesprekken worden met de jaren steeds waardevoller en ik denk dat ik nog steeds veel van jullie leer. Bedankt voor al jullie wijsheid. Hoewel de agenda nu wat voller is, en ik een stukje verder weg ben gaan wonen, doet het me deugd om elkaar vaak te zien. Bovendien vind ik het prachtig om jullie nu als grootouders te zien! Maria, lieve mams, het is heerlijk hoe Sofie zich thuis voelt bij jou en dat ze de familieband zo sterk aanvoelt. Dat we nog maar vaak Hoogte 80 en het vergane klooster van Monnikenhuizen mogen bewandelen. Henk, Hendrik, pa, ik lach me echt doormidden als ik Sofie met jou die gekke bekken zie doen. Het herinnert me aan mijn fijne kindertijd. Die was natuurlijk niet compleet zonder Leo. Bedankt geweldige zus! Super dat we elkaar na alle buitenland-ervaring nu meer zien. Wellicht heeft het ook iets te maken met Thomas en die andere leuke vent van je. We kijken uit naar je bruiloft en zijn vereerd om de doopouders van Floris te worden! En natuurlijk hartstikke tof dat je mijn paranimf

wilde zijn, ik kon me geen betere wensen. Dat de familieaangelegenheden een hoogtepunt zijn mag duidelijk zijn. Ik wil daarom ook alle ooms en tantes, neven en nichten graag bedanken voor de borrels, etentjes, kaartspelletjes, en weekendjes weg. Paul en Louise, Tiny en Frank, Sjoerd, Aniek, Iris, Rowdy, Floor, Lola, Sam, een goed stuk worst dat zie je niet, en bij probleem'n, poar neem'n! Vesna en Nico, bedankt dat jullie er zo voor ons zijn. Nicole had het niet zo heel gek bedacht om bij jullie in de buurt te gaan wonen. Lekker eten en drinken, ontspannen aan het strand, af en toe een duik in de sneeuw, de vaste oppasbrigade, helemaal prima. Jullie zijn een fijn luisterend oor en de beste *Schwiegereltern* die een man kan wensen. Bedankt voor alles! Bertie en Alessandra, we kijken uit naar de volgende vakantie in Lenzerheide of Locarno, deze keer samen met Guus. Bedankt voor de heerlijke ontspanning samen.

Nicole. Mijn lieve, warme, mooie Nicole. *Life is a rollercoaster, going up and down, but you hold on uphill and let go during the falls: I couldn't do it without you.* Jij bent mijn nummer 1. Ik hoop dat we over een paar jaar terugkijken op deze drukke en leuke tijd met veel plezier en trots. Je mag absoluut geweldig trots zijn op wie je bent en wat je dagelijks doet, zowel in je veeleisende baan als met onze eindbaas, miss know-it-all, Soof, onze kleine en nu al grote meid. Ik ben erg blij dat we samen zoveel tijd kunnen vrijmaken om haar de aandacht, opvoeding, lering en liefde te geven die ze verdient, maar dat we daarnaast ook onze diners, feestjes, film-avondjes, vakanties en vrije tijd hebben. Het is geweldig om de tijd te zien vliegen met de datum van onze trouwdag om mijn vinger. Ik hou van je. Sofie, schat van me, als je ooit toch zou begrijpen wat papa en mama voor jou over hebben. Je bent me er een. "Papa, je mag niet van je mes likken. Mama, vandaag is geen chocopasta-dag, doe maar honing op mijn brood. Papa, kun je me alsjeblieft helpen met deze stickers, ze plakken niet meer. Mama, kom jij me vanavond ophalen want papa brengt me vandaag al. Papa, wat heb ik een grote rommel gemaakt hè, zullen we het samen gaan opruimen. Mama, aan de kant ik ga heel ver in het zwembad springen. Goedemorgen papa, ik heb trek, kom we gaan naar beneden! Papa, je krant is er weer!" En je befaamde: familie Wezendonk knuffel! Ik ben zo blij dat jij iedere dag de grootste lol hebt en het bij iedereen naar je zin hebt. Het is heel leuk om met al je juffen over je te praten, zo krijg ik een goed idee van wat je allemaal uitspookt als wij er niet zijn. Geweldig dat ik na vier jaar Dr. Papa ben, ik wens je heel veel plezier op school, dat heb ik ook altijd gehad. *Trust me, I'm an engineer.*

Koog aan de Zaan, februari 2018

List of Publications

Google Scholar profile of Tim A. Wezendonk, last accessed February 2018; H-index 7.

Total of 12 peer-reviewed publications, 1 book chapter, 1 patent, 4 unpublished manuscripts.

Authors, title and journal	*Cited by*	*Year*
Santos, V.P., **Wezendonk, T.A.,** Jaén, J.J.D., Dugulan, A.I., Nasalevich, M.A., Islam, H., Chojecki, A., Sartipi, S., Sun, X., Hakeem, A.A., Koeken, A.C.J., Ruitenbeek, M., Davidian, T., Meima, G.R., Sankar, G., Kapteijn, F., Makkee, M., and Gascon, J., Metal organic framework-mediated synthesis of highly active and stable Fischer-Tropsch catalysts, *Nature Communications*, 6:6451	88	2015
Boekhoven, J., Koot., M., **Wezendonk, T.A.**, Eelkema, R., and Van Esch, J.H., A self-assemble delivery platform with post-production tunable release rate, *Journal of the American Chemical Society*, 134 (31), 12908-12911	63	2012
Diaz-Morales, O., Raaijman, S., Kortlever, R., Kooyman, P.J., **Wezendonk, T.A.,** Gascon, J., Fu, W.T., and Koper, M.T.M., Iridium-based double perovskites for efficient water oxidation in acid media, *Nature Communications*, 7, 12363	30	2016
Wezendonk, T.A., Santos, V.P., Nasalevich, M.A., Warringa, Q.S.E., Dugulan, A.I., Chojecki, A., Koeken, A.C.J., Ruitenbeek, M., Meima, G.R., Islam, H., Sankar, G., Makkee, M., Kapteijn, F., and Gascon, J., Elucidating the Nature of Fe Species during Pyrolysis of the Fe-BTC MOF into Highly Active and Stable Fischer-Tropsch Catalysts, *ACS Catalysis*, 6 (5), 3236-3247	27	2016
Bavykina, A.V., Rozhko, E., Goesten, M.G., **Wezendonk, T.A.,** Seoane, B., Kapteijn, F., Makkee, M., and Gascon, J., Shaping covalent triazine frameworks for the hydrogenation of carbon dioxide to formic acid, ChemCatChem, 8 (13), 2217-2221	17	2016
Alvarez, A., Bansode, A., Urakawa, A., Bavykina, A.V., **Wezendonk, T.A.,** Makkee, M., Gascon, J., and Kapteijn, F., Challenges in the Greener Production of Formates/Formica Acid, Methanol, and DME by Heterogeneously Catalyzed CO_2 Hydrogenation Processes, *Chemical Reviews*, 117 (14), 9804	15	2017
Oar-Arteta, L., **Wezendonk, T.A.,** Sun, X., Kapteijn, F., and Gascon, J., Metal organic frameworks as precursors for the manufacture of advanced catalytic materials, *Materials Chemistry Frontiers*, 1, 1709-1745	7	2017

Rico-Frances, S., Jardim, E.O., **Wezendonk, T.A.,** Kapteijn, F., Gascon, J., Sepúlveda-Escribano, A., and Ramos-Fernandez, E.V., Highly dispersed Pt on $Ti_xCe_{1-x}O_2$ as an active phase in preferential oxidation of CO, *Applied Catalysis B: Environmental*, 180, 169-178	7	2016
Serra-Crespo, P., **Wezendonk, T.A.,** Bach-Samario, C., Sundar, N., Verouden, K., Zweemer, M., Gascon, J., Van den Berg, H., and Kapteijn, F., Preliminary Design of a Vacuum Pressure Swing Adsorption Process for Natural Gas Upgrading Based on Amino-Functionalized MIL-53, *Chemical Engineering & Technology*, 38 (7), 1183-1194	7	2015
Van Driel, B.A., **Wezendonk, T.A.,** Van den Berg, K.J., Kooyman, P.K., Gascon, J., and Dik, J., Determination of early warning signs for photocatalytic degradation of titanium white oil paints by means of surface analysis, *Spectrochimica Acta Part A: Molecular and Biomolecular Spectroscopy*, 172, 100-108	6	2017
Wezendonk, T.A., Santos, V.P., Warringa, Q.S.E., Chojecki, A., Ruitenbeek, M., Meima, G.R., Makkee, M., Kapteijn, F., and Gascon, J., Structural and elemental influence from various MOFs on the performance of Fe@C catalysts for Fischer-Tropsch Synthesis, *Faraday Discussions,* 197, 225-242	2	2017
Oar-Arteta, L., Valero-Romero, M.J., **Wezendonk, T.A.,** Kapteijn, F., and Gascon, J., Formulation and catalytic performance of MOF-derived Fe@C/Al composites for high temperature Fischer-Tropsch Synthesis, *Catalysis Science & Technology,* 2018		2018
Oar-Arteta, L., **Wezendonk, T.A.,** Sun, X., Kapteijn, F., and Gascon, J., Metal organic frameworks as precursors for the manufacture of advanced catalytic materials, *Nanotechnology in Catalysis: Applications in the Chemical Industry, Energy Development and Environment Protection,* 225-250, Wiley-VCH Verlag GmbH & Co. KgaA		2017
Santos, V.P., Chojecki, A., Meima, G.R., Koeken, A., Ruitenbeek, M., Gascon, J., Makkee, M., Kapteijn, F., and **Wezendonk, T.A.,** Process for synthesizing iron carbide Fischer-Tropsch catalysts, US Patent US 9,833,774 (B2)	1	2017

Presentations (selection)

The Route toward Fe-based Fischer-Tropsch Catalysts using MOFs: from Fundamentals to Industrial Performance | Denver, USA, 25th NACS. **Oral, 08.06.2017**

Structural and Elemental Influence of various MOFs of the Performance of Fe@ Catalysts for Fischer-Tropsch Synthesis | San Francisco, USA, ACS 253rd National Meeting. **Oral and Poster, 03.04.2017**

The Nature of Fe Species during MOF Pyrolysis and FTS | Cape Town, South Africa, Catalysis for Fuels: Faraday Discussion. **Paper and Poster, 24.01.2017**

Elucidating the Nature of Fe Species during Pyrolysis of the Fe-BTC MOF into Highly Active and Stable Fischer-Tropsch Catalysts | Long Beach, USA, MOF2016. **Oral, 28.07.2016**

Electrochemical CO2 Reduction over MOF-derived Cu Catalysts | Noordwijkerhout, The Netherlands, NCCC-XVII. **Oral, 08.03.2016**

Highly Active and Stable Fischer-Tropsch Catalysts obtained through Unconventional Metal-Organic Framework Mediated Synthesis | Salt Lake City, USA, 15 AIChE Annual Meeting. **Oral, 11.11.2015**

Highly Active and Stable Fe-based Fischer-Tropsch Catalysts obtained through MOF Mediated Synthesis | Potsdam, Germany, EuroMOF 2015. **Poster, 13.10.2015**

Metal Organic Mediated Synthesis of Highly Stable and Active FTO Catalysts | Denver, USA, ACS 249th National Meeting. **Oral, 26.03.2015**

Highly active and stable FTS catalysts obtained through MOF mediated synthesis | Noordwijkerhout, The Netherlands, NCCC-XVI. **Oral, 03.03.2015**

New Synthetic Avenues toward Metal-Supported Catalysts | CHAINS 2014, Veldhoven, NL. **Oral, 17.11.2014**

Highly active and stable Fe-based FTS catalysts from MOFs | DPTI Annual Event 2014, Rotterdam, The Netherlands. **Poster, 07.11.2014**

Methane/Carbon Dioxide Separation from Natural Gas: A Conceptual Design using Metal-Organic Framework based Pressure Swing Adsorption | CHISA 2014, Prague, Czech Republic.

Oral, 27.08.2014

Conceptual Design of a PSA System for Natural Gas Upgrading based on Amino-Modified Metal-Organic Frameworks | ECCE9, The Hague, The Netherlands. **Oral and Poster, 24.04.2013**

About the Author

Tim Arnold Wezendonk was born on December 22nd during the cold Dutch winter of 1986, in a town called Duiven in the province of Gelderland. Stories say that his first name was changed last-minute amidst a snow storm during which his father was watching a re-run of Dickens' *A Christmas Carol* on television. Tiny Tim completed his VWO on the Candea College in Duiven with a specialization in *Natuur & Gezondheid* and specific focus on chemistry. His final project comprised the synthesis of nitrocellulose and the investigation of the material as propellant; effectively blowing up parts of the lab with guncotton.

After graduation, he moved to the city of Delft where he obtained his BSc in Molecular Science and Technology and his MSc in Chemical Engineering. His BSc thesis research together with Mathijs Koot on a tunable drug-delivery system was highly recognized and resulted in his first co-authorship in the *Journal of the American Chemical Society*. During the MSc study, he applied his process engineering knowledge in practice whilst working as an intern at Fluor in Haarlem, as part of a design team of a polymer plant in Germany. Together with Matthijs Zweemer, he presented the conceptual design of a methane-enrichment plant with MOF sorbent at the 9th European Congress of Chemical Engineering in The Hague. The presentation of this MSc student-team design project, carried out under the supervision of dr. Pablo Serra Crespo, was further developed into a publication in *Chemical Engineering & Technology*. Tim carried out his MSc thesis research on the development of stable catalysts for high-temperature Fischer-Tropsch synthesis under the supervision of dr. Vera Santos and professor Gascon. For this work, ir. Wezendonk was awarded with the MSc Research Thesis Prize by the department of Netherlands Process Technology from the Royal Dutch Institute of Engineers. He continued and further expanded the research of his MSc thesis under supervision of professor Gascon in professor Kapteijn's Catalysis Engineering group as a PhD candidate. The findings of his PhD project on the development of a novel synthesis method for heterogeneous iron catalysts for Fischer-Tropsch synthesis using metal-organic frameworks as a template are described in this book.

Tim is married to Nicole and they together have a wonderful daughter Sofie, born in the first year of his PhD candidacy.

TUSSENSCHIET:

DIT VEL WORDT TIJDENS DE AFWERKING VERWIJDERD

SEPARATION:

THIS SHEET WILL BE REMOVED DURING THE BINDING PROCESS

TUSSENSCHIET:

DIT VEL WORDT TIJDENS DE AFWERKING VERWIJDERD

SEPARATION:

THIS SHEET WILL BE REMOVED DURING THE BINDING PROCESS